5

Localization Transport in Granular and Nanoporous Carbon Systems

by

Alex Weng Pui Fung

S.M., Massachusetts Institute of Technology (1991)
B.Sc.(Eng.), Queen's University, Canada (1988)

Submitted to the Department of Electrical Engineering and Computer Science
in partial fulfillment of the requirements for the degree of

Doctor of Philosophy

at the

MASSACHUSETTS INSTITUTE OF TECHNOLOGY

September 1994

Author .....
Department of Electrical Engineering and Computer Science
September 6, 1994

Certified by .....
Mildred S. Dresselhaus
Institute Professor of Physics and Electrical Engineering
Thesis Supervisor

Accepted by .....
Frederic R. Morgenthaler
Chairman, Departmental Committee on Graduate Students
Department of Electrical Engineering and Computer Science

Localization Transport in Granular and Nanoporous Carbon Systems

by

Alex Weng Pui Fung

Submitted to the Department of Electrical Engineering and Computer Science
on September 6, 1994, in partial fulfillment of the
requirements for the degree of
Doctor of Philosophy

Abstract

Porous carbon materials have long since been used in industry to make capacitors and adsorption agents because of their high specific surface area. Although their adsorption properties have been extensively studied, we have not seen the same vigor in the investigation of their physical properties, which are important not only for providing complementary characterization methods, but also for understanding the physics which underlies the manufacturing process and motivates intelligent design of these materials. The study of the new physics in these novel nanoporous materials also straddles the scientific forefronts of nanodimensional and disordered systems.

In this thesis, we study the structural and electrical properties of two nanoporous carbons, namely activated carbon fibers and carbon aerogels. Specifically, we perform Raman scattering, x-ray diffraction, magnetic susceptibility, electrical transport and magnetotransport experiments. Results from other experiments reported in the literature or communicated to us by our collaborators, such as porosity and surface area measurements by adsorption methods, electron spin resonance, transmission electron microscopy, mechanical properties measurements and so on, are also frequently used in this thesis for additional characterization information. By correlating all the relevant results, we obtain the structure-property relationships in these nanoporous materials.

This study shows that the transport properties of these porous materials can be used on one hand for sensitive characterization of complex materials, and on the other hand, for observing interesting and unusual physical phenomena. For example, as-prepared nanoporous carbon systems, exhibit in their low-temperature electrical conductivity a universal temperature dependence which is characteristic of a granular metallic system, despite their morphological differences. By studying further the magnetoresistance in these carbon materials, it is found that the variable-range hopping mechanism cannot be totally disregarded in the understanding of the low-temperature conduction process in some granular metals having a similar morphology. In the transport study of the heat-treated activated carbon fibers, the surprising observation of a negative magnetoresistance at room temperature has also provided some insight into the weak localization phenomenon in the percolation limit. In particular, the effects of anomalous diffusion in a percolating system is now included in the calculations of the weak-localization corrections to the conductivity and magnetoresistance, yielding a new temperature dependence of the dephasing distance.

These localization phenomena in the nanoporous carbon structures studied here are mostly understandable in terms of the existing theories for disordered systems, but their detailed interpretations often indicate problems and shortcomings in some of these theories, at times because the physical properties of the nanoporous carbon materials studied here

are unique among disordered materials. Hence, nanoporous carbons belong to a distinct class of disordered systems in their own rights. In the field of transport in disordered systems, porous media also seem to have been an oversight of the general research community, although theoretical percolation studies have often touched upon systems with similar morphologies. This thesis presents a study of the transport behavior in nanoporous carbons over the full spectrum of disorder, controlled by heat treatment, starting from the strong localization regime, then crossing the metal-insulator transition, and finally to the weak localization limit. In each regime of disorder, the existing theories are either adapted, and when necessary, extended to explain the observed transport behavior in these fascinating materials.

Thesis Supervisor: Mildred S. Dresselhaus
Title: Institute Professor of Physics and Electrical Engineering

Acknowledgements

A Ph.D. education is not merely an ordinary path to a career. It is rather a priviledge in which some are fortunate enough to be included, even more so when the precious opportunity happens to be granted by MIT. The glamor of course belongs to MIT but I am still thankful to MIT for my admission.

During my stay in Boston, there are many individuals who deserve thanks for their roles in molding my work, and myself as a person. Foremost important among these people is my thesis supervisor, Prof. Mildred S. Dresselhaus. Not only has she been very responsive to my needs in spite of her busy schedule (which every student expects (wishes?) his/her supervisor to do), but she has also instilled into me a vision, a sense of confidence, and other intangible qualities that combine to make a successful scientist like herself (This, I'm not sure how many supervisors can do with their students). Without overstating the fact, the completion of my Ph.D. degree and my future success are owed to Millie.

I also want to thank Dr. Gene Dresselhaus, who in many ways has been like another supervisor to me. I am very grateful to his acute opinion on many facets of my work and my career, and will miss his humor and counsel when I leave this place.

Dr. Donald E. Heiman of the National Magnet Laboratory is a mentor as well as a friend. I regret not seeking to work more closely with Don, from whom I could have learned more. His offer of a short-term postdoc position at the NML upon my graduation will be remembered as a token of needed help.

I value the enlightening discussions with my collaborators. They include Dr. Robert W. Pekala of the Lawrence Livermore National Laboratories and Prof. M. Endo from Shinshu University in Japan. I would also like to thank Prof. Erich Ippen of MIT for permitting me to try out some experiments in his femtosecond optics laboratory.

My stay at MIT overlapped the periods of several postdoctoral fellows in Millie's group.

I learnt my Raman spectroscopy skill from Dr. Gary Doll and Dr. Apparao Rao, enriched my knowledge of transport and disorder from my collaboration with Dr. Joey Z. H. Wang, and enjoyed the sharing of the outlook on a physicist's career with Dr. X. X. Bi. Their presence was beneficial to me and, I'm sure, to other students in Millie's group too.

Former colleagues Dr. Chi-Chung Chin, Masahiro Hosoya, Dr. Ali Kazeroonian, Kazuyashi Kuriyama, Dr. James Nicholls, Dr. Jim Speck and Anthony Thomas left too soon, but Dr. Steve Cheng, Dr. Paul Nguyen, Dr. Stan diVittorio and Dr. Jordina Vidal stayed long enough to give me a memory that will last a lifetime. I enjoyed playing bridge, going out to dinner in China Town, and running experiments with Steve. Stan liked to throw parties and his perspective on arguable issues in life, and I have never minded being on the receiving end. Jordina has always had her eyes focussed on the more important things in life, giving me a refreshing scent of humanistic values. This experience was strengthened by Paul, who was probably little known for his big heart.

Current members of Millie's group are acknowledged for... No, I won't go as formal as this for they are a fun group of people to be around with. Lyndon Hicks shares my passion for sports, and I couldn't be happier to have him as my officemate. Gillian Reynolds has been a big help to both my work and my English writing. Had it not been for her, some of the long sentences in my papers would have stretched out to the west coast. I love spending coffee breaks in the office of James Chen, who makes good coffee and lively conversations. I admire Siegfried Fleischer for his engineering skills and would recommend anyone to take a look at the amazing gadgets he built in the lab. After a long leave from electrical engineering, I enjoy being reminded of my root via the "communication" with Boris Pevzner in encripted EECS jargons. Manyalibo Matthews has been an eager participant in my projects and also a delight to work with or talk to. Nathan Belk, Joe Habib, Sun and Dr. Herb Zeiger are appreciated for their friendliness from a distance. Laura Doughty, our administrative assistant, is commendable for she is always on top of everything.

I wish to thank Prof. T. Orlando and Prof. M. Schlecht, both from the EECS department of MIT, for their support and advice which have made my life a lot easier here at MIT.

My values are more than once influenced by the interactions with my friends in Toronto, Hong Kong, and Boston. I am also fortunate to have my parents refocus my perspective of life whenever I went astray. These people shine bigger on my mind than my thesis, and the seemingly irrelevant mention of their names in this acknowledgement would do them more

injustice than honor.

Finally, I want to acknowledge MIT, in particular the department of Electrical Engineering and Computer Science, for the two teaching assistantships and the Lawrence Livermore National Laboratory for support of my thesis research under subcontract B130530.

September, 1994

Contents

List of Figures

List of Tables

Chapter 1

Introduction

In this thesis, we study the localization transport in granular and nanoporous carbon systems. Localization is a general term used to describe the tendency of the charge carriers to be localized or non-mobile in a disordered system. Specifically, there are two regimes of localization, namely the regime of strong localization, in which carriers are localized in a finite region in space in a similar manner to a hydrogenic impurity state, and the regime of weak localization, in which the probability of a diffusing carrier returning to the origin is enhanced due to the wave-like nature of the carrier in the case of quantum diffusion. Since the characteristics of each regime are manifested by the temperature and magnetic field dependences of the electrical conductivity, these transport properties are measured for our nanoporous carbon systems, which are naturally disordered but have a degree of disorder that can be controlled by either heat treatment or other preparation procedures. To illuminate the structure-property relationship, structural characterizations such as BET adsorption, Raman scattering, x-ray diffraction, and magnetic susceptibility measurements are performed, when appropriate. Because the transport properties of porous carbon systems have never been studied before, it is interesting to initiate a detailed study of these systems over a wide spectrum of disorder so that a comparison can be made in each regime of disorder with other disordered systems previously studied in the literature.

The granular and nanoporous carbon systems studied in this thesis include Activated Carbon Fibers (ACFs) and carbon aerogels. Not only do these materials present two morphologically different systems for the transport study, but each material also has its own potential for wide industrial applications, thus making their characterizations by various

means of some general interest.

ACFs are of great interest because they have a huge Specific Surface Area (SSA), exceeding that in other solids. A nominal SSA up to $3000\,m^2/g$ is not beyond reach of the technology to date, as reported by at least one manufacturer of ACFs. The large SSA is ascribed to the unusually large nanoporosity that results from the activation of the carbon fiber precursors. The activation process is essentially a violent oxidation process, by means of which carbon atoms are stripped from the graphite sheets by the reagents to open up randomly distributed and oriented nanopores with average size on the order of 10 Å. Because of their large SSA, ACFs are used in industry to build double-layer capacitors and rechargeable batteries [1.1]. Like other active carbons, ACFs are also a good adsorption agent for solvents and vapors.

Carbon aerogels, on the other hand, are a type of low-density microcellular material (LDMM). Carbon aerogels are derived by pyrolysis from resorcinol-formaldehyde (RF) aerogels, which consist of a highly cross-linked aromatic polymer. After the carbonization process, an amorphous carbon aerogel material results but the basic aerogel microstructure is retained. Further graphitization can be achieved by heat treatment but full graphitization is impossible even at high heat treatment because of the convoluted polymeric microstructure of the material. Carbon aerogels are known to possess many unique properties useful for industrial applications [1.2]. They include low mass density, low atomic number, low thermal conductivity, low thermal expansion, good chemical resistance, a wide range of acoustic impedance, high morphological homogeneity (e.g., spatially uniform cellular size distribution and mass density), easy control of structural parameters (such as particle size and porosity), and environmentally benign manufacturability. In general, LDMM are developed at several U.S. Department of Energy (DOE) National Laboratories mainly for high energy physics applications [1.2], such as making precursors or substrates for forming high-density gases or expanded plasmas to facilitate the study of expanded states of matter in laser and particle beam physics experiments, and building detectors for high energy particles (via the Čerenkov effect in solid-state LDMM). Other potential industrial uses include thermal insulation, sound barriers and support substrates for catalysts.

Although the adsorption properties of activated carbons and carbon aerogels have been extensively studied [1.3,1.4], the optical and the electrical properties of these porous materials have not been investigated with equal vigor. So far as optical spectroscopy is concerned,

infrared experiments have been carried out, for example, for activated carbon [1.5,1.6], but only to the extent of determining the surface species and their physi-sorption and chemisorption characteristics. Our Raman spectroscopic measurements, however, yield information about the intrinsic crystalline structure of the carbon system and help to elucidate the electrical transport results. Furthermore, the development of new characterization tools for porous materials in general should be beneficial to the engineering of their nanostructures (also known as nanoengineering), which is crucial for several industries, such as the optoelectronics industry where the unique properties of porous silicon are exploited.

Besides their commercial interest, porous carbons also provide a natural medium for studying the transport properties of mesoscopic systems. Since the advent of the synthesis of quantum structures (e.g., quantum dots, Coulomb island [1.7]), new transport phenomena have been observed and detailed studies of the transport properties of nanosize structures have become subjects of particular interest. The recent interest in mesoscopic systems consisting of clusters of atoms in the 1-100 nm size and possessing physical properties between the molecular and the bulk solid-state limits [1.8] also adds appeal to the study of nanoporous materials like carbon aerogels. Although the synthesis and properties of metal and semiconductor clusters (e.g., quantum dots) are the subject of extensive investigations, little attention has been paid to cluster-assembled porous materials [1.9]. This oversight is of particular interest to us since we believe that aerogels are one of the few monolithic materials presently available where the benefits of cluster assembly can be demonstrated. In particular, the unique optical, thermal, acoustic, mechanical, and electrical properties of aerogels are directly related to their nanostructure, which is composed of interconnected clusters (3-25 nm) with small interstitial pores (< 50 nm). This structure leads to extremely high surface areas (400-1000 m^2/g). With a large fraction of the atoms covering the surface of the interconnected clusters as compared to the interior, the molecular and the solid-state limits are indeed blurred.

As noted earlier, porous carbons are also a good material for studying strong localization and disorder-related phenomena in the transport properties because of their unusually high density of defects and grain boundaries. As our transport study traverses a wide spectrum of disorder from strong localization to weak localization, crossing a metal-insulator transition, we observed many interesting transport properties ranging from a universal temperature dependence of conductivity in both granular metals and our nanoporous carbon systems

in the strong localization regime, to a negative magnetoresistance near room temperature in heat-treated ACFs in the weak localization limit. The main theme of the thesis focuses not only on explaining these special properties for an individual system, but also on generalizing our explanations for these phenomena to other granular systems. In particular, we extend the Coulomb gap variable range hopping model [1.10], originally used for doped semiconductors, to cover the low temperature hopping conduction behavior in nanoporous carbons, and in general, sub-percolating granular metallic systems. We also utilize the concept of anomalous diffusion within the context of the weak localization theory to successfully explain the anomalous temperature dependences of the magnetoresistance and the dephasing length in our heat-treated ACFs as well as other weakly disordered systems near the percolating transition.

We begin by introducing the microstructures and the structural characterizations of as-prepared ACFs and carbon aerogels, respectively, in Chapters 2 and 3. Then, the magnetotransport studies of these as-prepared nanoporous carbons are presented in Chapter 4. Following a qualitative discussion in Chapter 5 of the structural, magnetic and transport properties of heat-treated carbon aerogels, a more systematic approach is used in Chapter 6 to describe the structural transformations in ACFs induced by heat treatment. Chapter 7 then studies the corresponding changes in the transport properties of those heat-treated ACFs. Chapter 8 presents the experimental results pertaining to the negative magnetoresistance near room temperature observed in weakly disordered ACFs, and provides an explanation based on the theories of weak localization and anomalous diffusion.

References

[1.1] M. Endo, Y. Okada, and H. Nakamura, Synth. Met. **34**, 739 (1989).

[1.2] J. D. LeMay, R. W. Hopper, L. W. Hrubesh, and R. W. Pekala, MRS Bulletin **15**, 19 (1990).

[1.3] K. Kaneko and N. Shindo, Carbon **27**, 815 (1989).

[1.4] E. Tanaka, Fuel and Combustion **54**, 241 (1987).

[1.5] M. Smíšek and S. Černý, *Active Carbon : Manufacture, Properties and Applications* (American Elsevier Publishing Company, New York, 1967).

[1.6] D. D. Saperstein, J. Phys. Chem. **90**, 3883 (1986).

[1.7] E. B. Foxman, P. L. McEuen, U. Meirav, N. S. Wingreen, Y. Meir, P. A. Belk, N. R. Belk, and M. A. Kastner, Phys. Rev. **B 47**, 10020 (1992).

[1.8] M. P. J. van Staveren, H. B. Brom, and L. J. de Jongh, Phys. Rep. (Rev. sect. of Phys. Lett.) **208**, 1 (1991).

[1.9] A. W. P. Fung, Z. H. Wang, K. Lu, M. S. Dresselhaus, and R. W. Pekala, J. Mat. Res. **8**, 1875 (1993), and the references therein.

[1.10] A. L. Efros and B. I. Shklovskii, J. Phys. **C8**, L49 (1975).

Chapter 2

Microstructures & Characterizations of Porous Carbons I: ACFs

In this chapter and the next, the fabrication and the characterizations of ACFs and carbon aerogels are described, respectively. The structural parameters which are used to form a detailed picture of the microstructures of the two materials are obtained from the various structural characterizations listed in Table 2.1. The transport characterization is also introduced to complement the structural studies. Some of the experiments are not sensitive enough for characterizing the as-prepared material, but are used because they are susceptible to the microstructural changes induced by variations in the external parameters, such as the heat treatment temperatures of ACFs and carbon aerogels, and the reactant/catalyst molar ratio in carbon aerogels. Hence, a brief discussion of these partially sensitive experiments in these 2 early chapters could serve as background material for later chapters on the effects of changing the external parameters.

In view of the fact that the particles in ACFs consist only of a few layers of graphitic sheets and no more internal structures like the polymeric filaments in carbon aerogels, ACFs are justifiably simpler in their nanostructures than carbon aerogels and are therefore chosen to be discussed in the first chapter of the 2-part sequence.

There are several books and review articles written on activated carbons [2.1–2.6], to which ACFs are likened. Together, these references form a general picture for the mi-

Characterizations	Materials	As-prepared (AP) /Heat-treated (HT)	Structural parameters measured
Brunauer-Emmett-Teller adsorption analysis	ACFs	AP & HT	Specific surface area
	Aerogels	AP only	
Gas/vapor adsorption	ACFs & Aerogels	AP	pore size distribution
Transmission Electron Microscopy	ACFs & Aerogels	AP & HT	Microstructural pictures
X-ray diffraction	ACFs	AP & HT	Interlayer distance (turbostraticity)
Raman spectroscopy	ACFs & Aerogels	AP & HT	In-plane microcrystallite size
Magnetic susceptibility	ACFs & Aerogels	AP & HT	Concentration of unpaired spins (dangling bonds)
Compressive modulus	Aerogels	AP & HT	Cellular morphology & interparticle connectivity

Table 2.1: Structural characterization experiments for ACFs and carbon aerogels, the materials (as-prepared vs heat-treated) they measured and the structural parameters under study. The characterizations of the heat-treated samples are discussed in Chapter 4.

crostructure of activated carbons, their adsorption properties, their applications in industry and the characterization methods used to determine their porosity and specific surface areas. Details, specific to ACFs and not discussed in these references, are emphasized in this section.

The fabrication of ACFs is of interest not only to electrical and chemical engineers, but also to our research group studying the transport properties of porous carbons. Traditionally prepared activated carbons exist only in powder form, necessitating the pelletization process for transport measurements. ACFs, on the other hand, have their fiber geometry retained by the activation process and are therefore naturally amenable to transport measurements.

Following the description of the fabrication process, the results obtained from water adsorption, transmission electron microscopy, x-ray diffraction, Raman scattering and magnetic susceptibility experiments are presented with their implications for the microstructure of ACFs. Then, a summary schematic description is given for the microstructure of ACFs.

2.1 Fabrication of ACFs

There are more than one precursors that can be used to produce ACFs. Some examples are PAN [2.7, 2.8], cellulose [2.9], pitch [2.10] and phenol [2.11, 2.12]. The precursor

materials of the ACFs we studied are isotropic pitch and phenol. The specific surface areas (SSAs) range from $1000\,m^2/g$ to $3000\,m^2/g$ for the pitch-based ACFs and from $1000\,m^2/g$ to $2000\,m^2/g$ for the phenolic ones.

The precursor is first spun to form the fiber. Then, the fiber is prepared for activation in an antiflammable process at a temperature of 200 to 400°C. Finally, the fiber is activated. In the activation process, the fiber is heated in the temperature range 800–1200°C for pitch-based fibers and 1100–1400°C for phenolic fibers in O_2, H_2O, CO_2, N_2 or other oxidizing atmospheres [2.13–2.17]. As examples, the first two oxidation processes are described below:

$$C + H_2O \longrightarrow H_2 + CO - 31 \text{ kcal} \tag{2.1}$$

$$C + O_2 \longrightarrow CO_2 + 92.4 \text{ kcal} \tag{2.2}$$

$$2\,C + O_2 \longrightarrow 2\,CO + 53.96 \text{ kcal} \ . \tag{2.3}$$

It is worth mentioning that an endothermal process is preferred to an exothermal one because the nature of the latter prevents accurate control of the temperature, and consequently of the specific surface area. It is seen in the above chemical reactions that carbon atoms, in reacting with the oxydizing agents, are turned into gaseous form and are stripped from the bulk material, leaving a large number of pores behind. The activation process for the phenolic ACFs used in this thesis is described in Ref. [2.12]. The main parameter that characterizes ACFs, the SSA, is controlled by the temperature and the time for activation, the activation process and the precursor materials. The SSA is measured using Brunauer-Emmett-Teller (BET) analysis of the adsorption isotherms of N_2 at 78 K and CO_2 at 195 K [2.12, 2.19].

The ACFs studied include 3 categories, namely pitch-based fibers (ACP), long phenolic fibers (FRL) and short phenolic fibers (FRS), where the manufacturer's designations are indicated in parentheses. Although the FRL fibers and the FRS fibers originated from the same precursor, they were treated differently by the manufacturer during their activation processes, resulting in differences in their microstructures and physical properties so that the resultant degree of disorder in these two types of ACFs could be quite different. FRL fibers are typically more than 10 cm long and FRS fibers are generally shorter than 1 cm. The ACP fibers, having a different precursor material, were expected to show yet a different microstructure.

2.2 Characterization Results

2.2.1 Water Vapor Adsorption

Like all activated carbons, ACFs have a highly porous structure and therefore a large SSA. This similarity merits a direct comparison between the microstructures of these two porous carbon materials and also validates the structural characterization of ACFs using the traditional adsorption methods originally employed for activated carbons. Because the microstructure of activated carbons had been well known even before ACFs became available, its immediate discussion below could help define the terminologies named for the unique features in a porous microstructure, which are essential for the later description of ACFs.

In the microstructure of a typical activated carbon material, there are four kinds of pores, categorized according to their sizes. The general picture can be likened to that of a human lung, in which bronchioles branch from bronchi. Similarly in activated carbons, branching from the macropores are some smaller mesopores which in turn have branches leading deeper into the bulk via a large density of even smaller and randomly distributed micropores and/or nanopores. The categorization criterion is not unique, but it is generally based on both the size and the adsorption properties of the pore, as described below and in Ref. [2.5]:

1. Macropores (> 50 nm) are responsible for bulk condensation of the vapor entering.
2. Mesopores/Transition pores ($2 - 50$ nm) are characterized by the existence of capillary condensation, liquid meniscus formation and a hysteresis loop in the benzene adsorption isotherm at 293 K. They are so named because their pore radius falls at the transition found in the plot of cumulative pore volume versus pore radius, usually obtained from mercury porosimetry or the water vapor adsorption method [2.12] (see below).
3. Micropores (< 2 nm) are the major component of adsorption and are defined to have a pore radius just below the sharp transition in the pore size distribution plot described above.
4. Nanopores (< 1 nm) are micropores in different locations and with smaller di-

Properties	FR10	FR12	FR15	FR20
SSA (m^2/g)	1000	1200	1500	2000
Micropore Radius (Å)	9	10	12	16
Pore volume (cc/g)	.22	.35	.50	.75
Benzene adsorption capacity (wt %)	22	35	45	65
Ash (%)	.03	.03	.03	.04
Conductivity at 300 K (S/cm)	~ 9	~ 11	$\sim 12 - 17$	$\sim 18 - 24$

Table 2.2: The physical properties of phenolic ACFs with different SSAs are listed. The conductivity depends to some extent on the amount of gas adsorbed in the material and in reality, a range of values around the tabulated numbers are found for the conductivity of ACFs [2.20].

mensions. While micropores are usually bounded by the *c*-faces of the platelets, nanopores are more likely to be found as punctures in the surfaces of platelets or as broken links as wide as a single-atom vacancy between neighboring platelets in the in-plane direction. Nanopores are probably not as important in activated carbons as in ACFs where the SSA could go up to $3000\,m^2/g$. In this regard, although the names nanopores and micropores are often used interchangeably (and inadvertently in this thesis), the distinction is convenient for the explanation of the extremely high SSA observed in ACFs (see Section 2.3).

The distribution of these pores in an activated carbon is usually described by a plot of cumulative pore volume against pore radius. Using the method of water vapor adsorption, the pore distribution was obtained for different grades of ACFs as well as granular activated carbon, as shown in Fig. 2-1. Each of the pore distribution curves for ACFs has a sharp transition at a definite pore radius and a flat slope on both sides of the transition, whereas for granular activated carbon, the transition is not as sharp and the curve continues to rise after the transition. As discussed previously, typical activated carbons have both mesopores, which smooth out the transition, and macropores, which yield a positive slope when the pore radius exceeds that at the transition. The behavior of the pore distribution curve for granular activated carbon is therefore consistent.

ACFs, however, show a very different characteristic behavior. Beyond the vertical transition, the slope of the curve for ACFs becomes very flat, indicating that pores with radii larger than the pore size at the vertical transition do not contribute significantly to the

effective pore volume. It is therefore concluded that almost all of the pore volume in ACFs is made up of micropores, and that ACFs do not possess many macropores and mesopores. This constitutes the major difference between common activated carbons and ACFs. It is not surprising then that the adsorption rate of the latter is 100 – 1000 times faster and its adsorption capacity 10 times greater than the former [2.12]. In Fig. 2-1, the grade numbers stand for the SSA divided by $100\,m^2/g$. It can be seen that the micropore size increases with SSA. Listed in Table 2.2 are some properties of the different types of phenol-based ACFs, extracted from Ref. [2.12].

2.2.2 Transmission Electron Microscopy

The Transmission Electron Microscopy (TEM) micrographs were taken by our collaborator Prof. M. Endo of Shinshu University in Japan. A selected picture, shown in Fig. 2-2, though for a pitch-based ACF, is believed to be typical of the microstructure of ACFs.

In this picture, the length of an elongated platelet in the longitudinal direction (a), which is believed to be the in-plane crystallite size L_a, is about 30Å while the length in the transverse direction (b) is about 10Å. While b could be the thickness of a platelet, it might also be the transverse length of a non-circular platelet or the projection of a platelet oriented with its c-axis not normal to the incident electron beam. Consequently, a mere look at a TEM picture without quantitative image analysis can only give an order-of-magnitude estimate of the thickness of a platelet, but such pictures reveal the existence of graphite platelets in ACFs, and gives a value for L_a consistent with the Raman results discussed below.

TEM pictures taken at different points of an ACF revealed no macropores or mesopores[1], not only confirming the finding of the vapor adsorption results of the previous section that micropores are indeed predominant in ACFs, but also further showing that the near absence of mesopores and micropores is ubiquitous.

2.2.3 X-Ray Diffraction

The x-ray powder diffraction experiments were performed on the phenol-based ACFs by the sample supplier, Kuraray Chemical Co. in Japan. The diffraction spectrum obtained

[1]Private communication with Prof. M. Endo, Faculty of Engineering, Shinshu University, Nagano, Japan

for the FRS12 fibers [2.20], as shown in Fig. 2-3 and typical of all ACFs measured, has a very broad feature centered near the angular position of the (002) Bragg peak of pristine graphite, indicating a highly inhomogeneous microstructure.

From the center position (2θ) and the integral breadth (B_h) of the broad feature in Fig. 2-3, the average interlayer distance $\hat{c}$ and the thickness L_c of the well-stacked graphite platelets described in Section 2.2.2 can be estimated, respectively. The value of $\hat{c}$ thus estimated is always greater than the $\hat{c}$ value of 3.35 Å in graphite, indicative of a *turbostratic* structure in ACFs, turbostratic meaning that the neighboring graphene planes are out of registry along the c-axis, unlike 3D graphite. The L_c value can be obtained from Scherrer's formula [2.21]:

$$L_c \simeq \frac{\lambda}{B_h \cos(\theta)} \tag{2.4}$$

where λ is the x-ray wavelength, and is found to be ~ 10 Å, corresponding to approximately 3 graphene layers when the thickness of each graphene layer is taken to be the $\hat{c}$ value for graphite (i.e., ~ 3.35 Å).

The Scherrer analysis should only be regarded as an order-of-magnitude estimation because line broadening in an x-ray diffraction spectrum could also be caused by strain, misorientation of graphite platelets, and microcrystallite size distribution [2.21]. For a consistency check, it is also noted that the BET measurements of the SSA indirectly provide an independent estimate for L_c. Using a simple structural model, in which the SSA of ACFs is made up of the surfaces of the platelets dissociated along the c-axis, we can write,

$$L_c = \frac{2}{(\mathrm{SSA})\,\rho} \tag{2.5}$$

where $\rho = 2.25\,\mathrm{g/cm^3}$ is the density of graphite. For SSA$= 1000\,\mathrm{m^2/g}$, L_c is again approximately 3 graphite layers, indeed consistent with the value obtained from the x-ray diffraction experiment.

2.2.4 Raman Scattering

The Raman scattering experiments were performed in the back-scattered configuration. An Argon-ion source was used to provide coherent radiation of less than 100 mW at a wavelength of 4880 Å. In order that the results be truly characteristic of the type of fibers under study, the laser beam was deliberately slightly defocussed on the sample so that more

fibers could be sampled and radiation heating could be avoided. The scattered beam from the sample was collected by a 50-mm camera lens into the entrance slits of a SPEX-1403 monochromator, the setting of which corresponded to a bandpass of $\sim 6\,\mathrm{cm}^{-1}$. This bandwidth is sufficiently narrow to preserve the lineshape of the broad Raman peaks observed. To avoid fluoresence which would otherwise be produced if the samples were held in some transparent medium, such as a capillary tube or a sandwich of glass plates, we used parafilm strips to wrap the ends of the fiber bundle onto a glass plate substrate with the middle part of the fiber bundle conveniently exposed to the incident radiation. Samples made of short fibers about 1 cm long did not fall apart when prepared in this fashion because static electricity held the fibers together. A good signal-to-noise ratio was obtained after averaging each spectrum over six 25-minute scans.

Raman measurements were made on a series of FRL, FRS and ACP fiber samples to examine how the in-plane microcrystallite size L_a varies with SSA, precursor material and its morphology. The effects of SSA, precursor material and morphology have been thoroughly studied in my Master's thesis [2.22], and the results will only be briefly summarized here. The main focus of this section is to extract structural information relevant to the transport study (e.g., L_a) and also to provide the background material for later discussion of the Raman characterizations of other disordered carbons, such as carbon aerogels and heat-treated ACFs.

Shown in Fig. 2-4 are the Raman spectra for FRL20, FRS20 and ACP20 fibers and their corresponding fitting curves. Each of these spectra is typical of all the fibers with different SSAs in the same fiber category. The alphabetic labels indicate whether the fibers are long phenolic, short phenolic or pitch-based ACFs. The numbers in the labels represent the SSA divided by $100\,\mathrm{m}^2/\mathrm{g}$, so that SSA $= 2000\,\mathrm{m}^2/\mathrm{g}$ for all the ACFs in Fig. 2-4.

Two peaks were observed in the Raman spectrum for each of the 10 samples studied. The peak near $1610\,\mathrm{cm}^{-1}$ is associated with the E_{2g_2} mode Raman-allowed in graphite ($1582\,\mathrm{cm}^{-1}$) while the other peak near $1360\,\mathrm{cm}^{-1}$ is attributed to the peak in the density-of-states spectrum for phonons, the appearance of which is not Raman-allowed in pristine graphite but is induced by disorder. The upshift of the graphitic peak from the HOPG value could be due to strain, contribution from another disorder-induced peak near $1620\,\mathrm{cm}^{-1}$, or the combined effects of charge transfer and charge-transfer-induced lattice contraction. The fact that ACFs are observed to be p-type at room temperature [2.20] is consistent with

parameters	FRL10	FRL15	FRL20	FRS12	FRS15	FRS20	ACP10	ACP15	ACP20	ACP30
ν_{1360}	1348	1350	1350	1348	1348	1347	1347	1345	1345	1342
Γ_{1360}	152	156	141	120	124	118	114	113	102	103
ν_{1580}	1611	1612	1611	1606	1612	1610	1610	1607	1609	1606
Γ_{1580}	67	64	68	61	61	57	57	57	54	56
$1/q$	-0.23	-0.19	-0.23	-0.10	-0.18	-0.18	-0.17	-0.16	-0.16	-0.17
Γ_{1580}/q	-15	-12	-16	-6	-11	-10	-10	-9	-9	-10
I_{1360}/I_{1580}	1.89	1.90	1.92	1.67	1.69	1.70	1.69	1.81	1.70	1.84

Table 2.3: Listed are the fitting parameters obtained from fitting a Lorentzian line at $\sim 1350\,\mathrm{cm}^{-1}$ and a BWF line at $\sim 1610\,\mathrm{cm}^{-1}$ to the data. The numbers in the fiber labels indicate their specific surface area in $100\,\mathrm{m}^2/\mathrm{g}$.

the direction of the frequency shift similarly observed in acceptor-doped GICs [2.23, 2.24]. Notwithstanding the frequency upshift, the presence of a graphitic peak indicates that despite the disorder due to the small size of the platelets, the platelets themselves remain quite graphitic in the plane.

The best fit to the data was obtained with a Lorentzian fit to the broad line near $1360\,\mathrm{cm}^{-1}$ and a Breit-Wigner-Fano (BWF) lineshape around $1610\,\mathrm{cm}^{-1}$. The latter lineshape results from the interaction of a Raman-active continuum with the discrete Raman-allowed E_{2g_2} mode [2.25]. The BWF lineshape was also observed in the Raman spectra for other disordered graphitic systems, such as ion-implanted graphite [2.26], and stage-1 alkali metal graphite intercalation compounds (GICs) C_8K, C_8Rb and C_8Cs [2.23]. The BWF lineshape is described by the following expression:

$$I(\omega) = \frac{I_0[1 + 2(\omega - \omega_0)/q\Gamma]^2}{1 + [2(\omega - \omega_0)/\Gamma]^2} \tag{2.6}$$

where $I(\omega)$ is the intensity as a function of frequency, I_0 the peak intensity, $1/q$ the interaction between the discrete E_{2g_2} mode and the Raman-active continuum, ω_0 the center phonon position and Γ the full-width-at-half-maximum-intensity (FWHM) of the unweighted Lorentzian (for which $q \to \infty$). The broad peak near $1360\,\mathrm{cm}^{-1}$ is disorder-induced, and has also been observed in other disordered graphitic systems such as benzene-derived carbon fibers [2.27]. Analysis of these two lines yields values for the central frequencies (ν), the FWHMs (Γ), and the relative integrated intensities I_{1360}/I_{1580} of the disorder-induced peak near $1360\,\mathrm{cm}^{-1}$ to the BWF peak around $1610\,\mathrm{cm}^{-1}$, as well as values for Γ_{1580}/q and the dimensionless interaction parameter $(1/q)$ for the Raman-active mode with the BWF lineshape. The results are summarized in Table 2.3.

From Table 2.3, we can see that all the fitting parameters for the Raman scattering experiments are sensitive only to the type of ACFs, but not to the SSA. The one parameter which is of relevance to the transport study is the ratio (R) of the integrated intensity of the disorder-induced line at $1360\,\mathrm{cm}^{-1}$ (I_{1360}) to that of the Raman-active line at $1580\,\mathrm{cm}^{-1}$ (I_{1580}), because the in-plane microcrystalline size L_a of a graphitic system can be determined from Knight's empirical formula given by [2.28]:

$$L_a = 44 \left(\frac{I_{1580}}{I_{1360}}\right)^{-1} \equiv \frac{44}{R} \ . \tag{2.7}$$

It is interesting to see that the ratios R for ACFs are always larger than 1.65, whereas those for all the disordered carbon-based materials listed in Ref. [2.28] for finding Eq. (2.7) are below 1.5. The microcrystallite size is thus estimated from extrapolation and found to be $\sim$ 23Å – 26Å, as listed in Table 2.3 for each ACF studied here. In this limit, the Raman scattering characterization technique becomes less sensitive and this may explain the insensitivity of the R ratio, the linewidths and the Fano $1/q$ parameter to SSA in Table 2.3. The insensitivity of L_a to SSA is, however, consistent with our simple platelet model for SSA, previously described by Eq. (2.5).

2.2.5 Magnetic Susceptibility

The magnetic susceptibility (χ) measurements do not usually give direct information about the microstructure of a material because it measures the concentration of (localized and/or conduction) unpaired spins. However, for porous materials with a very large surface area, the localized unpaired spins can be demonstrated, as discussed below, to be the dangling bonds, thus making the determination of their concentration a measure of the degree of disorder within the microstructure.

S. L. diVittorio *et al.* [2.18] used the electron spin resonance (ESR) technique to measure χ for ACFs with SSAs of $2000\,\mathrm{m}^2/\mathrm{g}$ and $3000\,\mathrm{m}^2/\mathrm{g}$, respectively and found the following results.

1. A narrow peak that appeared in the ESR spectrum after the desorption process (evacuation of the ESR cell to a $\sim 10^{-5}$-Torr high vacuum at heat-treatment temperatures between room temperature and 350°C) is ascribed to the dangling bonds because this peak exhibits a Curie-like temperature dependence, and disappears when the ACFs

were reexposed to air. Furthermore, the χ response to the desorption-readsorption process is reversible. The concentration of these localized spins in the ACP30 samples is estimated to be 2×10^{19}/g.

2. An extremely broad peak was also observed, with linewidth on the order of 950 ± 50 Gauss and 450 ± 20 Gauss for the ACP30 and the ACP20 fibers, respectively. Chemical analysis rules out the presence of magnetic species in the ACF samples. The broad linewidth is attributed to the boundary scattering of the conduction carriers (a T_1 spin-lattice relaxation process) and their dipole interactions with the dangling bonds (a T_2 spin-spin relaxation process).

3. The conduction carrier concentration, estimated by the analysis of the broad peak to be 3.2×10^{21}/g for the ACP30 fibers and 1.8×10^{20}/g for the ACP20 fibers, increases with SSA, consistent with the band structure model often used for disordered carbonic materials, in which the Fermi level is pushed down below the mobility edge in the valence band by the presence of disorder, creating hole carriers.

2.2.6 DC Electrical Resistivity

We now investigate the use of transport properties as a characterization tool for ACFs. Although the electrical conductivity (σ) is actually shown in this section to be weakly dependent on SSAs, Chapter 7 will show that σ is very sensitive to heat treatment. Another purpose of this section is to demonstrate an interesting phenomenon of a universal temperature dependence of σ in ACFs prepared in different conditions.

The transport experiment involved measurements of the resistance of single fibers over a range of temperature spanning 4.2 K to 300 K using the four-point probe method. The temperature scans were allowed to take place by natural warming. Silver paint was used to establish contacts between the fiber resting on a glass plate and four copper wires placed in the proximity of the fiber. The contact resistance measured in this experiment was on the order of $10\,\Omega$ typically and was much smaller than the sample resistance ($> 1\text{k}\Omega$).

The voltage across the middle contacts was measured by a Keithley model-181 digital nano-voltmeter while the current to the fiber was provided by a Keithley model-225 nanoampere source. Because the sample resistance could go up to tens of megaohms at low temperature, measurements of such high resistances required a few precautions. First, the

current level was adjusted so that the power dissipated in the sample was less than 10^{-7}W. Secondly, a resistor of $\sim 10\,\mathrm{M}\Omega$ was placed across the input terminals of the nano-voltmeter. At low temperature, it could divert the current from the sample so that the current source could now provide an output current above its minimum range without causing overflow in the nanovoltmeter. The resistor also reduced the total impedance seen by the nanovoltmeter so that a voltage correction was not necessary. Finally, neighbouring samples were placed at least 5 cm apart, a distance observed to be long enough to avoid the problem of signal coupling of two large resistances at low temperature. The resistivity of each sample was calculated using the diameter and length of the sample measured by Scanning Electron Microscopy (SEM). A typical diameter for a phenolic ACF was about $10\,\mu$m.

Fig. 2-5 shows the temperature-dependent electrical conductivities we measured for three long phenolic fibers (FRL10, FRL15 and FRL20) and three short ones (FRS12, FRS15 and FRS20). The error bars are about 20 % of the absolute value and are mainly due to uncertainty involved in measuring the diameter of a non-uniformly thick fiber. It is to be noted that while the values of the conductivities relative to the room-temperature value are adequate to describe the temperature dependence, knowledge of the absolute values of the conductivities of various ACFs is important for making comparisons between these fibers.

In this connection, we observe in Fig. 2-5 that room-temperature $\sigma(300\mathrm{K})$ measurements can be a sensitive characterization parameter for the SSA and type (FRL vs. FRS) of ACFs. As will be demonstrated below, hopping of some kind is dominant in ACFs. Hopping conductivity, being proportional to the density of *localized* states according to the Einstein relation, should therefore increase with the degree of disorder. As a result, we deduce from Fig. 2-5 that the amount of disorder increases with SSA and that the FRL fibers are more disordered than the FRS fibers. This agrees with our observations in the Raman scattering experiment described above. Further support can be found in the photoconductivity data obtained by Kuriyama and Dresselhaus [2.20]. Their results show that both the photoconductivity and the decay time increase with SSA, with the decay time less dependent on SSA than the photoconductivity. This trend is internally consistent only if the photo-carrier mobility increases with SSA. Consequently, if the conduction by the photo-carriers is also governed by hopping at low temperature, the disorder must increase with increasing SSA.

To understand the temperature dependence of σ, it is suggestive to make a comparison

Fiber	FRL10	FRL15	FRL20	FRS12	FRS15	FRS20	ACP10
p (robust fit)	1.8	2.1	1.9	2.0	2.0	1.9	2.2

Table 2.4: Values for the numerical constant p in the exponent of Eq. (2.8) as determined by a robust fit to the log-log plot of the temperature dependence of the local activation energy. The conductivity data for the ACP10 fibers were extracted from Ref. [2.40].

between the room-temperature (RT) conductivity of ACFs and those of other carbon systems because systems with conductivities of about the same magnitude at RT may exhibit the same kind of conducting behavior at low temperature. A typical range of RT conductivity for phenolic ACFs is approximately 10–30 S/cm, which is comparable to that for active carbon rods [2.29], Saran carbon [2.30] and glassy carbon [2.31]. ACFs are slightly more conductive than evaporated carbon thin films [2.32] and a great deal less conductive than vapor-grown carbon fibers [2.33]. At low temperature, thin carbon films have been reported to conduct by 2-dimensional variable-range hopping conduction (VRHC), and at high temperature, transport is enhanced by the thermal activation of carriers [2.34]. The temperature dependence of the conductivity of glassy carbon, however, has been reported to follow the behavior of 3-D VRHC, with some corrections at low temperature [2.35].

VRHC is generally governed by Mott's law in the form of [2.36]:

$$\sigma(T) = \sigma_0 \exp\left[-\left(\frac{T_0}{T}\right)^{1/p}\right] \tag{2.8}$$

where σ_0 is the high-temperature conductivity value, T_0 a fitting parameter sensitive to the energy needed for hopping, and $p = d+1$ with d equal to the dimensionality of the system. We determined the values for p and T_0 using 3 different procedures, as shown below.

1. The comparison of the plots of the logarithm of the electrical resistivity against $1/T$, $1/T^{1/2}$ (Fig. 2-6), $1/T^{1/3}$ and $1/T^{1/4}$ (not shown) for all phenolic ACFs shows that the $1/T^{1/2}$ plots are the most linear curves over the entire measurement temperature range, thus yielding $p = 2$.

2. Because of the near linearity observed at the low-temperature portion of almost all $1/T^{1/p}$ plots for ACFs and for other disordered materials previously reported in the literature, there is some ambiguity in the value for p in Eq. (2.8). Following Hill [2.37] and Zabrodskii [2.38], we can confirm the value for p more quantitatively by plotting

Fiber	FRL10	FRL15	FRL20	FRS12	FRS15	FRS20
σ_0 (S/cm)	35	37	61	29	47	55
T_0 (K)	530	580	330	350	360	430

Table 2.5: Values for the parameters obtained from the fit to the conductivity data using Mott's law with $p = 2$.

$\log T$ against the local activation energy e_a defined by:

$$e_a \equiv \frac{d(\log \rho)}{d(k_B T)^{-1}} \tag{2.9}$$

where k_B is the Boltzmann constant. Deemphasizing the large fluctuation in the high-temperature portion of the plot, induced by the process of differentiation, we obtained the values for p in Table 2.4 using a robust linear fit [2.39]. All the listed p values center around 2, consistent with the linearity in the $1/T^{1/2}$ plot.

3. The best non-linear fits of the $\sigma(T)$ data for all phenolic ACFs to Eq. (2.8) over the range 4 K $< T <$ 300 K were obtained with $p = 2$ and are shown in Fig. 2-5(a). Because the least-square value for p becomes closer to 2 when the fit is over temperatures below 100 K, we also fit our data only over this temperature range to obtain more accurate values for the fitting parameters, which were generally found to change by less than 30 % from the original values. The fits for $T < 100K$ is shown as solid lines in Fig. 2-5(b) and the corresponding fitting parameters are listed in Table 2.5. A linear fit to the $1/T^{1/2}$ plots in Fig. 2-6 for low-temperature regions also yields fitting values consistent within 10 % with those listed in Table 2.5.

DiVittorio *et al.* have examined the temperature dependence of the dc electrical conductivity of ACP10 fibers (where SSA = $1000\,\mathrm{m}^2/\mathrm{g}$) over the temperature range 25 K$<$ T $<$300 K [2.40] and found that it follows 2D VRHC. Their conductivity data were extracted and analyzed according to our previous procedure. Comparisons of the different $1/T^{1/p}$ plots yields $p = 3$, in agreement with their conclusion [2.40], but the $1/T^{1/2}$ plot has almost as good a linear fit. Furthermore, the e_a plot in accordance with Eq. (2.9) yields $p = 2$, which is also listed in Table 2.4. In fact, it was found that non-linearly fitting our $\sigma(T)$ data for phenol-based ACFs to Eq. (2.8) over a lower temperature range (e.g., $T <$ 100K) always yields a value of p closer to 2. Hence, the $p = 3$ value reported in

Ref. [2.40] could be a result of the lack of data below 20 K.

The $p = 2$ behavior is universal for ACFs, irrespective of their precursors, manufacturing conditions, SSAs, and perhaps in general, degrees of disorder. Several transport models including 1D variable-range hopping (VRH), Coulomb-gap VRH and charge-energy-limited tunneling can give rise to Eq. (2.8), and the choice of the most likely model will be discussed in Chapter 4.

2.3 Summary of the Microstructure of ACFs

In this section, a schematic diagram representative of the microstructure of ACFs is proposed in accordance with the experimental evidence presented so far in this chapter. This schematic forms the basis for the discussions in later chapters of the transport experiments and the structural transformations induced by heat treatment. The similarity between ACFs and granular metallic systems is highlighted. The role of nanopores in forming an SSA of $3000\,\mathrm{m}^2/\mathrm{g}$ in ACFs is also elaborated at the end.

Figure 2-7 is a schematic diagram based on the TEM micrograph for the microstructure of ACFs, showing the randomly oriented and uniformly distributed micropores and graphite platelets. The platelets are observed by TEM to be locally aligned for a distance of a few platelets in the in-plane direction but are, on the global scale, randomly oriented. Each micropore is of an almost fixed size, determined by the water adsorption method to be on the order of $\sim 10\,\text{Å}$, and is bounded by graphite platelets, each found by Raman spectroscopy to be approximately 30 Å in diameter and by x-ray diffraction to be fewer than 3 graphene layers in thickness. The number of layers drawn for each platelet in Fig. 2-7 is therefore only a crude approximation. These platelets are believed to be quite graphitic individually because of the presence of the Raman-active peak in the Raman spectrum. Such an admixture of conductive (the platelets) and insulating (the micropores) regions constitutes a unique granular metallic system, which is discussed in connection with the transport results in Chapter 4.

To be a legitimate granular metallic system, the platelet boundary must have the effect of confining the carriers. In fact, when the universal $p = 2$ temperature dependence of the conductivity is explored in Chapter 4, the platelets are treated as localization sites in order to adapt the Coulomb-gap variable-range hopping model to ACFs. We found some partial

evidence of carrier localization by the platelets by associating the increase in the density of states in ACFs of higher SSAs, evidenced by both the conductivity and photoconductivity experiments [2.20,2.41], to the increase in platelet density, which must result from both the reduction in platelet thickness with increasing SSA, according to Eq. (2.5), and the weak SSA dependence of mass density.

It is implicit in Fig. 2-7 that since the micropores are bounded by the c-faces of the platelets, Eq. (2.5) should explain the high SSA of ACFs. However, according to this simple model, a graphite platelet inside a $3000\,m^2/g$ fiber can only be one layer thick, which is impossible in view of the fact that in order to hold this ACF in fiber form, there need to be some thicker platelets. It is even more difficult to use this simple model to explain the maximum SSA ($5000\,m^2/g$) reported for ACFs in powder form[2].

We propose yet another simple model in which nanopores of the size of a few atomic vacancies are allowed to form on the c-surfaces of each platelet and be accessible to adsorbant species to contribute to the total SSA. These nanopores could be the relics and the platelets the remnants left behind by an oxidizing reagent along its destructive path.

The smallest theoretical nanopore within a platelet is formed by a single atomic vacancy. Such an elemental vacancy can be modeled as the space bounded by 3 perpendicularly bisecting surfaces between nearest-neighbouring atom distances in the in-plane direction (each denoted by S_s) and 2 in the c-axis direction (each contributing S_t). Nanopores of any size can be made up of any number of these elemental vacancies clustered together. Both 1-layer and 2-layer graphite platelets are supposed to be present. The pores on the two graphene layers are very likely to overlap and have the same size according to the above discussion on the formation of nanopores. Therefore, for a platelet n layers thick, with a number N of M-atom cluster stripped from each layer, without double-counting the overlapped surfaces from the nearest neighbors within the cluster, the SSA becomes:

$$\mathrm{SSA} = \frac{2S - 2NMS_t + nN(M+2)S_s}{\rho_m ncS - nNMm} \tag{2.10}$$

where S is the surface area of one c-surface of the platelet, ρ_m the mass density of graphite, c the inter-layer distance in pure graphite, and m the mass of a carbon atom.

[2]Private communication with Prof. M. Endo, Faculty of Engineering, Shinshu University, Nagano, Japan. It is worth noting that this SSA value is not measured by the N_2 adsorption method, as the entry to a micropore becomes too small to admit an N_2 molecule, but rather by the capacitance method.

M	1	2	3	Max.
NM (%) for 1-layer platelets	16	22	26	35
$2NM$ (%) for 2-layer platelets	23	30	34	46

Table 2.6: Percentages of the total number of atoms (NM and $2NM$) taken away from platelets of 1 layer thick and also of 2 layers thick, respectively, as we increase the size (M number of atoms) of the pores within each layer. The maximum M value corresponds to $N = 1$. The SSA is taken to be $5000\,m^2/g$ and the size of the platelet is irrelevant for each model considered.

In Table 2.6, we have listed the percentage of the total number of atoms that has to be taken off a platelet (the size is irrelevant after normalization by the total number of atoms) to obtain an SSA of $5000\,m^2/g$. Both 1-layer and 2-layer platelets are considered. Considering that the maximum number of atoms allowed to be stripped from a 1-layer platelet is more tolerable than that allowed from a 2-layer platelet, we think that a 5000-m^2/g ACF consists of relatively more 1-layer platelets, consistent with the fact that this carbon actually exists in powder form. For an SSA of $3000\,m^2/g$, similar calculations should result in even a lesser population of nanopores, a number that is certainly smaller than the percolation threshold required to break apart the fiber. Hence, the existence of nanopores is a feasible explanation for the huge SSA observed in ACFs.

References

[2.1] J. W. Hassler, *Activated Carbon* (Chemical Publishing Company, New York, 1963).

[2.2] M. M. Dubinin, "Porous structure and adsorption properties of active carbons", in *Chemistry and Physics of Carbon, vol. 2*, edited by Philip L. Walker, Jr. (Marcel Dekker, New York, 1966), p. 51.

[2.3] M. Smíšek and S. Černý, *Active Carbon : Manufacture, Properties and Applications* (American Elsevier Publishing Company, New York, 1967).

[2.4] J. S. Mattson and H. Mark, Jr., *Activated Carbon : Surface Chemistry and Adsorption from Solution* (Marcel Dekkar, New York, 1971).

[2.5] R. C. Bansal, J.-B. Donnet, and F. Stoeckli, *Active Carbon* (Marcel Dekkar, New York, 1988).

[2.6] F. Rodríguez-Reinoso and A. Linares-Solano, "Microporous structure of activated carbons as revealed by adsorption methods", in *Chemistry and Physics of Carbon, vol. 21*, edited by Peter A. Thrower (Marcel Dekker, New York, 1989), p. 1.

[2.7] H. Nagata and T. Yoshida, Chemical Economics, 44 (April 1977).

[2.8] S. Ikegami and K. Shimazaki, Fuel and Combustion **54**, 2 (1987).

[2.9] N. Ishizaki, Chem. Eng., 24 (July 1984).

[2.10] K. Tai and N. Shishido, Polym. Processing **35**, 384 (1986).

[2.11] G. N. Arons and R. N. Macnair, Textile Res. J. **42**, 60 (1972).

[2.12] E. Tanaka, Fuel and Combustion **54**, 241 (1987).

[2.13] A. Yoshida, I. Tanahashi, Y. Takeuchi, and A. Nishino, IEEE CHMT-10 **1**, 100 (1987).

[2.14] N. Kasaoka, Y. Sakata, E. Tanaka, and R. Naito, J. Chem. Soc. Jpn, **5**, 990 (1987).

[2.15] G. M. Nieh and D. T. Grow, J. Colloid Interface Sci. **119**, 280 (1987).

[2.16] J. W. Herrick, in 23rd Ann. Tech. Conf. SPI Reinforced Plastics/Composites, 16A (1968).

[2.17] Y. Komatsubara, S. Ida, H. Fujitsu, and I. Mochida, Fuel **63**, 1738 (1984).

[2.18] S. L. di Vittorio, A. Nakayama, T. Enoki, M . S. Dresselhaus, M. Endo, and N. Shindo, J. Mater. Res. **8**, 2282 (1993).

[2.19] S. Brunauer, P. H. Emmett, and E. Teller, J. Am. Chem. Soc. **60**, 309 (1938).

[2.20] K. Kuriyama and M. S. Dresselhaus, J. Mater. Res. **6**, 1040 (1991).

[2.21] M. S. Dresselhaus, G. Dresselhaus, K. Sugihara, I. L. Spain, and H. A. Goldberg, *Graphite Fibers and Filaments* (Springer, Berlin, Heidelberg, 1988).

[2.22] A. W. P. Fung, *Characterization of Activated Carbon Fibers*, Master's thesis, Department of Electrical Engineering and Computer Science, MIT, 1991.

[2.23] M. S. Dresselhaus and G. Dresselhaus, in *Light Scattering in Solids III*, edited by M. Cardona and G. Güntherodt, Topics in Applied Physics, vol. 51 (Springer, Berlin, Heidelberg, 1982), p. 3.

[2.24] C. T. Chan, K. M. Ho, and W. A. Kamitakahara, Phys. Rev. **B36**, 3499 (1987).

[2.25] M. V. Klein, in *Light Scattering in Solids*, edited by M. Cardona, Topics in Applied Physics, vol. 8 (Springer, Berlin, Heidelberg, 1975), p. 147.

[2.26] B. S. Elman, M. S. Dresselhaus, G. Dresselhaus, E. W. Maby, and H. Mazurek, Phys. Rev. **B24**, 1027 (1981).

[2.27] T. C. Chieu, M. S. Dresselhaus, and M. Endo, Phys. Rev. **B26**, 5867 (1982).

[2.28] D S. Knight and W. B. White, J. Mater. Res. **4**, 385 (1989).

[2.29] W. W. Smeltzer and R. McIntosh, Can. J. Chem. **31**, 1239 (1953).

[2.30] J. R. Dacey, D. F. Quinn, and J. T. Gallagher, Carbon **4**, 73 (1966).

[2.31] F. Carmona, P. Delhaès, G. Keryer, and J. P. Manceau, Solid State Commun. **14**, 1183 (1974).

[2.32] T. Hanawa and J. Kakinoki, Carbon **1**, 403 (1964).

[2.33] J. Heremans, Carbon **23**, 431 (1985).

[2.34] P. Delhaès and F. Carmona, in *Chemistry and Physics of Carbon, vol. 17*, edited by P. L. Walker, Jr. and P. A. Thrower (Marcel Dekker, Inc., New York, 1981), p. 89.

[2.35] Dennis F. Baker and Robert H. Bragg, Phys. Rev. **B 28**, 2219 (1983).

[2.36] N. F. Mott, *Conduction in Non-Crystalline Materials* (Oxford University Press, New York, 1987).

[2.37] R. M. Hill, Phys. Status Solidi **A35**, K29 (1976).

[2.38] A. G. Zabrodskii, Sov. Phys.–Semicond. **11**, 345 (1977).

[2.39] W. H. Press, B. P. Flannery, S. A. Teukolsky, and W. T. Vetterling, *Numerical Recipes in C* (Cambridge University Press, New York, 1988).

[2.40] S. L. di Vittorio, M. S. Dresselhaus, M. Endo, J. P. Issi, and L. Piraux, and V. Bayot, J. Mater. Res. **6**, 778 (1991).

[2.41] A. W. P. Fung, A. M. Rao, K. Kuriyama, M. S. Dresselhaus, G. Dresselhaus, M. Endo, and N. Shindo, J. Mater. Res. **8**, 489 (1993).

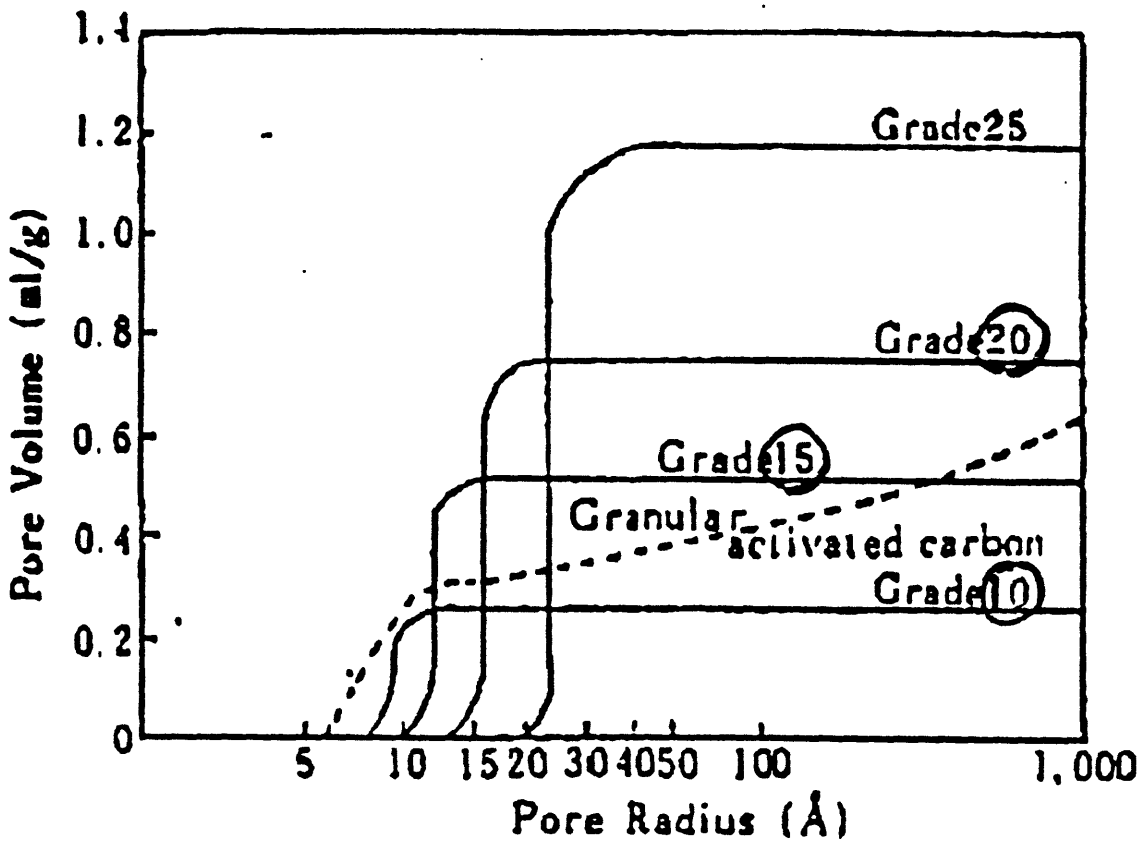

Figure 2-1: Cumulative porous volume is plotted against pore radius for various grades of phenolic ACFs and ordinary granular activated carbon. The almost vertical transition in the pore distribution and the flat slope after the transition for phenolic fibers suggests that micropores make up almost the entire porous volume. The transition is not as sharp for granular active carbon, indicating that mesopores might play an important role in adsorption for these materials. [2.12]

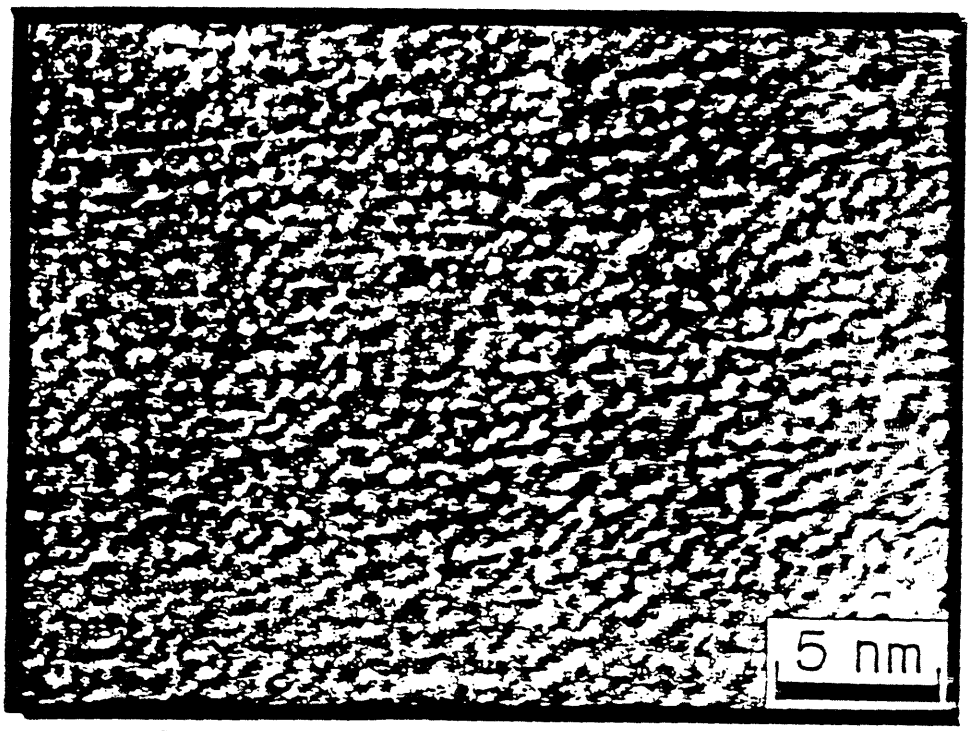

Figure 2-2: The TEM picture shows that the size of a micropore in ACP30 (a pitch-based ACF with SSA = 3000 m^2/g) is $\sim 8 - 30$ Å. A graphite platelet, as estimated from Raman scattering, is of about the same size. (Courtesy of Professor M. Endo, Faculty of Engineering, Shinshu University, Japan)

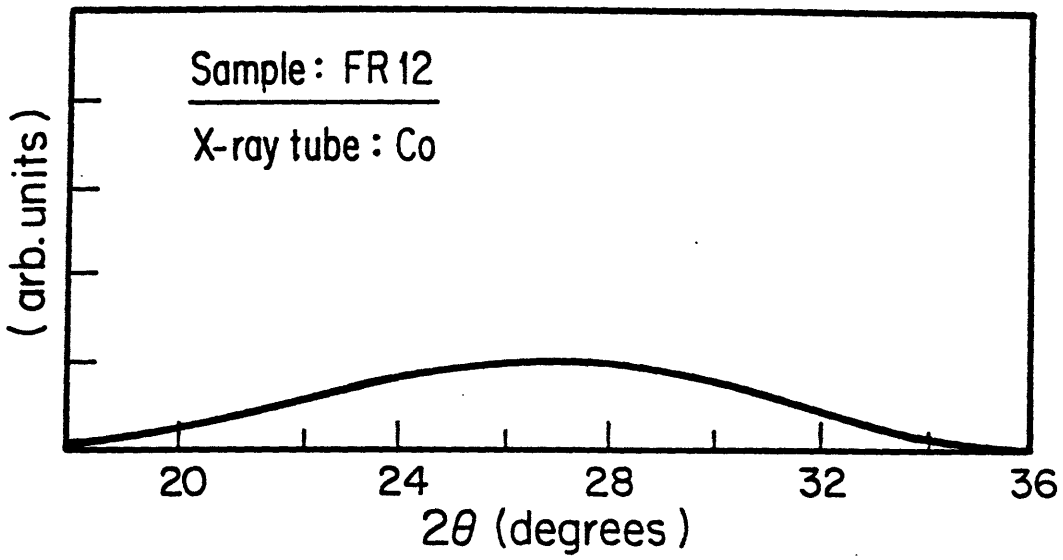

Figure 2-3: The X-ray diffraction pattern for the 002 reflection for the FRS12 ACFs shows an abnormally broad line-width, indicating strong disorder. The figure is extracted from Ref. [2.20] and the label FR12 in the figure is equivalent to our label FRS12 used in the text.

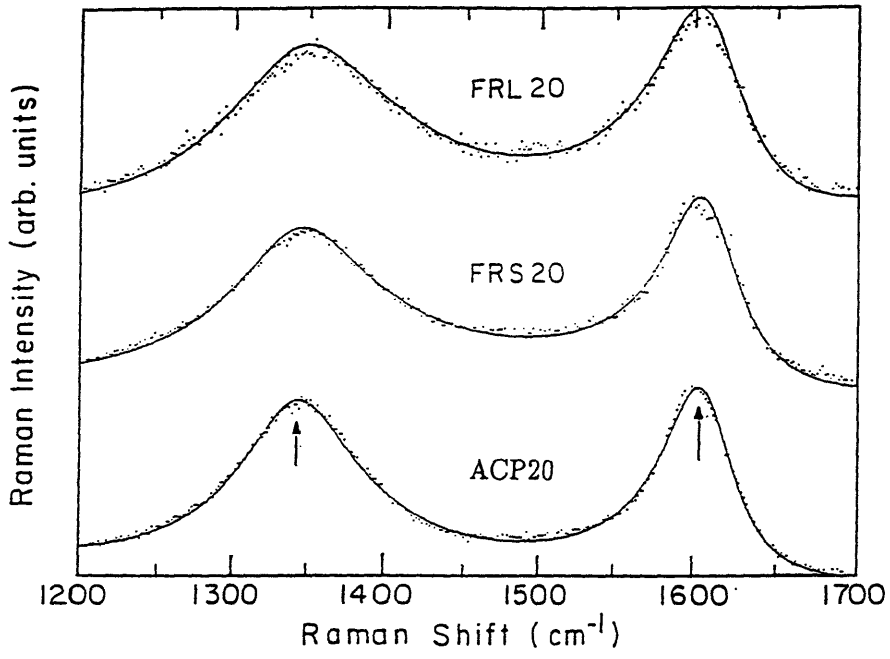

Figure 2-4: Raman spectra for FRL20 (top figure), FRS20 (middle figure) and ACP20 (bottom figure) activated carbon fibers. The solid line is the fit to a BWF line at around 1610 cm^{-1} and a Lorentzian line at $\sim$ 1350 cm^{-1}, indicated by vertical arrows.

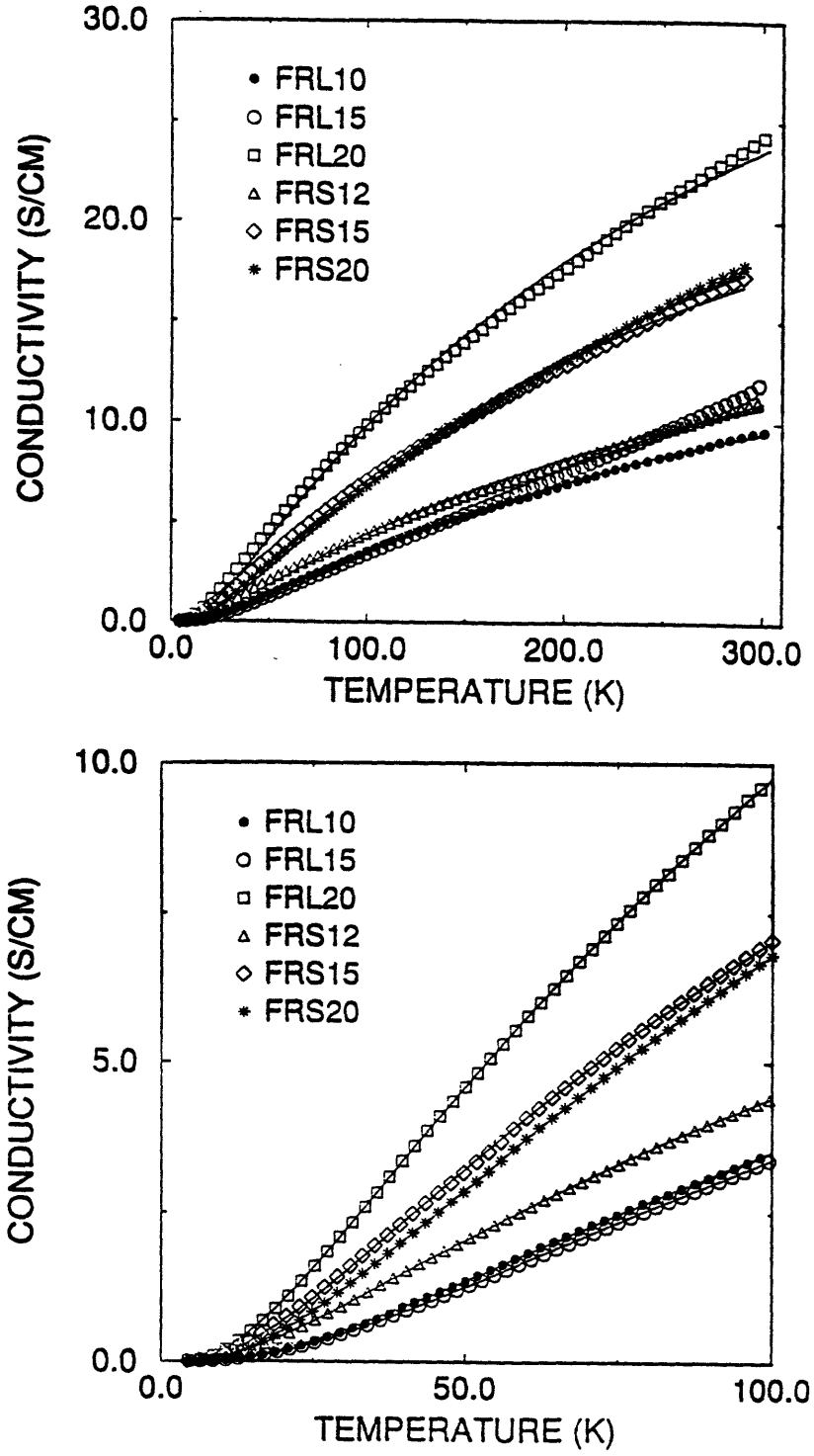

Figure 2-5: Temperature dependence of the conductivity for phenolic ACFs with the listed specific surface area values and the fits using Eq. (2.8) with $p = 2$ (a) over the entire measurement temperature range 4 K $< T <$ 300 K and (b) over 4 K $< T <$ 100 K, where the p values are very close to 2.

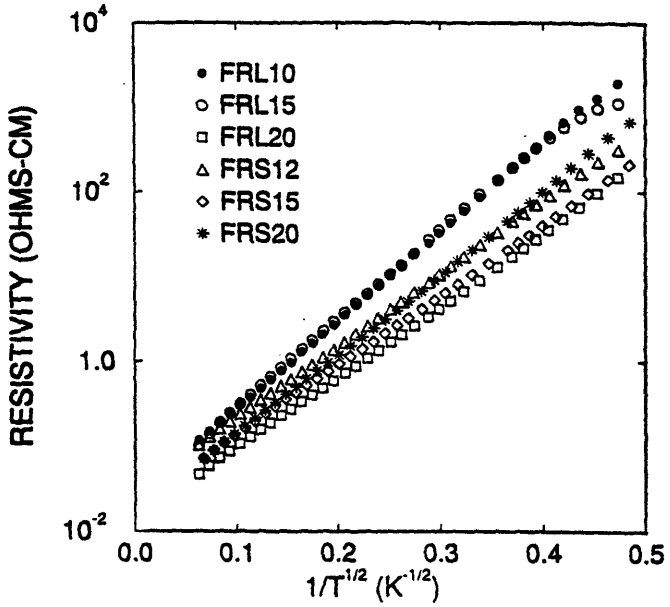

Figure 2-6: The logarithm of the resistivity is plotted against $1/T^{1/2}$ for the phenolic ACFs. A good linear fit is obtained over the temperature range 4 K< T <~300 K. The linearity of the curve over a wide temperature range might be evidence for the charge-energy-limited tunneling conduction model.

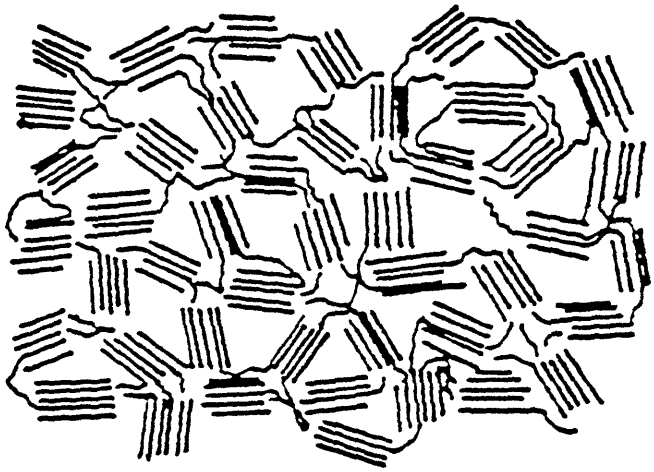

Figure 2-7: A schematic diagram showing the nanostructure of as-prepared ACFs. The thickness of the microcrystallites shown in the figure is only approximate. The microcrystallites in ACFs should really be 1-3 layers thick. (Figures extracted from Ref. [2.3])

Chapter 3

Microstructures & Characterizations of Porous Carbons II: Carbon Aerogels

Carbon aerogels are a special class of low-density microcellular foams. These materials are composed of interconnected carbon particles with diameters of approximately 100 Å. The structure-property relationship is very pronounced, as can be demonstrated through controlling the structure.

In terms of controlling the structure, only sol-gel chemistry permits the design or engineering of porous materials at the nanometer scale. Benefits arising from engineering the structure at the nano-scale (hence the name *nanoengineering*) are observed during the characterization of aerogel monoliths. The ultrafine cell/pore size of these materials minimizes light scattering; and thus, aerogels can be transparent even at very low densities [3.1]. This feature contrasts with other foams that are opaque because their cell size is larger than the wavelength of light. The nanoporosity of aerogels makes them excellent thermal insulators with conductivities of only $\sim$ 0.015 W/mK in air [3.2, 3.3]. This value is a factor of 3-4 times lower than conventional chlorofluorocarbon (CFC)-blown foams. Furthermore, the manufacture of aerogels is environmentally benign. The aerogel skeleton is responsible for the low sound velocities (i.e., 20-300 m/s) and the wide range of acoustic impedances available in aerogels [3.4]. This property can be used to match the high impedance of ultrasonic transducers with the low impedance of air. Finally, the mechanical properties of aerogels

exhibit much larger scaling exponents than conventional foams [3.5–3.7].

In this thesis, carbon aerogels are characterized primarily in terms of their transport properties. In the following, structural characterizations, including transmission electron microscopy, gas adsorption, mechanical properties, Raman spectroscopy and SQUID magnetometry measurements as a function of aerogel density are discussed first in order to draw a picture for the microstructure of carbon aerogels. Then, results from the electrical conductivity and magnetoresistance experiments on carbon aerogels of various densities are presented and correlated with the microstructural picture.

3.1 Fabrication of Carbon Aerogels

Traditional sol-gel polymerizations involve the hydrolysis and condensation of metal alkoxides (e.g., tetra-methoxysilane) to form inorganic aerogels [3.8,3.9]. Several organic reactions that proceed through a sol-gel transition have also been identified. The most-studied reaction involves the aqueous polycondensation of resorcinol (1,3 dihydroxybenzene) with formaldehyde. The resultant gels are supercritically dried from carbon dioxide (at a critical temperature and pressure of $T_c = 31°C$; $P_c = 7.4$ MPa) to give resorcinol-formaldehyde (RF) aerogels. Because RF aerogels are composed of a highly cross-linked aromatic polymer, they can be pyrolyzed in an inert atmosphere to form vitreous carbon monoliths. The resultant aerogels are black in color and no longer transparent, yet they retain the high porosity (40-98 %), ultrafine cell/pore size (< 50 nm), high surface area (600-800 m^2/g), and the interconnected particle (cluster) morphology of their organic precursors [3.10–3.12].

The above morphology differs dramatically from other carbon foams or fibers. At least 4 other methods have been used to produce carbon foams: (1) syntactic carbon foams with a combination of closed and open cells result from the pyrolysis of lightly bonded phenolic microballoons [3.13], (2) replica carbon foams are derived from the pyrolysis of a phenolic resin within a sacrificial substrate [3.14], (3) microcellular carbon foams result from the oxidation and pyrolysis of phase-separated polyacrylonitrile foams [3.15], and (4) reticulated vitreous carbon foams are produced by pyrolyzing an open-cell polyurethane foam that is infused with a reactive monomer (e.g., furfuryl alcohol) [3.16]. In each of these cases, low densities (0.1 g/cm^3) can be achieved, but it is difficult to obtain average cell sizes less than 1 micron and surface areas greater than a few square meters per gram. In

contrast, activated carbon fibers (ACFs) with ultrafine pore sizes and large surface areas (> 1000 m^2/g) have been obtained from phenolic precursors. The ACFs, however, have relatively high bulk densities (i.e., 1.6 g/cm^3) [3.17].

The preparation of carbon aerogels and their organic precursors studied in this thesis has been described elsewhere [3.10, 3.11, 3.18]. Briefly, resorcinol powder (Aldrich; 98%) and formaldehyde (Aldrich; 37.5%; methanol stabilized) were mixed in a 1:2 molar ratio. Deionized and distilled water was added as the dilutent and sodium carbonate as the base catalyst. After stirring to form a homogeneous solution, the mixture was poured into glass vials (25 mm dia. x 80 mm long), sealed, and cured at elevated temperature. For solutions containing less than 10% w/v reactants, the sol-gel polymerization was carried out for 7 days at 85-95°C. At higher reactant concentrations, the solutions were cured for 1 day at room temperature, followed by 1 day at 50°C and 3 days at 85-95°C. All gels for this study were synthesized at a [Resorcinol]/[Catalyst] (R/C) ratio of 200.

Upon completion of the cure cycle, the RF gels were removed from their glass containers and placed in an agitated acetone bath. The first acetone wash contained a small amount of trifluoroacetic acid (~0.1 %) to promote further cross-linking of the gel. Two additional washes with fresh acetone were carried out to ensure complete replacement of the water that previously occupied the pores of the gel. The RF gels were then supercritically dried from carbon dioxide to form aerogels. The RF aerogels were subsequently pyrolyzed in a 3-zone Lindberg furnace under nitrogen gas flow. The furnace was ramped to 1050°C in approximately 16 hours and held at this temperature for 4 hours. Pyrolysis led to volumetric shrinkages of 65-75% with an accompanying mass loss of ~50%.

Changing the reactant concentration while keeping the R/C ratio fixed has the effect of changing the particle packing ratio without changing the particle size. All samples studied in this chapter and the next were synthesized at the same R/C ratio of 200, and have approximately the same particle size of 120 ± 15 Å.

3.2 Characterizations Results

3.2.1 Transmission Electron Microscopy

Transmission electron microscopy (TEM) of carbon aerogels was performed on a JEOL 200 CX instrument at the Lawrence Livermore National Laboratories. Samples were pre-

pared for TEM by atomizing a carbon aerogel/methanol mixture onto a Formvar grid. Thin sections of the aerogel were examined at an accelerating voltage of 80 kV. Rewetting of the aerogels with methanol did not damage the structure of the solid matrix or change the average particle size. Accurate pore size information, however, could not be obtained with this technique.

TEM micrograph show that carbon aerogels, of all mass densities, and R/C ratios of 200 and above, are composed of interconnected colloidal-like particles, derived from the clusters formed during the RF sol-gel polymerization. The R/C ratio is the dominant factor that controls the particle size, surface area, and mechanical properties of RF aerogels and their carbonized derivatives. The resorcinol concentration, on the other hand, determines the mass density and the particle packing ratio. Figure 3-1 shows a typical TEM micrograph of a carbon aerogel (density $\sim 0.1\,\mathrm{g/cm^3}$), synthesized at R/C=200. A "string of pearls" morphology is observed with the individual particles being approximately 12 nm in diameter, with little variation in particle size (± 1.5 nm). The particle size is almost invariant with respect to change in the mass density, as shown by TEM micrographs taken for aerogels of the same R/C ratio but different densities.

High-resolution TEM micrographs taken by Ruben *et al.* [3.19] reveal in more detail the nanostructure of carbon aerogels. Within each individual particle, a convoluted network of glassy-carbon-like ribbons is observed. These ribbons have a width of $\sim$ 10–30 Å, which is on the same order of magnitude as the microcrytallite size obtained from our Raman scattering experiments discussed below.

3.2.2 Gas Adsorption Analyses

Pore size distributions were determined from gas adsorption data obtained with the ASAP 2000 Surface Area Analyzer (Micrometitics Instrument Corp.). All samples ($\sim$10 mg) were outgassed for 20 hours at 100°C prior to analysis. BET surface areas were determined from nitrogen adsorption measurements at 77 K. Mesopore distributions were determined from the desorption branch of the nitrogen isotherm using the Barrett, Joyner, and Halenda (BJH) method [3.20]. Micropore distributions were determined from argon adsorption at 87 K using the Horvath-Kawazoe (HK) theory [3.21]. The results from these two pore measurements are summarized in Table 3.1.

In this study, all carbon aerogels were synthesized at the same R/C ratio and pyrolyzed

ρ_m g/cc	T_{HT} °C	V_{total} cc/g	V_{meso}/V_{total} %	V_{micro}/V_{total} %	Med. D_{meso} Å	Med. D_{micro} Å
0.155	1050	4.179	97.8	2.2	263	7.7
0.305	1050	3.041	90.3	9.7	143	6.8
0.436	1050	1.876	90.8	9.2	95	6.6
0.582	1050	1.279	87.1	12.9	65	6.5
0.803	1050	0.767	88.0	12.0	49	6.4

Table 3.1: Total pore volume (V_{total}), proportions of mesopore volume (V_{meso}) and micropore volume (V_{micro}), and median diameters for mesopores (D_{meso}) and micropores (D_{micro}) as a function of mass density (ρ_m) for carbon aerogels pyrolyzed at $T_{HT} = 1050°C$.

at 1050°C. The aerogel density was controlled by varying the reactant concentration of the starting solution. BET nitrogen adsorption data show a specific surface area of 647±49 m^2/g for carbon aerogels with densities ranging from 0.1-0.8 g/cm^3 [3.12]. These data and TEM micrographs show that the interconnected particles are approximately the same size, independent of the bulk aerogel density. Thus, carbon aerogels with a high bulk density simply have more interconnected particles per unit volume than their low density counterparts.

The pore size distribution of carbon aerogels was determined from gas adsorption analyses [3.12,3.22]. Two pore size regimes can be differentiated in carbon aerogels: (1) mesopores (2-50 nm) that span the distance between the "strings-of-pearls", and (2) micropores (< 2 nm) that primarily reside within the individual carbon particles. As expected, the mesopore size decreases with aerogel density as a result of the increased particle packing. The average mesopore size (diameter) displays a power-law dependence on aerogel density (ρ_m) as follows:

$$d = (3.86 \pm 0.40)\ \rho_m^{-1.05\pm0.05} \tag{3.1}$$

where d is the diameter in nm and ρ_m the bulk density in g/cm^3. Micropores contribute $\sim$ 2 % of the total pore volume for low density carbon aerogels (0.15 g/cm^3), $\sim$ 9.5 % for intermediate densities (0.30-0.45 g/cm^3), and $\sim$ 12.5 % for high density specimens (0.55-0.80 g/cm^3). The average micropore size decreases slightly from 0.77 nm to 0.64 nm over the above density range. The micropore volume fraction, however, increases with increasing density.

If all of the micropores resided within the individual carbon particles, one would ex-

pect the skeletal density to vary as a function of the bulk aerogel density. Helium pycnometry reveals a skeletal density of 2.06 ± 0.06 g/cm^3 for carbon aerogels synthesized at R/C= 200 [3.12]. This mass density is much higher than that of typical glassy carbons (1.46-1.50 g/cm^3), but lower than that of graphite (2.25 g/cm^3), suggesting that there are relatively few closed pores within the carbon particles, but rather there are approximately the same number of accessible micropores, independent of the bulk aerogel density. Furthermore, if we assume that the structural disorder in the particles is correlated with the microporosity within the particles and that the concentration of localized spins is some measure of this disorder, then the observation of roughly the same spin concentration (see the magnetic susceptibility section below) indicates that the number of micropores within each carbon particle is the same. The additional micropore volume for the intermediate and high density aerogels is thus attributed to micropores that are sandwiched between carbon particles. These micropores result from the breakdown of the mesopores caused by the increase in the particle packing ratio.

3.2.3 Mechanical Properties

The moduli of carbon aerogels were measured in uniaxial compression with an Instron machine (model #1125). All specimens were machined into $1 \times 1 \times 1$ cm^3 cubes with a high speed circular saw. Great care was exercised to ensure that the specimens were machined with flat smooth faces and plane-parallel opposing faces. The tests were performed at an initial strain rate of 0.1%/sec. All measurements were made under ambient conditions at ~22°C and 50–70% relative humidity.

Carbon aerogels are superior in both stiffness and strength when compared to their RF precursors at equivalent densities and R/C ratios. In general, pyrolysis leads to a 10-25 fold increase in stiffness and strength. The compressive modulus of carbon aerogels increases with bulk density and displays a power-law dependence that has been observed in many other low density materials [3.7]. This relationship is expressed as

$$E \propto \rho_m^n \tag{3.2}$$

where ρ_m is the bulk density in g/cm^3 and n a non-integer exponent that usually ranges from 2 to 4. For highly regular open-cell foams, the exponent usually equals 2.0, while ideal

closed-cell foams give an exponent of 3.0. Foams with irregular, fractal type morphologies generally have a value that exceeds 3.0. In the case of carbon aerogels, the scaling exponent equals 2.7 ± 0.2 for all formulations, but the prefactor depends upon the R/C ratio. For carbon aerogels synthesized at R/C= 200, the modulus can be calculated in MPa from Eq.(3.2) using a prefactor of 3.55×10^3 [3.5].

Although the increase of the compressive modulus with density is compatible with the picture of increased particle packing, one cannot unambiguously rule out the possibility of increased interconnectivity between particles as a result of close packing. The compressive modulus characterization is, however, more useful when comparing carbon aerogels of the same density but prepared with different R/C ratios. The results show a decrease in R/C ratio does lead to an increase in particle interconnectivity as well as mechanical strength, implying the formation of polymeric links between particles in carbon aerogels, as can be confirmed by the TEM micrographs of these so-called *polymeric* carbon aerogels of low R/C ratios.

3.2.4 Raman Spectroscopy

Raman scattering measurements were performed in the back-scattering configuration using a 4880-Å Argon-ion source with its power limited to below ~50 mW at the sample to avoid sample damage. The laser was deliberately defocussed to sample more area of this inhomogeneous material and to prevent the overheating of the sample. Because the Raman linewidths for this disordered material were on the order of $100\,\mathrm{cm}^{-1}$ linewidth, we used wide monochromator slits (of width corresponding to a few cm^{-1}) to maximize the signal. Each spectrum took $\sim$ 8 scans, each of which was $\sim$ 15 minutes long, for good signal-to-noise level detection.

Readers are referred to Section 2.2.4 for a review of the use of Raman spectroscopy as a sensitive method for monitoring local order in disordered carbons. In the Raman spectra for the R/C= 200 carbon aerogels of various densities (Fig. 3-2), we observed the same features observed previously in ACFs, namely the Breit-Wigner-Fano (BWF) line in the vicinity of $1580\,\mathrm{cm}^{-1}$, which is associated with a disorder-broadened Raman-active E_{2g_2} mode, and the Lorentzian line in the vicinity of $1360\,\mathrm{cm}^{-1}$, which is associated with disorder-induced scattering and normally unobservable in a perfect crystal. Figure 3-2 also shows the fit as solid lines, with the fitting parameters for these samples given in Table 3.2 and their

R/C	50	100	200	200	200	200	300	300	200*
R[(a)]	3.0	5.0	5.0	7.5	30.0	40.0	5.0	40.0	10.0
Density (g/cm^3)	0.189	0.136	0.103	0.123	0.451	0.670	0.085	0.543	1.17
ν_{1360} (cm^{-1})	1346	1346	1348	1349	1350	1350	1348	1354	1355
Γ_{1360} (cm^{-1})	137	137	132	143	124	123	135	140	144
ν_{1580} (cm^{-1})	1603	1602	1602	1604	1610	1607	1601	1613	1613
Γ_{1580} (cm^{-1})	73	74	74	86	76	73	71	80	82
$1/q$	-0.21	-0.22	-0.18	-0.23	-0.25	-0.23	-0.18	-0.28	-0.28
I_{1360}/I_{1580}	1.90	1.75	1.54	1.52	1.68	1.63	1.76	1.74	1.64
L_a (Å)	23	25	29	29	26	27	25	25	27

[(a)] Initial reactant concentration (% w/v)

Table 3.2: Values for the center frequencies (ν) and linewidths (Γ) of the disorder-induced Lorentzian line near 1360 cm^{-1} and the Raman-active Breit-Wigner-Fano line near 1580 cm^{-1} for various carbon aerogel samples with different densities and R/C ratios and one carbon xerogel sample (indicated by an asterisk in the table). For the Raman-active line, the Fano interaction coefficients $1/q$ are also listed. The ratios of the integrated intensity of the disorder-induced line to that of the Raman-active line (I_{1360}/I_{1580}) are then computed and the results are used to calculate the in-plane microcrystallite size (L_a) according to Knight's formula.

meanings explained in Section 2.2.4.

The observed Raman spectra in Fig. 3-2 are almost the same for all samples, though a small reduction in the linewidth is seen with increasing density. More complete data taken on 9 samples, synthesized over a wide range of R/C values, show little variation from one sample to another regarding the peak position, integrated line intensities, or linewidths, for either the Raman-allowed R or the disorder-induced D lines. Of interest is the in-plane microcrystallite size of 25-30 Å, which is nearly the same for all samples. Although Raman measurements are not very sensitive to L_a in this range of L_a, we can nevertheless safely conclude that all L_a values measured on the carbon aerogels are much smaller than the particle (cluster) size. This indicates that the microstructure within each particle is similar, independent of the particle size or density, in agreement with the conclusions reached from TEM and BET characterization measurements.

3.2.5 Magnetic Susceptibility

The SQUID measurements were made in a field of 1 T using a Quantum Design magnetometer. The samples were mounted inside a drinking straw. A field scan was performed

before the actual measurements to ensure a linear sample response to the magnetic field.

Temperature-dependent magnetic susceptibility measurements $\chi(T)$ are often made for disordered carbons to determine the concentration of unpaired spins [3.23,3.24]. Results are given in Fig. 3-3 for $\chi(T)$ per mole as a function of $1/T$, taken with a SQUID magnetometer for the three samples in Fig. 3-2. At high temperatures, diamagnetic behavior is observed, while at low temperatures, Curie-like behavior is found. More detailed analysis shows that the data can be fit to the exchange-coupled pair model originally proposed for the random-exchange Heisenberg antiferromagnetic chain [3.25], the functional form of which is given by:

$$\chi = \chi_0 + \frac{C}{(T-\theta)^\alpha} \tag{3.3}$$

in terms of the fitting parameters χ_0, C, θ and α, where for the low-temperature, low-field case ($g\mu_B H << k_B T << J_0$), the parameter C is written as:

$$C = \frac{g^2\mu_B^2 N_v y}{J_0 A}\left[\frac{2J_0}{k_B}\right]^\alpha \int_0^\infty \frac{x^{1-\alpha}e^{-x}dx}{(1+3e^{-x})^2} \tag{3.4}$$

in which $g = 2$ is the g-factor, μ_B the Bohr magneton ($\mu_B = 0.923 \times 10^{-20}$ erg/gauss), k_B the Boltzmann constant ($k_B = 1.38 \times 10^{-16}$ erg/K), N_v the carbon atom density per mole, A the molar weight for carbon, and y the number of spins/atom. The integral can be approximated by $0.445\exp(-0.633\alpha)$ [3.25]. J_0 is either the exchange energy associated with the minimum distance between coupled spins or merely a non-physical cut-off parameter for the normalization of the exchange distribution $P(J) \propto J^{-\alpha}$. For α close to unity, it can be demonstrated that the J_0 terms cancel within an order of magnitude in Eq. (3.4). For example, for $\alpha = 0.69$ and 25 meV $< J_0 <$ 1.0 eV, then $J_0^{\alpha-1}$ changes only by a factor of 3 and is therefore a very smooth function indeed.

Values for the parameters χ_0, θ, C, α, and y for the 3 samples in Fig. 3-3 are given in Table 3.3 and the fits to Eq. (3.3) for all three samples are shown in Fig. 3-3. In Table 3.3, $\alpha \sim 0.8$ and $\theta = 0$ K universally for all three samples, consistent with the values typically encountered in the exchange-coupled pair model [3.25]. The low spin density, which is about the same for all samples, corresponds to approximately 60-110 spins/particle, considering the particle size to consist of a sphere of 12 nm diameter. We know from Helium pycnometry (see section IV. B) that the micropore volume within carbon particles is almost independent of the aerogel density. We therefore take the micropore volume observed in the less dense

Density(g/cm^3)	0.124	0.451	0.670
χ_0 (10^{-6} emu/g)	-2.3	-1.0	-1.0
θ (K)	0	0	0
C (10^{-6} emu-K$^\alpha$/g)	4.0	7.0	5.3
α	0.69	0.82	0.79
y (10^{-4} spins/atom)	12.7	6.5	6.5
# spins/particle[(a)]	110	56	56

Table 3.3: Values for the fitting parameters used in the exchange-coupled pair model [Eq. (3.3)] and the corresponding values for the unpaired spin concentration for the three measured carbon aerogels.
[(a)] Each particle is modeled as a sphere with diameter of 12 nm and containing micropores within.

aerogels (e.g., density = 0.155 g/cm^3, micropore volume = 0.091 cm^3/g), where micropores are primarily found within carbon particles, as the micropore volume within particles for aerogels of all densities. Then, by using a skeletal density of 2.06 g/cm^3, we can estimate the proportion of micropore volume within each particle to be $\sim$ 16 %. The number of atoms within a particle with micropores is therefore only $\sim$ 84 % of that within a 12-nm solid sphere.

The diamagnetic background values, χ_0, are to be compared to χ_0(avg.) = -7.32×10^{-6} emu/g for graphite and to similar room-temperature values obtained for microcrystalline carbons studied by Adamson and Blayden [3.26]. Their study correlating L_a and L_c with χ_0 showed that both L_a and L_c should grow with increasing magnitude of χ_0, inconsistent with our Raman results. It is believed that the decrease in the negative susceptibility background (χ_0) with increasing density is associated with the increasing contribution from the Pauli paramagnetic susceptibility due to free carriers. Using the Pauli susceptibility form $\chi = 3N\mu_B^2/2E_F$ and assuming a Fermi energy $E_F \sim 1$ meV, which is typical of disordered carbon materials, we estimate from the difference between the χ_0 value of the most dense sample and that of the least dense sample the free carrier concentration N to be on the order of $\sim 2 \times 10^{19}$/g, a value characteristic of other disordered carbons with similar conductivity and L_a values. An ESR experiment should clarify, with the appropriate lineshape and linewidth analyses, whether or not this positive increase in the background of χ with density is related to the free carrier paramagnetic contribution.

3.2.6 Resistivity

All transport measurements were made using the 4-point technique. Silver epoxy was used to establish the contacts because of its high viscosity and its good adhesion to the aerogel surface. Since aerogels are very fragile materials, large samples of size $\sim 8 \times 3 \times 3$ mm were used for the measurements. Poor thermal conductors of this thickness (especially the low-density sample), however, require the exercise of much care during the measurements to ensure temperature homogeneity and equilibrium both within the sample and between the sample and the environment. All temperature scans took place by natural warming.

The temperature dependence of the resistivity ρ(T) is shown in Fig. 3-4 on a semi-log plot for 3 carbon aerogel samples with density values similar to those in Fig. 3-2. The results show that the resistivity falls as the mass density ρ_m increases, as would be expected for a percolating network [3.27]. Of particular interest is the sharp increase in resistivity at low temperature (below 30 K) for all samples. The effect is most striking for the least dense sample. These transport measurements show that the temperature dependence of the resistivity is a sensitive characterization probe for the carbon aerogels.

At room temperature, the variation of the resistivity ρ from the least to the most dense aerogel is a factor of about 30, thus providing one characterization parameter for carbon aerogels, as shown in Fig. 3-5. Here we find on the basis of three different mass density samples that $\rho \propto \rho_m^{-1.9}$ at room temperature, which is to be compared with the mass density dependence of the electrical conductivity $\sigma \propto \rho_m^{1.5}$ reported by Lu *et al.* [3.28]. The error bar for the parameter ρ(300K) due to the uncertainty in the measurements of the sample dimensions is actually larger than the change of ρ(300K) due to the variation in the mass density, especially for mass density > 0.4 g/cm^3, where the resistivity is only weakly dependent on the mass density. At low temperatures, ρ(4.2K) for carbon aerogels with different densities differs by several orders of magnitude, thus providing a second more sensitive characterization parameter for carbon aerogels. This strong dependence of the resistivity at 4.2 K on mass density is seen in Fig. 3-5 where the plot (based on only 3 points) indicates a $\rho \sim \rho_m^{-8.0}$ dependence. Also of interest is the ratio ρ(4.2K)/ρ(300K), which varies approximately as $\rho_m^{-6.0}$. Values for ρ(300K), ρ(4.2K) and their ratio are given for the three carbon aerogel samples in Table 3.4.

As shown in the TEM pictures, the aerogel system is a conductive network consisting of interconnecting carbon particles. The electrical conduction should take place by both

the drift of the delocalized charge carriers within the carbon particles and the transfer of carriers from one large conducting segment to another by hopping or tunneling. A good fit to the measured $\rho(T)$ data can be obtained from the fluctuation-induced tunneling (FIT) model [3.29], which is based on metallic-particles-imbedded microstructures similar to that of carbon aerogels and gives rise to a temperature-dependent conductivity $\sigma(T)$ given by the following expression:

$$\sigma(T) = \sigma_0 \exp\left[-\left(\frac{T_1}{T+T_0}\right)\right] \tag{3.5}$$

where $T_1/T_0 = \pi s\sqrt{2m\phi_s/\hbar^2}/2$, s the width and ϕ_s the barrier height of the insulating gap between neighboring particles. The characterization parameter σ_0 is a prefactor that approximates the room temperature value of the conductivity, and T_0 and T_1 are characteristic temperatures. The fitting values for T_0 and T_1 as a function of density are listed in Table 3.4 together with ρ(300K), ρ(4.2K), $\log(\rho(4.2\text{K})/\rho(300\text{K}))$ and the magnetoresistance $(\Delta\rho/\rho)$ discussed in the next section, all of which are also sensitive characterization parameters. The results show that as the density increases, the ratio (T_1/T_0) decreases drastically, hence constituting another very sensitive and yet dimensionless characterization parameter for carbon aerogels.

It is noted that the usefulness of the FIT model is only limited to the characterization of carbon aerogels in terms of their density. Despite the appeal of this model as a good fit to the transport data, the physics is not correct. Essentially, the FIT model describes the tunneling conduction between large conducting grains with a negligible amount of electrostatic charge energy [3.29]. These large conducting grains could be identified with the 12-nm particles of the carbon aerogel. However, the lower limits for the effective mass m/m_0, estimated using the FIT model with $\phi_s = 4.4$ eV being the work function of graphite and $s \sim 7$ Å, are 36, 4.7 and 0.20 for the LD, MD and the HD samples, respectively, two of which are unreasonably large ($>> 1$) for a conductive solid matrix of graphitic material and probably inconsistent with the SQUID measurements above showing the existence of free carriers, which should have a large mobility. The widely varied values for m in the 3 samples also make the FIT model unsatisfactory since both the Raman scattering and the magnetization results imply the same degree of disorder within the carbon particles in each sample, irrespective of mass density. Our magnetoresistance (MR) results, to be discussed next, also call into question whether a tunneling mechanism like FIT can give rise to the large MR we observed. We

therefore believe that FIT is not likely in carbon aerogels. In the next chapter, a more promising conduction model based on variable-range hopping will be used to explain the transport behavior in both ACFs and carbon aerogels.

3.2.7 Magnetoresistance

The magnetoresistance was measured with a 15 T superconducting magnet in the Francis Bitter National Magnet Laboratory at MIT. Magnetic field scans at any fixed temperature were carried out only after the resistances of the samples had reached their steady state values.

The transverse magnetoresistance (MR) denoted by $[\rho(B) - \rho(0)]/\rho(0) \equiv \Delta\rho/\rho$ also provides a sensitive characterization tool for the carbon aerogel samples. For all 3 carbon aerogel samples, the MR is positive and large compared with other carbon-based materials [3.30], especially at the lowest temperature shown (1.52 K). The positive MR, like the strong temperature dependence of the conductivity, is attributed to effects of strong localization, and not to the Bloch-states MR observed in single-crystal graphite.

At each of the temperatures in Fig. 3-6, where the observed MR is plotted for a R/C=200 sample with density 0.457 g/cm^3, the magnetic field dependence of the resistivity at low fields exhibits a quadratic behavior $\Delta\rho/\rho = AB^2$ which then saturates at higher field values, the saturation field decreasing with decreasing temperature. Figure 3-7 shows a plot of the MR as a function of B^2 for the same curves shown in Fig. 3-6, and the results yield a good fit to a quadratic field dependence. In Fig. 3-7, a saturation effect above 6 T is clearly seen for the data at the lowest temperature 1.52 K.

From the data in Fig. 3-7 and the results for other mass densities, the temperature dependence of the quadratic coefficient A can be plotted, and the results are shown in Fig. 3-8. For each density, an approximately linear dependence of $\log A$ on T is observed, with deviations found below $\sim$ 5 K. The MR behavior below 5 K is studied in more detail in Chapter 4. In contrast to the other data points in Fig. 3-8, the quadratic coefficients at 4.2 K in Fig. 3-8 were not obtained from the corresponding curves shown in Fig. 3-9, which plots the mass density dependence of the MR, but were specifically obtained more accurately through a second set of measurements (not shown) in a magnetic field up to 10 T, when the temperature of the higher-density carbon aerogel samples at 4.2 K had been ensured.

Density (g/cm^3)	0.119	0.457	0.645
T_1 (K)	32.0	16.5	15.0
T_0 (K)	0.8	4.5	9.1
T_1/T_0	40	3.7	1.6
ρ(300K) (Ω-cm)	1.5	0.14	0.061
ρ(4.2K) (Ω-cm)	3.9×10^5	5.5	0.58
$\log(\rho(4.2K)/\rho(300K))$	5.4	1.6	0.98
A at 4.2 K (% per $(Tesla)^2$)	0.43	0.18	0.11

Table 3.4: Values for the fitting parameters (T_1 and T_0) used in the fluctuation-induced tunneling conduction model and their ratio. Also listed are $\log(\rho(4.2K)/\rho(300K))$ and the quadratic coefficient (A) of the magnetoresistance $\Delta\rho/\rho$ at 4.2 K, both of which are also very sensitive characterization parameters.

Not only are large characteristic effects found in the MR, but these effects are sample dependent as shown in Fig. 3-9, where $\Delta\rho/\rho$ at 4.2 K is plotted for three carbon aerogel samples with different densities, but with the same R/C=200 ratio. The results show a good quadratic field dependence for all three mass density samples, with the MR increasing as ρ_m decreases, consistent with the stronger T dependence of the resistivity for the lower-density carbon aerogels, and also with the notion that strong localization induces the observed positive MR. The quadratic coefficients A at 4.2 K are also listed in Table 3.4 for sample comparison. These data show that either the temperature dependence of the quadratic coefficient A or the coefficient at a specified temperature (e.g., 4.2 K) can be used as a characterization parameter for carbon aerogels. The physical significance of A will be discussed in Chapter 4.

3.3 Summary of the Microstructure of Carbon Aerogels

For porous materials, the traditional and common structural characterization parameters are usually the pore/particle size and specific surface area inside the materials. In this regard, high-resolution TEM pictures show within each particle a glassy-carbon-like nanostructure consisting of an intertwined network of narrow graphitic ribbons of width $\sim$ 10–30 Å, consistent with the L_a size measured by Raman scattering. TEM micrographs further show that the particle size ($\sim$ 120 Å) is almost independent of mass density. With increasing density at constant R/C ratio, the packing ratio or average number of contacts per particle increases, forming a highly linked network inside the material, and at an even

higher density, the particles become interconnected and cross-linked. Mesopores are formed between these links while micropores are found within each individual particle and between touching particles.

Gas adsorption analyses are generally used to determine the porosity and the specific surface area. The BET nitrogen adsorption analysis shows that the specific surface area is almost independent of the density, agreeing with the TEM results that the particle size is not a strong function of density. The gas adsorption data show a large increase in the mesopore size with decreasing density and a weakly density-dependent micropore size (~ 7 Å) [3.22].

Using Raman scattering as a new nanostructural probe for porous carbons, we confirm that the in-plane microcrystallite size $L_a \sim 25$ Å, a dimension smaller than the particle size (~ 120 Å). The small value of L_a is thus likely to be associated with the width of one carbon ribbon in the glassy-carbon-like structure inside a particle. The low density of unpaired localized spins found from SQUID measurements indicates that there are few dangling bonds inside a particle, also suggesting that each particle consists of more connected structures than small isolated balls. Furthermore, L_a is found to be independent of the aerogel density.

The skeletal density of $2.06 \pm 0.06\,\mathrm{g/cm^3}$ found by helium pycnometry [3.12] for carbon aerogels synthesized at a [Resorcinol]/[Catalyst] (R/C) ratio of 200 also suggests that these glassy carbon ribbons (nanoparticles) are probably relatively graphitic, since the density of typical glassy carbons is 1.46-1.50 $\mathrm{g/cm^3}$, whereas that of graphite is 2.26 $\mathrm{g/cm^3}$.

Based on the above structural information, a schematic diagram for the micro- and the nano-structure of carbon aerogels with different mass densities but a fixed R/C= 200 is drawn in Fig. 3-10. This schematic forms the basis for later discussions of our transport results in Chapter 4. The unique "string of pearls" morphology is composed of chains of particles of approximately uniform size [feature (c)] and mesopores bounded by these particle chains [feature (a)]. The neck region [feature (e)] forms a loose link between neighboring particles. Micropores [feature (d)] of size less than 1 nm abound within the neck regions as well as individual particles. In high-density samples, mesopores are broken down into micropores [feature (b)] in regions of close-packed particles. Fig. 3-10 also shows that the mass density determines the packing ratio or interconnectivity. With increasing mass density, the particle size remains constant but the packing ratio of these particles increases.

Because of the interconnectivity of carbon aerogels, unlike other porous materials in powder form, there are now sensitive characterization tools available to characterize these

materials, such as the measurements of mechanical and transport properties.

The bulk modulus for carbon aerogels was found to follow a power-law dependence on mass density of $\rho_m^{2.7}$, consistent with the TEM finding that the interconnectivity increases with density. Hence, unlike the R/C ratio which affects both the particle size and the interconnectivity between particles in carbon aerogels, it appears that the mass density factor solely tunes the amount of interconnectivity, with higher density resulting in better inter-particle adhesion. The result for the bulk modulus is also consistent with the small-angle x-ray scattering (SAXS) measurements which show that carbon aerogels possess no mass or surface fractal geometry [3.31, 3.32].

We have presented in this chapter yet another set of new characterization tools to complement the others mentioned above. As far as we know, there have only been few extensive transport studies of aerogel materials. Previous thermal conductivity measurements at room temperature [3.28] show that the thermal conductivity increases with mass density. At lower densities, this increase is related to the increasing contribution from the thermal conductivity of the solid phase material which makes a conduction path. At higher densities, the thermal conductivity increases with density because of the reduction of the boundary scattering of phonons, which are the dominant heat carriers at room temperature. It would be interesting to see whether the same trend is observed at very low temperature where the electronic component of the thermal conductivity starts to contribute. Such a study would either confirm or refute our SQUID finding that there are more free electrons in samples of higher densities.

Our transport studies include measurements of the temperature-dependent conductivity and magnetoresistance in carbon aerogels. We found that the electrical conductivity at all temperatures increases with density, with the difference between the most dense and the least dense samples being particularly large (several orders of magnitude) at low temperature. Several properties can be used to characterize the carbon aerogels, including the values of the resistivity at convenient fixed temperatures such as 300 K and 4.2 K or the temperature dependence of ρ(T). Although a good fit of the $\sigma(T)$ data was obtained with the fluctuation-induced tunneling model, it is to be seen in the next chapter that this model is unsatisfactory, and that the Coulomb-gap variable-range hopping model is better. Because the particle size and the degree of disorder inside the particles are not a strong function of density, the dominant conduction mechanism is most likely associated with the

interconnection between particles. In support of this hypothesis, Chapter 5 demonstrates that the localization sites are to be identified with the particles and not with the intrinsic disorder contained within.

Magnetoresistance (MR) measurements show that the MR is a very strong function of density at low temperature. The large magnitude of the MR cannot be due to any graphitic structure inside the particles, because the MR would then have to increase with increasing density, contrary to observations. The observed increase of the MR with decreasing density probably results from the decrease of the density of localized states for hopping. A more thorough discussion of our transport results will be presented in the forthcoming Chapter 4.

References

[3.1] L.W. Hrubesh, T.M. Tillotson, and J.F. Poco, in *Better Ceramics Through Chemistry IV*, C.J. Brinker, D.E. Clark, D.R. Ulrich, and B.J. Zelinski, eds., MRS Symp. Proc. 180, 315 (1990).

[3.2] D. Buttner, R. Caps, U. Heinemann, E. Hummer, A. Kadur, P. Scheuerpflug, and J. Fricke, in *Aerogels*, edited by J. Fricke (Springer-Verlag, New York, 1986), p. 104.

[3.3] X. Lu, M.C. Arduini-Schuster, J. Kuhn, O. Nilsson, J. Fricke, and R.W. Pekala, Science **255**, 971 (1992).

[3.4] J. Gross, J. Fricke, and L.W. Hrubesh, J. Acoust. Soc. Am. **91**, Pt. 1, 2004 (1992).

[3.5] R.W. Pekala, C.T. Alviso, and J.D. LeMay, J. Non-Cryst. Solids **125**, 67 (1990).

[3.6] T. Woignier, J. Phalippou, and R. Vacher, J. Mater. Res. **4**, 688 (1989).

[3.7] L.J. Gibson and M.F. Ashby, *Cellular Solids - Structure & Properties* (Pergamon Press, New York, 1988).

[3.8] C.J. Brinker and G.W. Scherer, *Sol-Gel Science* (Academic Press Inc., New York, 1990).

[3.9] S.J. Teichner, G.A. Nicolaon, M.A. Vicarini, G.E.E. Gardes, Adv. Coll. Interf. Sci. **5**, 245 (1976).

[3.10] R.W. Pekala and F.M. Kong, Polym. Prpts. **30**, 221 (1989).

[3.11] R.W. Pekala and F.M. Kong, J. Phys. (Paris) Coll. Suppl. **50**, C4-33 (1989).

[3.12] R.W. Pekala and C.T. Alviso, in *Novel Forms of Carbon*, edited by C. L. Renschler, J. J. Pouch, and D. M. Cox, MRS Symposia Proceedings No. 270 (Materials Research Society, Pittsburgh, 1992), p. 3.

[3.13] S.T. Benton and C.R. Schmitt, Carbon **10**, 185 (1972).

[3.14] R.W. Pekala and R.W. Hopper, J. Mat. Sci. **22**, 1840 (1987).

[3.15] A.P. Sylwester, J.H. Aubert, P.B. Rand, C. Arnold Jr., and R.L. Clough, ACS Polymeric Materials Science and Engineering **57**, 113 (1987).

[3.16] H.C. Geer, in *Encyclopedia of Polymer Science and Technology*, H.F. Mark, N.G. Gaylord, and N.M. Bikales, eds., (Interscience, New York, 1970), p. 102.

[3.17] J.S. Hayes, Jr., in *Kirk-Othmer: Encyclopedia of Chemical Technology*, Vol. 16 (John Wiley & Sons, Inc., New York, 1981), p. 135.

[3.18] R.W. Pekala, J. Mat. Sci. **24**, 3221 (1989).

[3.19] G. C. Ruben, R. W. Pekala, T. M. Tillotson, and L. W. Hrubesh, J. Mat. Sci. **27**, 4341 (1992).

[3.20] E.P. Barrett, L.G. Joyner, and P.P. Helenda, J. Am. Chem. Soc. **73**, 373 (1951).

[3.21] G. Horvath and K. Kawazoe, J. Chem. Eng. (Japan) **18**, 470 (1983).

[3.22] S.S. Hulsey, C.T. Alviso, F.M. Kong, and R.W. Pekala, in *Novel Forms of Carbon*, edited by C. L. Renschler, J. J. Pouch, and D. M. Cox, MRS Symposia Proceedings No. 270 (Materials Research Society, Pittsburgh, 1992), p. 53.

[3.23] S. Mrozowski, Carbon **3**, 305 (1965).

[3.24] P. Delhaès and F. Carmona, Carbon **10**, 677 (1972).

[3.25] W. G. Clark and L. C. Tippie, Phys. Rev. **B20**, 2914 (1979).

[3.26] A. F. Adamson and H. E. Blayden, in the 1st Conference on Industrial Carbon and Graphite, organized by the Society of Chemical Industry, 1958.

[3.27] S. Kirkpatrick, Rev. Mod. Phys. **45**, 574 (1973).

[3.28] X. Lu, O. Nilsson, J. Fricke and R.W. Pekala, J. Appl. Phys., (submitted).

[3.29] P. Sheng, E. K. Sichel, and J. J. Gittleman, Phys. Rev. Lett. **40**, 1197 (1978).

[3.30] P. Delhaès and F. Carmona, in *Chemistry and Physics of Carbon*, Vol. 17, P. C. Walker and P. A. Thrower, eds., (Marcel Dekkar, New York, 1981), p. 89.

[3.31] R. Pahl, U. Bonse, R. W. Pekala, and J. H. Kinney, J. Appl. Cryst. **24**, 771 (1991).

[3.32] D.W. Schaefer, Sandia National Laboratory (private communication).

Figure 3-1: A transmission electron micrograph of a carbon aerogel ($0.1 g/cm^3$, R/C = 200), providing a basis for the schematic diagram in Fig. 3-10.

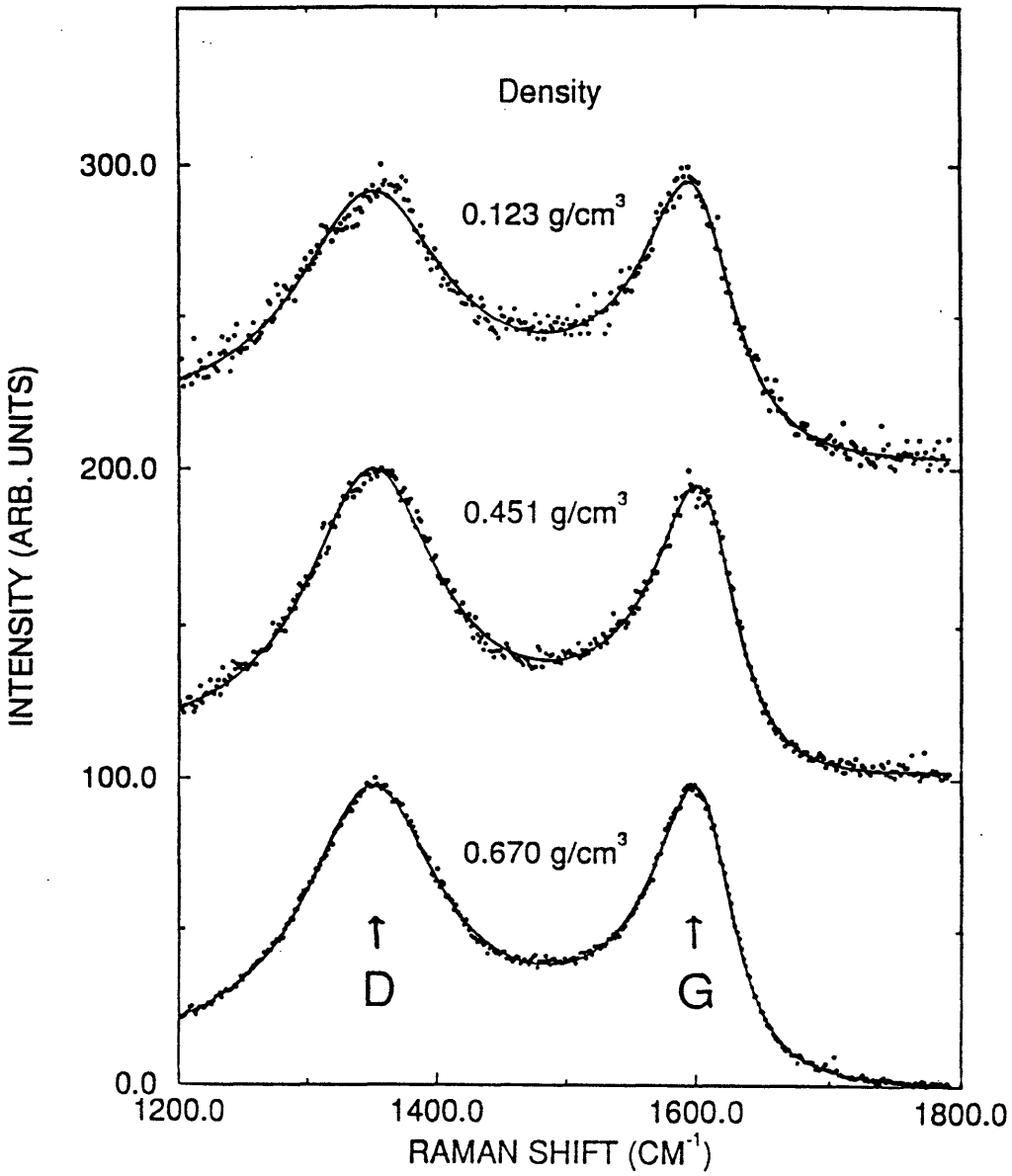

Figure 3-2: Raman spectra for 3 carbon aerogels with densities as listed. The solid curves are a model fit to the data using the parameters of Table 3.2. The Raman-allowed G line and the disorder-induced D line are indicated by arrows.

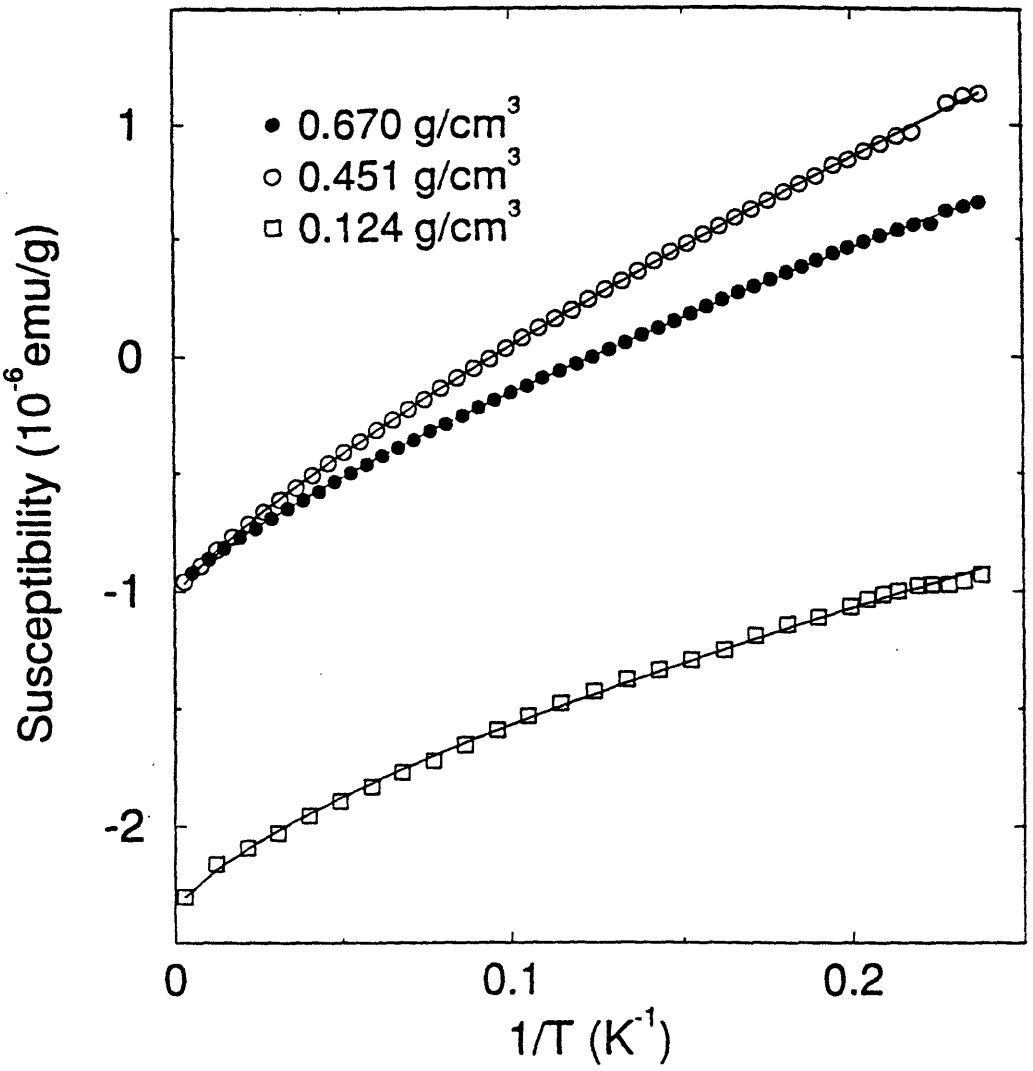

Figure 3-3: Temperature dependence of the magnetic susceptibility plotted as χ vs $1/T$ for 3 carbon aerogel samples with different densities and the fits of these data to the exchange-coupled pair model [Eq.(3.3)] corresponding to the random-exchange-energy model.

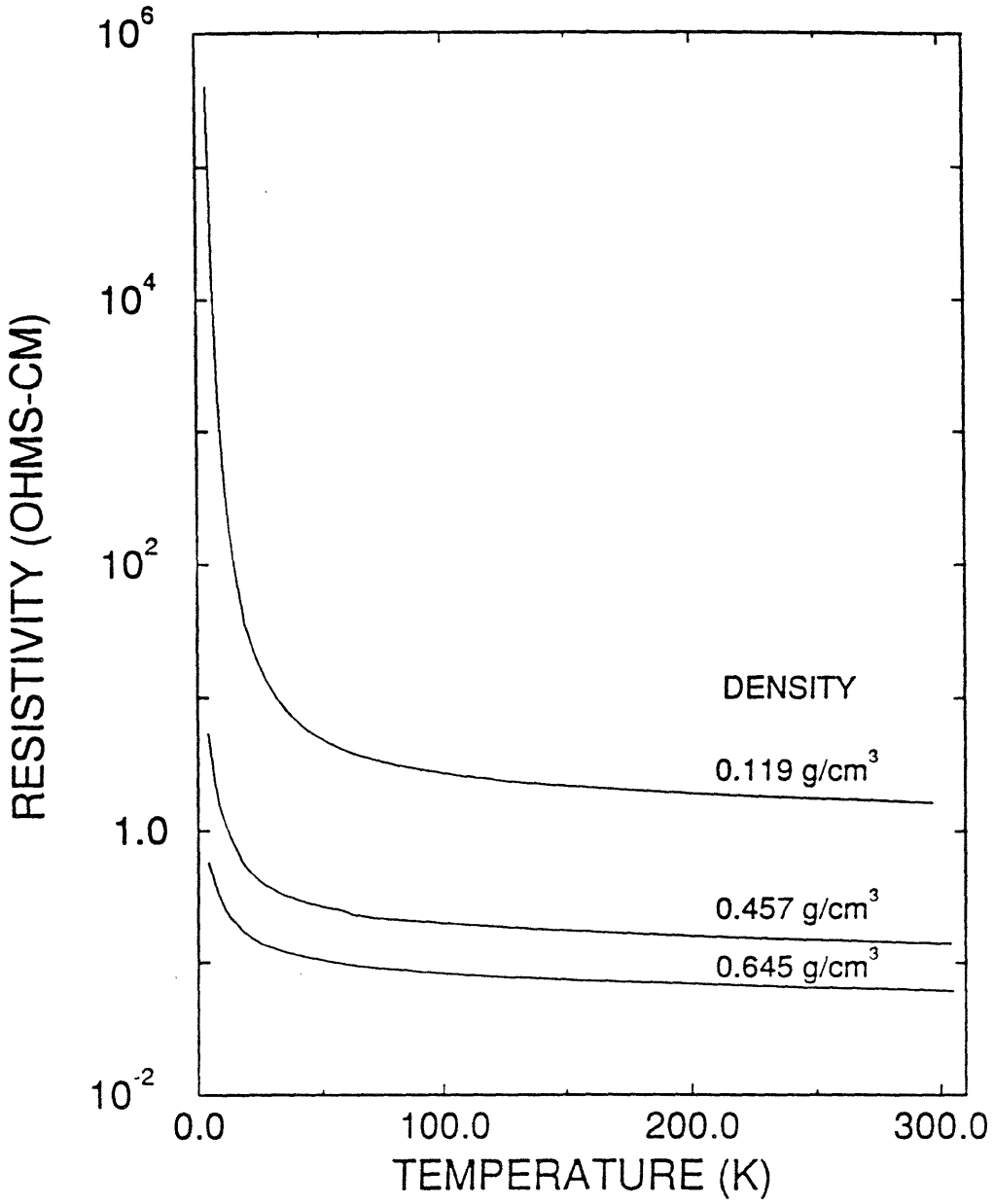

Figure 3-4: DC electrical resistivity vs temperature for 3 carbon aerogel samples with different densities.

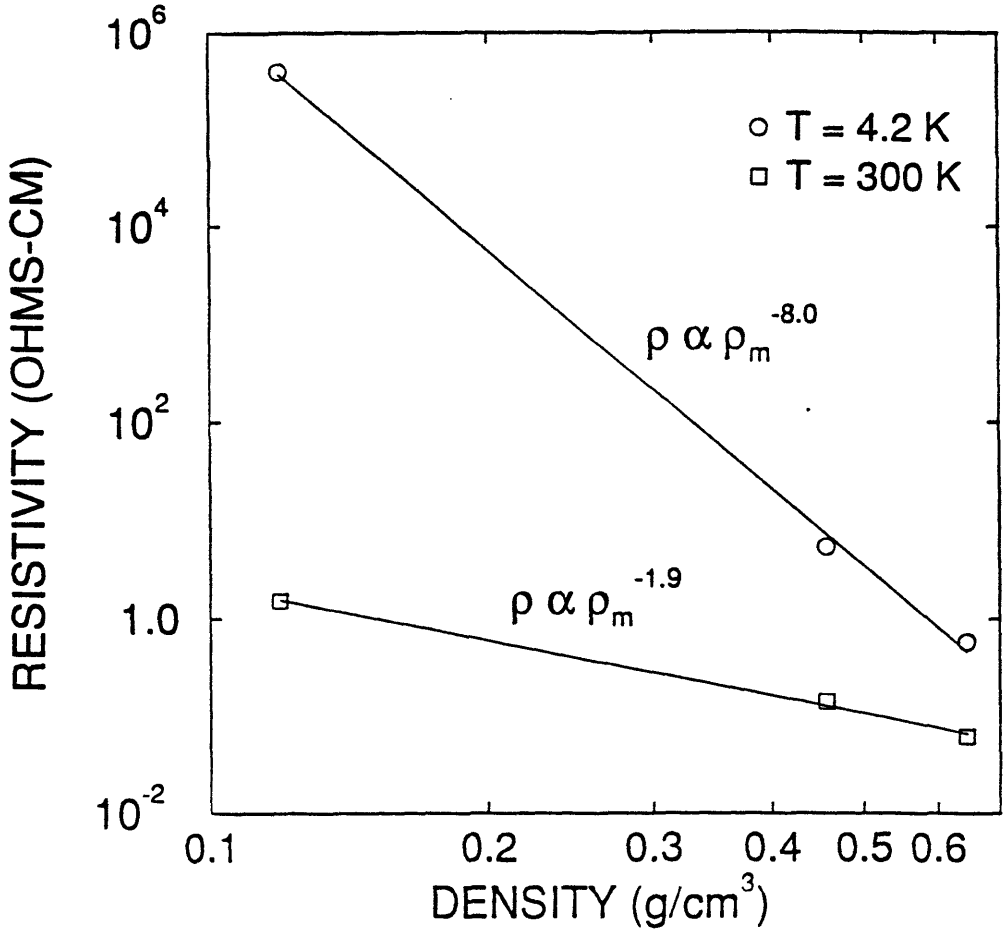

Figure 3-5: Absolute electrical resistivity values vs mass density for 3 carbon aerogel samples at 4.2 K and 300 K, respectively.

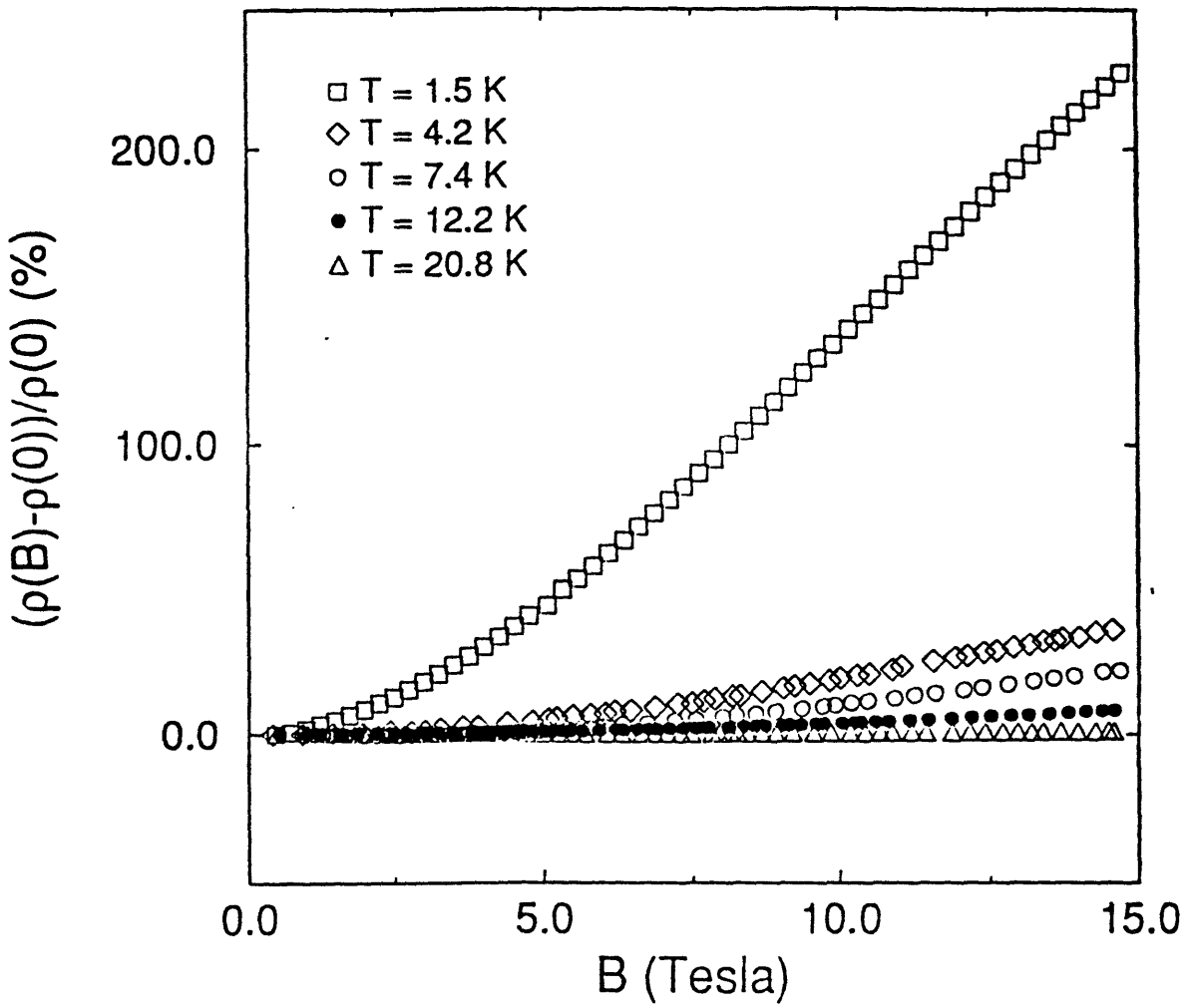

Figure 3-6: Magnetoresistance $[(\rho(B) - \rho(0))/\rho(0)]$ for the carbon aerogel sample with density = 0.457 g/cm^3 at 5 values of temperature.

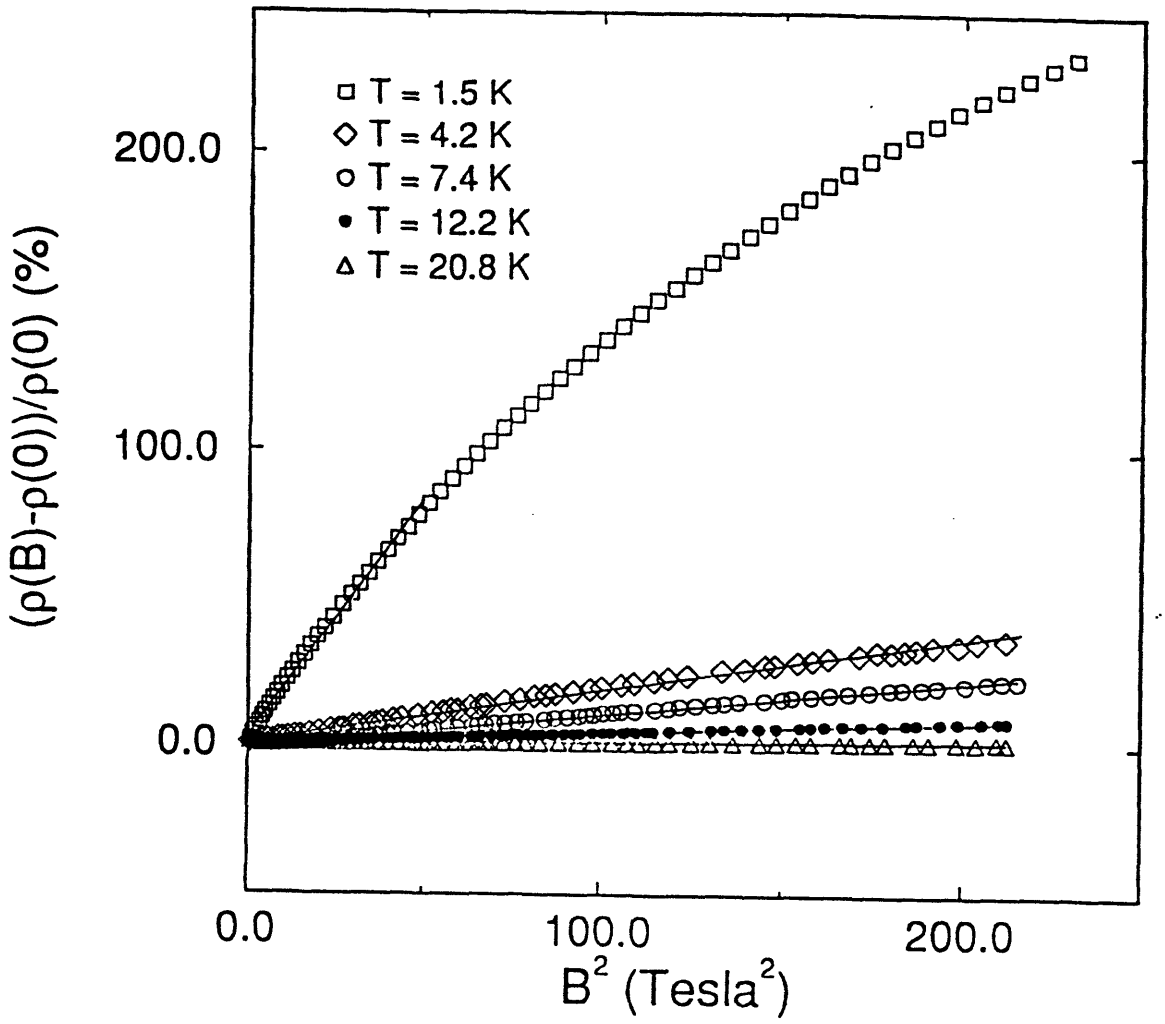

Figure 3-7: Magnetoresistance $[(\rho(B) - \rho(0))/\rho(0)]$ for the carbon aerogel sample with density = 0.457 g/cm^3 plotted for various temperatures against the squared magnetic field (B^2) to show the quadratic field dependence of the magnetoresistance. Only the data taken at 1.52 K show saturation effects and departures from quadratic behavior at high field values.

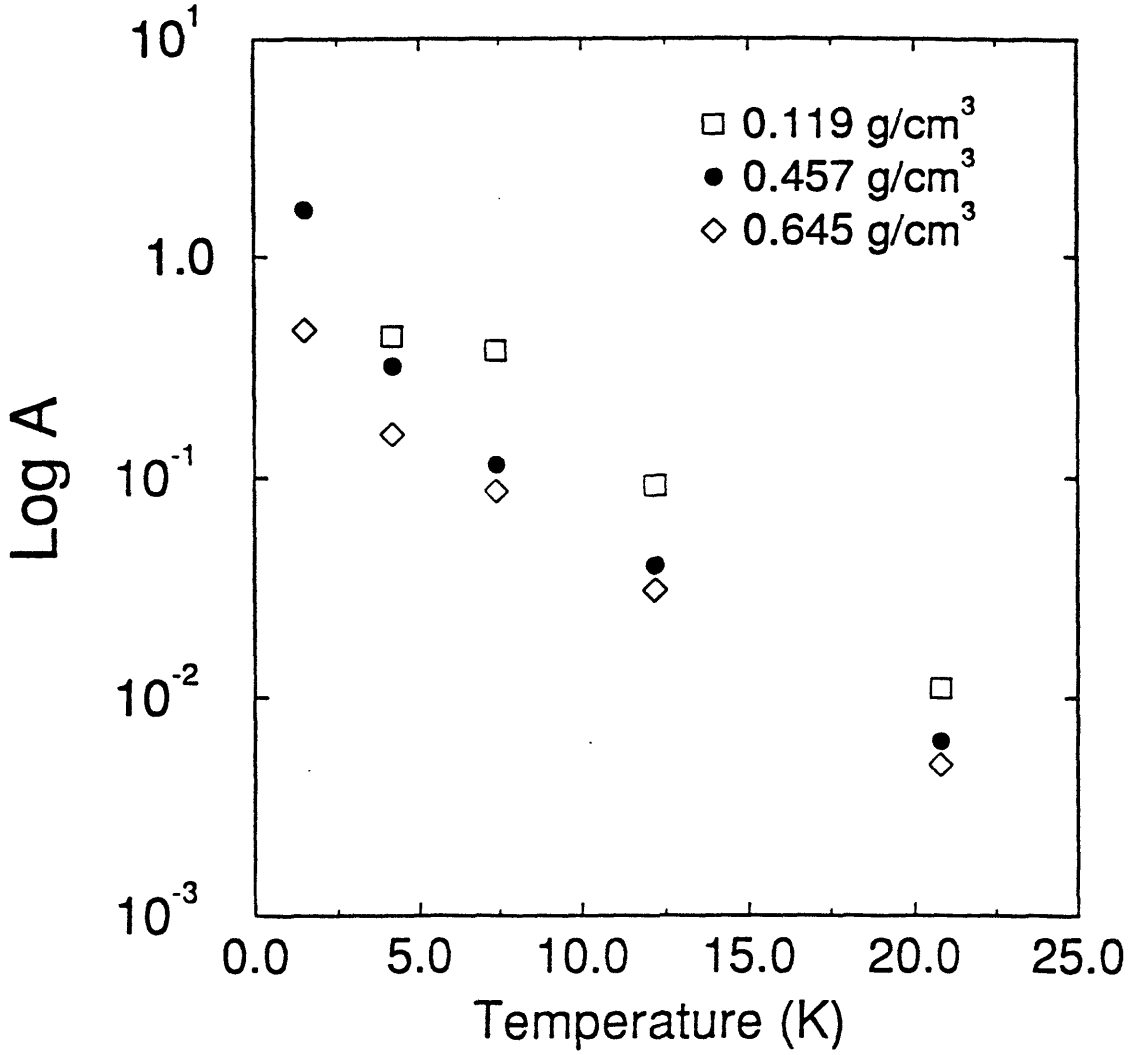

Figure 3-8: Quadratic coefficients A obtained from fitting the magnetoresistance data to a parabolic field dependence for 3 carbon aerogel samples with different densities. The data are presented on a semi-log plot.

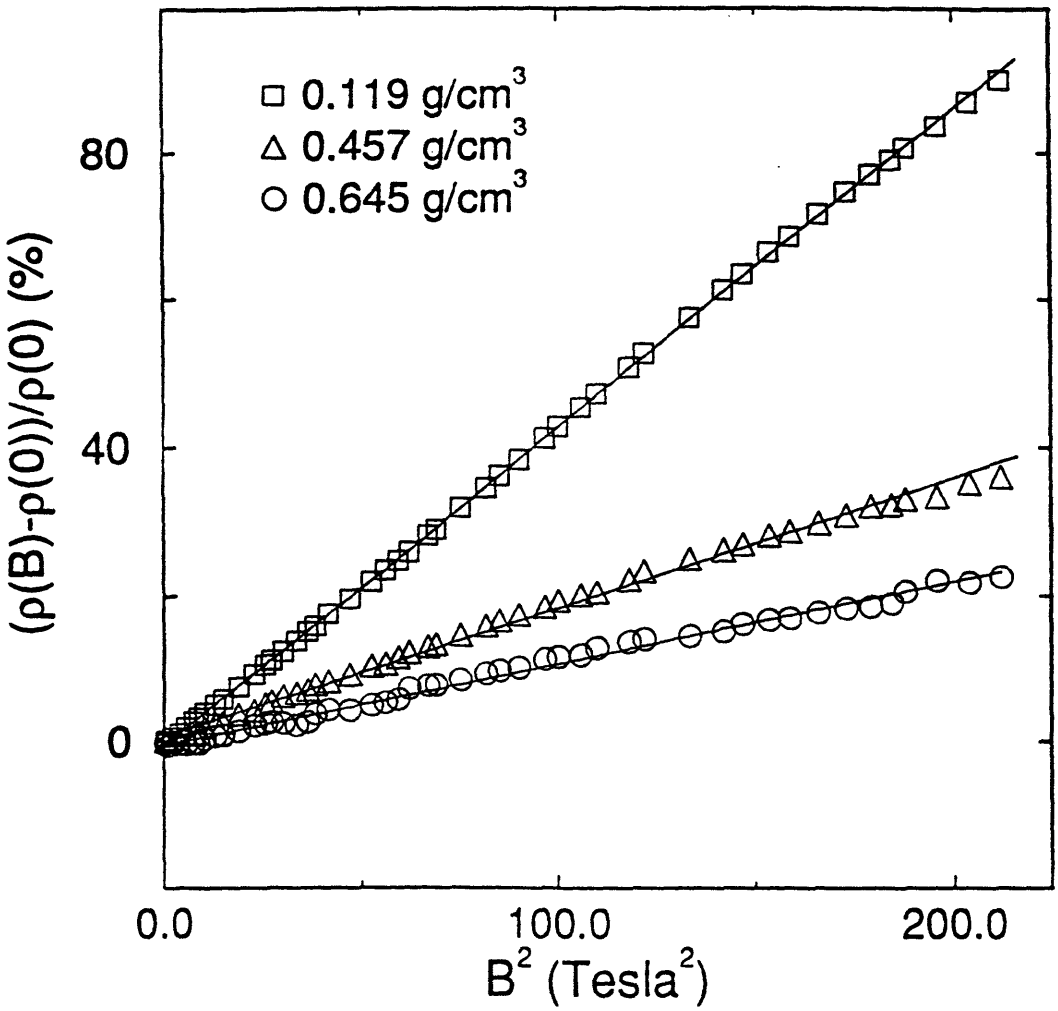

Figure 3-9: Magnetoresistance $[(\rho(B)-\rho(0))/\rho(0)]$ at 4.2 K plotted vs B^2 for carbon aerogel samples with densities = 0.119, 0.457 and 0.645 g/cm^3, respectively.

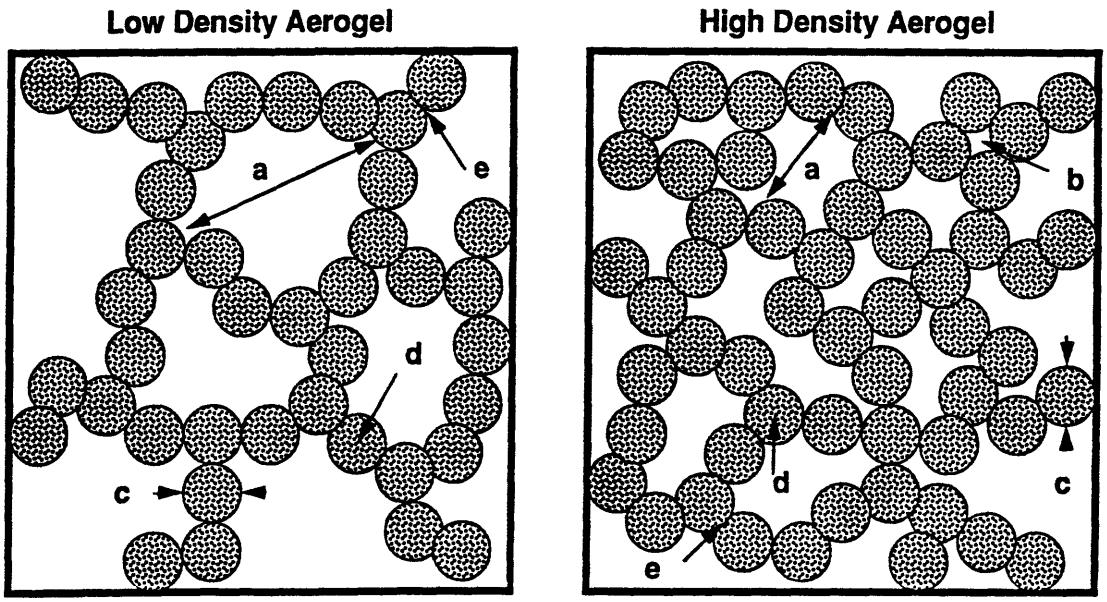

Figure 3-10: Schematic diagram showing the following features of the carbon aerogel microstructure as a function of bulk density: (a) mesopore that spans the distance between chains of interconnected particles, (b) micropore sandwiched between particles, (c) individual particle ($\sim$ 12 nm diameter), (d) micropore within the particles and (e) neck region beween contiguous particles.

Chapter 4

Coulomb-Gap Magneto-Transport in Granular and Nanoporous Carbons

Since the first comprehensive study of granular metals (GMs) by Sheng and Abeles *et al.* [4.1], the question of whether variable-range hopping (VRH) or tunneling between nearest neighbors (N-N) is responsible for the transport behavior of specific sub-percolating GM systems remains an open issue. GMs typically exhibit a temperature-dependent dc electrical resistivity $[\rho(T)]$ of the form:

$$\rho(T) = \rho_0 \exp\left[\left(\frac{T_0}{T}\right)^{1/p}\right] \tag{4.1}$$

where $p = 2$, ρ_0 is some proportionality constant, and T_0 varies between 10^2 K and 10^4 K depending on the metallic volume fraction (x) in the system. The same $\rho(T)$ behavior is observed in our transport results for both carbon aerogels [4.2] and activated carbon fibers (ACFs) [4.3, 4.4], thus prompting this study of the relationship between the general localization phenomena and the granular nature of porous materials.

Earlier attempts to provide an explanation for observing Eq. (4.1) with $p = 2$ in GM systems have been criticized for their limitations and unrealistic assumptions [4.5, 4.6]. While the critical percolation method (CPM) [4.7–4.9] gives a likely explanation for the $p = 2$ behavior for GM systems in which the granular size d is on the same order as the

granular separation s, our porous systems, in which the conducting particles are necessarily non-uniformly distributed in space in order to hold the sample together, even without a solid-phase insulating matrix, consists of close-packed regions with $d >> s$ and requires a new model. Our new model takes into account the effective potential barriers presented by the intervening grains, which are essential for the VRH to be operative, thus complementing previous CPM studies.

We discuss in this work why VRH becomes more likely than tunneling in GM systems with $d >> s$. In particular, both our $\rho(T)$ and the magnetoresistance (MR) results, when correlated with the previous structural characterization measurements, indicate that VRH in a Coulomb gap [4.10] plays a more dominant role in porous materials than tunneling, thus ruling out the fluctuation-induced tunneling model [4.11]. Not only does the Coulomb gap VRH model provide information about the effective dielectric constant and the grain size (given the effective mass of the charge carrier), but it also has potential applicability to GM systems near the metal-insulator transition and other porous materials.

In the following, the nanostructures of carbon aerogels and ACFs relevant to the discussion of the transport results are briefly reviewed. Following the discussion of the shortcomings and the limitations of previous transport models relevant to GM systems, the Coulomb gap VRH model is rederived for systems with finite-size particles in a formalism that encompasses previous models in their limiting regimes. The present model is then applied to explain the different T_0 values as well as the temperature and field dependences of the magnetoresistance in carbon aerogels, ACFs, and other GM systems.

4.1 Nanostructures of Carbon Aerogels and ACFs

The microstructures of both carbon aerogels and activated carbon fibers (ACFs) consist of *nanoparticles* and *nanopores* (so named because they are of nanometer size) and are therefore sometimes termed nanostructures. The nanoparticles in these porous carbons are found to be rather graphitic by Raman scattering [4.3, 4.12]. In carbon aerogels, these nanoparticles further cluster to form larger *particles.* The admixtures of the conducting grains, namely the nanoparticles in ACFs and the particles in carbon aerogels, and the insulating pores hence constitute a new class of GM systems, possibly complementary to those found in cermets [4.1] and discontinuous thin films [4.6] because of the different spatial

distributions of the grains in these materials. The different morphologies of carbon aerogels, as compared to ACFs, further allow the study of two strongly localized systems with totally different structural characteristics (regarding granular size, grain separation, distribution, interconnection and dimensionality). Within each class of materials, further fine tuning of the nanostructural parameters is possible, as described below.

Carbon aerogels possess a "string of pearls" morphology, as illustrated in Fig. 3-10. Five different features can be identified in typical Transmission Electron Microscope (TEM) micrographs for aerogels, on which Fig. 3-10 is based [4.13]. Of relevance to the transport study are the bead-like particles [feature (c)] and the neck region between neighboring particles [feature (e)], which constitute the conducting and the insulating regions, respectively, as in a granular metallic system. The samples used in this work have a particle size $\sim 12 \pm 1.5$ nm in diameter. As shown in Chapter 3, high-resolution TEM, Raman scattering and Helium pycnometry experiments reveal the glassy-carbon-like nanostructure in the particles and the neck regions, both of which are composed of nanoparticles and nanopores. With frequent contacts among the glassy carbon ribbons which are entangled with each other within the particle, the particle can be thought of as the conductive grain in this GM system. The nanopores in the neck region between particles thus provide an upper limit for the tunneling distance between two conductive grains.

While the R/C ratio can be used to control the particle size in carbon aerogels, the mass density determines the packing ratio or interconnectivity. With increasing mass density, the particle size remains constant but the packing ratio of these particles increases. In this study, the R/C ratio is fixed at 200 (which fixes the particle size to be 12 ± 1.5 nm diameter) and the mass density is varied so that a density dependence of the transport properties can be studied.

In as-prepared ACFs [4.3], the conductive grains are the nanoparticles, which are graphite platelets 1-3 layers thick and $\sim$2.5 nm in diameter. ACFs are also a unique class of porous materials in which the total porous volume is almost entirely made up of micropores, whose average size is on the order of 1 nm. Hence, the specific surface area (SSA) (up to $3000\,m^2/g$) and the mean number of nanopores per unit volume of as-prepared ACFs are much larger than in carbon aerogels. However, the mass density of ACFs ($\sim 1.6\,g/cm^3$) is much higher because of the low density of mesopores, which are typically larger than 2 nm in size, and the large packing ratio of graphite platelets, as depicted in Fig. 6-7. Locally,

some neighboring platelets that are separated on an atomic scale are more or less aligned in short sections in the in-plane direction, but globally, the platelet-to-platelet angles are randomly and widely distributed. The micropores are accordingly bounded by the c-faces of the graphite platelets and their narrowest dimension is measured to be $\sim 10\,\text{Å}$.

Heat treatment at temperatures below 1000°C causes the platelets in ACFs to align without registry along the c-axis, but such heat treatment does not change the in-plane size of the platelets significantly [4.14, 4.15]. The effects of heat treatment are further discussed in Chapter 6.

4.2 Experimental Details

The preparation and characterization of carbon aerogels have been described in Chapter 3 and in Ref. [4.12]. The carbon aerogels in this study were all synthesized at the same R/C ratio of 200 and pyrolyzed at 1050°C, a temperature value within the range of that typical for disordered carbons to undergo a metal-insulator transition (1000-1200°C for ACFs [4.4].) The density was controlled (from $\rho_m \sim 0.1$ to $\sim 0.65\,\text{g/cm}^3$) by varying the reactant concentrations of the starting solution.

The manufacturing procedure for the synthesis of the as-prepared phenol-based ACFs (supplied by Kuraray Chemical Co. in Japan) is described in Chapter 2 and also in Refs. [4.3, 4.16, 4.17]. Prior to heat treatment, the phenol-based ACFs studied in this chapter have an SSA of $1000\,\text{m}^2/\text{g}$. These ACFs are subsequently heat-treated at 850°C in an Argon atmosphere for about 1 hour. The length of the fiber sample is measured by an optical microscope (~1 cm) and the diameter by a Scanning Electron Microscope ($\sim 10\,\mu\text{m}$).

The details of the transport experiments are described in Chapters 2 and 3. Extreme care was exercised to ensure the temperature homogeneity throughout the thermally insulating carbon aerogel samples. In particular, the low-temperature scan of the resistivity from 1.5 K to 4.2 K was rate-controlled to take 2 hours.

4.3 Experimental Results

The temperature-dependent electrical conductivity and magnetoresistance for both ACFs and carbon aerogels are presented in this section, in a fashion illustrative of the Coulomb-gap variable-range hopping behavior to be discussed later. Results from other

relevant characterization measurements are used to interpret these transport results.

In Chapter 2, we have established that all the ACFs with various specific surface areas (SSA) have exhibited resistivity behavior conforming to Eq. (4.1) with $p = 2$. To study this behavior further, we proposed previously to measure the magnetoresisitance, preferably at low temperatures, where the strong localization behavior is more pronounced. Unfortunately, the resistance of the ACFs, as prepared, rises drastically with decreasing temperature and eventually become too high for accurate measurements at very low temperatures. Resistivity measurements from 4.2 K to 300 K, however, show that Eq. (4.1) with $p = 2$ describes the transport behavior in all the as-prepared ACFs, as we have seen in Chapter 2, and also the behavior of the ACF heat-treated at $T_{\rm HT} = 850°$C, as will be shown below, implying universality in the transport properties of all ACFs, irrepective of their SSA and heat treatment temperature $T_{\rm HT}$. This universality facilitates the study of the effect of heat treatment by concentrating on one individual type of ACFs (e.g., same SSA and precursor material), and suggests the use of the heat-treated ACFs, which have a lower resistance at low temperature, in a representative study of the magnetoresistance (MR).

As shown in the $\log \rho$ versus T plots in the inset to Fig. 4-1, the many-decade change of ρ in both the as-prepared and the heat-treated ACFs at low temperature ($T < 100$ K) is characterisitic of a strongly localized system. It is remarkable that the strongly temperature-dependent ρ over the temperature range 4 K $< T <$ 100 K for both the as-prepared and the heat-treated ACFs were well fitted by Eq. (4.1) for $p = 2$ and with $T_0 = 530$ K and 92 K, respectively, as shown by the solid lines in Fig. 4-1, where the data points for $\log \rho$ are also plotted versus $1/T^{1/2}$. In both the inset and the figure in Fig. 4-1, the temperature dependence of $\rho(T)$ is weaker and the absolute magnitude of ρ is lower in the heat-treated ACF than in the as-prepared ACF because heat treatment brings ACFs closer to the metal-insulator (MI) transition conditions.

Raman scattering measurements [4.15,4.18] show that the in-plane microcrystallite size does not increase by much upon heat treatment at $T_{\rm HT} = 850°$C [see Fig. 6-5(b)]. Thus, fusion between neighboring platelets has not yet taken place and the granular size can be assumed to remain at ~ 30 Å, the same value observed in the as-prepared ACFs [4.3]. BET measurements [4.15] indicate, however, that the collapse of micropores begins when $T_{\rm HT}$ reaches $\sim 1000°$C. It is conceivable that the graphite platelets have at least begun to realign

preferentially along the c-axis, consequently forming an easier path for conduction than in the as-prepared ACFs. Nevertheless, metallic conductivity is still not achievable in these heat-treated ACFs, as indicated by the zero value of the conductivity $\sigma(T = 0)$ at zero temperature and the negative temperature coefficient of resistivity (TCR). This is because the narrow necks (constrictions) connecting the neighboring platelets (approximately a single-bond length apart) *are not necessarily electrically conductive*, although coupled platelets are needed to hold the porous sample together. The short distance of this somewhat insulating spatial gap is essential for the applicability of the variable-range hopping mechanism discussed later.

The magnetoresistance (MR) curves for the ACF heat-treated at 850°C at different measurement temperatures are plotted in Fig. 4-2 on different vertical scales to illustrate the approximately parabolic field dependence at low field. The anomalous MR curve at 50 K (with a magnitude greater than that at 30 K) might have been due to the ineffectiveness of the capacitance temperature sensor in holding the temperature steady in a high field at this temperature. All MR curves follow a quadratic field dependence at low field. While the magnitude of the MR increases with decreasing temperature, the field value for the onset of deviations from the quadratic field dependence decreases at the lowest measurement temperatures (< 7 K). Though not the focus of this chapter, the effect of progressive heat treatment at temperatures below that needed for the MI transition is to cause the positive MR of the heat-treated ACFs to gradually decrease in magnitude, as is seen in Ref. [4.4] and Chapter 7 in this thesis.

Positive MR in a VRH system can be explained by the field-induced shrinkage of the wavefunction [4.19]. Accompanying the reduced wavefunction overlap is a decrease in the probability of tunneling and hence an increase in the resistance. The temperature and the field dependence of the positive MR in the low-field limit is given by [4.19]:

$$\ln\left[\frac{\rho(H)}{\rho(0)}\right] = t\left(\frac{\xi}{\lambda}\right)^4\left(\frac{T_0}{T}\right)^{3/p} \equiv AH^2 \tag{4.2}$$

where $\lambda = \sqrt{\hbar c/eH}$ is the magnetic length, ξ is the localization length of the wavefunction, p is the same exponent as in Eq. (4.1) and t, a constant typically on the order of 0.001, is p-dependent. From fitting the $\ln[\rho(H)/\rho(0)]$ data at low field versus H^2, the quadratic coefficients A as defined in Eq. (4.2) are obtained as a function of temperature. As plotted

in Fig. 4-3, the slope of $\log A$ versus $\log T$ obtained from a linear fit is $\simeq 1.8 \pm 0.2$, implying that $p \sim 2$ if $A \propto 1/T^{3/p}$.

In Fig. 4-4, the logarithmic resistivities are plotted against $1/T^{1/2}$ for carbon aerogels of different densities. Except for the low density (LD) sample which exhibits a 7-decade increase in the resistivity from 10 K down to 2 K, the temperature dependence of the resisitivity for both the intermediate density (MD) and the high density (HD) samples is relatively weak, changing by less than 2 decades over the entire measurement temperature range 1.5 K $< T <$ 300 K. Indeed, the high packing ratio of the grains in the MD and the HD samples resembles the situation in the heat-treated ACF discussed above, or in general, in any GM system close to the MI transition.

All samples in Fig. 4-4 show the $p = 2$ behavior in Eq. (4.1) at very low temperature ($<$ 10 K) with $T_0 = 2100$, 200 and 30 K for the LD, MD and HD aerogel samples, respectively. As discussed later, the large dielectric constant near the MI transition narrows the spread of the charging energy of the grains. Being a measure of this energy spread, T_0 should decrease with increasing density. At higher temperatures, deviations from linearity of $\log \rho$ with $1/T^{1/2}$ are observed for the LD and MD samples for complicated reasons given later.

The MR data for the 0.457 g/cm^3 (MD) carbon aerogel sample are plotted in Fig. 4-5 as a function of magnetic field for various temperatures. Similar MR curves (not shown) with lesser magnitude for the quadratic field dependence at a given temperature are observed for aerogel samples with higher densities and were published elsewhere [4.12]. We made two series of measurements with each sample to eliminate the artifacts in the MR measurements due to temperature inhomogeneity and non-equilibrium effects. For graphical clarity, only the second set of quadratic coefficients A, which are close to the A values obtained from the first run, are plotted in Fig. 4-6. The slopes for the $\log A$ versus $\log T$ curves in Fig. 4-6 all read approximately 1.5 ± 0.3 below 10 K, corresponding to $p \sim 2$, again consistent with the $\sigma(T)$ behavior at low temperature.

4.4 Discussion of Transport Models

The limitations and shortcomings of previous transport models are discussed in connection with porous materials in this section.

The first attempt to explain the $p = 2$ conductivity behavior of Eq. (4.1) was Sheng's

model [4.1], which utilizes the concept of a charging energy $E_c \sim e^2/\kappa d$ that is required to put a charge e through a medium with dielectric constant κ onto a neutral grain of diameter d. This single-junction tunneling model and a later numerical study [4.20] using the critical path method (CPM) both suffer from their two underlying assumptions, namely that the grain separation s and diameter d are locally correlated, and that both are widely distributed, both of which are unsubstantiated by the experimental observations in most GM systems [4.7, 4.21], including our porous carbon systems.

The most promising nearest-neighbor (N-N) hopping model so far is provided by the numerical and theoretical studies using the critical path method (CPM) with independent sets of uncorrelated distributions for s and d, which are on the same order [4.7–4.9]. It was found theoretically [4.8, 4.9] that VRH exists in GM systems only at very low temperature and that the $p = 2$ behavior is merely an interpolation between VRH over multiple grains at low temperature and N-N grain-to-grain hopping at high temperature. In porous carbons, however, $d >> s$ and the hopping distance, given by $R \sim (\hbar/\sqrt{2m\phi})(T_0/T)^{1/p} d/(s+d)$, where ϕ is the tunneling barrier, could exceed the N-N center-to-center distance $s + d$, implying the possibility of VRH.

The 1-dimensional VRH model is one VRH model with $p = 2$ but neither the glassy-carbon structure within a grain in carbon aerogels nor the bead-like granular configuration can be a medium for 1D VRH. Regarding the glassy-carbon structure, transport is dominated by free carriers, not localized carriers, because the photoconductivity ($\Delta\sigma_{ph}$) results for both the ACFs [4.22] and the carbon aerogels [4.23] show that $\Delta\sigma_{ph}/\sigma < 1$ even at low temperature, and hence that the dark carrier concentration, being larger than the photocarrier concentration, is not small. Although localization is in the present case achieved with a grain boundary, quasi-1D structures composed of these grains is still lacking because of the high packing ratio and hence high coordination number of grains in ACFs and high-density carbon aerogels. The high packing ratio should also preclude the possibility of any high-resistance blockade predicted by the quasi-1D localization transport model proposed by Brenig *et al.* [4.24] for a bundle of parallel and uncoupled 1D chains of finite length. Indeed, the temperature-dependent transport properties in both the ACFs and the carbon aerogels with different mass densities are very similar despite the difference in their chain lengths L.

Another VRH model with $p = 2$ is proposed in connection with the Miller-Abrahams

network [4.25] which models the conductivity σ between any pair of nodes (e.g., i and j), separated by r_{ij} in distance and ϵ_{ij} in energy, according to:

$$\sigma = \sigma_0 \exp\left(-\frac{2r_{ij}}{\xi} - \frac{\epsilon_{ij}}{k_B T}\right) \tag{4.3}$$

where σ_0 is some conductivity constant and ξ the localization length. If carrier-carrier (excitonic) interaction is included,

$$\epsilon_{ij} = \begin{cases} |\epsilon_j - \epsilon_i| - \frac{e^2}{\kappa r_{ij}} \ , \ (\epsilon_i - E_F)(\epsilon_j - E_F) < 0 \\ \\ \max\{\, |\epsilon_i - E_F| \, , \, |\epsilon_j - E_F| \,\} \ , \\ \qquad\qquad (\epsilon_i - E_F)(\epsilon_j - E_F) > 0 \ , \end{cases} \tag{4.4}$$

resulting in a stability condition:

$$|\epsilon_j - \epsilon_i| - \frac{e^2}{\kappa r_{ij}} \geq 0 \tag{4.5}$$

because neutral grains abound in a low-energy system. Efros and Shklovskii (ES) [4.10] showed that the above inequality [Eq. (4.5)] causes a Coulomb gap to develop near E_F and that the resistivity $\rho(T)$ should follow Eq. (4.1) with $p = 2$ and

$$T_0 = \frac{\beta e^2}{k_B \kappa \xi} \tag{4.6}$$

where β is a dimensionless factor on the order of unity.

The Coulomb gap variable-range hopping (CGVRH) expression has also been shown to fail to apply to GM systems [4.6], with the mere substitution [4.6, 4.26] of the effective decay length $s/\chi(s+d)$ [see Eq. (4.7)] for ξ, because the hopping distance $R \sim \xi\sqrt{T_0/T}$ was shown not to convincingly exceed the N-N distance $s + d$ when $s \sim d$, without yielding an unrealistically small insulating gap barrier. Yet, both conditions can be satisfied in porous carbons or possibly GM sytems near the metal-insulator (MI) transition, where $d >> s$, as discussed below.

4.5 Coulomb Gap Variable Range Hopping

In this section, we describe the CGVRH model and show that the model is not affected by the finite size of the grains at low temperature.

Hopping beyond the N-N sites dictates that Eq. (4.6) be extended to include the wavefunction decay within the hopping distance r_{ij}. The decay occurs over both the intervening gaps with average barrier height ϕ_s and width s, and the intervening grains with average barrier height ϕ_d (see below) and width d. Noting that the total distances over the intervening gaps and over the grains are on the average given by $rs/(s+d)$ and $(r-s)d/(s+d)$, respectively, we replace the WKB reciprocal decay length by its average:

$$\chi_{eff} = \chi_s \frac{s}{s+d} + \chi_d \frac{d}{s+d} \tag{4.7}$$

where $\chi_i = \sqrt{2m_i\phi_i/\hbar^2}$ with the subscript i denoting either s or d depending on the region of relevance. With $\exp[-2\chi_d sd/(s+d)]$ absorbed into the prefactor σ_0 and the substitution of χ_{eff} for $1/\xi$, Eq. (4.3) now describes a Miller-Abrahams network of finite-size localization sites.

We now discuss and estimate the effective barrier presented by a grain, i.e., ϕ_d. When the wavefunction decay in a metallic grain is negligible, then N-N hopping should be more likely than VRH to be the transport mechanism, as pointed out in Ref. [4.27]. Fluctuations in the granular energy, however, make VRH possible by providing a scenario in which a N-N hop is not as energetically favourable as a distant hop. Fluctuations also provide a means of carrier localization in the form of an effective barrier in the case that the gap barrier is small ($\chi_s s < 1$), such as in porous carbon materials. In porous materials, it is necessary that the grains be linked structurally (but not necessarily electrically) in order to hold the sample together. These links as well as the image force between the N-N grains could significantly narrow s and lower ϕ_s so that $\chi_s s << \chi_d d$ and only the wavefunction decay in the intervening grains due to granular energy fluctuations becomes important. The difficulty previously encountered when applying the original CGVRH model, namely that a large hopping distance and a large hopping barrier are inconsistent with each other, can now be circumvented because ϕ_d is typically much smaller than the work function of metals, and the hopping distance $R \sim \chi_d^{-1}\sqrt{T_0/T}$ can be quite long relative to d provided that the χ_d associated with ϕ_d is small.

There are two kinds of fluctuations in the granular energy. Adkins [4.5] postulated that in a disordered system like GM, there exists a random disorder potential in the surroundings of each grain, changing the charging energy E_c of that grain by an amount not exceeding its original charging energy, since a discharge to the ground state would result for a larger change in E_c. Consequently, given a sharp distribution for the granular size as in carbon aerogels, the perturbed energy of the system is then uniformly distributed within the range $E_F \pm 2E_c$. The second kind of energy fluctuation arises from the quantum size effects of the grains, which cause an energy level splitting within an individual grain on the order of E_F/N, where $N \propto d^3$ is the number of carriers present on the grain [4.28,4.29]. In carbon aerogels, $d \sim 120\,\text{Å}$, $E_c \sim 120/\sqrt{\kappa}$ meV, $E_F \sim 1$ meV and the free carrier concentration is $n \sim 10^{19}\,\text{cm}^{-3}$ [typical of disordered carbons and also supported by superconducting quantum interference device (SQUID) measurements [4.12]]. Therefore, we conclude that $E_c >> E_F/N$ in porous carbons. The same condition applies in GM well below the percolation threshold [4.1].

The effective barrier ϕ_d should be on the order of the fluctuation of the charging energy. Hence, on averaging over the energy width of $E_F \pm 2E_c$,

$$\phi_d \simeq 2E_c = \frac{2e^2}{\kappa d} \quad . \tag{4.8}$$

The full algebraic details leading to a rigorous percolation solution to the Miller-Abrahams network associated with a GM or porous system involving the excitonic interaction can be found in analogy with the approximate solution by ES (Efros *et al.* [4.19,4.30]) for the point-size site percolation problem and will only be outlined below. We use for GM systems the same density of states (DOS) derived [4.31,4.32] for point-size localization sites because the low DOS inside the Coulomb gap implies a large effective grain-to-grain separation which renders the finite size of the grains irrelevant.

In the doped semiconductor case, the critical volume fraction for quantum percolation (Θ_c) is assumed to be temperature invariant, so that the high-temperature Θ_c value can be used to solve the full VRH equation at low temperature. It is well documented [4.19, 4.30] that $\Theta_c = 0.23$ for impurity conduction in semiconductors in the high temperature regime, where N-N hopping dominates. It is tempting to follow the same procedure for GM systems with finite-size particles by using the Monte Carlo results obtained by Scher

and Zallen (SZ) [4.33] for the site percolation problem in lattices morphologically similar to our porous carbons. However, we note that Θ_c is in fact *not* temperature-invariant in GM systems, in which the low-temperature Θ_c value is changed to 0.15 due to the finite size of the grains [4.33]. Further noting that the long hopping distance implied by VRH could readily nullify the finite-size effect, we propose that $\Theta_c = 0.23$ for both GM and doped semiconductors at low temperature, and that Θ_c remains temperature-invariant in GM sytems at least throughout the VRH regime. Equation (4.1) is therefore obtained with $p = 2$ and $\beta = 2.6$ for 3D, which agrees with the empirical value of $\beta = 2.8$ from a numerical simulation [4.30]. Since no empirical or theoretical value for β in 2D is available, we use the same approximate, yet reliable, procedure with the 2D DOS to obtain $p = 2$ and $\beta = 6.2$ for 2D CGVRH.

In analogy with the Green's function formalism used by ES [4.19], the derivation for the magnetoresistance (MR) in the CGVRH model can be reproduced for the GM case by replacing the Coulomb potential with a step potential and substituting $1/\chi_{eff}$ for ξ. The resultant magnetic energy term ($r_{ij}^3/18\lambda^4\chi_{eff}$ in 3D and $r_{ij}^3/24\lambda^4\chi_{eff}$ in 2D, where r_{ij} is the distance between the two grains involved in a hop) is then added to the exponent in Eq. (4.3). Under the two conditions [4.19] that: (i) the wavefunction inside the step potential well is not significantly affected by the applied magnetic field (i.e., $\lambda \equiv \sqrt{\hbar c/eH} >> d$), and (ii) the magnetic potential is smaller than the step potential well (i.e., $d << r_{ij} << \lambda^2\chi$), the MR in the weak-field limit is then given by Eq. (4.2) with $p = 2$, $\xi = \chi_{eff}^{-1}$, $t = 0.0015$ for 3D [4.34], and $t = 0.0020$ for 2D. Both conditions hold true for our carbon aerogel and ACF samples within the restricted field values of $B < 5$ T and < 73 T, respectively.

Measurements of the temperature dependence of the MR thus serve as a good check for the model in that a consistent set of values for both the effective mass m and the dielectric constant κ, which are shown in Table 4.1, should be obtained from Eqs. (4.2) and (4.6).

4.6 Applications to Granular and Porous Systems

The application of the CGVRH model to various localization media with different nanostructures is discussed in this section. Each nanostructure studied below corresponds to a limiting case of Eq. (4.7). For reference, the physical parameters are listed in Table 4.1. The cermet and the granular aluminum film selected here are the same ones selected in

Materials	Cermet	Granular Al Film	Carbon Aerogel			ACF	
			0.119 g/cm^3	0.457 g/cm^3	0.645 g/cm^3	as-prepared	850°C
x	0.24	0.5	0.058	0.222	0.313	-	-
d(Å)	24†	30	120	120	120	30	> 30
s(Å)	11†	2	2	2	2	2	2
T_0 (K) (expt.)	16000	200	2100	200	30	530	92
Conduction Mechanism	NNH	CGVRH	CGVRH & NNH*	CGVRH & NNH*	CGVRH	CGVRH	CGVRH
κ_{ins}	4	8	2	2	2	2	2
κ (EMT)	14	80	2	6	33	-	-
κ (expt.)	-	110	6	31	110	27	110
χ_{eff}^{-1} (Å)	1	21	35‡	74‡	140‡	33	100‡
m/m_0	1	1	0.084	0.090	0.089	0.1	> 0.022

† Extracted from Ref. [4.1].

‡ Deduced from the magnetoresistance data.

* Nearest-neighbor hopping only at high temperature.

Table 4.1: Various physical parameters for the granular metals and the porous materials under study, including the metallic volume fraction (x), the granular size (d) and separation distance (s), the experimental value of T_0, the dielectric constant measured (or assumed) in the insulator (κ_{ins}), calculated by Bruggeman's effective medium theory [κ(EMT)] and extracted from T_0 [κ(exp)], the conduction mechanism involved, and its associated effective decay length χ_{eff}^{-1}, and finally the effective mass (m/m_0).

Ref. [4.6], in which the original CGVRH theory was applied to GM systems.

4.6.1 Doped Semiconductors

In doped semiconductors, $d << s$ (in fact, $d \to 0$). Equation (4.7) reduces to the situation in doped semiconductors where $\chi_{eff} = \chi_s = 1/\xi$ if ϕ_s is taken to be the ionization potential of a carrier localized in a donor site (i.e., $\hbar^2/2m\xi^2$).

4.6.2 Granular Metals

Granular metals (GM) with a low metallic volume fraction (x) and a large experimental T_0 value are usually referred to as cermets. They differ in structure from the GM systems near the metal-insulator (MI) transition in that in the latter, matrix inversion begins to take place, as corroborated by the observation of a finite empirical value for $\sigma(T = 0)$ in some granular Al films [4.35, 4.36]. The matrix inversion was also directly observed in the TEM micrographs which show similar morphologies for both the insulating phase and the conducting phase (e.g., see the TEM micrograph for the $x = 0.35$ Au-Al_2O_3 film shown in Ref. [4.1]). The protrusions from the metallic grains into the insulating matrix

effectively narrow the gap tunneling distance and allow the image force to lower the gap barrier significantly. The morphology is then similar in both GM near the MI transition and porous carbons in which $s << d$, and suggests the same conduction mechanism for both systems.

A granular aluminum film measured by Chui [4.37] and other GM films [4.1] near the metal-insulator (MI) transition all have very low values for s and T_0. Using $T_0 = 200$ K from Table 4.1, $\chi_{eff} \simeq \chi_d$ and $\beta = 2.8$, we found that $\kappa \sim 110$ from Eq. (4.6). Then, $\chi_d^{-1} = 21$ Å, $\chi_d d > 1$ and CGVRH is indeed possible below 30 K, which is about the same temperature at which the experimental $\sigma(T)$ curve begins to deviate from the $p = 2$ law [4.37].

On the other hand, in a Ni-SiO_2 cermet film studied in Ref. [4.1], in which the $p = 2$ law is followed from 25 K to 300 K, we observe that $\chi_s s >> \chi_d d$ if κ is taken to be the effective dielectric constant obtained from Bruggeman's effective medium theory (EMT). Then, the N-N hopping should dominate above $T_0/(2\chi_s s)^2 \simeq 30$ K, where the hopping distance is $R < 2(s + d)$. In this limit, the distributions in both s and d seem to be adequate for recovering the $p = 2$ law without considering the Coulomb gap [4.7–4.9], which should be exceeded by the hopping energy in the N-N hopping regime. Šimánek [4.7] derived the following expression for T_0 by solving the bond percolation problem:

$$k_B T_0 = 0.25 \chi_s s_{max}^{loc} \epsilon_{max} \tag{4.9}$$

where s_{max}^{loc} and ϵ_{max} are, respectively, the maximum s in the local distribution and the maximum ϵ in the energy distribution. Assuming $s_{max}^{loc} \sim 2s_{avg} = 22$ Å and $\chi_s \simeq 1$ Å^{-1}, we obtained $\epsilon_{max} \simeq 4e^2/\kappa d \simeq 0.25$ eV, which would give $\kappa \simeq 10$, in good agreement with the κ(EMT) listed in Table 4.1.

In general, the magnetoresistance as a function of both H and T behaves quite differently from one GM to another [4.9, 4.36]. Because the origin of the magnetoresistance is not limited to the wavefunction shrinkage effect studied here, its discussion is beyond the scope of this thesis.

4.6.3 Activated Carbon Fibers

In ACFs, the hopping of a charge carrier takes place between two platelets in the in-plane direction because the platelet-to-platelet separation of ~ 10 Å along the c-axis, given

by the micropore size (see section 4.1), is much larger than that in the in-plane direction. The platelets in the heat-treated ACFs can then be modelled as circular discs mostly aligned in a 2D plane locally as long as the hopping distance is within this local scale. The 2D CGVRH model is therefore used to explain the experimental data for ACFs. The charging energy of each grain also becomes $E_c \sim e^2/\kappa C$, where $C = d/2$ is the capacitance for a circular disc.

When s is as small as a single bond length, the image-force lowering of ϕ_s (e.g., 11.44 eV-Å/$\kappa_{ins}s$, where κ_{ins} is the dielectric constant in the insulating gap [4.38]) could be comparable in magnitude to the work function ($\sim$ 4.4 eV in graphite), resulting in $\chi_s s << \chi_d d$. Applying Eq. (4.2) with $t = 0.002$ to the temperature-dependent magnetoresistance data in Fig. 4-3 for the heat-treated ACF yields $\chi_{eff}^{-1} \simeq 100$ Å. Substituting χ_{eff} and T_0 extracted from Table 4.1 back into Eq. (4.6) with $\beta = 6.2$ gives $\kappa = 110$, which in turn gives $m_d = 0.022m_0$, where m_0 is the free-electron mass. We note that a larger and more reasonable value of m_d should be obtained if the divergence of the effective d and κ due to the possible delocalization of carriers over a few grains is considered near the MI transition. For example, when the carrier delocalization is over 5 grains, $m_d \sim 0.1m_0$, which is a more reasonable value.

For the as-prepared ACF, using the same 2D CGVRH model and assuming a valence-band effective mass of $0.1m_0$ for the majority hole carriers, we obtain a κ of 58 from Eq. (4.6) with $\beta = 6.2$. Because there is probably no extended in-plane alignment of the platelets in the as-prepared ACF, as shown in Fig. 6-7, the 3D CGVRH model might be more appropriate. Using $m_d = 0.1m_0$, we obtain a more reasonable κ value of 27 for this strongly disordered system.

The large κ values obtained from the CGVRH model reflects the divergence of the dielectric constant of an effective medium near the metal-insulator transition. It is noted that κ is not related to the dielectric constant of the solvent trapped in the micropores, as measured by the capacitance method.

4.6.4 Carbon Aerogels

As mentioned in section 4.1, carrier hopping takes place between the 12 nm particles in carbon aerogels because of the relative ease of charge transport within one such particle. The view that the transport between nanoparticles cannot be the dominant conduction

mechanism is experimentally supported by the strong dependence of both the temperature-dependent conductivity $\sigma(T)$ and the MR on mass density because only the packing ratio of the particles, and not the internal nanostructure inside the particles, is affected by the mass density.

Constrictions between adjacent grains and an image force again could lower ϕ_s so that $\chi_{eff} \simeq \chi_d$. Following the same procedure used above in the calculation for the heat-treated ACF, and using the average of the two sets of magnetoresistance data in Fig. 4-6, we estimate that $\chi_{eff}^{-1} \sim 35$, 74 and 140 Å, yielding $\kappa \sim 6$, 31 and 110 and consequently $m_d/m_0 = 0.084$, 0.090 and 0.089 for the $\rho_m = 0.119$ (LD for low density), 0.457 (MD) and 0.645 g/cm^3 (HD) aerogel samples, respectively. The fact that m_d/m_0 varies within a few percent agrees well with the SQUID measurements which show that the concentration of localized spins within the grains is approximately independent of mass density [4.12], thus providing evidence in support for identical nanostructural ordering in samples of all densities. This conclusion is also supported by the photoconductivity measurements [4.39]. The progressive increase in κ is expected as the aerogel approaches the MI transition. Again, as in the ACF case, the high κ values for the MD and the HD samples are only order-of-magnitude estimates because of the overlap effect near the MI transition. The κ(EMT) values should not be taken literally because EMT is found to be inapplicable to GM systems in general [4.9], and near the MI transition, κ should follow some scaling laws instead.

The onset temperatures (T_c) for CGVRH in Fig. 4-4 are different for aerogels with different densities. Besides the VRH requirement that $R > 2(s+d)$, namely that $T_c = 45$, 19 and 10 K for the LD, MD and HD samples, respectively, we can find a more stringent condition in carbon aerogels specifically, because they consist of crosslinked chains of grains. We define L_n as the average distance within which there is no crosslinking. Then within L_n, only 1D hops are possible and CGVRH only takes place when $R > L_n$. Since the size of the mesopores bounded by the particle chains is approximately inversely proportional to the mass density, L_n should decrease with increasing density. As shown in Fig. 3-10, which is based on a structural model presented in a previous TEM study [4.40], while $L_n \sim 2(s+d)$ in aerogels with higher densities, $L_n >> 2(s+d)$ for the LD sample, effectively imposing a new condition that $T < T_0/(\chi_d L_n)^2$ for CGVRH in the LD sample. Using $T_c \sim 10$ K and $1/\chi_d = 35$ Å, we can then estimate that in the LD sample, $L_n \sim 500$ Å, in agreement with the schematic diagram shown on the left hand side of Fig. 3-10, which shows $L_n \sim 4(s+d)$,

where $s + d \simeq 120$ Å is the N-N center-to-center distance. Above T_c, N-N hopping within a chain segment dominates, taking the form of simple thermal activation [4.24,4.41], which is observed in the present work ($p \sim 0.8$ above 10 K). Equation (4.9) is not followed because there can be no choice in selecting R (an essential ingredient for observing $p \neq 1$ behavior) without a lot of crosslinking.

For the HD sample, the $p = 2$ dependence of $\sigma(T)$ extends up to 300 K, a value higher than T_c. Similarly, a low T_0 value of 190 K was observed up to 300 K in an Au-Al_2O_3 film just below the MI transition with the metallic volume fraction $x = 0.38$. A transition from CGVRH to N-N hopping might have taken place at T_c. As discussed in the conduction mechanism for GM above, subpercolating systems could exhibit N-N hopping in the form of Eq. (4.9). The change of the *linear* slopes observed in the $\sigma(T)$ curve for the MD sample in Fig. 4-4 could be indicative of such a transition. The T_0 values on both sides of the transition are, however, very close as shown for the HD sample. If we equate $4e^2/\kappa d$ with ϵ_{max} when comparing Eq. (4.9) with Eq. (4.6), T_0 would be approximately identical in the two equations provided that $\chi_s s_{max}^{loc}/\chi_d d \simeq 2.6$, which is possible in view of the χ_d and d values listed in Table 4.1, and because of the micropore size of 7 Å, which sets an upper limit for s. In fact, for very small T_0 values, the $1/T^{1/2}$ dependence of $\log[\sigma(T)]$ is just too weak to permit an accurate evaluation of any change in the T_0 values.

Finally, we comment on the advantage of the CGVRH model over the fluctuation-induced tunneling (FIT) model [4.11] used earlier in Chapter 3 for the purpose of aerogel characterization. First, unlike the FIT model, the CGVRH model yields effective masses much smaller than m_0 for all 3 carbon aerogels of different densities, reflective of the conductive nature of the particles. Secondly, the density-independent nanostructure within the particles in carbon aerogels calls for identical values for the effective mass irrespective of density, which are observed in the CGVRH model but not in the FIT model. Thirdly, both the large magnitude and the temperature dependence of the magnetoresistance at low temperature are much better explained by the CGVRH model than a tunneling model. Therefore, we believe that CGVRH is a more dominant conduction mechanism in carbon aerogels than FIT.

References

[4.1] B. Abeles, P. Sheng, M. D. Coutts and Y. Arie, Adv. Phys. **24**, 407 (1975).

[4.2] A. W. P. Fung, J. J. Chen, Z. H. Wang, M. S. Dresselhaus, and R. W. Pekala, in *Extended Abstracts of the 21st Biennial Conference on Carbon, Buffalo, NY, 1993*, edited by D. D. L. Chung (American Carbon Society, State College, PA, 1993), p. 659.

[4.3] A. W. P. Fung, A. M. Rao, K. Kuriyama, M. S. Dresselhaus, G. Dresselhaus, and M. Endo, J. Mater. Res. **8**, 489 (1993).

[4.4] A. W. P. Fung, M. S. Dresselhaus, and M. Endo, Phys. Rev. **B 48**, 14953 (1993).

[4.5] C. J. Adkins, J. Phys. C **20**, 235 (1987).

[4.6] C. J. Adkins, in *Hopping and Related Phenomena*, edited by H. Fritzsche and M. Pollak (World Scientific, Singapore, 1990), p. 93.

[4.7] E. Šimánek, Solid State Comm. **40**, 1021 (1981).

[4.8] P. Sheng and J. Klafter, Phys. Rev. **B27**, 2583 (1983).

[4.9] P. Sheng, Phil. Mag. **B 65**, 357 (1992).

[4.10] A. L. Efros and B. I. Shklovskii, J. Phys. **C8**, L49 (1975).

[4.11] P. Sheng, E. K. Sichel, and J. J. Gittleman, Phys. Rev. Lett. **40**, 1197 (1978).

[4.12] A. W. P. Fung, Z. H. Wang, K. Lu, M. S. Dresselhaus, and R. W. Pekala, J. Mater. Res. **8**, 1875 (1993), and the references therein.

[4.13] R.W. Pekala and C.T. Alviso, in *Novel Forms of Carbon*, edited by C. L. Renschler, J. J. Pouch, and D. M. Cox, MRS Symposia Proceedings No. 270 (Materials Research Society, Pittsburgh, 1992), p. 3.

[4.14] A. M. Rao, A. W. P. Fung, M. S. Dresselhaus, G. Dresselhaus, and M. Endo, in *Extended Abstracts of the 20th Biennial Conference on Carbon, Santa Barbara, CA, 1991*, edited by R. A. Meyer (American Carbon Society, State College, PA), p. 242.

[4.15] A. M. Rao, A. W. P. Fung, M. S. Dresselhaus, and M. Endo, J. Mater. Res. **7**, 1788 (1992).

[4.16] E. Tanaka, Fuel and Combustion **54**, 241 (1987).

[4.17] A. W. P. Fung, A. M. Rao, K. Kuriyama, M. S. Dresselhaus, and G. Dresselhaus. in *Defects in Materials*, edited by P. D. Bristowe, J. E. Epperson, J. E. Griffith, and Z. Liliental-Weber, MRS Symposia Proceedings, No. 209 (Materials Research Society, Pittsburgh, 1991), p. 335.

[4.18] K. Kuriyama and M. S. Dresselhaus, J. Mater. Res. **7**, 940 (1992).

[4.19] B. I. Shklovskii and A. L. Efros, *Electronic Properties of Doped Semiconductors* (Springer, Berlin, Heidelberg, 1984).

[4.20] J. Heinrichs, A. A. Kumar, and N. Kumar, J. Phys. **C 9**, 3249 (1976).

[4.21] K. D. Leaver, J. Phys. **C 10**, 249 (1977).

[4.22] K. Kuriyama and M. S. Dresselhaus, J. Mater. Res. **6**, 1040 (1991).

[4.23] G. A. M. Reynolds, Z. H. Wang, M. S. Dresselhaus, A. W. P. Fung and R. W. Pekala, Phys. Rev. **B 49**, 15027 (1994).

[4.24] W. Brenig, G. H. Döhler, and H. Heyszenau, Phil. Mag. **27**, 1093 (1973).

[4.25] A. Miller and E. Abrahams, Phys. Rev. **120**, 745 (1960).

[4.26] O. Entin-Wohlman, Y. Gefen, Y. Shapira, J. Phys. **C 16**, 1161 (1983).

[4.27] M. P. J. van Staveren, H. B. Brom, and L. J. de Jongh, Phys. Rep. (Rev. sect. of Phys. Lett.) **208**, 1 (1991).

[4.28] R. Kubo, J. Phys. Soc. Japan **17**, 975 (1962).

[4.29] W. P. Halperin, Rev. Mod. Phys. **58**, 533 (1986).

[4.30] A. L. Efros, N. Van Lien, and B. I. Shklovskii, Solid State Commun. **32**, 851 (1979).

[4.31] A. L. Efros, J. Phys. **C 9**, 2021 (1976).

[4.32] S. D. Baranovskii, A. L. Efros, B. L. Gelmont, and B. I. Shklovskii, Solid State Commun. **27**, 1 (1978).

[4.33] H. Scher and R. Zallen, J. Chem. Phys. **53**, 3759 (1970).

[4.34] I. S. Shlimak, A. N. Ionov, and B. I. Shklovskii, Fiz. Tekh. Poluprovodn. **17**, 503 (1983) [Sov. Phys.-Semicond. **17**, 314 (1983)].

[4.35] W. L. McLean, P. Lindenfeld, and T. Worthington, in *Electrical Transport and Optical Properties of Inhomogeneous Media*, edited by J. C. Garland and D. B. Tanner, AIP Conf. Proc. No. 40 (American Institute of Physics, New York, 1978), p. 403.

[4.36] W. L. McLean, T. Chui, B. Bandyopadhyay, and P. Lindenfeld, in *Inhomogeneous Superconductors*, Proceedings of the International Conference on Inhomogeneous Superconductors, Berkeley Springs, WV, 1979, edited by D. U. Gubser, T. L. Francavilla, S. A. Wolf, and J. R. Leibowitz, AIP Conf. Proc. No. 58 (American Institute of Physics, New York, 1980), p. 42.

[4.37] T. Chui, G. Deutscher, P. Lindenfeld, and W. L. McLean, Phys. Rev. **B 23**, 6172 (1980).

[4.38] J. G. Simmons, in *Tunneling Phenomena in Solids*, edited by E. Burstein and S. Lundqvist, (Plenum Press, New York, 1969), p. 135.

[4.39] M. Hosoya, G. Reynolds, and M. S. Dresselhaus, J. Mater. Res. **8**, 811 (1993).

[4.40] G. C. Ruben, R. W. Pekala, T. M. Tillotson, and L. W. Hrubesh, J. Mat. Sci. **27**, 4341 (1992).

[4.41] J. Kurkijärvi, Phys. Rev. **B 8**, 922 (1973).

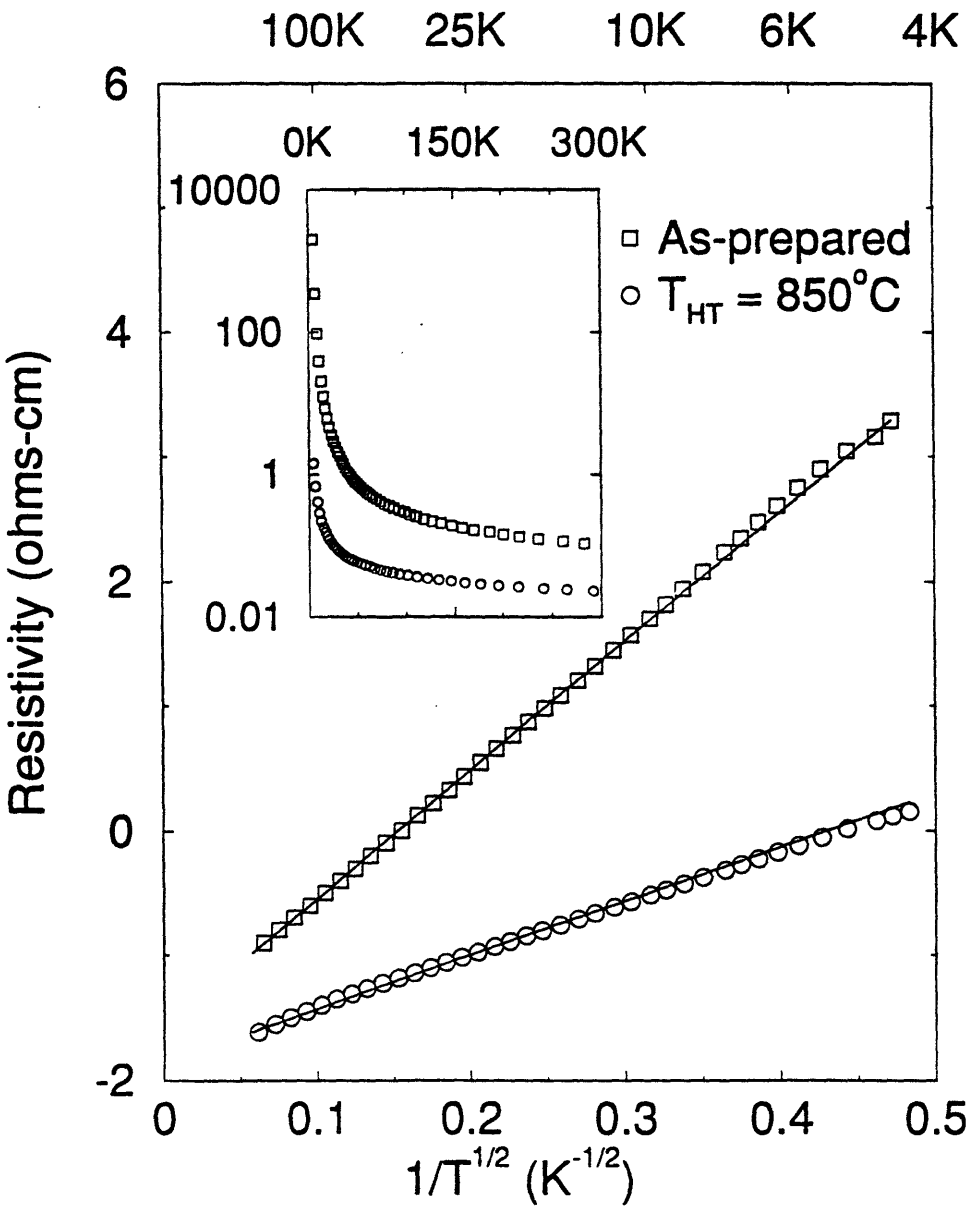

Figure 4-1: Logarithmic resistivity versus $1/T^{1/2}$ for both the as-prepared ACF and the ACF heat-treated at 850°C, with specific surface area SSA = $1000\,m^2/g$ for both samples. The x-axis on top of the figure gives the temperature directly. The inset plots the same logarithmic resistivity curves as a function of linear temperature to show the drastic change in resistivity at low temperature.

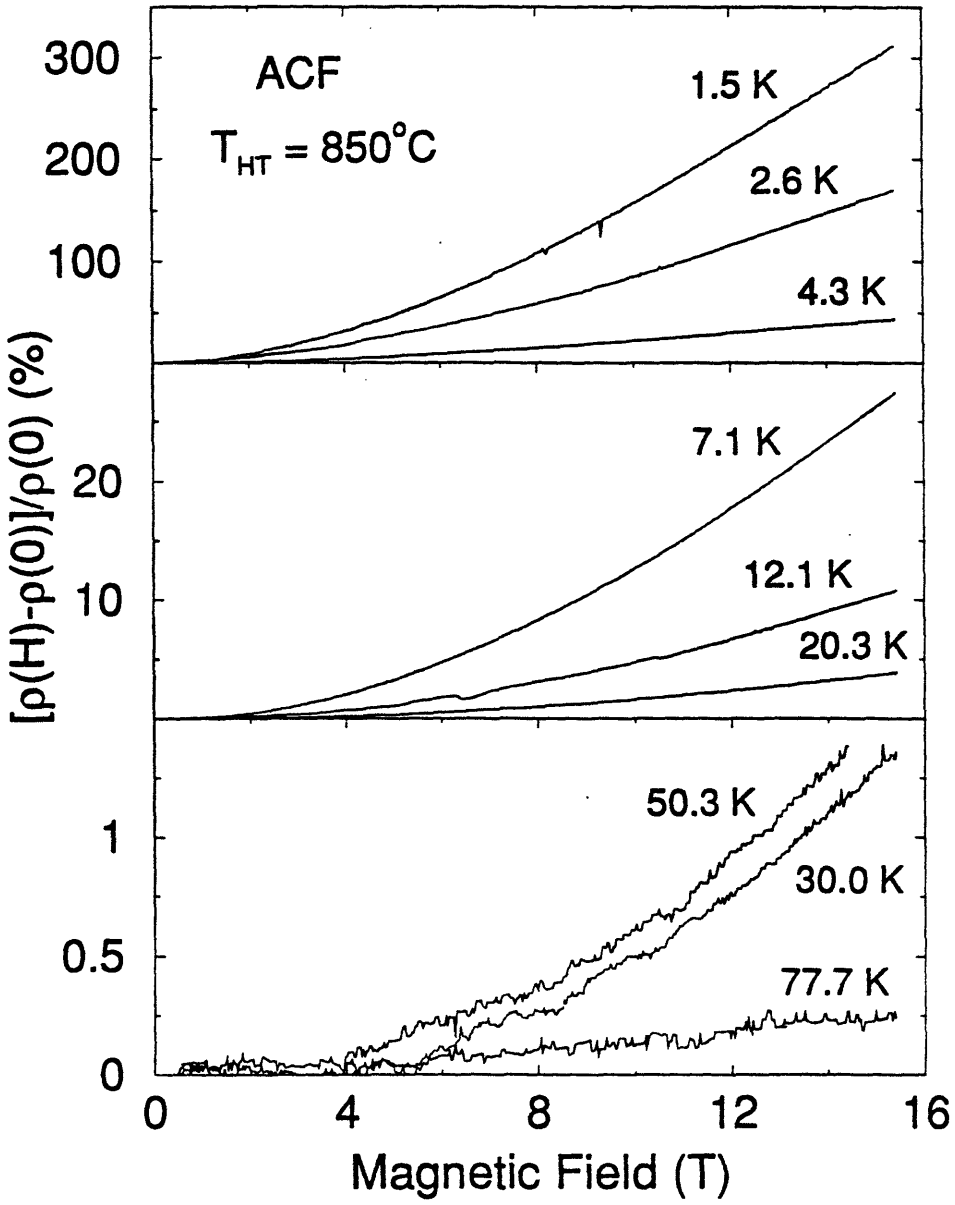

Figure 4-2: Transverse magnetoresistance for the ACFs heat-treated at 850°C at the indicated measurement temperatures. The y-axis is divided for clarity into 3 different scales according to the relative magnitudes of the data.

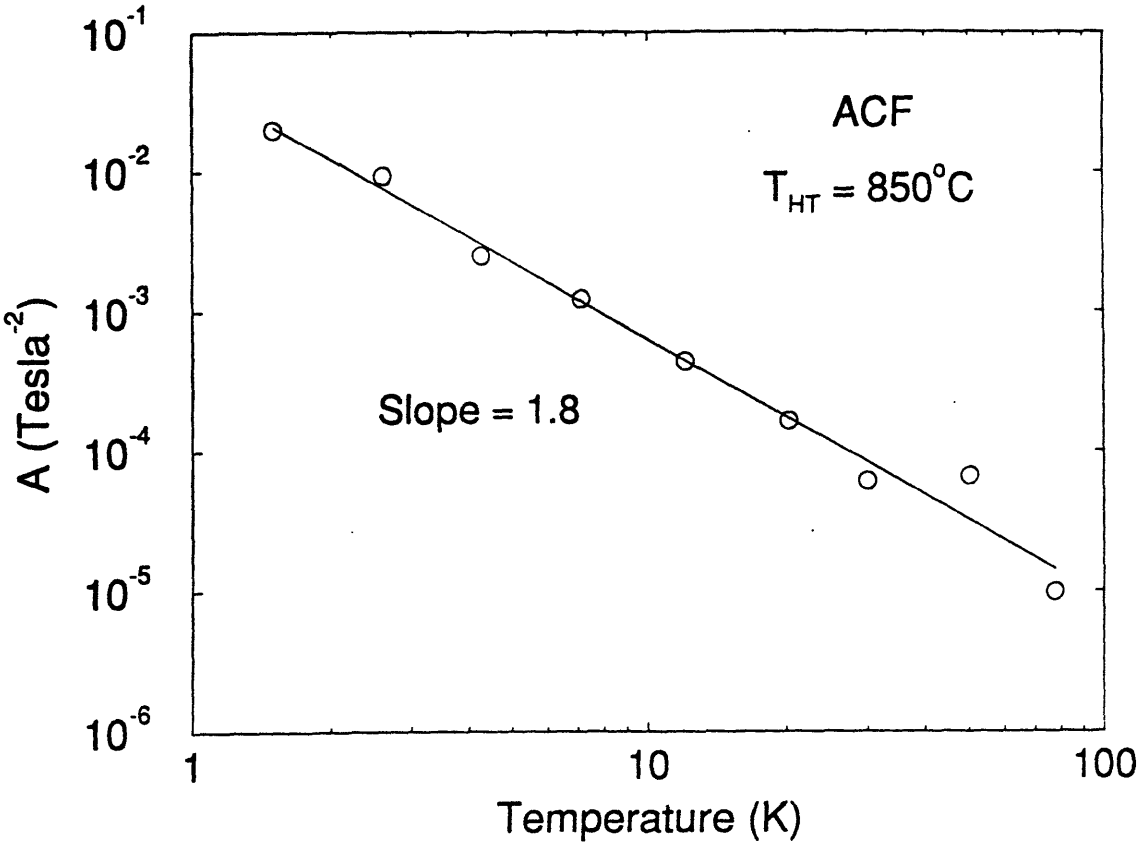

Figure 4-3: Log-log plot of the quadratic coefficients A (see definition in text) extracted from the low-field transverse magnetoresistance measured for the ACF heat-treated at 850°C. Each data point is for magnetoresistance measurements made at the indicated measurement temperature. The solid line is a linear fit to the log-log plot which shows a slope of ~ 1.8.

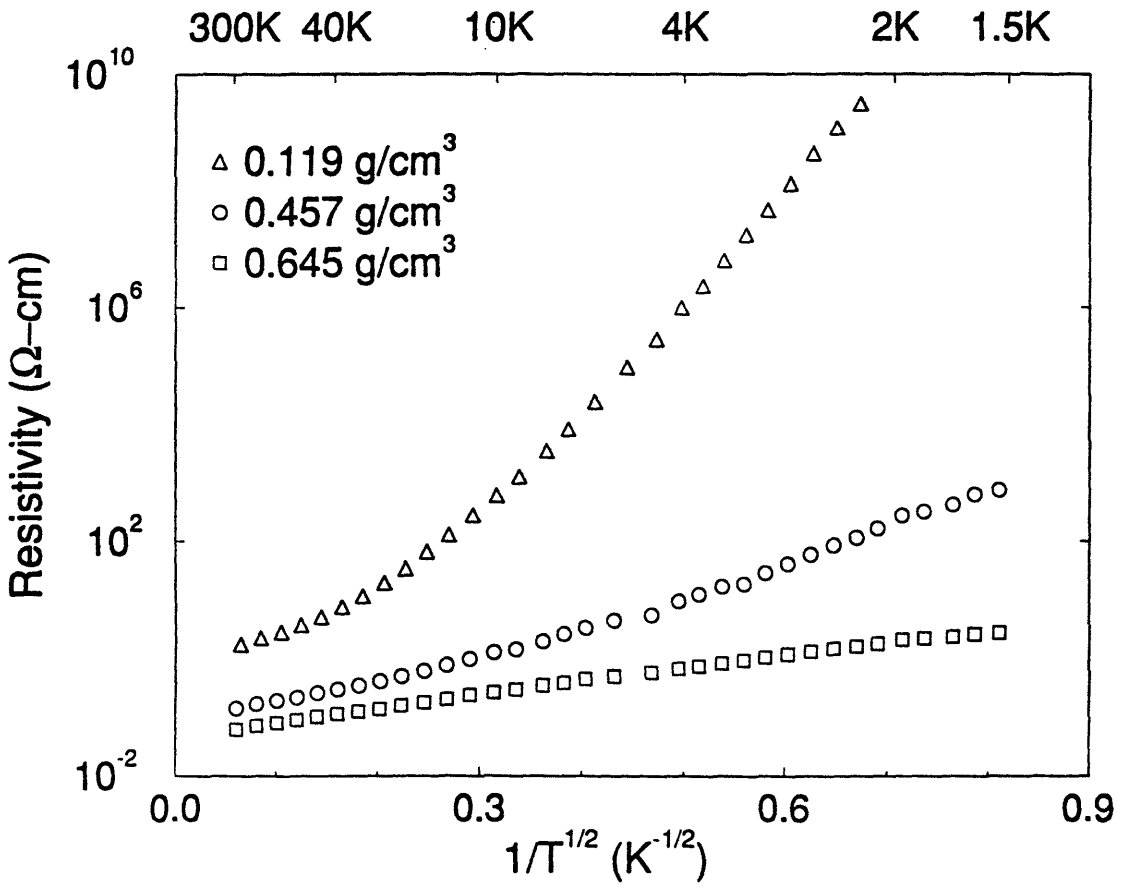

Figure 4-4: Logarithmic resistivity versus $1/T^{1/2}$ for carbon aerogels of labelled densities. The upper scale gives the actual measurement temperatures.

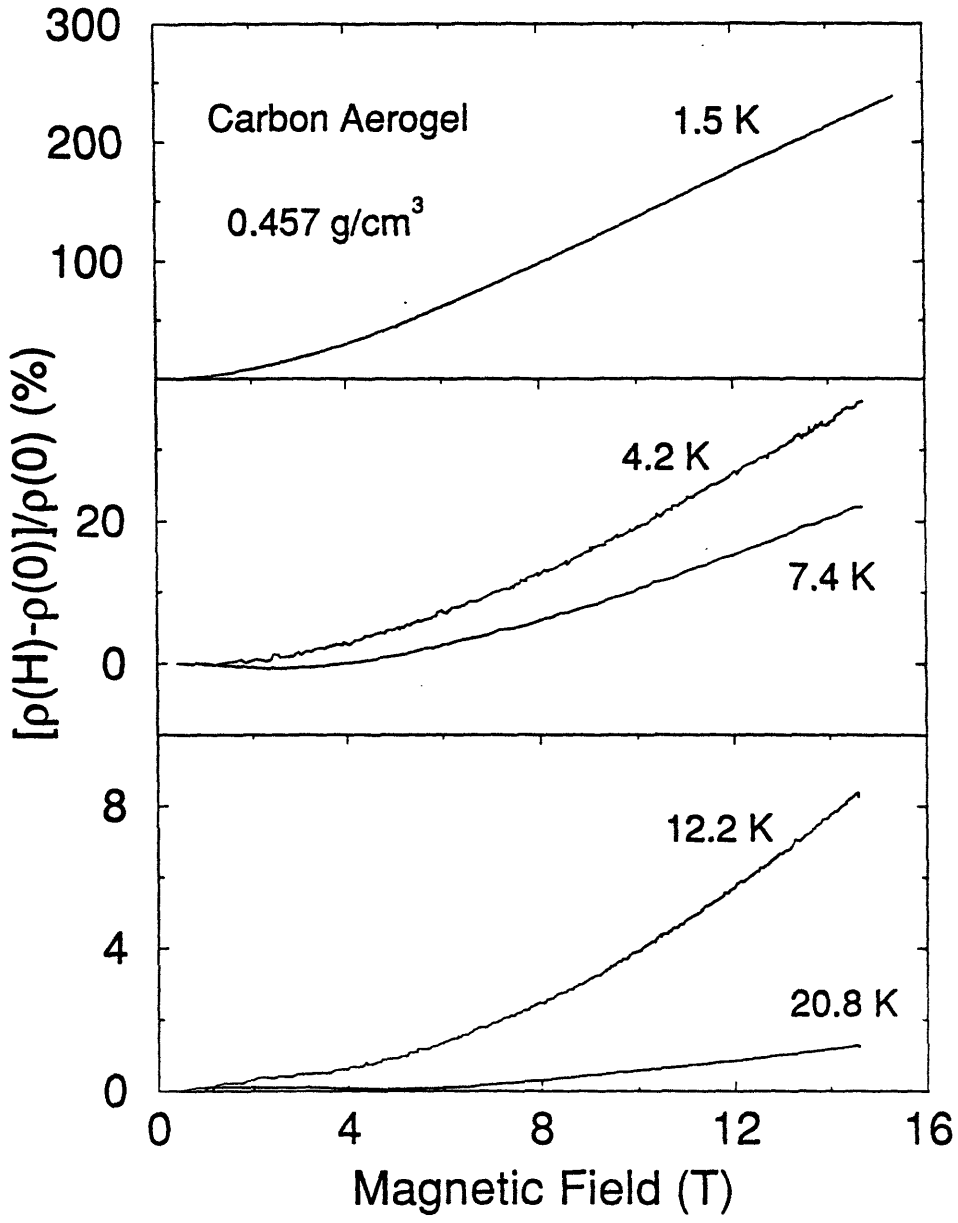

Figure 4-5: Transverse magnetoresistance for a carbon aerogel sample with a mass density of $0.457\,\mathrm{g/cm^3}$ at various temperatures.

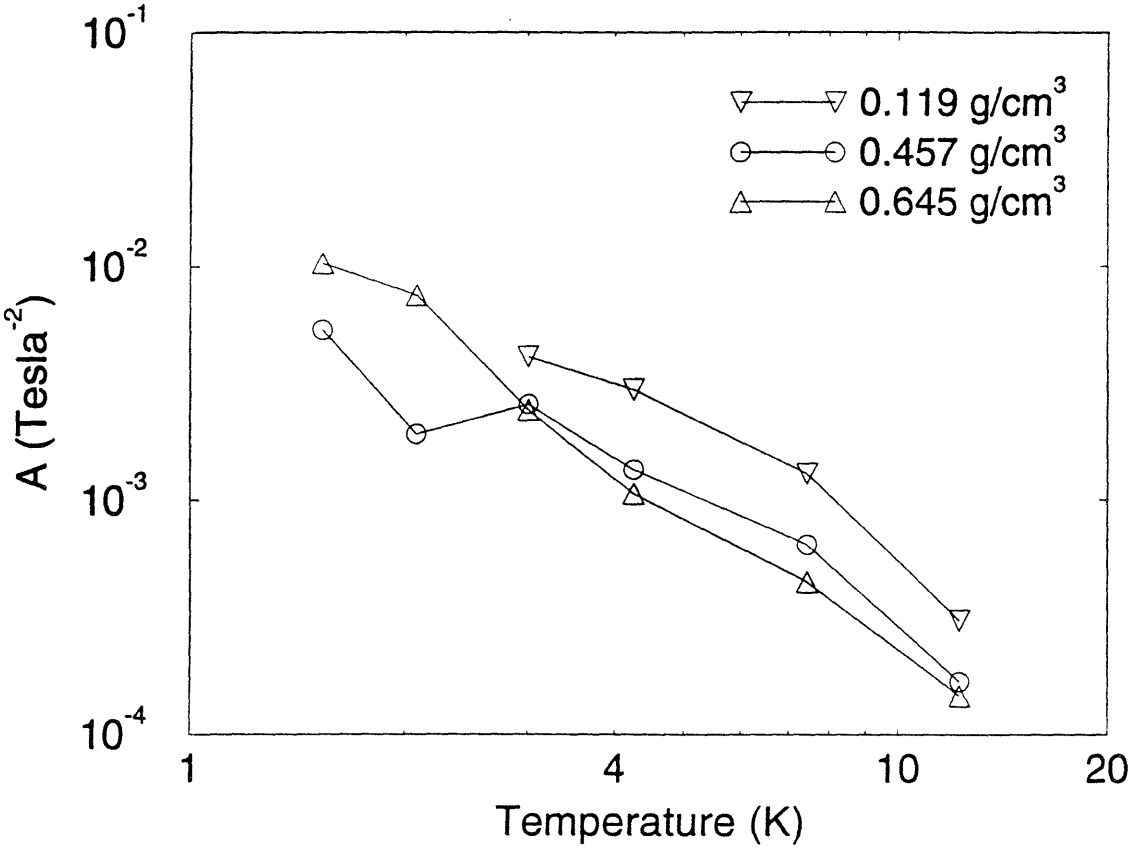

Figure 4-6: Log-log plot of the quadratic coefficients A (see text) extracted from the temperature-dependent magnetoresistance data obtained for carbon aerogels of three different mass densities in the second run. Below 10 K, the slopes of all the $\log A$ versus $\log T$ curves are ~ 1.5.

Chapter 5

Transport, Magnetic and Structural Properties in Heat-Treated Carbon Aerogels

In previous chapters, we have shown that as nanoporous materials, both ACFs and carbon aerogels exhibit strong localization behavior in their low-temperature transport properties. It was also shown that the nanostructures of these two strongly disordered materials are separately tunable by varying the specific surface area (SSA) and heat treatment temperature T_{HT} for ACFs, and in addition, the mass density and resorcinol/catalyst (R/C) ratio for carbon aerogels. We can briefly summarize the results by stating that while the structural properties of both materials have stronger dependences on all these characterization parameters, the transport properties are only sensitive to T_{HT}, mass density and R/C ratio.

Each of these factors affects the nanostructure in different ways. For later discussions, we attempt to give definitions for two types of disorder likely to play some role in electrical transport, in general. Porous materials are also granular materials, consisting of particles on the $\sim$ 10 nm scale. Within the particles as well as on their surface, impurities, vacancies, dangling bonds and defects alike abound, with sizes on the atomic scale. The first type of disorder is now associated with the granularity and defined as *mesoscopic* disorder, according to its size relative to the second type of disorder, known as *microscopic* disorder, which consists of defects such as dangling bonds, vacancies, impurities, etc.

The effects of the R/C ratio on the structural, magnetic and transport properties have already been studied in a collaborative effort with my fellow colleague Gillian A. M. Reynolds [5.1]. The results will be fully presented in her Ph.D. dissertation [5.2], and are only briefly referred to in this chapter. The mass density factor has also been discussed in Chapters 3 and 4. The strong effects of heat treatment on the transport properties have only been hinted at in Chapter 4, where the ACF heat-treated at 850°C were shown to exhibit the same conduction mechanism. The carbon aerogels show a much higher magnitude and a much weaker temperature dependence, in its conductivity, in comparison with that for the as-prepared ACF. In the remaining chapters, we therefore investigate the full extent of the effects of heat treatment on the structural and transport properties of both carbon aerogels and ACFs by varying T_{HT} over a wide range of values.

From the point of view of nanospace engineering, these chapters serve as a guide to industrial applications, where heat treatment can be used as a potential means of manipulating the nanostructures. From an academic point of view, depending on the graphitizability of the material and the magnitude of T_{HT}, heat treatment can induce either a minor change in a few nanostructural parameters or a major change in the nanostructural morphology to effect a total transition to a new regime of disorder, allowing the study of a granular metallic system over a spectrum of disorder in either case. Because carbon aerogels are not as graphitizable as ACFs, they do not exhibit as distinct a metal-insulator transition in their transport properties, nor as identifiable a sequence of changes in their structural properties as those observed in ACFs. Therefore, the dependences on heat treatment of the structural and transport properties of ACFs, both being more amenable to theoretical treatment than those of carbon aerogels, are individually detailed in 3 separate chapters later, while those lesser-understood properties of the heat-treated carbon aerogels are together discussed in this chapter to form an overall picture of the effects of heat treatment on both the mesoscopic and the microscopic disorder.

As mentioned above, even without causing a distinct transition, heat treatment could still be useful in tuning some nanostructural parameters relevant for the transport study. In particular, by reducing the unpaired spin concentration via heat treatment, we can verify that there is little correlation between the transport properties and the amount of microscopic disorder, thus establishing the localization sites to be the particles and not the dangling bonds or defects, and adding credibility to our Coulomb-gap variable-range

hopping (CGVRH) model [5.3]. The same conclusion can be reached by varying the particle size through changing the Resorcinol/Catalyst (R/C) ratio, as will also be discussed below.

In this chapter, the same carbon aerogel samples studied in Chapters 3 and 4, of both high density (HD, $\sim 0.1\,\mathrm{g/cm^3}$) and low density (LD, $\sim 0.65\,\mathrm{g/cm^3}$), are each heat treated to 1500, 1800 and 2100°C. Raman scattering and magnetic susceptibility results show improved structural ordering in carbon aerogels after heat treatment. The dc conductivity and magnetoresistance (MR) studies on these heat treated samples further reveal an electronic transition from strong localization to weak localization at a certain measurement temperature T_c, depending on the heat treatment temperature. Such a metal-insulator transition is evidenced by a sign change of the MR from positive to negative, as well as a drastic reduction of the temperature coefficient of resistivity near T_c.

5.1 Experimental Details

The heat-treated carbon aerogel samples studied in this chapter follow the same manufacturing procedure as those used for the as-prepared samples studied in Chapter 3 and Ref. [5.4]. While the as-prepared carbon aerogels were pyrolyzed at 1050°C for 4 h (and are therefore labelled as having a T_{HT} of 1050°C in the figures in this chapter), the heat-treated samples were pyrolyzed at higher temperatures for a similar time period. All samples were machined using a high-speed circular saw into rectangular shapes of $\sim 3 \times 3 \times 6\,\mathrm{mm^3}$ [5.4].

Raman scattering experiments were carried out with an Ar-ion laser in a back-scattering configuration, with power limited to 50 mW and wavelength tuned at 488 nm. The double-monochromator had its slits set to bandpass 4-$\mathrm{cm^{-1}}$, a bandwidth deemed narrow enough not to obscure peaks which are typically much broader for disordered solid state samples. Each sample was measured over a period of 2 hours for 8 scans altogether, each scan spanning a frequency range from 1100 to $1800\,\mathrm{cm^{-1}}$.

Temperature-dependent magnetization measurements of heat-treated carbon aerogels were made using a Quantum Design SQUID (MPMS5), set at a magnetic field of 1 T to ensure a linear field response. The samples were mounted on slitted transparent drinking straws.

Both the dc electrical conductivity and the magnetoresistance (MR) measurements were obtained as a function of temperature by the four-point method with two current leads

attached to the ends (3 mm × 3 mm), and two voltage leads on top of the sample about 2 mm apart. For all measurements, Joule heating was kept below 10^{-8} W. The magnetoresistance was measured for field strengths up to 15 tesla in a superconducting magnet at the Francis Bitter National Magnet Laboratory.

5.2 Experimental Results

5.2.1 Raman Scattering

As was done previously for the as-prepared carbon aerogels [5.4], Raman scattering was performed for the heat-treated aerogels. Shown in Fig. 5-1 are the Raman spectra for the low-density (LD) carbon aerogels heat-treated at 1500, 1800 and 2100°C, respectively. Figure 5-2 shows the Raman spectra for the high-density (HD) samples with the same set of heat treatment temperatures. Spectra shown in the two figures all show two broad peaks, one near 1360 cm^{-1} and the other near 1580 cm^{-1}. The origins of the two peaks have been described in Chapter 2. Briefly, the lower frequency peak (D) is attributed to a peak in the phonon density of states, normally disallowed by symmetry, but induced to become Raman-active when the presence of disorder destroys that symmetry. The upper frequency peak (G) is associated with the Raman-allowed E_{2g_2} mode in pristine graphite, up-shifted in frequency because of Breit-Wigner-Fano interaction with a Raman-active continuum [5.5] or a possible overlap with a smaller peak in the phonon density of states near 1610 cm^{-1}, which is disorder-induced in a similar way to the above-mentioned D peak [5.6].

The two peaks observed in all the heat-treated samples are analyzed using Eq. (2.6), as previously used for the as-prepared samples. Similar to a typical spectrum for the as-prepared sample, the G peak can be fitted with a Breit-Wigner-Fano (BWF) lineshape and the D peak with a Lorentzian lineshape. The fitting parameters are listed in Table 5.1 and their definitions can be found in the discussion of Eq. (2.6).

With increasing T_{HT}, the G peak downshifts in frequency towards 1582 cm^{-1} and becomes more symmetrical ($1/q \to 0$) at the same time, signaling that a more graphitic structure is being formed in the basic structural units. It is also observed in Table 5.1 that both peaks are significantly narrowed as T_{HT} increases beyond 1050°C, indicating that the heat-treated system becomes more homogeneous. With the narrowing of the G peak, there is slight evidence that a second disorder-induced peak emerges at a frequency near

$1610\,\mathrm{cm}^{-1}$ in the spectra for ACFs heat-treated at $T_{\mathrm{HT}} \geq 1800°\mathrm{C}$. However, the overlap between this peak and the broad G peak induces too much uncertainty in resolving them by numerical fitting. Furthermore, the spectra for ACFs heat-treated at lower temperatures might also contain this disorder-induced peak despite a better fit of the G peak to the BWF lineshape. We therefore fit the G peaks in all our spectra to the BWF lineshape alone, in order to make a fair comparison between the microcrystallite sizes obtained below for all the heat-treated ACFs.

The in-plane microcrystallite size L_a, as found by Knight's empirical formula [5.7], shows a slow but steady increase with increasing T_{HT}. It will be shown later in Chapter 6 that extensive planar development is possible only for $T_{\mathrm{HT}} > 2000°\mathrm{C}$. Micrographs from transmission electron microscopy (TEM) did indeed reveal layers of extended graphene filaments encircling the particles on the surface and in some instances, even stretching out to link particles over a distance of a few hundred Å's [1], but since the highest L_a value in Table 5.1 is still much smaller than the filament length observed in TEM, Raman spectrosocpy is probably only probing the width of the glassy-carbon filaments contained within a single particle.

TEM also shows that the glassy-carbon ribbons (filaments) deep inside the particles remain entangled with one another. Therefore, unlike the close-packed graphite platelets in ACFs, the convoluted nature of the glassy-carbon ribbons within the particles in carbon aerogels is thought likely to prevent graphitization to a high degree. It would be interesting to verify this scenario at T_{HT} much higher than 2000°C, but for this study, the highest T_{HT} value reached is only 2100°C, partly due to the availability of the samples, and partly conforming to our focus on relating the transport behavior to the microscopic and the mesoscopic disorder, if possible, still within the regime of strong localization.

Again, in agreement with the findings in Chapter 3, Table 5.1 shows that for almost all T_{HT} values, the characteristics of the G peak as well as L_a are not very sensitive to variations in density.

[1] Private communication with our collaborator Dr. R. W. Pekala at the Lawrence Livermore National Laboratory.

Density (g/cm^3)	0.123†	0.117	0.117	0.137	0.670†	0.621	0.621	0.651
T_{HT} (°C)	1050	1500	1800	2100	1050	1500	1800	2100
ν_{1360} (cm^{-1})	1349	1348	1347	1352	1350	1351	1353	1355
Γ_{1360} (cm^{-1})	143	72	60	50	123	63	51	47
ν_{1580} (cm^{-1})	1604	1599	1590	1586	1607	1602	1593	1589
Γ_{1580} (cm^{-1})	86	69	63	58	73	65	61	56
$1/q$	-0.23	-0.16	-0.08	-0.03	-0.23	-0.12	-0.04	-0.01
L_a (Å)	29	35	28	49	27	33	38	40

† Data for the as-prepared samples were extracted from Chapter 3.

Table 5.1: Listed are the peak positions (ν) and the full-widths at half-maximum intensity for the Raman-active peak associated with the E_{2g_2} mode in pristine graphite (denoted by 1580 in the subscript) and the disorder-induced peak (denoted by 1360 in the subscript) in the Raman spectra for the heat-treated carbon aerogels of both high and low densities. Values for the Breit-Wigner-Fano interaction parameter for the graphitic peak are also listed. The in-plane microcrystallite size L_a is obtained from Knight's formula [5.7].

5.2.2 Magnetic Susceptibility

The temperature-dependent magnetic susceptibility $\chi(T)$ from 4 K to 300 K for carbon aerogel samples heat-treated at 1500, 1800 and 2100°C are plotted against $1/T$ in Figs. 5-3 and 5-4 for the LD and the HD samples, respectively. The linearity in these figures suggest a fit to the Curie law in the following form:

$$\chi(T) = \chi_0 + \frac{C}{T} \tag{5.1}$$

where χ_0 is the diamagnetic background, $C = g^2 s(s+1)\mu_B^2 N/3k_B$, $s = 1/2$, $g = 2$, μ_B the Bohr magneton, and N the unpaired spin concentration. The Curie law is slightly different from the random-exchange Heisenberg antiferromagnetic chain model [5.8] used in Chapter 3, but it is used here to obtain a convenient estimate of N, which is found for the as-prepared samples to be within the same order of magnitude as the values obtained in Chapter 3. The fitting parameters are listed in Table 5.2, as a function of T_{HT} for each density group.

In Table 5.2, it is observed that the heat-treated carbon aerogels generally have a diamagnetic background (χ_0) larger than that for the as-prepared carbon aerogels of the same density, approaching, but not yet reaching, the average diamagnetic susceptibility of graphite (-7.32×10^{-6} emu/g). The concentration of the unpaired spins, likely arising from dangling

Density (g/cm^3)	0.124†	0.117	0.117	0.137	0.670†	0.621	0.629	0.651
T_{HT} (°C)	1050	1500	1800	2100	1050	1500	1800	2100
N (10^{19} spins/g)	1.1	1.1	1.1	0.70	1.5	0.81	0.33	0.17
χ_0 (10^{-6} emu/g)	-2.3	-2.0	-3.0	-3.0	-1.0	-1.6	-2.4	-2.8

† Data for the as-prepared samples were extracted from Chapter 3.

Table 5.2: Listed are the diamagnetic background χ_0 and the unpaired spin concentration N for the heat-treated carbon aerogel samples of both high and low densities.

bonds, also decreases with increasing T_{HT}, further indicating some degree of graphitization in the heat-treated samples. Both trends are more clearly observed in Fig. 5-4 than in Fig. 5-3, suggesting the HD samples are more graphitizable than the LD samples, probably because the larger particle packing ratio in the HD samples allows more frequent contacts between neighboring particles and hence increases the effectiveness of heat treatment in mending dangling bonds.

The decrease in N for the LD carbon aerogels does not always coincide with the increase in χ_0. This is because the implications of the two trends are different. Since the diamagnetic background arises from the conduction electrons experiencing the Landau-level splitting in two-dimensional graphite [5.9, 5.10], its increase towards the graphitic value is often interpreted as the development of 2D structures. In carbon aerogels, 2D structures are indeed observed by TEM to form on the surface of and also in the space between the particles. It can be seen by comparing Figs. 5-4 and 5-3 that 2D structures are more readily developed by heat treatment in the HD sample than in the LD samples, probably because the larger particle packing ratio increases the probability of forming graphitic structures across from one particle to the next and over a more extended distance. The reduction of dangling bonds, on the other hand, could take place either by coalescing neighboring microcrystallites, thereby fulfilling the edge states of each microcrystallite, or by annealing the defects (microscopic disorder) within the graphitic ribbons.

Based on this understanding, we observe from Fig. 5-3 that 2D structures probably need to be developed first, signaled by an increase in the negative background χ_0, before the annealing of the dangling bonds can take place (i.e., the slope decreases) on a large scale. It is possible that extended in-plane order might enhance the process of annealing microscopic disorder. The slight decrease in χ_0 at $T_{HT} = 2100°C$ might be due to a depleted supply of conduction carriers in the graphitic sheets when the defects are annealed, thus reducing the

Density (g/cm^3)	0.124	0.117	0.117	0.137
T_{HT} (°C)	1050	1500	1800	2100
E_σ (meV)	5.1	3.1	3.7	4.5

Table 5.3: Values for the conductivity activation energy E_σ for the heat-treated carbon aerogels of both high and low densities.

free-carrier diamagnetism. This effect is only effective for the LD samples because they are short of conduction carriers and any carrier depletion becomes proportionately significant. For the more graphitizable HD samples, Fig. 5-4 shows that the two processes can coexist because 2D structures are readily formed, as explained above.

5.2.3 Conductivity

The temperature-dependent dc electrical conductivities [$\sigma(T)$] from 4 K to 300 K for heat-treated carbon aerogels of both HD and LD are plotted in Fig. 5-5, in which the LD carbon aerogels with different T_{HT} values all have densities close to 0.12 g/cc, while the three HD heat-treated samples have densities $\sim$ 0.63 g/cc. Plotted on a semi-log scale, the $\sigma(T)$ curves of the LD aerogels are observed to exhibit a much stronger temperature dependence (a change of 3 to 5 orders of magnitude in σ from 300 K to 4.2 K, depending on T_{HT}), as well as a much lower magnitude of conductivity than the HD samples, irrespective of T_{HT}. This indicates that mass density is a more dominant factor in transport than heat treatment.

Arrhenius plots of $\sigma(T)$ are shown in Fig. 5-6 for all the samples studied to magnify the strong temperature dependence in a narrow low temperature range, allowing the effect of heat treatment to be seen. For each density group, Fig. 5-6 shows that the temperature dependence of the conductivity is suppressed by heat treatment while the conductivity increases for all measurement temperatures with increasing T_{HT} in general. Both observations hold true for the entire range of T_{HT} values for the HD samples, but for the LD samples, progressive heat treatment to 2100°C seems to have caused the resistivity to increase in both its magnitude and its temperature dependence, probably because the annealing of the dangling bonds at such high T_{HT} has also deprived the sample of conduction electrons, thus adding to the conductivity activation an extra thermal activation energy necessary for carrier generation, as shown in Table 5.3. Apart from this exception, Fig. 5-6 does point

out that heat treatment could bring the system out of strong localization and closer to the metal-insulator (MI) transition, consistent with the findings from the Raman spectrum and the magnetic susceptibility measurements that heat treatment induces partial order development in the microstructure of carbon aerogels.

In Chapter 4, $\sigma(T)$ for LD carbon aerogels was shown to exhibit Coulomb-gap variable-range hopping behavior below 10 K and simple activation-like behavior above 10 K [5.3]. The activation behavior is now confirmed, by the Arhenius plots in Fig. 5-6, in all the heat-treated LD samples, albeit starting at different measurement temperatures which depend on $T_{\rm HT}$.

5.2.4 Magnetoresistance

The magnetoresistance (MR), defined as $[\rho(B) - \rho(0)]/\rho(0) \equiv \Delta R/R$, for the same samples as were used in the dc conductivity studies, were measured at various temperatures for magnetic field strengths up to 15 T. The results are plotted in Figs. 5-7, 5-8 and 5-9 for three representative carbon aerogel samples, respectively. They are the LD samples, one with $T_{\rm HT} = 1800°$C and the other with $T_{\rm HT} = 2100°$C, and the HD sample with $T_{\rm HT} = 1500°$C. For the LD samples, the positive and the negative MRs are plotted on separate vertical scales because there is a large difference in their magnitudes.

It is observed in general that, for both the HD and the LD heat-treated carbon aerogels, the MR is positive and large at very low temperatures, then decreases gradually to negative values with increasing measurement temperature (T), and eventually begins to drop to zero magnitude at sufficiently high T. Consistent with the conductivity results, the LD samples exhibit a much larger positive MR than the HD samples with the same or even lower $T_{\rm HT}$, indicating again that the density factor is a more dominant one in transport than $T_{\rm HT}$.

By comparing Figs. 5-7 and 5-8, we observe that the carbon aerogel with a higher $T_{\rm HT}$ tends to have a lower positive MR and a higher negative MR for the same T than the sample with lower $T_{\rm HT}$ and that the transition temperature for the sign change in MR decreases with $T_{\rm HT}$. The same observations are also made for the HD sample. Though not shown graphically, when $T_{\rm HT}$ reaches 1800°C and above for the HD sample, only negative MR is observed for the entire T range, implying likely a smaller positive MR and a lower transition temperature also for these heat-treated HD samples.

It is believed that the MR in heat-treated carbon aerogels is made up of a positive and

a negative component. With the negative component growing and the positive component shrinking with increasing T_{HT} and T, the negative MR will dominate for a higher T_{HT} while beginning at a lower T, consistent with experimental observations. The positive component can be ascribed to the same strong localization behavior observed in Chapters 3 and 4 for the as-prepared samples, showing similar magnitudes. Negative MR is usually associated with orbital effects such as the interference of the backscattered waves depicted in the weak localization theory [5.11] or the interference among random paths in the variable-range hopping process [5.12, 5.13]. It could also be due to the scaling behavior when the Zeeman splitting shifts the mobility edge relative to the Fermi level [5.14, 5.15]. It can be seen, however, that if the negative MR is related to the development of any kind of order, then the effects of heat treatment on the microstructure of carbon aerogels can be deduced. In the discussion section, we will try to determine which process contributes to the observed negative MR of carbon aerogels by correlating all the experiments, and we will also explain the downward turn observed in the positive component at high fields and very low T, which is probably also a result of Zeeman splitting.

5.3 Discussion

As was suggested by the MR results above, the transport behavior in heat-treated carbon aerogels can be separated into two different regimes. In the low T regime, strong localization behavior is dominant, resulting in a positive MR and a drastic drop of σ with decreasing T, much like the as-prepared samples. At higher T, the transport behavior is dominated by a negative MR. It will be seen in this section that the discussion of the effects of heat treatment on the structural properties of carbon aerogels is to be deeply influenced by the interpretation of the negative MR results.

For convenient notation, the low-density samples are labelled as LDxx and the high-density samples as HDxx hereafter, with xx indicating the value of T_{HT} in units of 100°C.

Judging from the similarity between the MR figures shown for the HD (Fig. 5-9) and the LD samples (Fig. 5-7 and 5-8), the negative MR for different density samples probably shares the same origin. Because variable-range hopping is not observed in any of the $\sigma(T)$ curves shown in Fig. 5-6, especially for the heat-treated HD samples, those models which are based on the interference among random hopping paths, and which predict a negative MR

only at disorder and temperatures deep in the variable-range hopping regime [5.12, 5.13], are now precluded.

A sign change in MR might be indicative of a metal-insulator (MI) transition. Near the MI transition, the Fermi level E_F lies very close to the mobility edge E_{ME}, an energy level marking the onset of high carrier mobility, however differently it is defined in granular metals than in semiconductors. The transport behavior near the MI transition is therefore very sensitive to the position of E_F relative to either E_{ME}, which can be changed by a number of ways, such as thermal broadening and Zeeman splitting.

For the LD21 sample, a downward turn observed in the positive MR curve (see Fig. 5-8) might possibly be seen as a manifestation of the Zeeman-splitting effect [5.15]. When E_{ME} is split by the magnetic field, the localized carriers with the E_{ME} level closer to E_F will have a divergence in many of their properties, such as the dielectric constant (which then decreases the charging energy of the particle if the picture of a granular metallic system is still useful) and the localization length (which increases the overlap of localization sites involved in a hop), and being the majority carriers now, they have the ability to increase the overall conductivity in either case. The decrease in the positive MR at $\sim$ 10 T for the LD21 sample in Fig. 5-8 therefore indicates that the distance between E_F and E_{ME} is on the order of 0.5 meV ($\sim$ 6 K), consistent with the observation that the positive MR gradually gradually disappears above 4 K for this sample, probably because of thermal broadening or thermal excitation. The LD18 sample has a higher saturation field value and coincidentally also a higher sign-reversal temperature ($\sim$10 K) for its positive MR, suggesting that heat treatment brings E_F closer to E_{ME}. The same conclusion can be reached by comparing the saturation field values of the more ordered HD samples, either among themselves or with the LD samples.

The carrier depletion effect was suggested as an explanation for the stronger temperature dependence of σ as well as the smaller diamagnetic susceptibility for the LD21 sample relative to the LD18 sample. Carrier depletion has the effect of pushing the E_F further away from E_{ME}, seemingly in contradiction with the MR finding above, that $|E_{ME} - E_F|$ should be smaller. The reconciliation can be found by noting that in turbostratic graphite [5.10], a narrow-gap semiconductor to which our LD21 sample is likened, E_F could be located in the bandgap intrinsically, accounting for the need of an extra thermal activation energy E_a for carrier generation. However, the divergent behavior of the physical properties near E_{ME} is

only relevant for the excited electrons which are already in a position to hop and have an energy E close to E_{ME}. Hence, whereas $\sigma(T)$ is probing the sum of E_a and $|E_{ME} - E|$, the Zeeman effect manifested in the high-field MR is probing $|E_{ME} - E|$ alone. It is therefore possible that the heat treatment at 2100°C has increased $E_a + |E_{ME} - E|$ while decreasing $|E_{ME} - E|$ at the same time.

The negative MR, observed at lower fields and higher temperatures, cannot be explained by the Zeeman-splitting effect, leaving the weak localization (WL) of the thermally generated carriers at energies above E_{ME} as the only explanation for the negative MR. The large magnitude of the negative MR is inconsistent with the conductivity correction due to WL [5.11], but *if* some qualitative features of the WL theory might still apply near the MI transition, then since the WL theory predicts a $\Delta R/R \propto 1/\sigma$, the low σ values at low temperatures for the LD samples might possibly account for the large magnitude of the negative MR. This assumption is further born out in Fig. 5-5 by noting that at low temperatures, the LD21 carbon aerogel has a much lower σ than does the LD18 sample, which in turn is more resistive than the HD15 sample , coinciding with the decrease in negative MR in the same order. Once the positive component of the MR vanishes at some temperatures (e.g., between 10 K and 19 K for both the LD18 and the LD21 samples), the negative MR will begin to drop in magnitude, in accordance with the destruction of the phase coherence of carriers by inelastic scattering events at high temperatures.

If WL indeed takes place in a 2D plane, then the large negative MR of the LD21 sample compared with that of the LD18 sample is indicative of the effect of heat treatment on extending graphitic structures. This is consistent with the Raman scattering and the SQUID results in general. In fact, TEM micrographs also reveal that the graphitic structures are concentrated on the circumference of the particles as well as between the particles.[2] Based on this information, we fit our magnetoresistance data to the 2D WL theory, which gives for an inhomogeneous system [5.11]:

$$\frac{\Delta\rho}{\rho} \equiv \frac{\rho(H) - \rho(0)}{\rho(0)} = -\lambda \frac{\rho(0)}{L_c} \frac{e^2}{2\pi^2\hbar} \left[\Psi\left(\frac{1}{2} + \frac{H_i}{H}\right) - \ln\left(\frac{H_i}{H}\right) \right] \tag{5.2}$$

where ρ is the measured resistivity of the sample, Ψ the digamma function, and L_c is the thickness of one graphitic layer. Only one characteristic field $H_i = \hbar c/4eD\tau_i$, namely that

[2]Private communication with Dr. Robert Pekala at the Lawrence Livermore National Laboratories.

which is associated with inelastic scattering, is used because magnetic scattering is only important at very low temperatures, where the strong localization behavior dominates the weak localization effect.

The inhomogeneity factor λ ($0 < \lambda \leq 1$) compensates: (i) the use of an over-estimate of the cross-sectional area in the calculation of ρ; (ii) the fraction of the graphitic structures with their c-axes approximately parallel to the applied magnetic field; and (iii) the underestimate of the number of graphitic layers constituting the 2D system. Of these three factors, only the first factor is likely to be temperature-dependent because thermal excitation of carriers over the low-energy gaps separating the particles could enlarge the effective cross-sectional area (A_{eff}) of the percolation path. The fitting values for λ are plotted in Fig. 5-10 for the LD18 and the LD21 carbon aeorgel samples, showing the sharp increase of A_{eff} with temperature below $\sim$10 K and a relatively weak temperature dependence at higher temperatures. The observed trend is consistent with our earlier finding from both the σ and the magnetoresistance measurements that a transition from strong localization to weak localization takes place around 10 K.

Further analysis of carbon aerogels based on the WL theory suffers from the difficulty in accurately determining the transition field value H_i [5.16], which separates the high-field from the low-field regime and defines the dephasing distance by its magnetic length, because either the negative MR curves are complicated by the inseparable positive component or they are quadratic and still in the low-field regime. Depending on the dimensionality of the WL, the $\Delta\sigma(T)$ curves should follow either a $\ln(T)$ or a power-law T^p dependence. Such identification is also difficult because the strong temperature dependence of $\sigma(T)$ in comparison with the perturbative correction predicted by the WL theory most likely arises from more than one conduction mechanism. The WL correction can be extracted by taking a temperature scan of $\sigma(T)$ in a constant high field, and then subtracting the result from the zero-field temperature scan. This will be done in Chapter 8 for the heat-treated ACFs which have a much weaker temperature-dependent $\sigma(T)$ and hence allow a more accurate extraction of the very small WL term. The full analysis of a weakly disordered system in porous carbons will have to await the study in Chapter 8 of the heat-treated ACFs, which have better-understood and more-ordered microstructures than the carbon aerogels.

In passing, we have also witnessed in all the different experiments that heat treatment plays a more important role in molding the structural properties than does density, but the

opposite is true for the transport properties. Of special interest is the transport behavior in the strong localization regime, where the heat-treated carbon aerogels not only exhibit the same conductivity and MR behavior as that of the as-prepared samples at very low temperatures, but they are also observed to share similar MR behavior among themselves at very low temperatures. A detailed comparison of the unpaired spin concentrations for the LD21 and the HD15 samples, made on a per-unit-mass basis, indicates that they could have approximately the same number of dangling bonds per gram of aerogel, even when their MR magnitudes are very different in the strong localization regime. This implies that the hopping process at low temperatures is more related to the particle packing ratio than to the spin concentration, and as a result, the particles are more likely to be the localization sites than the dangling bonds. In support of this conclusion, another transport study which focusses on the effects of the R/C ratio (or the particle size) [5.1] shows that the LD R/C= 200 sample, which has approximately the same spin concentration as the R/C= 300 sample of the same density, exhibits a stronger temperature dependence in $\sigma(T)$ while following the same Coulomb-gap variable-range hopping behavior. This suggests that the particle size also affects the transport properties more significantly than the spin concentration, again consistent with the notion that the particles, and not the dangling bonds, act as localization sites. This assumption is the basis of the Coulomb-gap variable-range hoppng model [5.3] established in Chapter 4 and it is now verified by experiments.

References

[5.1] G. A. M. Reynolds, A. W. P. Fung, Z. H. Wang, M. S. Dresselhaus, and R. W. Pekala, Phys. Rev. B, (1994), submitted.

[5.2] G. A. M. Reynolds, Doctoral thesis, Department of Physics, MIT (to be submitted).

[5.3] A. W. P. Fung, Z. H. Wang, M. S. Dresselhaus, G. Dresselhaus, R. W. Pekala, and M. Endo, Phys. Rev. **B49**, 17325 (1994).

[5.4] A. W. P. Fung, Z. H. Wang, K. Lu, M. S. Dresselhaus, and R. W. Pekala, J. Mater. Res. **8**, 1875 (1993).

[5.5] M. V. Klein, in *Light Scattering in Solids*, edited by M. Cardona, Topics in Applied Physics, vol. 8 (Springer, Berlin, Heidelberg, 1975), p. 147.

[5.6] T. C. Chieu, M. S. Dresselhaus, and M. Endo, Phys. Rev. **B26**, 5867 (1982).

[5.7] D S. Knight and W. B. White, J. Mater. Res. **4**, 385 (1989).

[5.8] W. G. Clark and L. C. Tippie, Phys. Rev. **B20**, 2914 (1979).

[5.9] J. W. McClure, Phys. Rev. **104**, 666 (1956).

[5.10] M. S. Dresselhaus, G. Dresselhaus, K. Sugihara, I. L. Spain, and H. A. Goldberg, *Graphite Fibers and Filaments* (Springer, Berlin, Heidelberg, 1988).

[5.11] B. L. Altshuler, D. E. Khmelnitskii, A. I. Larkin, and P. A. Lee, Phys Rev. **B22**, 5142 (1980).

[5.12] V. L. Nguen, B. Z. Spivak, and B. I. Shklovskii, Sov. Phys. JETP **62**, 1021 (1985).

[5.13] U. Sivan, O. Entin-Wohlman, and Y. Imry, Phys. Rev. Lett. **60**, 1566 (1988).

[5.14] B. L. Al'tshuler, A. G. Aronov, and D. E. Khmelnitskii, JETP Lett. **36**, 195 (1982).

[5.15] H. Kamimura and H. Aoki, *The Physics of Interacting Electrons in Disordered Systems* (Oxford University Press, New York, 1989).

[5.16] G. Bergmann, Phys. Rep., **107**, 1 (1984).

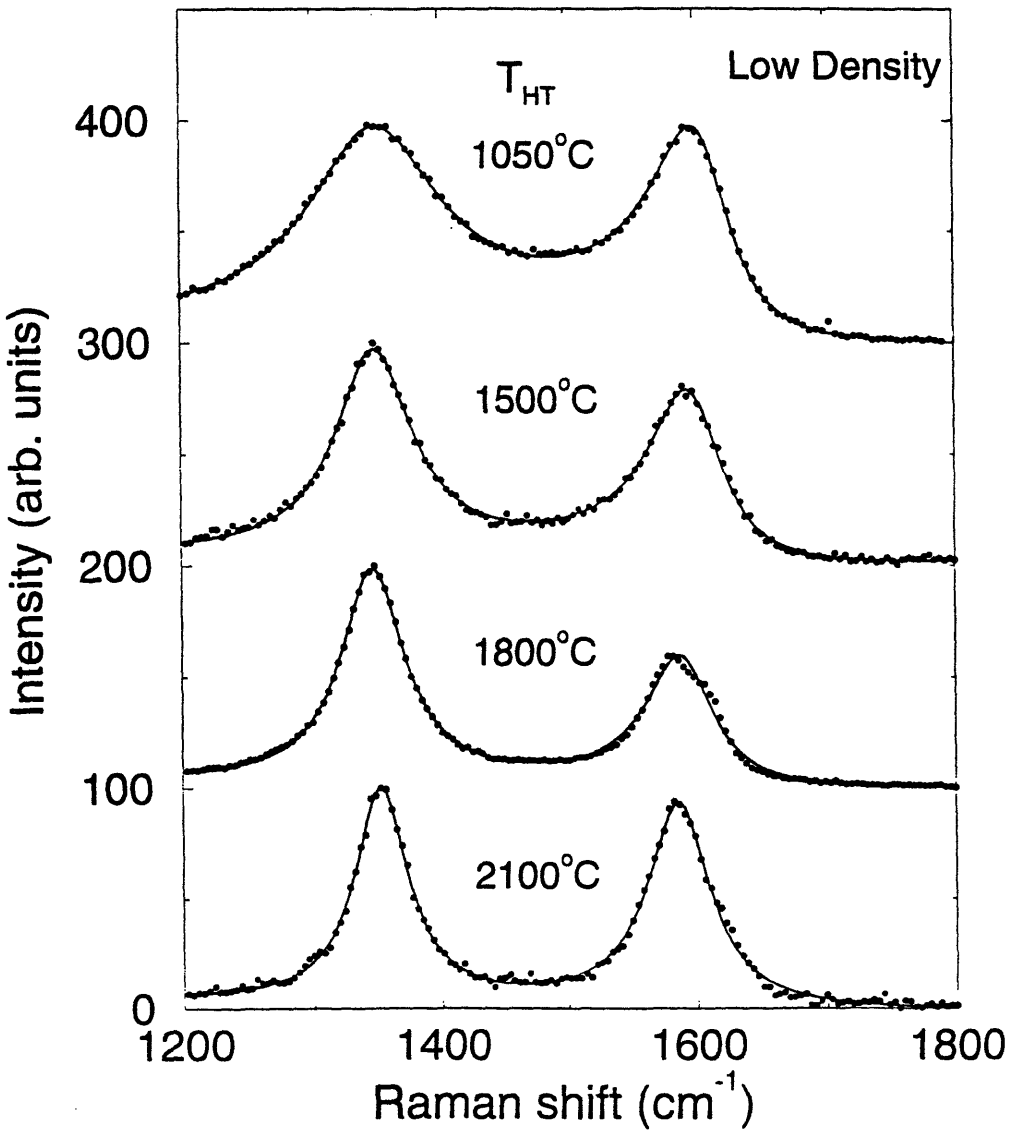

Figure 5-1: Raman spectra showing the effect of heat treatment on carbon aerogels of low density. The as-prepared sample is pyrolyzed at 1050°C and therefore is so labelled in all the figures in this chapter.

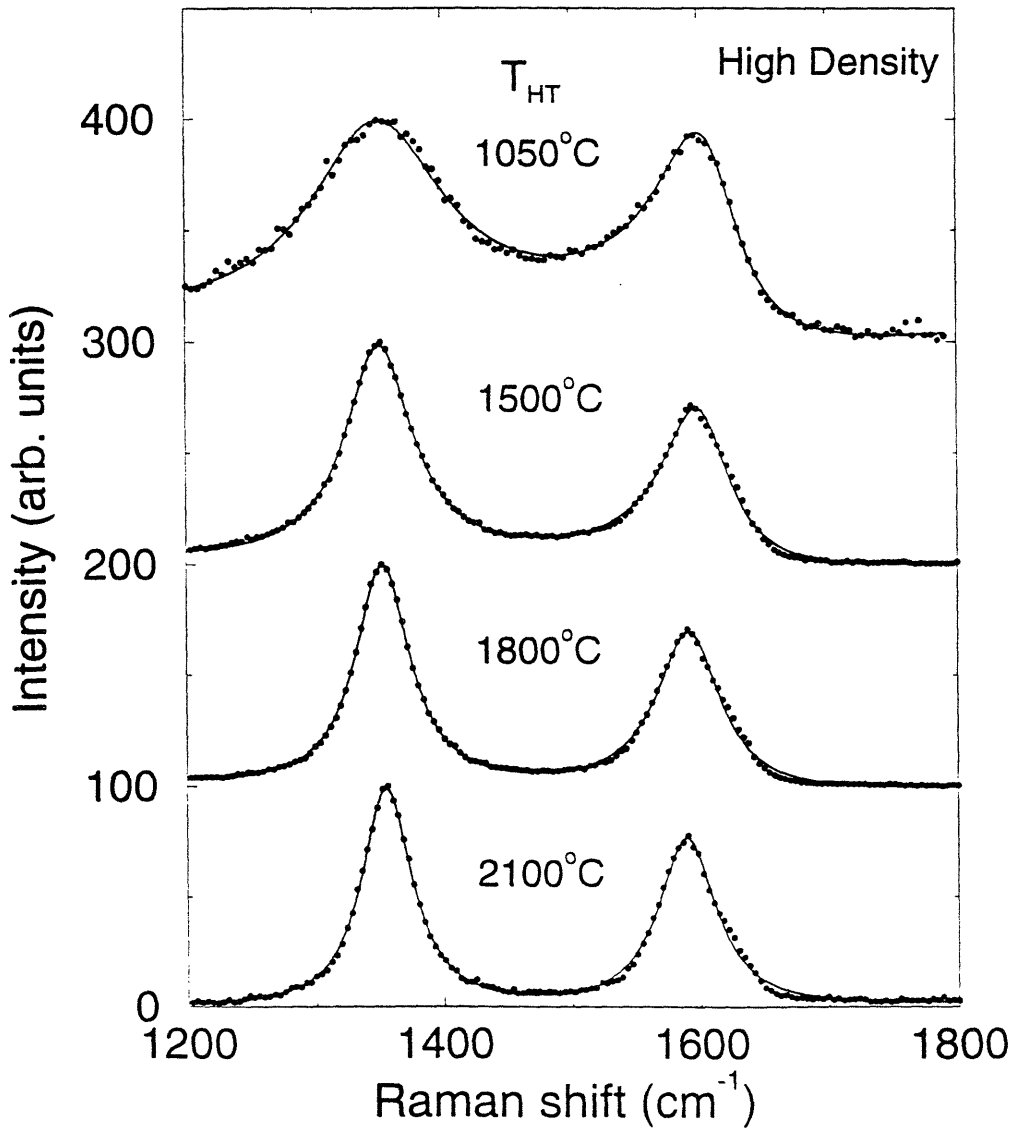

Figure 5-2: Raman spectra showing the effect of heat treatment on carbon aerogels of high density.

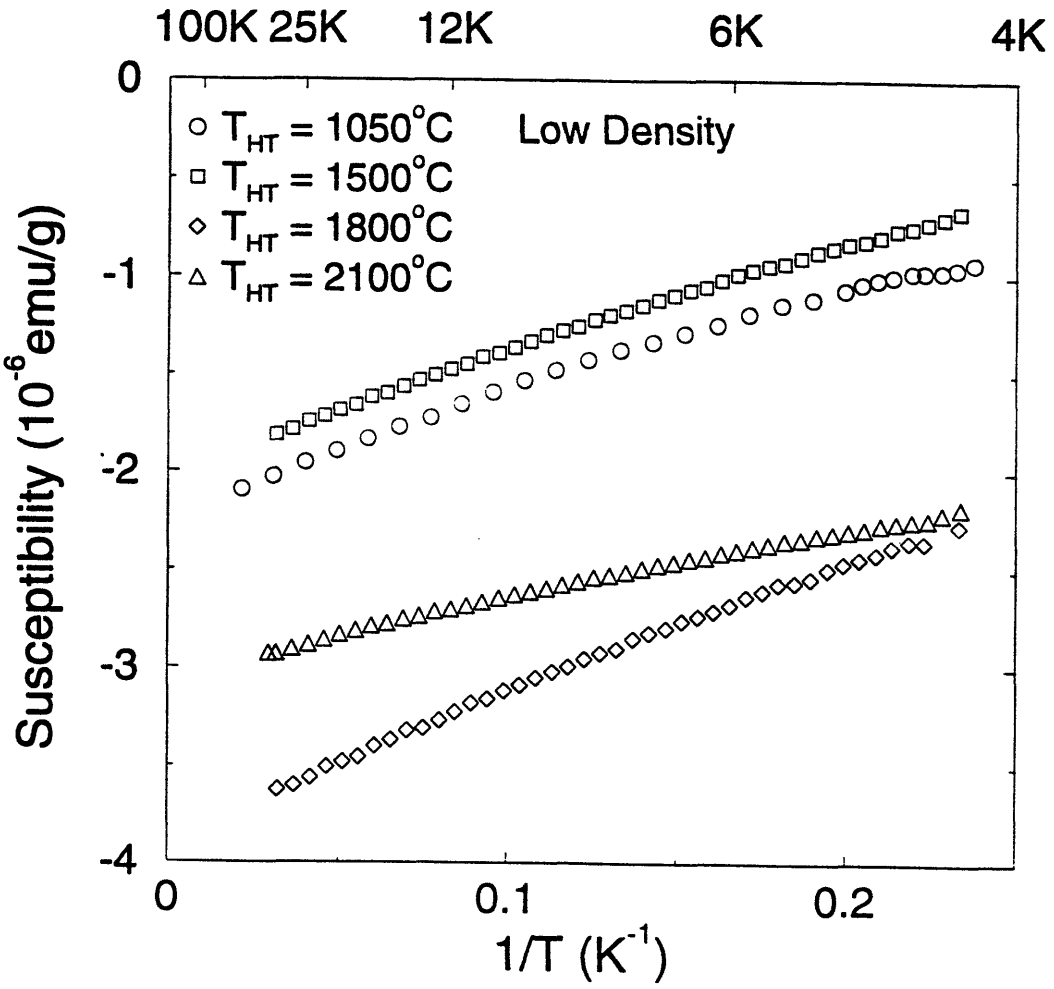

Figure 5-3: Temperature-dependent magnetic susceptibility measurements showing the effect of heat treatment on carbon aerogels of low density.

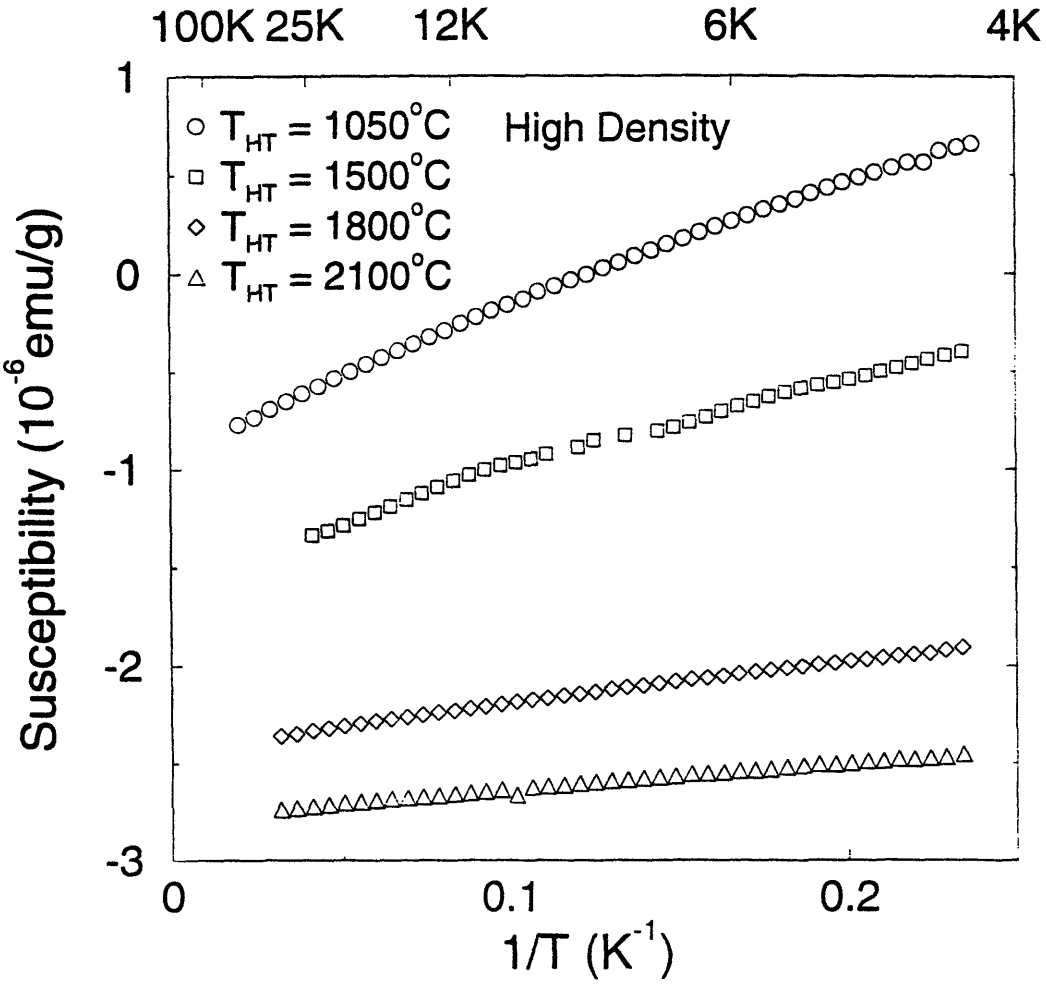

Figure 5-4: Temperature-dependent magnetic susceptibility measurements showing the effect of heat treatment on carbon aerogels of high density.

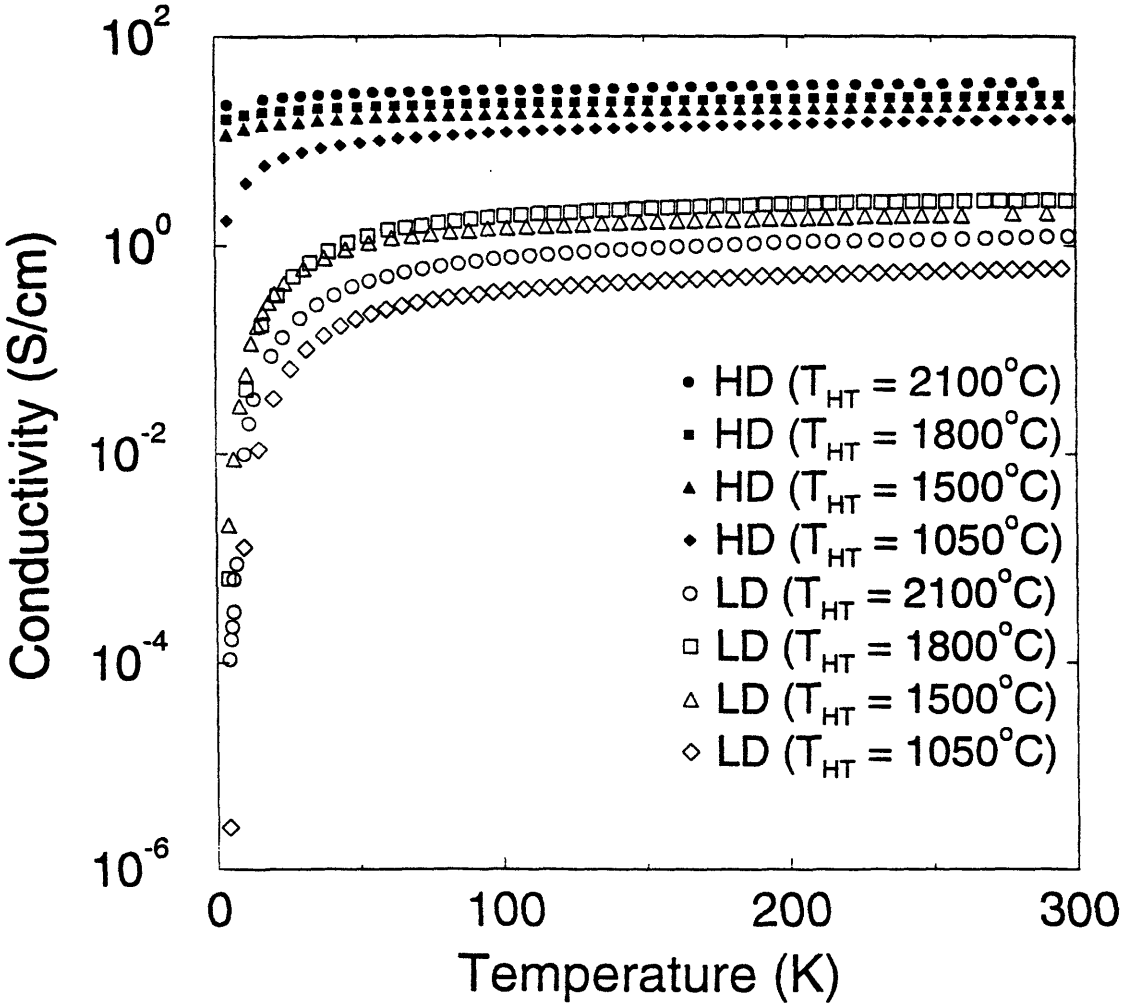

Figure 5-5: Temperature dependence of dc conductivity (plotted on a log scale) for carbon aerogels of both high density ($\sim 0.63\,g/cc$) and low density ($\sim 0.12\,g/cc$) for various heat treatment temperatures.

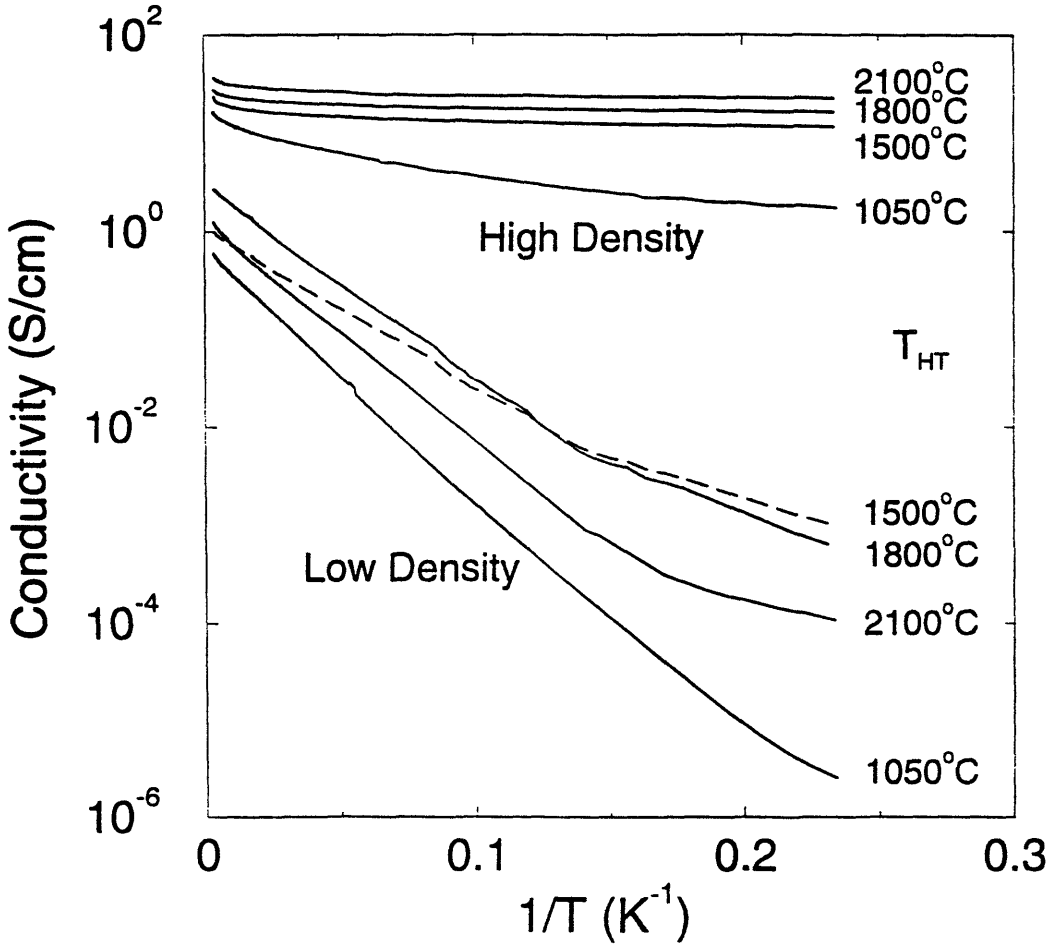

Figure 5-6: Arrhenius plot of the conductivity for carbon aerogels of both high density ($\sim 0.63\,g/cc$) and low density ($\sim 0.12\,g/cc$) for various heat treatment temperatures. The dashed line is used for the LD sample heat-treated at 1500°C to avoid confusion at the intersection with a similar curve for another sample. With progressive heat treatment, the conductivity activation energy for the LD samples initially decreases when graphitization first takes place, and then increases when conduction carriers are depleted.

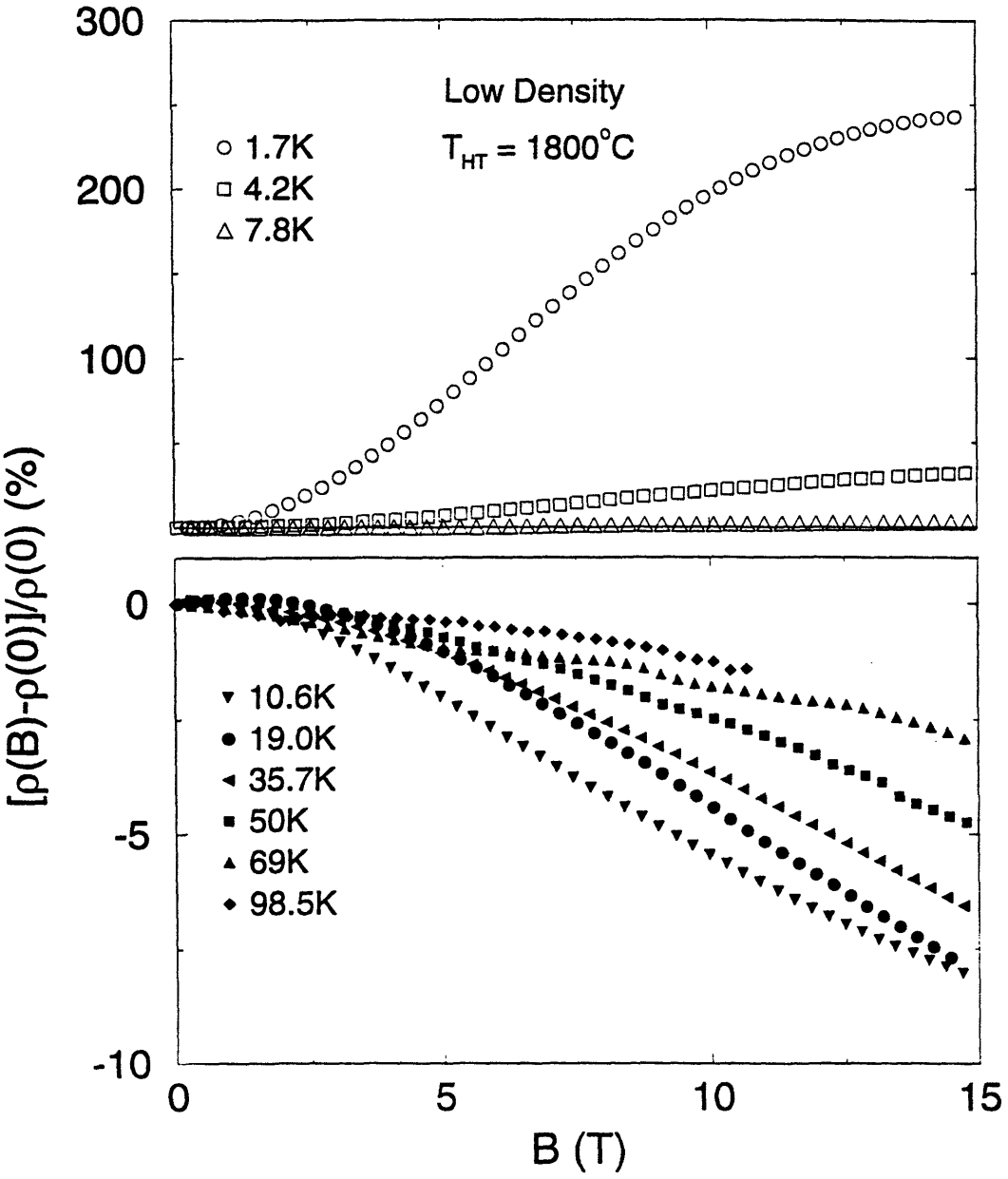

Figure 5-7: Magnetoresistance for a low density carbon aerogel heat-treated at 1800°C for various measurement temperatures. The positive MR is plotted in the top figure on a separate vertical scale because of its large magnitude compared with that of the negative MR.

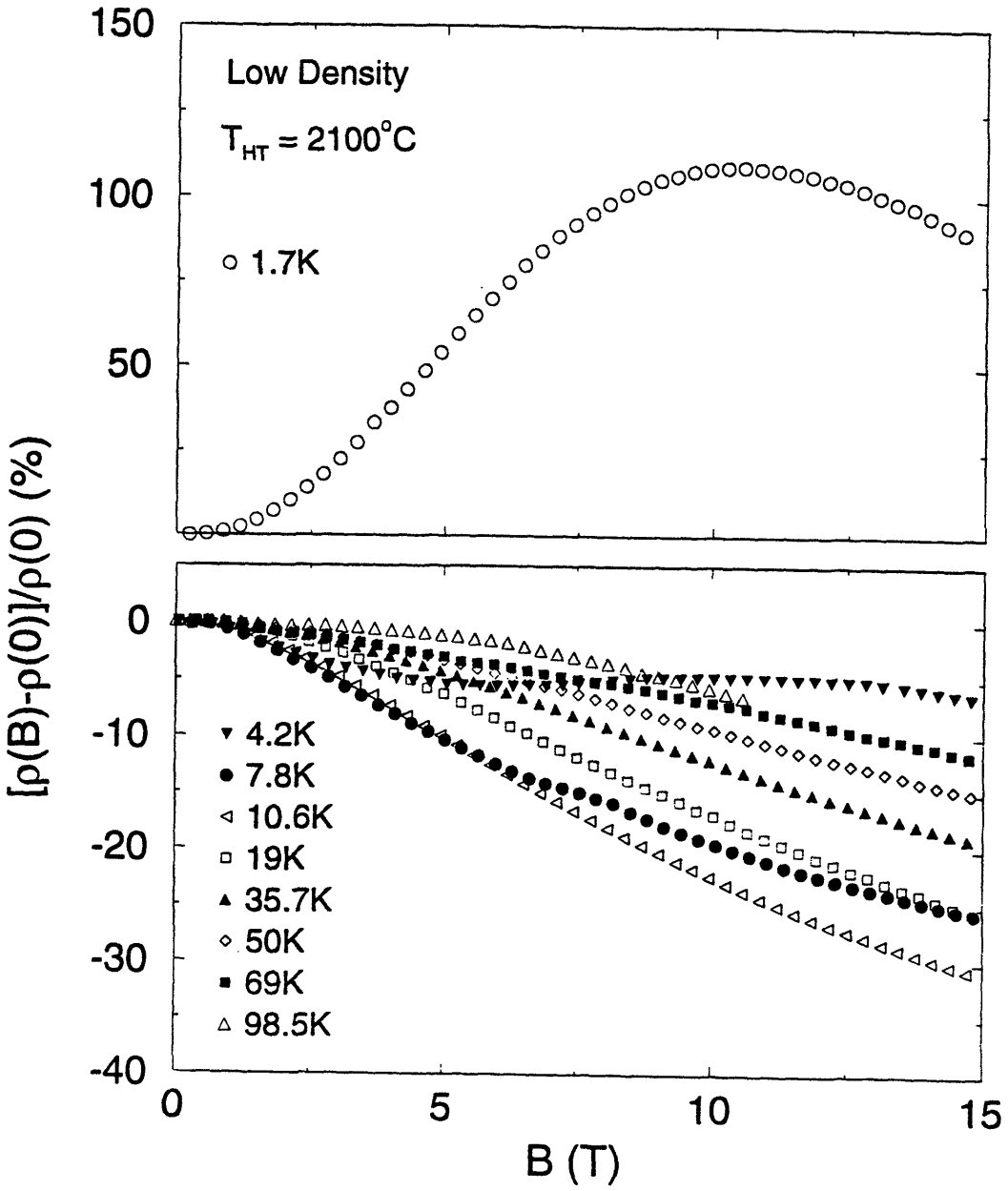

Figure 5-8: Magnetoresistance for a low density carbon aerogel heat-treated at 2100°C for various measurement temperatures. The positive MR is plotted in the top figure on a separate vertical scale because of its large magnitude compared with that of the negative MR.

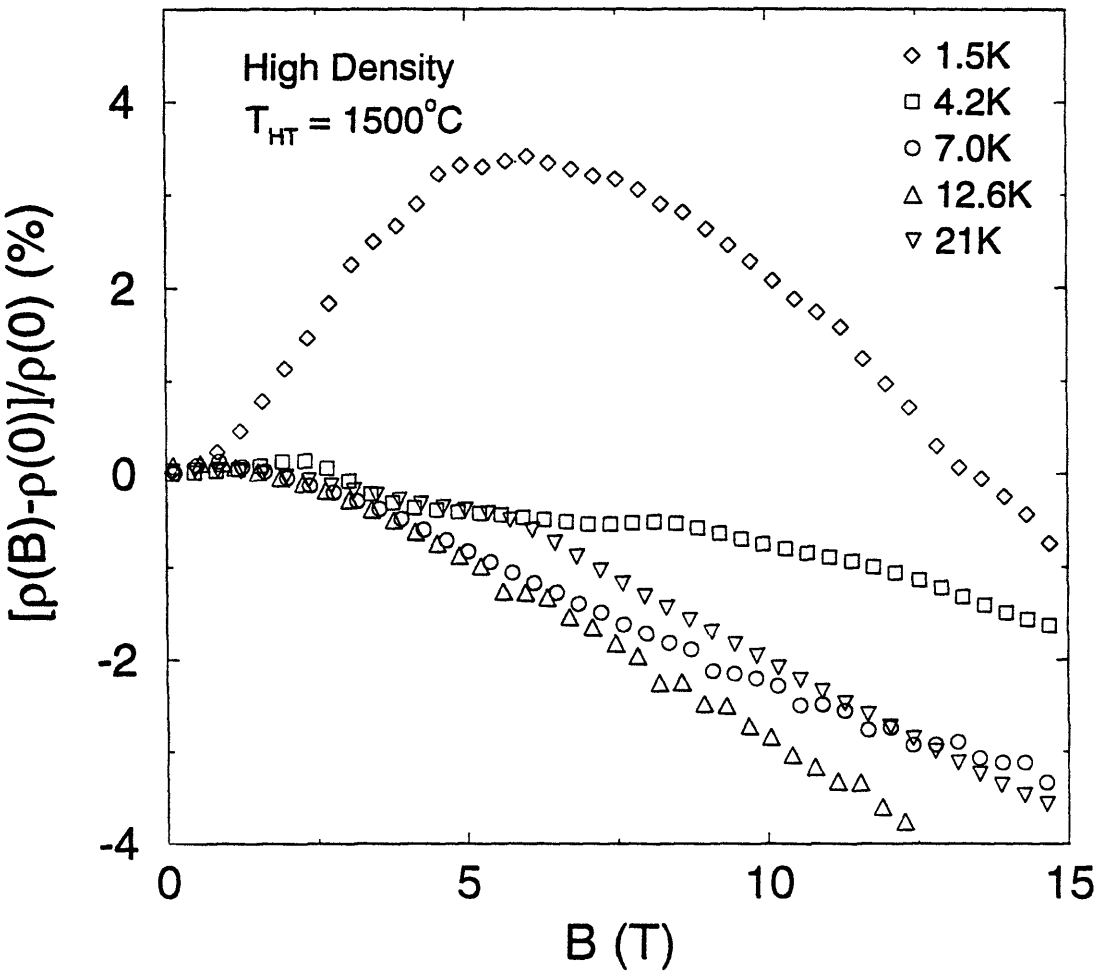

Figure 5-9: Magnetoresistance for a high density carbon aerogel heat-treated at 1500°C for various measurement temperatures. The behavior of this sample is complicated and can likely be treated in terms of two competing processes with opposite signs.

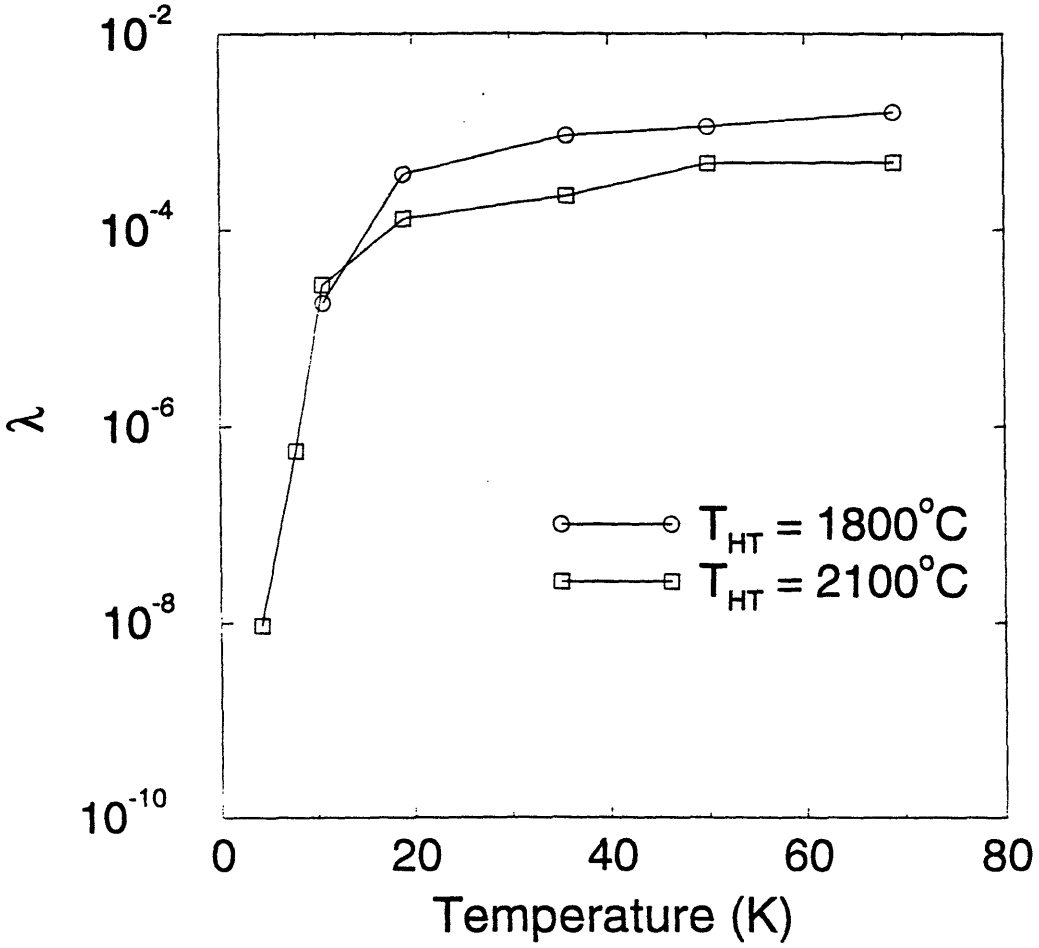

Figure 5-10: Temperature dependence of the inhomogeneity factor λ for low-density carbon aerogels heat-treated to 1800 and 2100°C.

Chapter 6

Structural Characterization of Heat-Treated ACFs

In the last chapter, it was found that heat treatment of carbon aerogels results in only partial order development in the microstructures because the convoluted nature of the polymeric links within the particles in carbon aeorogels prevents extended planar development. However, in the case of ACFs, as will be seen in this chapter, a more homogenous environment is achievable at high heat-treatment temperatures, because of the extra degrees of freedom afforded by the nanopores for the alignment and eventual fusion of the graphite platelets to form extended graphite sheets. This important difference between the two porous materials suggests that our transport studies from this chapter onwards, highlighted by the departure from the strong localization regime and then by the approach to the vicinity of the metal-insulator transition and beyond, should be focussed on ACFs. Because industries relying on the use of porous materials can benefit from the knowledge of a new engineering method of controlling the nanospace, we discuss in this chapter only the structural transformations in ACFs due to heat treatment, while postponing the discussion of the corresponding changes in the transport properties to the next chapter.

It is well established that the effect of heat treatment on as-prepared vapor-grown carbon fibers is to graphitize the fibers, leading to the growth of a highly crystalline graphite structure [6.1]. Raman scattering has been used as a powerful tool for characterizing the graphitization process in benzene derived-fibers (BDFs) [6.1] in the near-surface region (to a depth of ~ 600Å).

A more complete picture of the graphitization process in carboneous materials was provided by Oberlin [6.2] using results obtained from other characterization tools including x-ray diffraction, optical microscopy, Transmission Electron Microscopy (TEM) and infrared spectroscopy. It was found that in the graphitization process, basic structural units (BSUs) are formed initially. For $T_{\rm HT} < 800°$C, the release of heteroatoms allows adjacent BSUs to get close enough to each other to form distorted columns. These columns are, however, independent and are only approximately parallel to one another because of the presence of some single misoriented BSUs trapped between columns. These trapped BSUs begin to align when $T_{\rm HT}$ gets above 1500°C, and adjacent columns can then get hooked to one another, edge to edge, and distorted wrinkled layers thus form. The microcrystallite size in the c-axis (L_c) also grows very fast in the range 1500°C $< \rm T_{HT} <$ 1900°C. Above $T_{\rm HT} = 1700°$C, the in-plane zig-zag-like boundary defects are annealed away. In the range 1900°C $< \rm T_{HT} <$ 2100°C, de-wrinkling takes place rapidly and finally at $T_{\rm HT} > 2100°$C, the layers become stiff and crystalline, with nearly all of the in-plane defects removed. It is worth noting that non-graphitizing carbons, to which class ACFs probably belong, follow the same graphitization path although they cannot achieve as high a final degree of graphitization as graphitizing carbons, because their elemental domains in the bulk mesophase (pore walls) are much smaller before graphitization [6.2].

The goal of this study is not only to determine whether ACFs follow the same graphitization process as that described by Oberlin [6.2], but also to relate the electronic phase transition observed in the temperature-dependent resistivity, magnetoresistance and photoconductivity for $T_{\rm HT}$ between 1000°C and 1200°C to the structural transformations that take place as a result of heat treatment of ACFs, as is done in the next chapter.

With regard to the electronic phase transition, Fung *et al.* [6.3] and Kuriyama *et al.* [6.4, 6.5] have carried out, respectively, preliminary studies of the electrical transport and photoconductivity properties of ACFs subjected to various heat treatment temperatures ($T_{\rm HT}$). Both studies lead to consistent conclusions that ACFs exhibit a greater degree of graphitization with increasing $T_{\rm HT}$ and that ACFs undergo a metal-insulator (MI) transition for $T_{\rm HT} \sim 1200°$C. The details of the transport behavior near the MI tranistion are discussed in the next chapter.

In this chapter, Raman scattering, x-ray diffraction and BET measurements are used to study the effect of heat treatment on the microstructure of ACFs. Raman scattering and

x-ray diffraction measurements are used to obtain the in-plane microcrystallite size (L_a) and the c-axis d_{002} interlayer distance, respectively, for the ACFs subjected to various $T_{\rm HT}$. These structural parameters are both sensitive to the graphitization process. The Raman scattering results also provide strong evidence for the presence of 2-dimensional graphene structures, which is the basis for the transport phenomena observed in heat-treated ACFs.

Before ACFs graphitize, the graphite platelets have to be aligned. The alignment is correlated with the collapse of the micropores which exist between the c-faces of the platelets. We can monitor the microcollapse and thus the alignment along the c-axis by Brunauer-Emmett-Teller (BET) measurements for the SSA because all the SSA of ACFs can be attributed to these micropores, as shown in Chapter 2. Because SSA is a measure of porosity and hence of disorder, the BET experiment is presented first to provide a common starting point for our discussion of other characterization techniques.

6.1 Experimental Details

The precursor material of the ACFs used in this study is isotropic pitch. The fibers were activated by heating them at 800-1200°C in the presence of CO_2 or water vapor. Pitch-based ACFs with SSAs of $1000 m^2/g$, $2000 m^2/g$ and $3000 m^2/g$ were obtained by controlling the activation times and temperatures. The SSA was determined by BET analysis of the adsorption isotherm of N_2 at 78K and of CO_2 at 195K [6.6].

An Argon-ion laser operating at 4880Å was used in the Raman back-scattering geometry to provide $\sim$ 50 mW of incident radiation at the sample. The fiber bundle was held on a Pyrex glass slide by wrapping the ends of the fibers with parafilm strips. The central portion of the bundle was exposed to 50mW laser radiation. The scattered radiation was collected by a 50 mm camera lens and focused onto the entrance slit of a SPEX-1403 spectrometer. Similar sample preparation techniques were used for x-ray diffraction experiments and the central region of the fiber bundle was exposed to Cu-Kα radiation in a Diano diffractometer.

6.2 BET Characterization

BET measurements are shown as points in Fig. 6-1 for ACFs heat treated to various $T_{\rm HT}$. To justify why these points were joined by the solid lines, the curve of SSA against $T_{\rm HT}$ for activated carbon fiber cloth [6.7] is also shown. As $T_{\rm HT}$ is increased, the SSAs for

all the fibers show a precipitous drop in SSA from that for the as-prepared fibers to very small values for high T_{HT}.

We observe in the same figure that the higher the initial SSA, the higher the T_{HT} needed to produce a collapse in the pore volume. One possible explanation is that the desorption process tends to be more difficult in as-prepared ACFs with a higher initial SSA. During the heat treatment process, trapped adsorbed species have to be desorbed from the system first, before the platelets can get realigned. Before heat treatment, a larger proportion of the platelets in these ACFs are thin, single-layer platelets and naturally, the misorientation angles between neighboring graphite platelets are more likely to be larger because of the enhanced degrees of freedom associated with larger number of pores. Desorption should then take place by the capillary action of driving the gas out through small ducts formed between these misaligned micropores. On the other hand, ACFs with a lower initial SSA, and thicker platelets as a result, have their platelets more or less aligned (at least with respect to the c-axis). The process of desorption should involve diffusion mainly and should resemble that of de-intercalation [6.8], a relatively easy process compared with the capillary desorption in ACFs with a larger SSA.

That desorption has to take place before platelet realignment is corroborated by the ESR study [6.9] which shows that for $T_{HT} < 450°C$, a narrow peak, due to dangling bonds, appeared in the ESR spectrum for the pitch-based ACFs with SSA= $3000\,m^2/g$. The appearance of the dangling bonds on the surface can be attributed to the desorption of adsorbed species.

The BET data in Fig. 6-1 suggest that the pore size decreases in ACFs as a result of increasing T_{HT} to 2000°C. Beyond 2000°C, there is negligible change in the SSA of ACFs largely because of the low SSA values for $T_{HT} \geq 2000°C$.

6.3 X-ray Characterization

In order to study the structural ordering along the c-direction in ACFs, room temperature d_{002} x-ray diffraction profiles were measured for the various types of heat-treated ACFs. Figure 6-2 shows the d_{002} diffraction profiles for ACFs with SSA = $1000\,m^2/g$ heat treated to various T_{HT}. The width of the (002) diffraction peak is very broad for the ACFs with low T_{HT} but it becomes sharper with increasing T_{HT}. Also, the value of the peak

position for the (002) peak upshifts in 2θ values for increasing T_{HT}, indicating a decrease in the interlayer distance between the graphene layers. We believe that the broad (002) diffraction peak is composed of a range of contributions, each corresponding to a different d_{002} value in the structure of ACFs. Indeed, in the diffraction spectra for $3000\,m^2/g$ ACFs heat-treated above 2000°C, the diffraction profile clearly indicates the presence of several distinct peaks but we could not resolve each of them experimentally or numerically.

The observation of a range of discrete d_{002} spacings is consistent with previous diffraction experiments in disordered graphite [6.10,6.11]. The sharpening of the (002) diffraction peak width with increasing T_{HT} suggests that the BSUs in the ACFs become better aligned with respect to each other and larger in size in the direction of the c-axis as T_{HT} increases. The results further indicate that the distribution in d-spacings in the ACFs narrows when the ACFs are heat treated to 2500°C. Recently, Aladekoma *et al.* [6.11] have investigated in detail the factors that cause distortion of the x-ray diffraction line profiles in carbons by analyzing the diffraction profiles of mechanically ground graphite. Their study shows that the mechanical grinding of graphite continuously increases the interlayer spacing in the range $3.354Å \leq d_{002} \leq 3.375Å$ and widens the distribution of d-spacings. Further grinding caused discontinuous transformations of the material, forming metastable phases characterized by interlayer spacings of 3.40Å, 3.49Å and 3.55Å.

To characterize the ACFs, we used the simple centroid method to determine the average $\langle 2\theta \rangle$ of the x-ray data, as shown in Fig. 6-2. The average d_{002} interlayer spacing was then obtained from Bragg's formula. Representative d_{002} interlayer distances are plotted as points in Fig. 6-3 for the ACF samples used in this study. Irrespective of the SSA, the interlayer spacing decreases in ACFs with increasing T_{HT}. Solid, dashed and dotted lines are passed through the points to show the trends in the decrease of the d_{002} spacing for the 3000, 2000 and 1000 m^2/g SSA fibers, respectively. Even for heat treatment temperatures of 2500°C, the d_{002} interlayer spacing is $\sim 3.5Å$, indicating that the structure of the heat treated ACFs remains in the turbostratic regime. The rate of change of the d_{002} spacing with T_{HT} is the fastest for the ACFs with SSA of $3000\,m^2/g$, most probably because in this range of T_{HT}, the micropores in the $3000\,m^2/g$ fibers may just be beginning to collapse whereas the porosity of the ACFs with lower initial SSA has already been reduced to very low values.

The information obtained from the x-ray experiment (Fig. 6-3) and the BET experiment

(Fig. 6-1), when correlated, suggests that heat treatment reduces the misorientation angle between the BSUs, thereby closing up the micropores which contribute most importantly to the SSA of ACFs. With the reduction in misorientation angle, the graphene layers can grow and the interplanar distances can decrease. However, because the initial size of the BSUs is very small (about 10 Å thick and 20 Å wide in-plane), ACFs cannot be completely graphitized. Furthermore, the activation process naturally involves chemisorption of oxygen, which dehydrogenates the material, thereby depleting the ACF system of the CH groups that enhance graphitizability. With particular relevance to the present study is the observation that the collapse of the pore structure occurs at much lower T_{HT} than the formation of large in-plane platelets, as revealed by the Raman scattering experiments discussed below.

6.4 Raman Characterization

Room-temperature Raman spectra for ACFs with SSA values of $2000\,\mathrm{m}^2/\mathrm{g}$ are shown in Fig. 6-4 for the as-prepared fibers and for fibers with T_{HT} values of 1500°C, 2000°C and 2500°C. Similar spectra were obtained for the 1000 m^2/g and the 3000 m^2/g fibers and are not shown in Fig. 6-4. The spectra in Fig. 6-4 show two distinct peaks, namely, the disorder-induced (D) peak at $\sim 1360\,\mathrm{cm}^{-1}$ and the E_{2g_2} Raman-allowed graphitic (G) peak at $\sim 1580\,\mathrm{cm}^{-1}$. The $1580\,\mathrm{cm}^{-1}$ G line is associated with the zone-centered phonon whereas the $1360\,\mathrm{cm}^{-1}$ D line arises from the presence of a high density of phonon states near $\sim 1360\,\mathrm{cm}^{-1}$ for graphite. In the presence of disorder, the selection rules for Raman-active modes are relaxed and thus non-zone-centered peaks such as the $1360\,\mathrm{cm}^{-1}$ peak can be observed [6.12].

We note two main features of the lines in Fig. 6-4: (1) The intensity of the disorder-induced D peak at $\sim 1360\,\mathrm{cm}^{-1}$ decreases with increasing T_{HT} relative to that of the $1580\,\mathrm{cm}^{-1}$ G peak. (2) The half-width-at-half-maximum-intensity (HWHM) linewidth of the $1580\,\mathrm{cm}^{-1}$ G peak decreases with an increase in T_{HT}. These two features are also observed in the Raman spectra for the $1000\,\mathrm{m}^2/\mathrm{g}$ and $3000\,\mathrm{m}^2/\mathrm{g}$ ACFs although the detailed T_{HT} dependence of the line intensities and linewidths is sensitive to the SSA of the ACFs.

From a Lorentzian fit to the data in Fig. 6-4, important information about the microstructure of the fibers can be obtained. Similar experiments and analysis were used by Chieu *et al.* [6.1] for studying the microstructure of the benzene-derived vapor-grown fibers

(BDFs), and a measure of the in-plane crystalline size (L_a) was obtained for the heat-treated BDFs as a function of $T_{\rm HT}$. When $T_{\rm HT}$ was increased to $\sim$ 3000°C, the intensity of the 1360 $\rm cm^{-1}$ line in BDFs was reduced to very small values, as individual crystallites became well aligned with respect to the neighboring crystallites and the microstructure of the BDFs became close to that of HOPG [6.1].

The first study correlating the Raman data with x-ray data for disordered graphite was performed by Tuinstra and Koenig [6.13] and they used the relative ratio (R) of the integrated intensities for the D and G (1360 $\rm cm^{-1}$ and 1580 $\rm cm^{-1}$) lines to provide a measure of L_a. More recently, from a comprehensive study of the ratio R obtained from Raman scattering experiments in different carbon materials, Knight and White [6.14] obtained the empirical relation between L_a and R, given for 4880 Å laser radiation as

$$L_a(\text{Å}) = \frac{44}{R} \ . \tag{6.1}$$

Figures 6-5(a) and (b) are plots of R and L_a, respectively, for our ACFs as a function of $T_{\rm HT}$. In Fig. 6-5(b) the dotted, dashed and solid curves act as a guide to the eye and show the changes in L_a as a function of $T_{\rm HT}$ for the 1000 $\rm m^2/g$, 2000 $\rm m^2/g$ and the 3000 $\rm m^2/g$ ACFs, respectively. In Fig. 6-5, the changes in R and L_a for ACFs are also compared with those obtained by Chieu *et al.* [6.1, 6.13] for BDFs.

The results of Figs. 6-5(a) and (b) indicate that, irrespective of the SSA, the ACFs show a considerable degree of graphitization and exhibit similar behavior for the in-plane structure as that found for the BDFs for increasing $T_{\rm HT}$. It is interesting to note in Fig. 6-5(b) that L_a is only weakly sensitive to SSA for $T_{\rm HT} < 2000$°C, consistent with our Raman study of as-prepared ACFs with different SSAs [6.15]. On the other hand, for $T_{\rm HT} > 2000$°C, the 3000 $\rm m^2/g$ fibers show a significant increase in L_a, while the increase in L_a is less pronounced for the 2000 $\rm m^2/g$ and 1000 $\rm m^2/g$ fibers.

This behavior of L_a for the 3000 $\rm m^2/g$ fibers can be related to the resistivity results [6.3], which suggested that ACFs with a low SSA tend to be more graphitizable than those with a high SSA. The ACFs studied there [6.3] had SSA only up to 2000 $\rm m^2/g$ and according to Fig. 6-5, those fibers should have essentially the same values for L_a.

As a further check on the graphitization of ACFs with increasing $T_{\rm HT}$, we plot in Fig. 6-6(a) and (b) the HWHM intensity and the peak position of the Raman-allowed 1580 $\rm cm^{-1}$

mode for different SSA values, as given in the legend. As in Figs. 6-5(a) and (b), comparisons of the HWHM linewidths and the Raman frequency positions of ACFs with those of BDFs [6.1] show similar trends for increasing T_{HT}, indicating that such highly disordered ACFs are surprisingly graphitizable, but still not nearly as graphitizable as the BDFs [6.1], which extrapolate to the HWHM and Raman frequency values of highly oriented pyrolytic graphite (HOPG) with increasing T_{HT}, as shown in Fig. 6-6. Indeed, the linewidths for ACFs remain significantly larger at $T_{HT} = 2500°C$ than for BDF, consistent with the notion that disordered systems tend to have a larger variation of the atomic environments for various carbon atoms. Despite the error bars, the ACF material becomes reasonably ordered at $T_{HT} = 2500°C$, as evidenced by the large L_a values plotted in Fig. 6-5(b), and therefore Raman scattering may become a sensitive characterization tool for these materials [6.16]. The relative trends of the half-widths and Raman frequencies with respect to SSA may be indicative of the relationship between disorder and SSA upon heat treatment. It appears in Fig. 6-6 that the ACFs which have a higher SSA and more disorder before heat treatment graphitize more completely. As shown in Fig. 6-6, even for the most highly graphitized ACFs, they still remain turbostratic with regard to interplanar correlations after heat treatment, in agreement with Fig. 6-5(b).

6.5 Summary

When the results from all three characterization experiments are correlated, the sequence of events that happens in the course of graphitization induced by heat treatment can be identified. To complete our understanding, we also refer to results from an ESR study of ACFs [6.9] which shows that under heat treatment at $T_{HT} < 450°C$, desorption of adsorbed gases first takes place. Then, our BET and x-ray results provide direct and indirect evidence for the collapse of micropores upon heat treatment at some T_{HT} value much lower than 2000°C (see Fig. 6-1), depending on the SSA and T_{HT} values of the ACFs. At these T_{HT} values, the basic structural units begin to stack along the c-axis forming independent distorted columns. The interplanar distance decreases as the stacking continues and the columns begin to associate edge to edge with increasing T_{HT}. When T_{HT} exceeds 2000°C, in-plane order begins to develop as the waviness is reduced and L_a increases. Because the as-prepared ACF material initially contains a lot more micropores and adsorbed oxygen

than graphitizing carbons, ACFs cannot be completely graphitized and the turbostratic structure remains, consistent with the interlayer distance measured by x-ray diffraction (> 3.44Å).

We conclude that the graphitization process in ACFs follows the same sequence of events as described by Oberlin [6.2], except for the final formation of flat polycrystalline graphite with three-dimensional ordering which does not occur for ACFs. The microstructural change in ACFs under heat treatment can be illustrated by the schematic representation of non-graphitizing (Fig. 6-7(a)) versus graphitizing (Fig. 6-7(b)) structures of activated carbon (figures extracted from Ref. [6.17]). ACFs should have a microstructure similar to that shown in Fig. 6-7(a) before heat treatment. After heat treatment at high T_{HT}, the pores disappear, leaving a layered microstructure as shown in Fig. 6-7(b). The layers are, however, still turbostratic, i.e. uncorrelated with one another along the c-axis.

In Figs. 6-5 and 6-6 , we note that the effect of heat treatment on the development of full crystallinity in the benzene-derived fibers diminishes only after T_{HT} reaches 3000°C and beyond [6.1]. It would therefore be of interest to heat-treat our ACFs to temperatures of 3500°C or more to find out about the ultimate degree of crystallinity achievable in ACFs by heat treatment.

All the transport studies of the effect of heat treatment on ACFs have provided evidence for a metal-insulator transition at a transition temperature of about 1000°C to 1200°C, hinting that the metal-insulator transition is related to the collapsing of the micropores within these fibers and is not related to the in-plane development of crystalline order which happens above $T_{HT} \sim 2000$°C. This deduction is further tested in the next chapter.

References

[6.1] T. C. Chieu, M. S. Dresselhaus, and M. Endo, Phys. Rev. **B26**, 5867 (1982).

[6.2] A. Oberlin, Carbon **22**, 521 (1984).

[6.3] A. W. P. Fung, A. M. Rao, K. Kuriyama, M. S. Dresselhaus, G. Dresselhaus, and M. Endo, in *Extended Abstracts of the 20th Biennial Conference on Carbon, Santa Barbara, CA, 1991*, edited by R. A. Meyer (American Carbon Society, State College, PA), p. 296.

[6.4] K. Kuriyama, M. S. Dresselhaus, and A. W. P. Fung, in *Extended Abstracts of the 20th Biennial Conference on Carbon, Santa Barbara, CA, 1991*, edited by R. A. Meyer (American Carbon Society, State College, PA), p. 300.

[6.5] K. Kuriyama and M. S. Dresselhaus, J. Mater. Res. **7**, 940 (1992).

[6.6] E. Tanaka, Fuel and Combustion **54**, 241 (1987).

[6.7] I. Tanahashi, A. Yoshida, and A. Nishino, J. Appl. Electrochem. **21**, 28 (1991).

[6.8] M. S. Dresselhaus and G. Dresselhaus, Adv. Phys., **30**, 139 (1981).

[6.9] S. L. di Vittorio, A. Nakayama, T. Enoki, M . S. Dresselhaus, M. Endo, and N. Shindo, J. Mater. Res. **8**, 2282 (1993).

[6.10] J. Lachter, L. G. Henry, and R. H. Bragg, J. Appl. Cryst. **21**, 92 (1988).

[6.11] J. B. Aldekoma and R. H. Bragg, Carbon **28**, 897 (1990).

[6.12] M. S. Dresselhaus and G. Dresselhaus, in *Light Scattering in Solids III*, edited by M. Cardona and G. Güntherodt, Topics in Applied Physics, vol. 51 (Springer, Berlin, Heidelberg, 1982), p. 3.

[6.13] F. Tuinstra and J. L. Koenig, J. Chem. Phys. **53**, 1126 (1970).

[6.14] D. S. Knight and W. B. White, J. Mater. Res. **4**, 385 (1989).

[6.15] A. W. P. Fung, A. M. Rao, K. Kuriyama, M. S. Dresselhaus, and G. Dresselhaus. in *Defects in Materials*, edited by P. D. Bristowe, J. E. Epperson, J. E. Griffith, and Z. Liliental-Weber, MRS Symposia Proceedings, No. 209 (Materials Research Society, Pittsburgh, 1991), p. 335.

[6.16] M. S. Dresselhaus, G. Dresselhaus, K. Sugihara, I. L. Spain, and H. A. Goldberg, *Graphite Fibers and Filaments* (Springer, Berlin, Heidelberg, 1988).

[6.17] M. Smíšek and S. Černý, *Active Carbon: Manufacture, Properties and Applications* (Elsevier, New York, 1967).

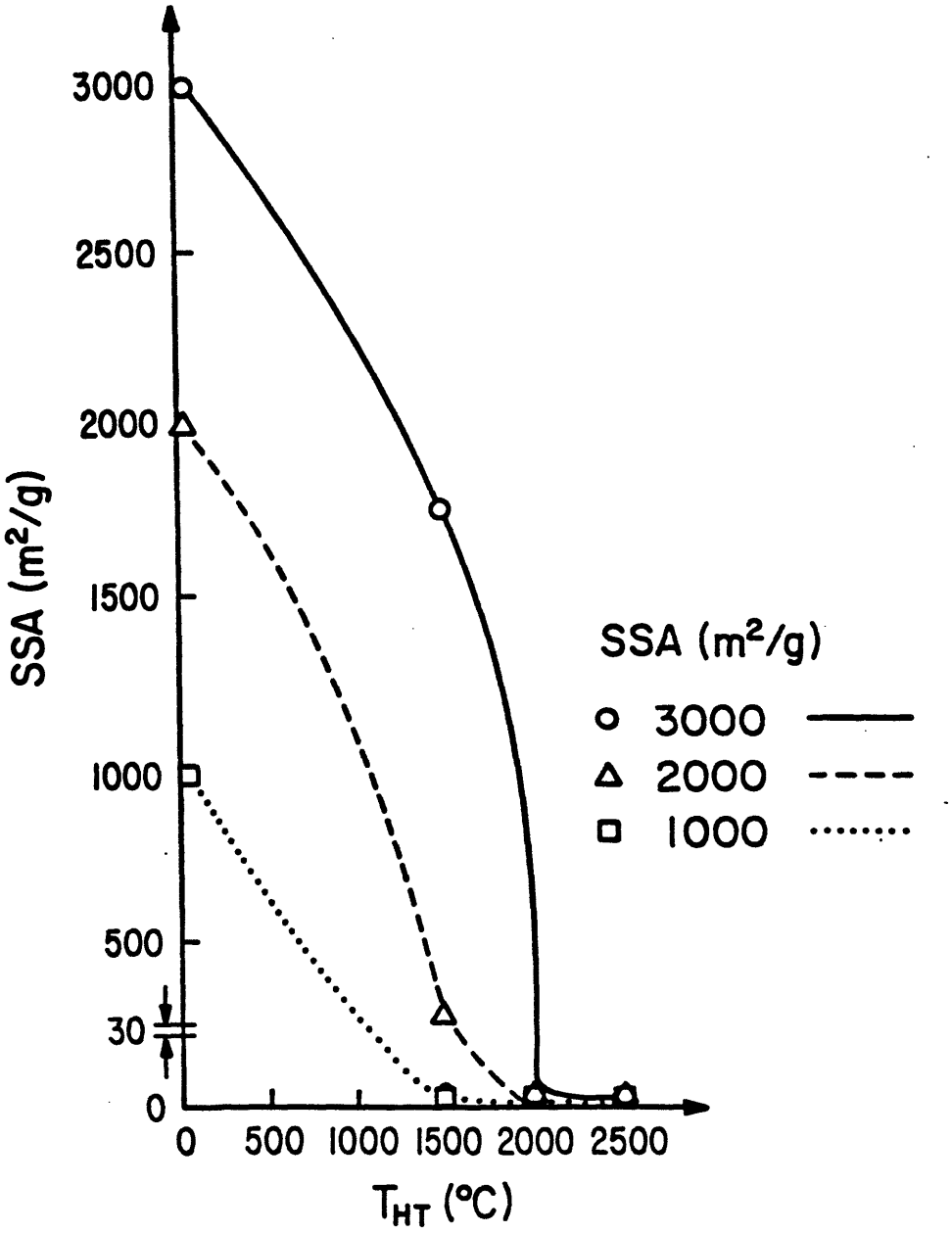

Figure 6-1: Plot of SSA for the ACFs as a function of T_{HT}. The solid curves indicate the drop in SSA value for the ACFs when subjected to heat treatment temperatures up to $\sim$ 2500°C. They are drawn to have the same shape as the solid curve for activated carbon fiber cloth (ACFC).

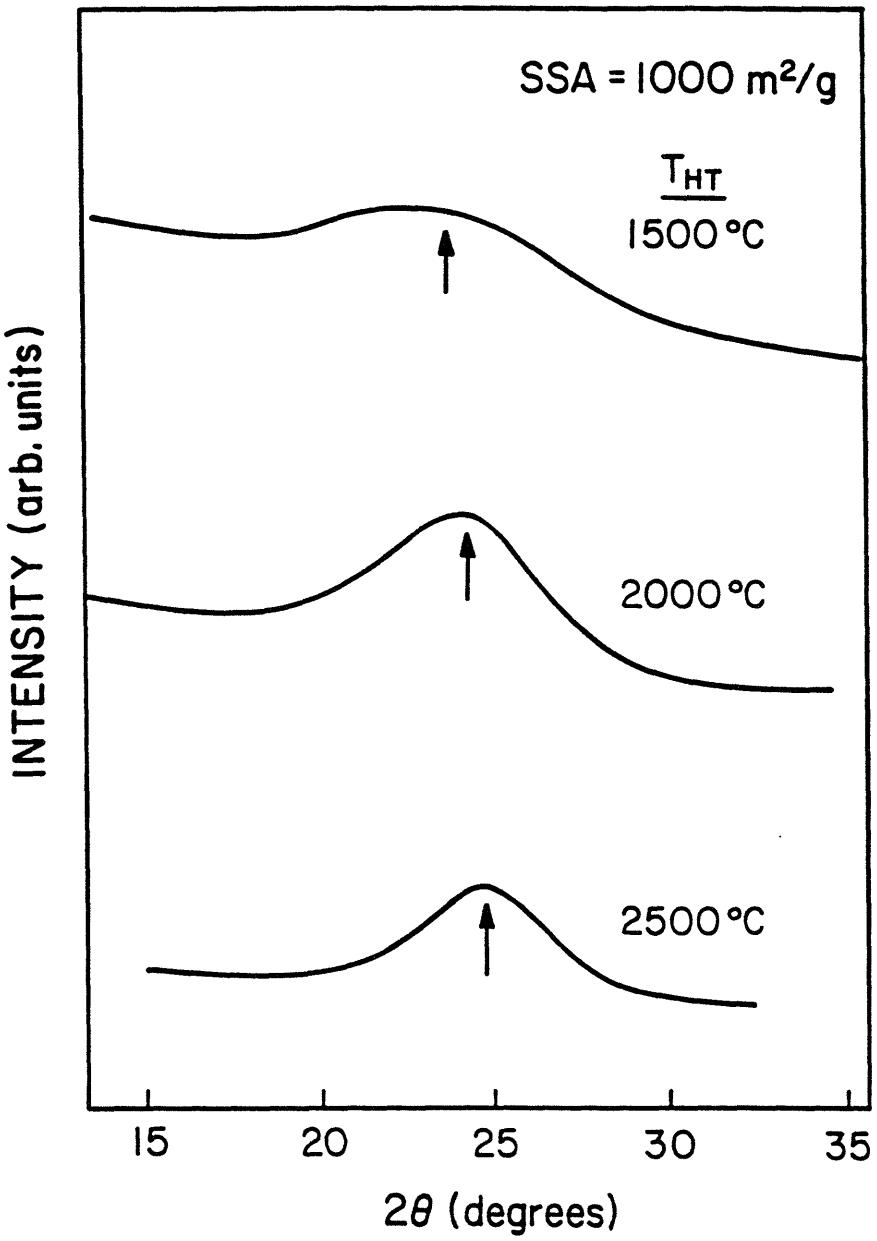

Figure 6-2: The x-ray diffraction profiles for ACFs with SSA=1000 m^2/g heat treated to various T_{HT} values. The peak positions are indicated by arrows.

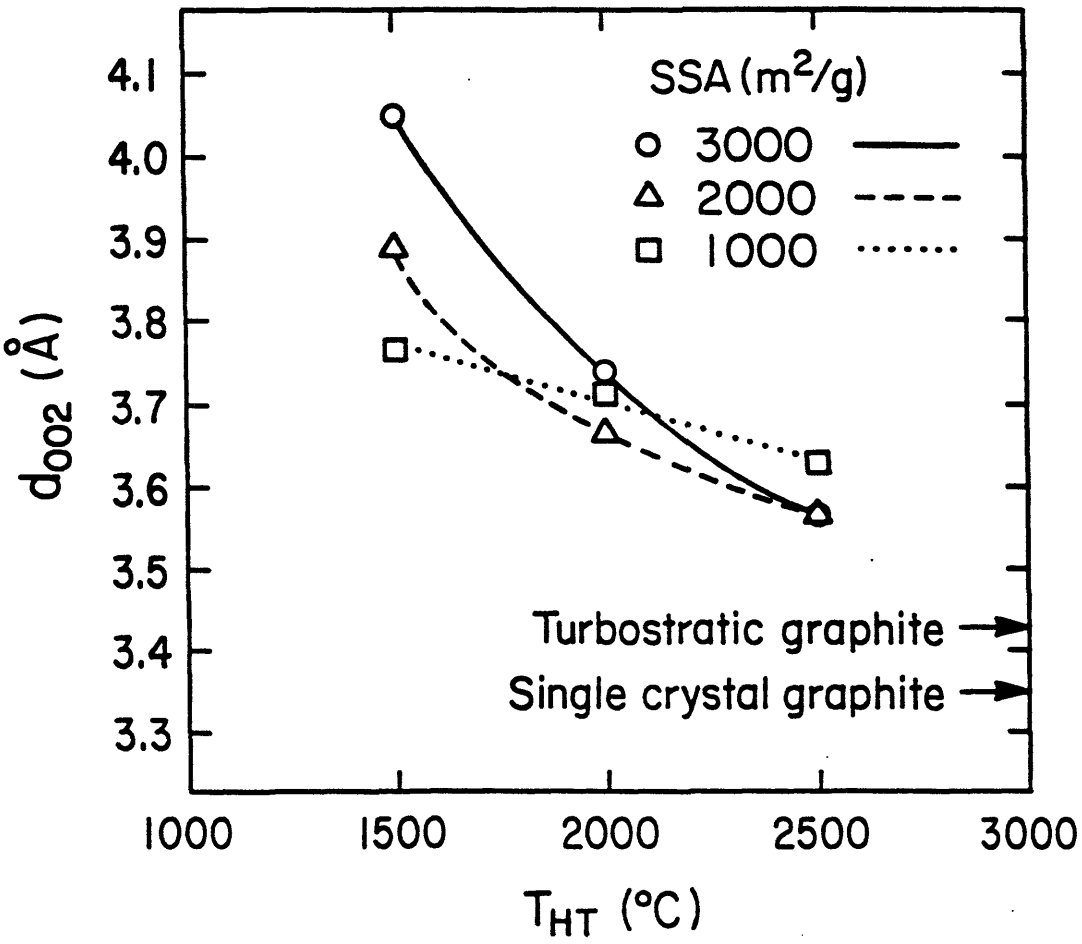

Figure 6-3: d_{002} interlayer distances obtained using the centroid method and Bragg's formula for ACFs heat treated to various T_{HT}. Also indicated on the figure (by arrows) are the d_{002} values for single crystal and turbostratic graphite.

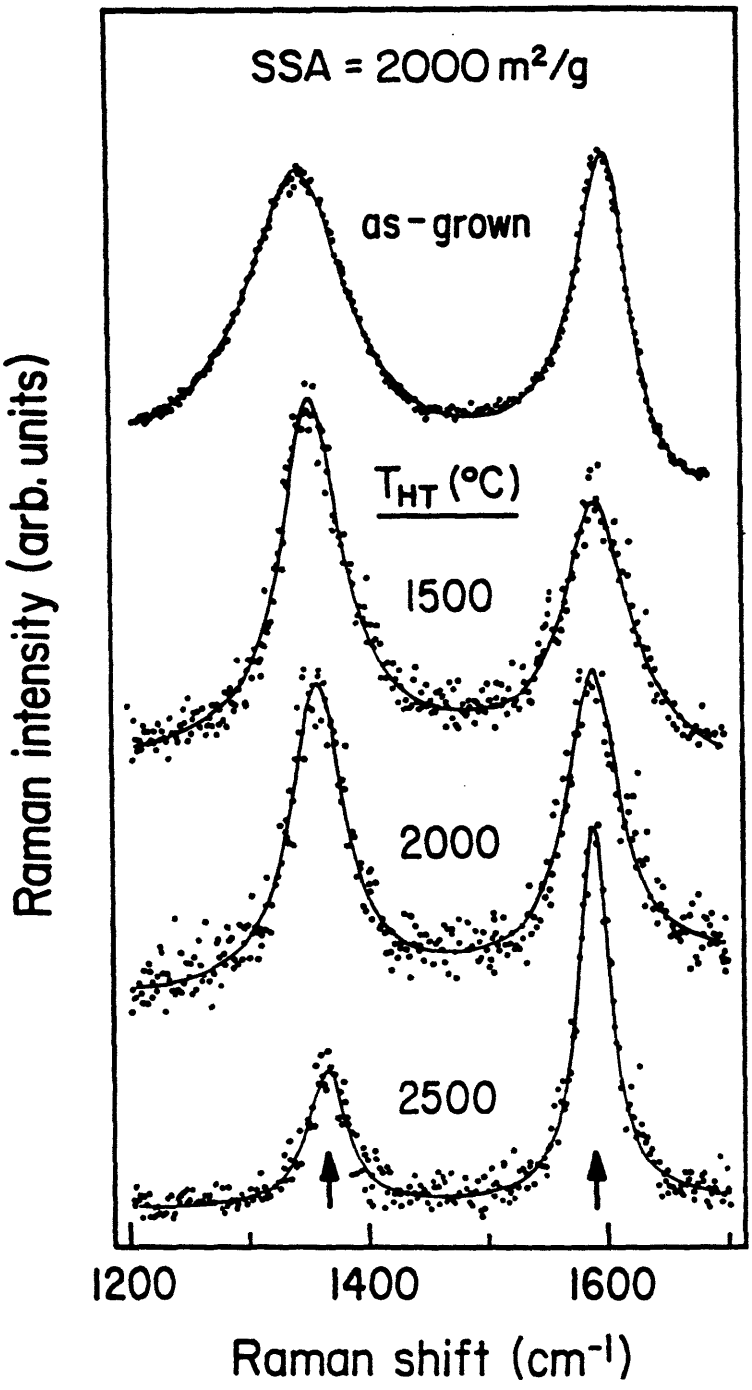

Figure 6-4: Room temperature Raman spectra for the 2000 m^2/g ACFs, including the as-prepared fibers and for T_{HT} values of 1500°C, 2000°C and 2500°C. The solid curves are the Lorentzian fits to the data. The peak positions are indicated by arrows.

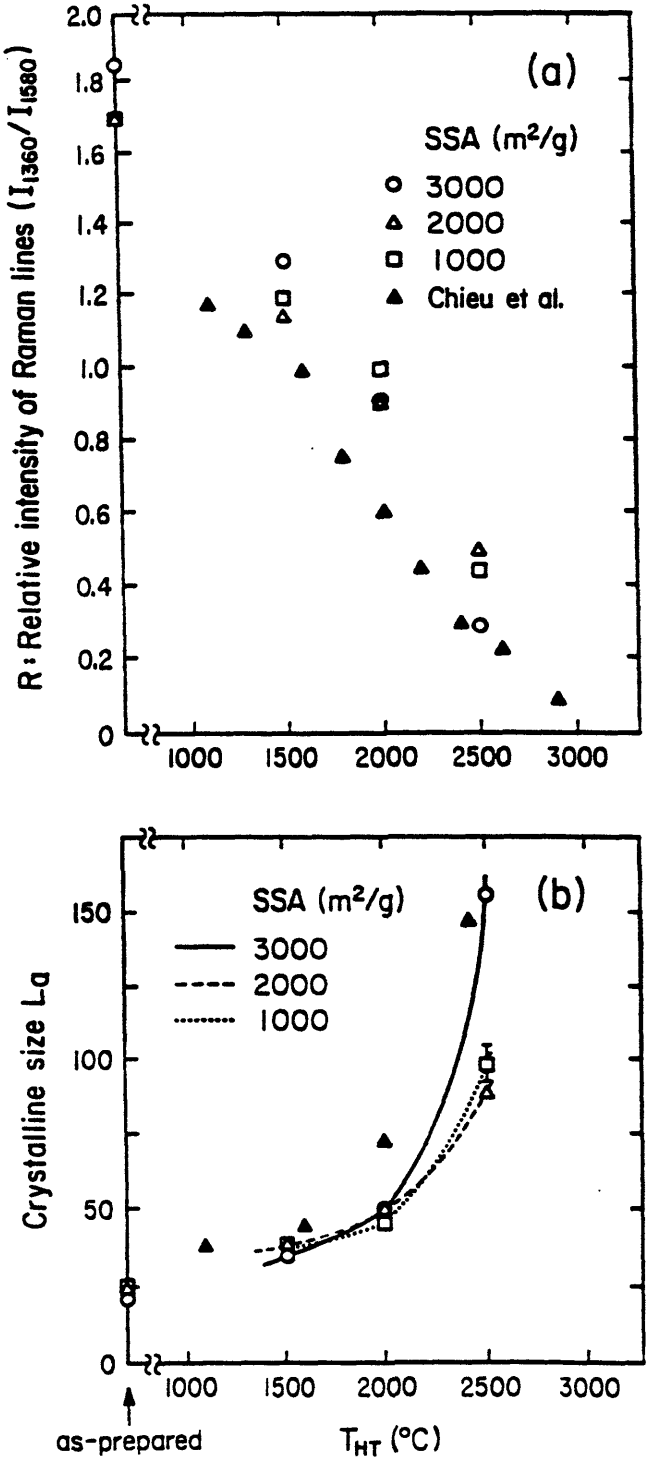

Figure 6-5: Plots of the (a) relative integrated intensity of Raman lines R and (b) in-plane microcrystallite size L_a for ACFs as a function of T_{HT}. In (b) the solid, dashed and dotted curves act as a guide to the eye and show the changes in L_a for increasing T_{HT} for the 3000 m^2/g, 2000 m^2/g and 1000 m^2/g fibers, respectively. For comparison, the corresponding data for benzene-derived vapor-grown fibers are also shown.

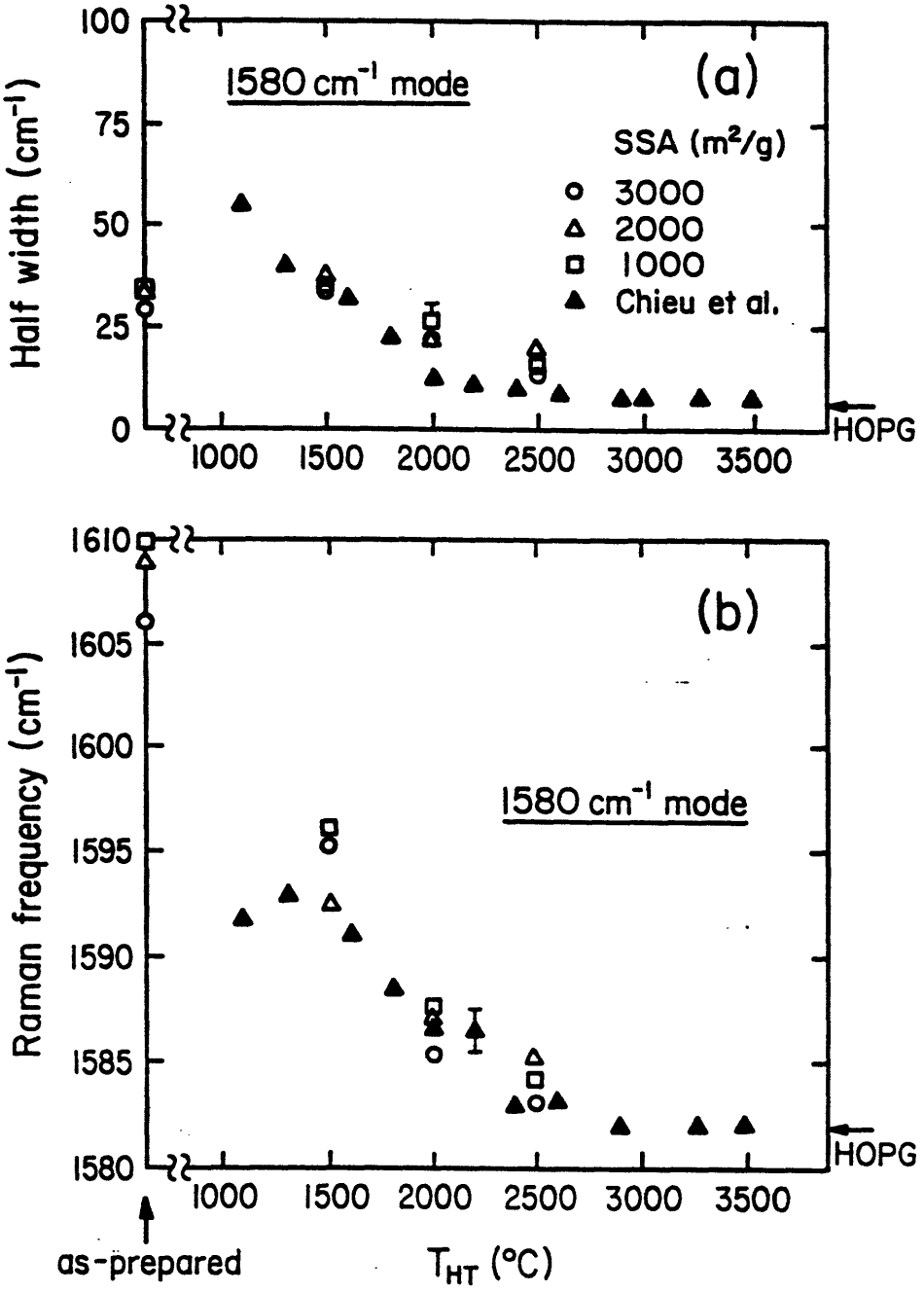

Figure 6-6: Plots of the (a) HWHM intensity and the (b) Raman frequency for the 1580 cm^{-1} mode for ACFs as a function of T_{HT}. For comparison, similar results are shown for BDFs, for which the data extrapolate to the HWHM and Raman frequency values for HOPG [6.1]. The legend gives the identification of the fibers according to SSA.

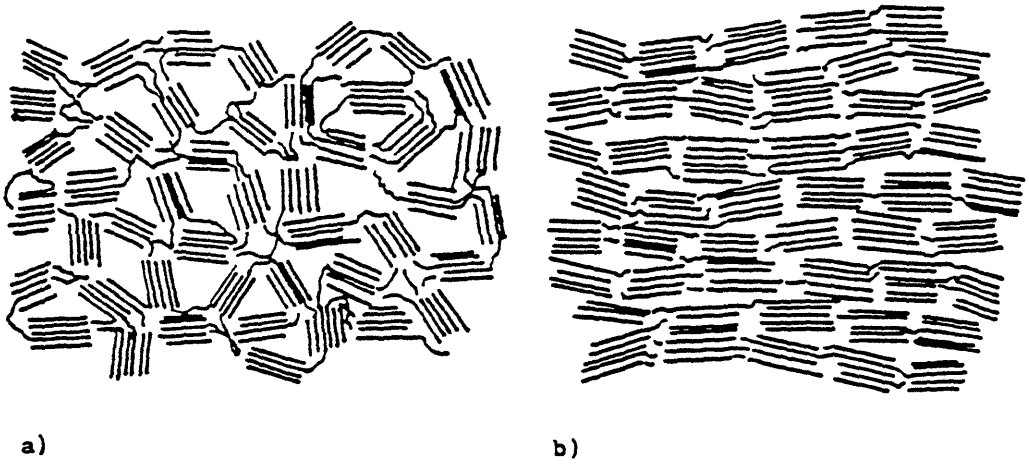

Figure 6-7: A schematic representation of the microstructures of (a) non-graphitizing and (b) graphitizing activated carbons. Figures (a) and (b) are used to illustrate the microstructures of ACFs before and after heat treatment, respectively. (Figures extracted from Ref. [6.17])

Chapter 7

Transport Properties near the Metal-Insulator Transition in Heat-Treated ACFs

Transport studies of granular systems in the past were typically carried out with amorphous semiconductors alloyed with metals, discontinuous thin films, cermets and granular metals. Nanoporous materials, though possessing a similar metal-insulator admixture, have not received much attention in the past. Based on the understanding gained in the last chapter of the microstructural transformation induced by heat treatment, we have acquired, in the form of an external parameter, namely the heat treatment temperature, a microstructural tuning capability so essential for the study of disorder near the metal-insulator (MI) transition. We therefore propose using activated carbon fibers (ACFs) as a nanoporous medium in the study of transport properties on either side of the MI transition.

The critical parameters on the two sides of the MI transition are different in the ACF system. On the metallic side, it is the in-plane alignment of the basic structural units (or graphite platelets) while on the insulator side, it is the granular size and separation. In general, the transition is initiated by changes in the nanopores in the system. The interest in ACFs is accordingly related to the tunability of their nanoporosity, through the initial activation process or the subsequent heat treatment process.

Through activation, graphite platelets with size reduced to the order of the mean free path of the charge carriers are formed, inducing strong localization in the system. The

platelets are randomly oriented with a narrow angular distribution locally and with a much wider angular distribution globally. Together with the micropores existing between platelets both in the in-plane direction (~ 2 Å) and in the out-of-plane direction (~ 10 Å), this system of platelets constitutes a new granular system. It is noted that within the platelets, defects and atomic vacancies which arise from the activation of the precursor material could affect the transport properties of bulk graphite and might therefore also play a role in the transport properties of ACFs. In this regard, heat treatment above $\sim$ 700°C could dramatically reduce the density of these defects and simplify the system to that of granular metals for the study of granularity alone. Through progressive heat treatment, these granular regions can realign themselves, fuse together with their neighbours, and at sufficiently high heat treatment temperature, form extended, partially ordered 2-dimensional planes. In Chapter 2 and subsequently Chapter 6, we have already given a more detailed description of the nanostructure of ACFs before and after heat treatment.

Recent work on ACFs has addressed the effect of heat treatment on the optical and transport properties of these fibrous materials. Kuriyama and Dresselhaus [7.1,7.2] observed in their photoconductivity study of heat-treated phenol-based ACFs that an electronic transition occurred when the ACFs were heat-treated near 1000°C. (It should be noted that this transition has no thermodynamic origin and is often termed a pseudo-transition or metal-insulator (MI) transition.) Kuriyama and Dresselhaus found that $\Delta\sigma$, the absolute value of the photoconductivity, peaks at a heat treatment temperature of $T_{\mathrm{HT}} \sim 1000$°C. They also showed that the dark conductivity $\sigma(T)$ loses its strong temperature dependence at low temperature at about the same value of T_{HT}. It was found in a preliminary transport study on pitch-based ACFs that, for $T_{\mathrm{HT}} > 1500$°C, the conductivity for the heat-treated ACFs is essentially independent of temperature and that the magnetoresistance has also changed its sign from positive to negative values [7.3]. In both investigations, the room-temperature conductivity was found to increase by about two orders of magnitude as a result of heat treatment of the ACFs, and to increase by many orders of magnitude at very low (< 30 K) measurement temperatures.

As a result of the structural study on ACFs heat-treated at temperatures between 1500°C and 2500°C [7.4, 7.5] (see Chapter 6), a more complete understanding of the relationship between heat treatment and the electronic transition has been achieved. This structural study can be summarized by two schematic diagrams representing the structure

before and after the graphitization process, as illustrated in Fig. 6-7. Such findings, when correlated with the photoconductivity study [7.1, 7.2], suggest that the heat-treatment-induced electronic transition is related to the collapse of interplanar micropores and the associated stacking of basic structural units, rather than with the development of in-plane crystallinity. This is also corroborated by the transport results presented in this chapter.

While the traditional characterization tools, such as the liquid and vapor adsorption methods [7.6, 7.7], can provide information about the nanoporosity of ACFs, the transport characterization techniques are shown to probe the configuration of nanoparticles (and by inference, also the configuration of nanopores), thus complementing the adsorption methods.

We first show that our experimental results provide strong supporting evidence for the models developed previously to explain the structural [7.4, 7.5] and photoconductivity [7.2] studies on the effect of heat treatment on ACFs. Our discussion will then focus on gaining an understanding of the transport properties of the heat-treated ACFs on both sides of the MI transition. It is shown that the Coulomb-gap variable-range hopping mechanism, used earlier in Chapter 4 to describe conduction in as-prepared ACFs, might also be in play in the heat-treated samples. An extension of the transport study of the heat-treated ACFs to the metallic side of the MI transition is the subject of Chapter 8.

7.1 Experimental Details

The ACFs under our transport study are derived from two different precursors, namely pitch (ACP) and phenol (FRL), using symbols based on manufacturers' designations. The manufacturing procedure for the synthesis of the as-prepared ACFs is described in Chapter 2 and also in Refs. [7.8–7.10]. Prior to heat treatment, the ACP fibers used in this study nominally have SSA= $1000\,\mathrm{m}^2/\mathrm{g}$ and SSA= $2000\,\mathrm{m}^2/\mathrm{g}$ values, respectively, while the FRL fibers possess an SSA of $1000\,\mathrm{m}^2/\mathrm{g}$. The ACFs are hereafter labelled as ACP10, ACP20 and FRL10, with the precursor types indicated by the three initial Roman letters, and with the subsequent numbers indicating the SSA before heat treatment in units of $100\,\mathrm{m}^2/\mathrm{g}$. The ACP10 and ACP20 fibers were each heat-treated at two different temperatures, $T_{\mathrm{HT}} = 1500^\circ\mathrm{C}$ and $T_{\mathrm{HT}} = 2500^\circ\mathrm{C}$, to study the transport properties of the relatively well-ordered ACF material, since both of these temperatures were later verified to be higher than the T_{HT} value required for the MI transition to take place (T_{MI}). The FRL10 fibers and ACP10 fibers

showed a remarkably similar magnitude of the room-temperature electrical conductivity, and similar temperature and magnetic field dependences of the electrical conductivity, both before and after heat treatment at the same T_{HT}. Because of these similarities and the availability of FRL samples over a wide range of heat treatment temperatures, we aimed our detailed study of the MI transition to the FRL fibers, which were heat-treated at temperatures T_{HT} ranging from 300°C to 2500°C. All heat treatments were done in an Argon atmosphere for about 1 hour.

All dc electrical transport measurements were made by the 4-point probe method. Silver paint was used to establish contacts with the fibers. The preparation of a single fiber for measurement is described in Refs. [7.9, 7.10]. To measure the magnetoresistance of the most resistive ACFs, we mounted on the sample holder 10 fibers in parallel, thus reducing the resistance 10-fold. Magnetoresistance data were obtained in a field up to 0.8 T. The temperature scan from 4 K to room temperature took place by natural warming. The diameter of the fiber was determined by SEM (scanning electron microscopy) and the length by an optical microscope.

7.2 Experimental Results

DiVittorio *et al.* [7.11] observed that the electrical conductivity of ACP10 fibers, as shown in the bottom of Fig. 7-1, has a very strong temperature dependence at low measurement temperatures (below 30 K), characteristic of hopping conduction behavior. In contrast, the top of Fig. 7-1 shows that after heat-treatment at temperatures above 1500°C, the ACFs generally exhibit a very weak dependence on temperature although the temperature coefficient of resisitivity (TCR) is still negative, indicating that carrier hopping between crystallites probably still exists to some extent. Furthermore, instead of dropping to zero conductivity as $T \rightarrow 0$ K, the zero-temperature conductivity seems to be finite. Both effects are indicative of the presence of boundary scattering [7.12], as is often observed in weakly disordered systems such as glassy carbons [7.13] and other polycrystalline metallic systems. The absolute value of the resisitivity of the heat-treated ACFs is decreased by several orders of magnitude relative to that for the same fibers before heat treatment, depending on the measurement temperature. Nevertheless, even after heat treatment, the resistivity of the ACFs is still greater than that typical of single-crystal graphite (by about two orders of

magnitude). Heat-treated ACFs are therefore a poor metal despite being on the metallic side of the MI transition.

In the same figure, we also observe that as T_{HT} increases, the magnitude of the conductivity increases. This is consistent with a structural study on the same ACFs [7.4, 7.5], which shows that heat treatment anneals the disordered system and transforms it into a more ordered system. Accordingly, the ACFs heat-treated to 1500°C must have already departed from the regime of strong localization, because for strongly disordered systems, the more ordered the fibers, the less conductive they become [7.9,7.10] (see also Chapter 2). By the same token, we would expect ACFs with a higher SSA to be more conductive if they were strongly localized systems. This is because the high porosity and huge SSA of ACFs increase the density of localization sites by increasing the density of dangling bonds and defects in the system. This is, however, not the case in Fig. 7-1, in which the heat-treated ACP10 fibers are more conductive than the ACP20 fibers. Hence, we have evidence from the $\sigma(T)$ measurements that heat treatment of ACFs to sufficiently high T_{HT} destroys strong localization. Furthermore, it seems that the less disordered fibers are more graphitizable because ACFs with a smaller SSA tend to have a higher conductivity after heat treatment at the same T_{HT} as was used for heat-treating the more disordered fibers.

Previous magnetoresistance (MR) measurements show that the as-prepared ACP10 fibers exhibit a large positive MR [7.3]. In Fig. 7-2, we observe negative (transverse) MR in the heat-treated ACFs ($T_{\mathrm{HT}} \geq 1500$°C), with the magnetic field (B) perpendicular to the fiber axis (I_z), i.e., the magnetic field is perpendicular to the current direction. This negative MR is not due to the quantum interference effect predicted by Nguen *et al.* [7.14] and Sivan *et al.* [7.15] in a variable-range-hopping system because for less disordered systems (higher T_{HT} in ACFs), they predicted a positive MR, which was not observed. Furthermore, our discussion above regarding Fig. 7-1 also indicates that these well heat-treated ACFs have already departed from the strong localization regime. Negative MR can also be observed in a weakly disordered system due to weak localization. The sign of the MR as a function of T_{HT} thus provides a sensitive indicator for the electronic transition, which takes place before T_{HT} reaches 1500°C. It is also noteworthy that the magnitude of the negative MR is more sensitive to T_{HT} than to SSA.

The inset to Fig. 7-2 shows both the transverse ($B \perp I_z$) and the longitudinal ($B \parallel I_z$) magnetoresistance for the heat-treated ACP10 fibers, where I_z again denotes the current in

the direction along the fiber axis. Both curves have the same sign, but a small anisotropy is observed in the field dependence of the MR. As will be discussed later, the positive MR, observed in the FRL fibers with low T_{HT} values, shows isotropic behavior as the B field direction is changed with respect to the current direction. Therefore, the anisotropy observed in the MR indicates that a quasi-two-dimensional system is being developed through the heat treatment process. From the above evidence, we conclude that an electronic transition has occurred for T_{HT} lower than 1500°C. The development of a layered structure also indicates that the shape of the micropores might become elongated, with the long axis preferentially oriented along the fiber axis.

We then carried out both $\sigma(T)$ and MR measurements on phenol-based FRL10 fibers, heat-treated to a series of T_{HT} values. Both $\sigma(T)$ and MR measurements were made on FRL10 samples with the same T_{HT} values. Before heat treatment, ACP and FRL fibers both exhibit a sharp drop in their electrical conductivity $\sigma(T)$ at low temperature, characteristic of a strongly disordered system, in which hopping conduction of some kind is typically at work. After heat treatment to the same T_{HT} values, the $\sigma(T)$ and the MR results for the two types of ACFs look very similar in terms of both the magnitude and the functional form. Hence, heat treatment has rendered the transport properties of the ACFs almost independent of their precursors. The main effect of heat treatment on the ACFs from each precursor is to induce planar alignment in the preferred direction along the fiber axis.

We therefore heat-treated the FRL10 fibers, which were in abundant supply for us, to temperatures between $300°C < T_{HT} < 2500°C$ with a view of studying more closely the MI transition in this disordered carbon system. For convenience, FRL10 fibers heat-treated at xx00°C will be labelled HTxx00 hereafter. In Fig. 7-3, we show the temperature-dependent conductivities of FRL fibers heat-treated at different T_{HT} values. It is worth noting that the y-axis of this figure is on a logarithmic scale, indicating an increase in the absolute value of the room-temperature conductivity by two orders of magnitude after heat treatment above $T_{HT} = 1500°C$. Also shown are the gradual disappearance of the sharp drop in the conductivity at low temperature and the emergence of a finite zero-temperature conductivity value as T_{HT} is increased above 1000°C. These drastic changes in $\sigma(T)$ are consistent with the $\sigma(T)$ measurements of the heat-treated ACP fibers. The conductivity value at which the MI transition takes place is approximately 100 S/cm at room temperature, consistent with that of Mott's minimum metallic conductivity. This σ value lies in the low end of the range

of conductivity values (100-2000 S/cm) over which the conductivity of heat-treated graphite fibers is observed to be nearly independent of temperature [7.16]. Therefore, heat-treated ACFs are indeed a poor metal. To separate the closely-spaced $\sigma(T)$ curves for ACFs with $T_{\rm HT} \geq 1500°$C in Fig. 7-3, these $\sigma(T)$ curves are magnified in Fig. 7-4 for later discussions.

The MR data obtained for the FRL activated carbon fibers heat-treated to different $T_{\rm HT}$ values are plotted in Fig. 7-5. The solid lines in the same figure are a least-square fit to the data in terms of a quadratic magnetic field dependence. In Fig. 7-5, we observe that as $T_{\rm HT}$ increases starting from 300°C, the positive MR gradually decreases in magnitude and eventually the magnetoresistance changes its sign between the curves for $T_{\rm HT} = 1200°$C and 1500°C, providing further evidence that heat treatment is destroying strong localization. If we identify the change of sign of the MR with $T_{\rm MI}$, then the observed value for $T_{\rm MI}$ is roughly consistent with that obtained from the $\sigma(T)$ study of the same fibers. The positive MR in the more disordered heat-treated fibers verifies that for ACFs, positive MR occurs irrespective of their precursors and most likely is a consequence of the strong localization nature of the as-prepared ACFs.

Although not shown, the magnitude of the positive MR $[[\rho(B) - \rho(0)]/\rho(0)]$ does not depend on the magnetic field direction with respect to the fiber axis, but the negative MR of the well heat-treated ($T_{\rm HT} = 2500°$C) FRL fibers does, in a manner similar to that found in Fig. 7-2 (inset). Hence, the anisotropy again shows the development of a somewhat 2-dimensional structure in the material as a result of the heat-treatment-induced reorientation and stacking up of basic structural units. This microstructure shows order on a short-range length scale but is random on a long-range length scale.

7.3 Discussion

Shown in Fig. 7-6 are plots of the conductivity ratio $\sigma(300\text{K})/\sigma(4.2\text{K})$ and the quadratic coefficient (A) for the positive magnetoresistance (MR $= AB^2$) at 4.2 K versus $T_{\rm HT}$, respectively. The drastic decrease of $\sigma(300\text{K})/\sigma(4.2\text{K})$ and the sign change of the magnetoresistance indicate that the MI transition temperature falls between 1000°C and 1400°C, in reasonably good agreement with the previous photoconductivity study of the FRL ACFs by Kuriyama and Dresselhaus [7.1,7.2]. Although the photoconductivity results suggested that the transition temperature $T_{\rm MI}$ was near 1000°C, it is noted that while the conductivity

probes the carrier concentration and the mobility, the photoconductivity gives information about the density of trap states and the carrier mobility. We therefore conclude that $T_{\rm MI}$ is in the 1000°C–1400°C range.

Our $T_{\rm MI}$ value is clearly below that of 2000°C required for the development of long range in-plane order [7.4,7.5]. The dominant change found by the structural study for the 1000°C–1400°C range of $T_{\rm HT}$ is the growth of independent, distorted and approximately parallel columns of platelets along the c-axis due to the collapse of the interplanar micropores [7.4, 7.5]. We therefore attribute the MI transition to the following mechanism. The formation of these parallel columns naturally limits the angle of platelet inclination from one column to the next, thus allowing a roughly 2-dimensional plane to form with wrinkles and gaps on an atomic scale at the boundaries between neighbouring columns. The in-plane carrier band transport (σ_B) should be close to that in a 2-dimensional plane, except for some low-energy hops (σ_h) across those wrinkled edges and single-vacancy gaps. These two transport processes should take place in parallel (in-plane conductivity $\sigma_a = \sigma_B + \sigma_h$) for $T_{\rm MI} < T_{\rm HT} < 2000$°C (the high temperature limit being the onset for platelet fusion and planar dewrinkling), since the zero-temperature conductivity values [$\sigma(0) = \sigma_B$] appear to be non-zero for $T_{\rm HT} \geq T_{\rm MI}$, signifying that a classical percolative network might have already formed when the distortion of the neighbouring columns allows some layers of each column to come into close contact. The inclusion of the σ_h term should account for the negative temperature coefficient of the resistivity observed. We do not consider interplanar hopping transport within an individual column to be important, not only because the in-plane nearest-neighbour hopping distance is much shorter, being 1-2 atomic vacancies wide, than the average interplanar distance (> 3.5 Å) found by x-ray diffraction study [7.5], but also because of the slight anisotropy demonstrated in the negative magnetoresistance measurements. The anisotropy is, however, not very pronounced for $T_{\rm HT} < 2000$°C probably because the platelets are only locally but not globally aligned. When $T_{\rm HT}$ reaches 2000°C and higher, the graphene planes are stretched and the fused platelets now become aligned on a much larger spatial scale. At the same time, the boundary defects are annealed, thereby eliminating the hopping conductivity σ_h term while enhancing σ_B as the mean free path of charge carriers is increased. However, it is noted that σ_a never reaches the conductivity value for crystalline graphite because of the residual amount of defects.

The identification of this transition temperature dictates that our numerical analysis on

the $\sigma(T)$ dependence of the various heat-treated ACFs, as plotted in Fig. 7-3, should use two different models depending on whether $T_{\rm HT}$ is above or below $T_{\rm MI}$. For $T_{\rm HT} < T_{\rm MI}$, $\sigma(0) = 0$, suggesting that the ACFs are in the strong localization regime and their $\sigma(T)$ should follow that of Mott's law [7.17, 7.18]:

$$\sigma(T) = \sigma_0 \exp\left[-\left(\frac{T_0}{T}\right)^{1/p}\right] \quad . \tag{7.1}$$

The expressions for p and T_0 vary according to different models. For d-dimensional variable-range hopping conduction (d-D VRH), $p = d + 1$ and

$$T_0 = \frac{C}{k_B(\xi^d g(\mu))^{1/(d+1)}} \tag{7.2}$$

where $g(\mu)$ is the density of states near the Fermi level (μ), ξ is the localization length, and $C = 4.0, 13.8, 21.2$ for $d = 1, 2, 3$, respectively. For Coulomb-gap VRH [7.18],

$$T_0 = \frac{\beta e^2}{k_B \kappa \xi} \tag{7.3}$$

where κ is the dielectric constant in the medium, and $\beta = 2.8$ in 3D and 6.2 in 2D, respectively, as has been shown in Chapter 4.

To extract the power p in Mott's law [Eq. (7.1)], we therefore plotted the logarithm of $\sigma(T)$ for ACFs heat-treated at $T_{\rm HT} \leq 1000°$C against powers of the reciprocal temperature $1/T$. We found that the $1/T^{1/2}$ plot yields the most linear dependence for all these heat-treated ACFs over the widest range of temperature (e.g., up to 100 K), as shown in Fig. 7-7, thus suggesting that the granular metallic conduction mechanism, thought to be at work in the non-heat-treated ACFs in Chapter 4, is also dominant in ACFs heat-treated at $T_{\rm HT} < 1000°$C. To obtain a more quantitative value for p, we have also plotted and then fit the logarithm of the derivative $d[\log \sigma(T)]/d(1/T)$ against $\log T$. The procedure yielded $p \simeq 2$ for all the disordered ACFs considered, as shown in Table 7.1. We only extended the linear fitting procedure to $\sim$ 100 K for the $T_{\rm HT} = 850°$C and 1000°C conductivity curves because non-linearity sets in at approximately this measurement temperature.

The non-linear least-square fits over the entire range of measurement temperatures (from 4 K to 300 K) gave $p = 3$ rather than $p = 2$ for $T_{\rm HT}$ as low as 300°C. However, when only the low temperature range (e.g., $T < 100$ K), where hopping takes place, was chosen for

T_{HT} (°C)	0	300	700	850	1000
p	1.8	2.2	2.2	1.9	2.1

Table 7.1: Values of the parameter p extracted from a linear fit to a log-log plot of $d[\log \sigma(T)]/d(1/T)$ against temperature for ACFs heat-treated below 1000°C.

T_{HT} (°C)	0	300	700	850	1000
p	2	2	2	2	2
$\sigma(T=0)$ (S/cm)	0	0	0	0	4.4
σ_0 (S/cm)	35	49	67	66	89
T_0 (K)	529	778	552	92	29
p	3	3	3	3	3
$\sigma(T=0)$ (S/cm)	0	0	0	0	5.3
σ_0 (S/cm)	96	230	240	140	150
T_0 (K)	3650	8000	4740	473	121

Table 7.2: Values for the fitting parameters obtained from the fit of $\sigma(T)$ data (see text) to $p = 2$ and $p = 3$.

the fitting, we obtained $p \simeq 2$, consistent with Fig. 7-7. We notice that the $p = 2$ fitting curve (not shown) is always below the real data near room temperature and we believe that this $\sigma(T)$ overshoot may be due to the thermal generation of carriers or the transition from VRH to nearest-neighbour hopping behavior. In contrast, the slow-rising $p = 3$ fitting curve can fit this high-temperature portion of the data well but fails to match the data at very low temperature (e.g., $T < 30$ K). The values for the non-linear least-square fitting parameters for both the $p = 2$ and $p = 3$ fits are listed in Table 7.2. The fitting parameters for the $p = 2$ fits are in good agreement with the values obtained from the linear fits to the $1/T^{1/2}$ plots in Fig. 7-7, even though an additional $\sigma(T = 0)$ term is added to Eq. (7.1) in all nonlinear fits.

When $p = 2$, several different models for conduction are possible, including one-dimensional VRH [7.19] , Coulomb-gap VRH (CGVRH) [7.18] and charge-energy-limited tunneling conduction (CELTC) [7.20]. As was discussed in Chapter 4, the Coulomb-gap VRH model is favoured since there are shortcomings with the other models. In Chapter 4, we have also seen how the 3D and 2D CGVRH model can be used to explain the conductivity behavior for the as-prepared ACF and the ACF heat-treated to 850°C, respectively. Now, the observation of the universal agreement with the $p = 2$ Mott's law among all the

heat-treated ACFs with $T_{HT} < T_{MI}$ justifies our previous treatment of as-prepared and heat-treated ACFs on the same footing, despite a variation in the correlation distance with heat treatment and consequently, a change in the dimensionality for transport.

The T_0 values obtained from the $p = 2$ fit are on the same order as those found in Ref. [7.10], except for the ACFs heat-treated at $T_{HT} \geq 850°C$, probably because of the overlap effect which would induce a multiplying factor of 0.2 in Eq. (7.3) [7.18]. Since the zero-temperature conductivity is finite for the HT1000 fibers, a percolating network might have already been forming in some regions of the sample, indicating that the CGVRH model might not be applicable to HT1000 fibers. The peak in T_0 for the HT300 fibers (see Table 7.2) is consistent with the peak in the ratio $\sigma(300K)/\sigma(4.2K)$ plotted in Fig. 7-6 and with the higher σ values over the temperature range $T < 100$ K observed in Fig. 7-3 for the same HT300 fibers compared to the as-prepared ACFs. The origin of the peak in Fig. 7-6 might be related to the release of heteroatoms at $T_{HT} < 450°C$, which produces a large number of dangling bonds in the system according to a previous electron spin resonance study [7.21]. These dangling bonds should increase the occupation number of the hole carriers within each platelet, effectively raising the tunneling barrier because of both the increased hole-hole Coulombic repulsion over the intervening platelets and the exclusion of a many-hole state on the destination platelet for a single hop.

In Fig. 7-5, the positive MR for the strongly disordered systems can be due to: (1) wavefunction shrinkage effects reducing wavefunction overlap [7.18] or (2) spin effects prohibiting certain charge transfer processes [7.22]. Both models predict a quadratic field dependence at low fields, as shown by the solid lines in Fig. 7-5. A detailed study of the MR as a function of temperature, as has been done in Chapter 4 for the ACF heat-treated at 850°C, verifies that the wavefunction shrinkage theory should apply, at least in low fields, to both as-prepared and heat-treated ACF systems.

The negative MR in the HT2000 and the HT2500 ACFs is not due to the orbital effect in the strong localization regime because no $\sigma(T)$ of the form of Eq. (7.1) is observed. The negative MR for these samples is probably due to the weak localization of charge carriers in a roughly 2-dimensional system with long-range order development induced by heat treatment. A quadratic field dependence, consistent with the weak localization theory at low fields, is also observed (see Figs. 7-2 and 7-5). For HT2500 ACFs, the quadratic fit was only extended to 0.45 T because at 4 K, the transition to the high-field regime has

already caused some deviation from the parabolic field dependence. A comparison with the negative MR curves for the S20T25 and S20T15 pitch-based ACFs in Fig. 7-2 shows that the low-field quadratic coefficients, and the field values at which the transition to the high-field characteristics takes place, are both very similar in magnitude for all the ACFs with the same $T_{HT} = 2500°C$, irrespective of precursors and specific surface area, signifying that heat treatment has a much larger effect on the nanostructure of ACFs than do the precursor and the specific surface area, and is indeed a better tuning parameter than the others.

The $\sigma(T)$ curves for these metallic ACF samples (see Fig. 7-4), instead of showing any logarithmic temperature dependence as would have been predicted by the 2-dimensional weak localization theory, vary linearly with temperature at low temperature, suggesting the possibility of a more dominant conductivity term than the weak localization correction. In the next chapter, temperature scans are performed in both zero field and high fields to extract the weak localization correction to the conductivity.

References

[7.1] K. Kuriyama, M. S. Dresselhaus, and A. W. P. Fung, in *Extended Abstracts of the 20th Biennial Conference on Carbon, Santa Barbara, CA, 1991*, edited by R. A. Meyer (American Carbon Society, State College, PA), p. 300.

[7.2] K. Kuriyama and M. S. Dresselhaus, J. Mater. Res. **7**, 940 (1992).

[7.3] A. W. P. Fung, A. M. Rao, K. Kuriyama, M. S. Dresselhaus, G. Dresselhaus, and M. Endo, in *Extended Abstracts of the 20th Biennial Conference on Carbon, Santa Barbara, CA, 1991*, edited by R. A. Meyer (American Carbon Society, State College, PA), p. 296.

[7.4] A. M. Rao, A. W. P. Fung, M. S. Dresselhaus, G. Dresselhaus, and M. Endo, in *Extended Abstracts of the 20th Biennial Conference on Carbon, Santa Barbara, CA, 1991*, edited by R. A. Meyer (American Carbon Society, State College, PA), p. 242.

[7.5] A. M. Rao, A. W. P. Fung, M. S. Dresselhaus, and M. Endo, J. Mater. Res., **7**, 1788 (1992).

[7.6] M. Smíšek and S. Černý, *Active Carbon: Manufacture, Properties and Applications* (Elsevier, New York, 1967).

[7.7] R. C. Bansal, J.-B. Donnet, and F. Stoeckli, *Active Carbon* (Marcel Dekkar, New York, 1988).

[7.8] E. Tanaka, Fuel and Combustion **54**, 241 (1987).

[7.9] A. W. P. Fung, A. M. Rao, K. Kuriyama, M. S. Dresselhaus, and G. Dresselhaus. in *Defects in Materials*, edited by P. D. Bristowe, J. E. Epperson, J. E. Griffith, and Z. Liliental-Weber, MRS Symposia Proceedings, No. 209 (Materials Research Society, Pittsburgh, 1991), p. 335.

[7.10] A. W. P. Fung, A. M. Rao, K. Kuriyama, M. S. Dresselhaus, G. Dresselhaus, and M. Endo, J. Mater. Res. **8**, 489 (1993).

[7.11] S. L. di Vittorio, M. S. Dresselhaus, M. Endo, J. P. Issi, L. Piraux, and V. Bayot, J. Mater. Res. **6**, 778 (1991).

[7.12] S. Mrozowski, Phys. Rev. **85**, 609 (1952).

[7.13] R. R. Saxena and R. H. Bragg, J. Non-Cryst. Solids **28** 45 (1978).

[7.14] V. L. Nguen, B. Z. Spivak and B. I. Shklovskii, Sov. Phys. JETP **62**, 1021 (1985).

[7.15] U. Sivan, O. Entin-Wohlman, and Y. Imry, Phys. Rev. Lett. **60**, 1566 (1988).

[7.16] M. S. Dresselhaus, G. Dresselhaus, K. Sugihara, I. L. Spain, and H. A. Goldberg, *Graphite Fibers and Filaments* (Springer, Berlin, Heidelberg, 1988).

[7.17] N. F. Mott, *Conduction in Non-Crystalline Materials* (Oxford University Press, New York, 1987).

[7.18] B. I. Shklovskii and A. L. Efros, *Electronic Properties of Doped Semiconductors* (Springer, Berlin, Heidelberg, 1984).

[7.19] V. K. S. Shante, C. M. Varma, and A. N. Bloch, Phys. Rev. **B 8**, 4885 (1973).

[7.20] B. Abeles, P. Sheng, M. D. Coutts and Y. Arie, Adv. Phys. **24**, 407 (1975).

[7.21] S. L. di Vittorio, A. Nakayama, T. Enoki, M . S. Dresselhaus, M. Endo, and N. Shindo, J. Mater. Res. **8**, 2282 (1993).

[7.22] A. Kurobe and H. Kamimura, J. Phys. Soc. Japan **51**, 1904 (1982).

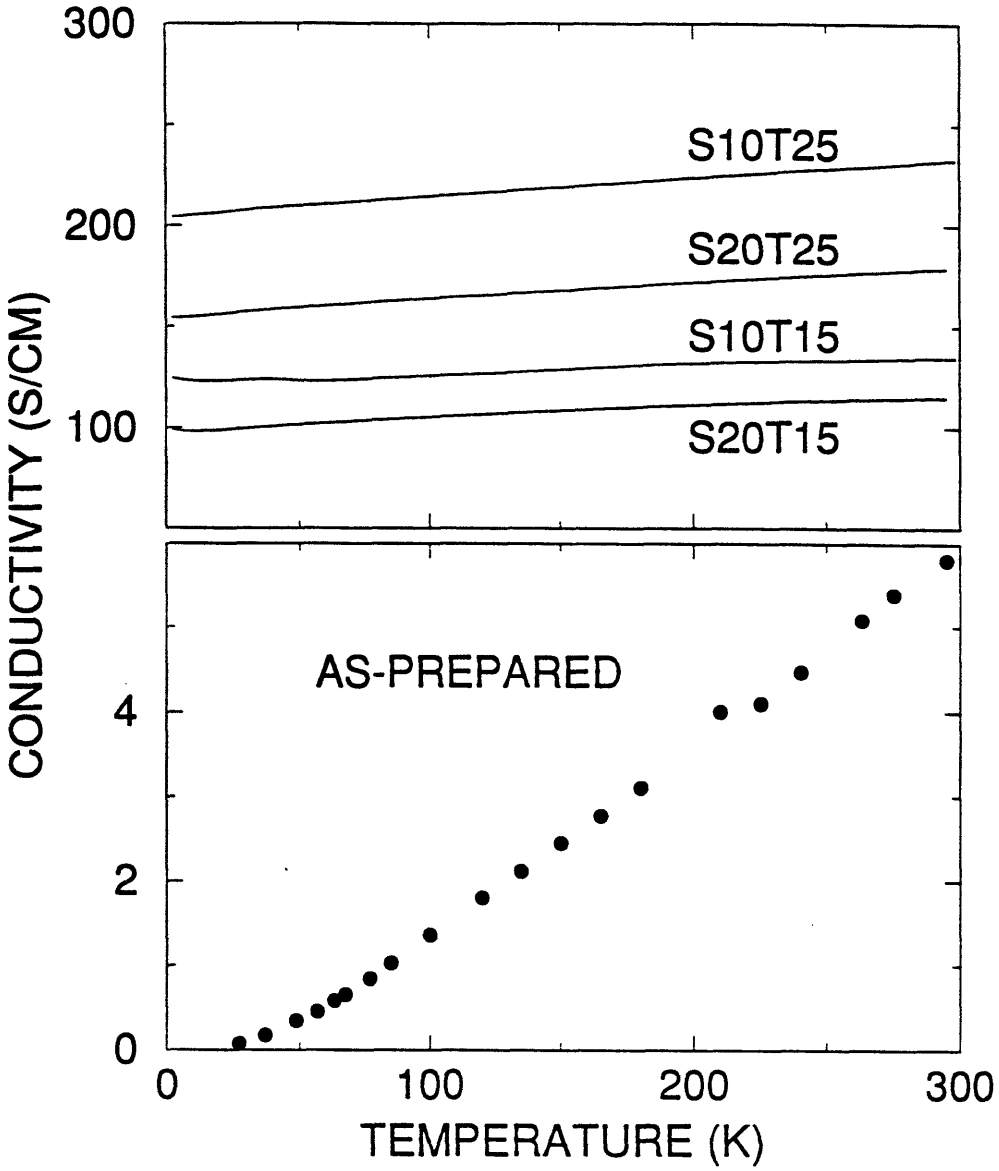

Figure 7-1: Temperature dependence of the conductivities $[\sigma(T)]$ of both the as-prepared pitch-based activated carbon fibers (ACFs) with a specific surface area of 1000 m^2/g (bottom figure) and the pitch-based ACFs heat-treated above 1500°C (top figure). ACFs labelled SxxTyy in the top figure have a specific surface area of xx00 m^2/g and are heat-treated at yy00°C. As prepared, $\sigma(T)$ of ACFs shows a strong temperature dependence. With heat treatment, the slope of $\sigma(T)$ becomes flat. The absolute values for the conductivity of the heat-treated ACFs are also much higher than those for the as-prepared ACFs.

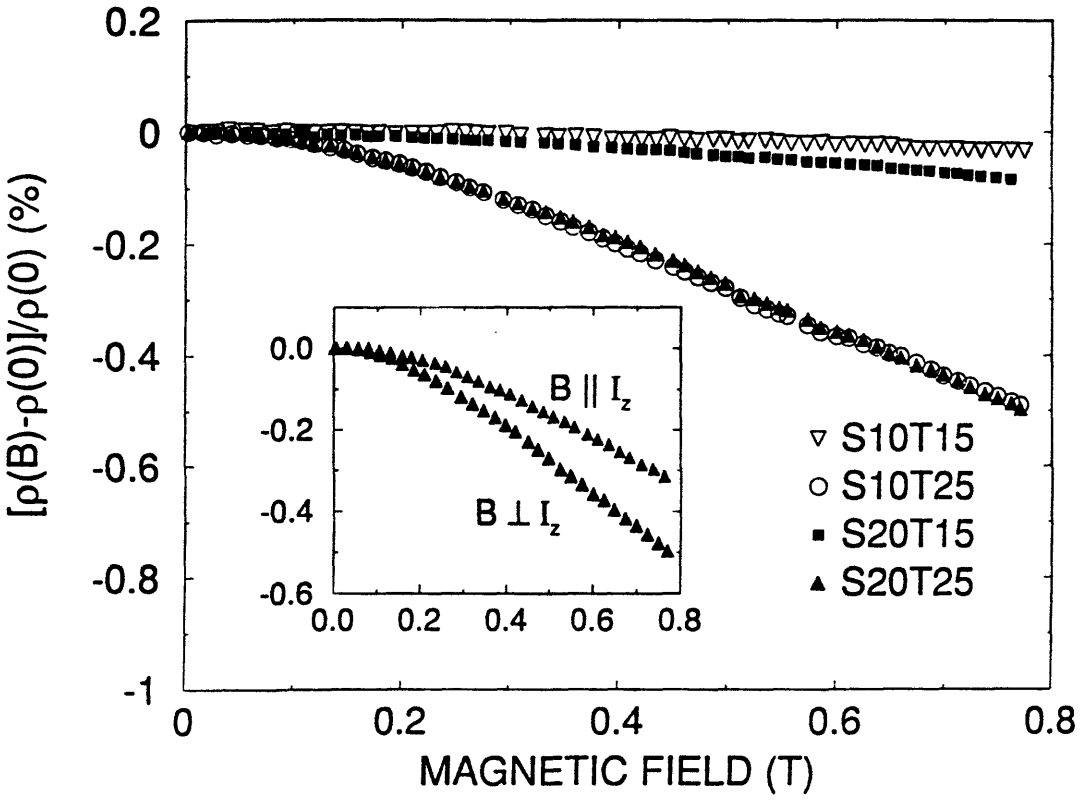

Figure 7-2: Transverse magnetoresistance of the ACFs labelled in the same way as in Fig. 7-1. It can be seen that ACFs heat-treated to a higher temperature exhibit a stronger magnetic-field dependence, irrespective of their specific surface area. Using the same set of axes, the inset shows the anisotropy in S20T25 ACFs as the magnetic field (B) direction is changed from perpendicular to parallel to the fiber axis. I_z denotes the current along the direction of the fiber axis.

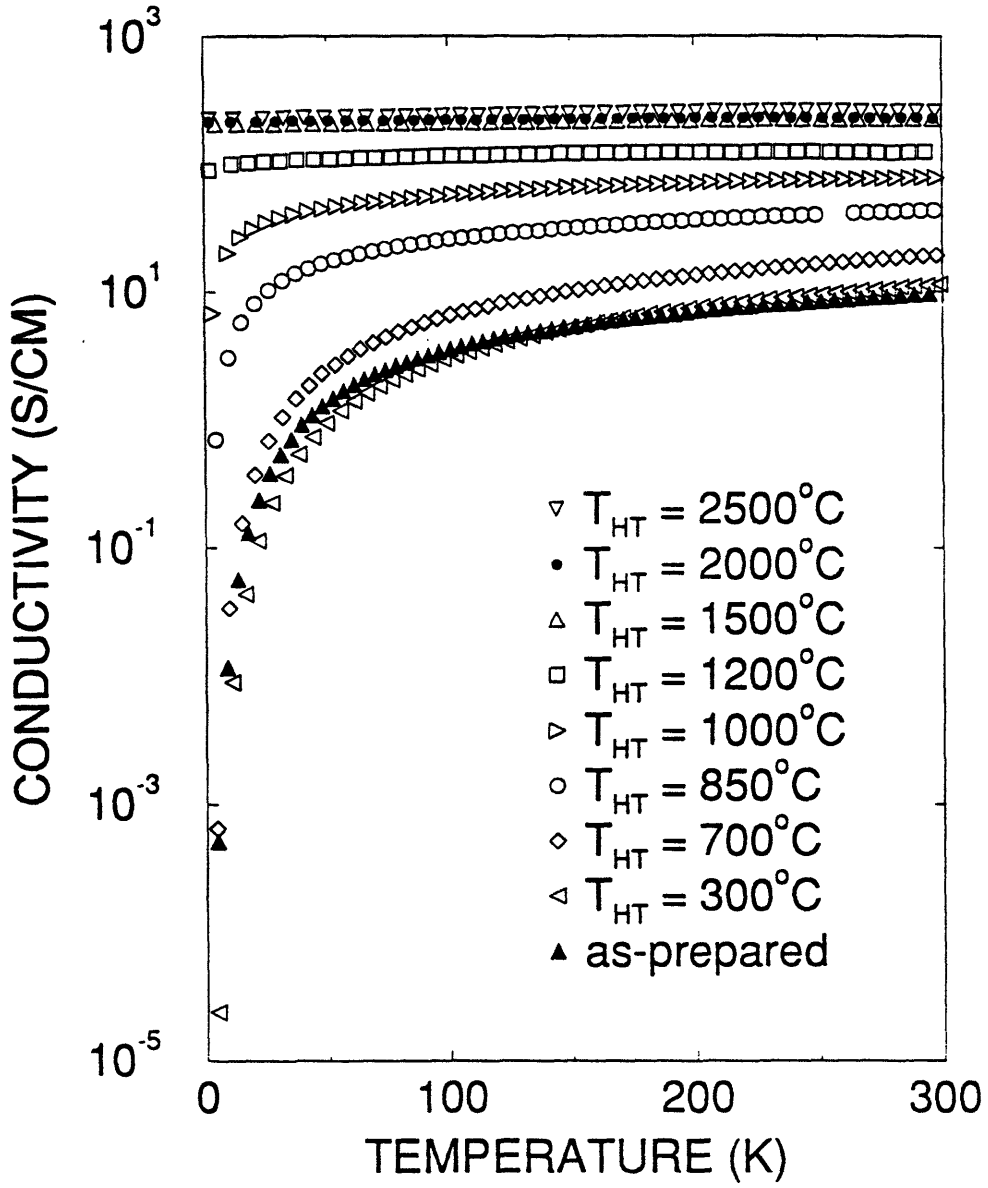

Figure 7-3: Temperature dependence of the conductivities $[\sigma(T)]$ of the phenol-based ACFs heat-treated in the range 300°C $< T_{HT} <$ 2500°C plotted on a semi-log scale. As T_{HT} is increased to $\sim$ 1200°C, the slope of $\sigma(T)$ for the heat-treated ACFs becomes relatively flat. The absolute value of σ for these heat-treated ACFs is more than 6 orders of magnitude greater than those for the as-prepared ACFs at 4.2 K. The points on the curves are only a sampling of the actual data points, which are spaced by only 0.2 K.

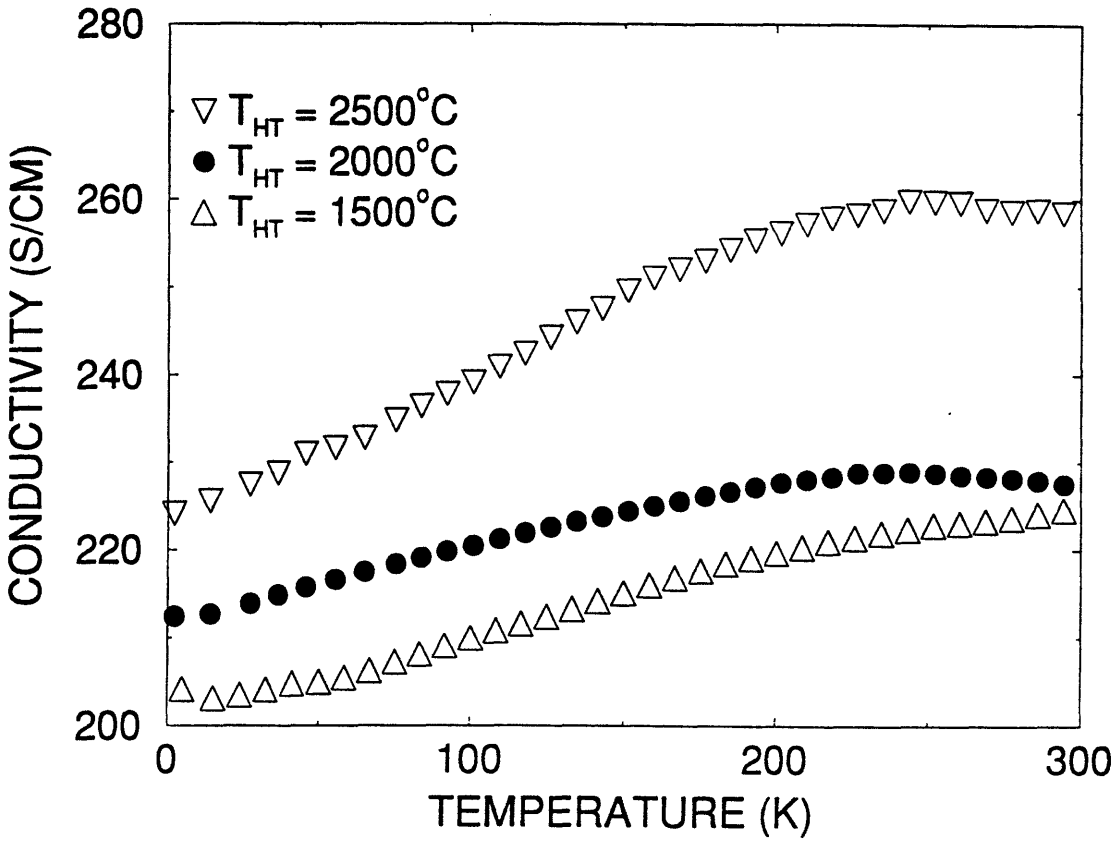

Figure 7-4: The same conductivity curves shown in Fig. 7-3 for the phenol-based ACFs heat-treated at 1500, 2000 and 2500°C, respectively, are plotted on a magnified linear scale to show the approximately linear temperature dependence of their low-temperature conductivities.

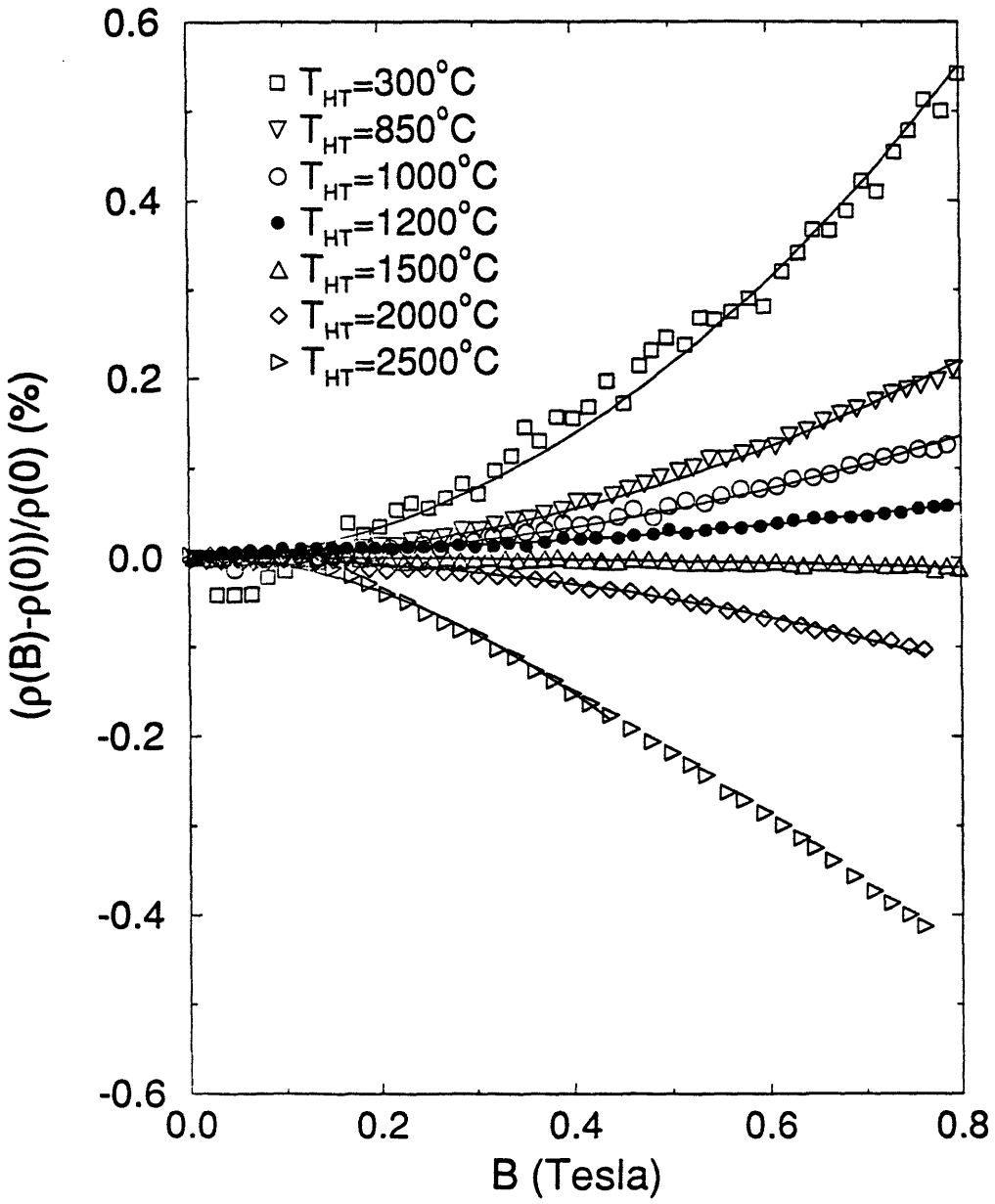

Figure 7-5: Transverse magnetoresistance of pitch-based ACFs heat-treated in the range 300°C $< T_{HT} <$ 2500°C. The sign change that occurs at $T_{HT} \sim$ 1500°C is indicative of the metal-insulator transition. The solid lines are the quadratic fits to the low-field data.

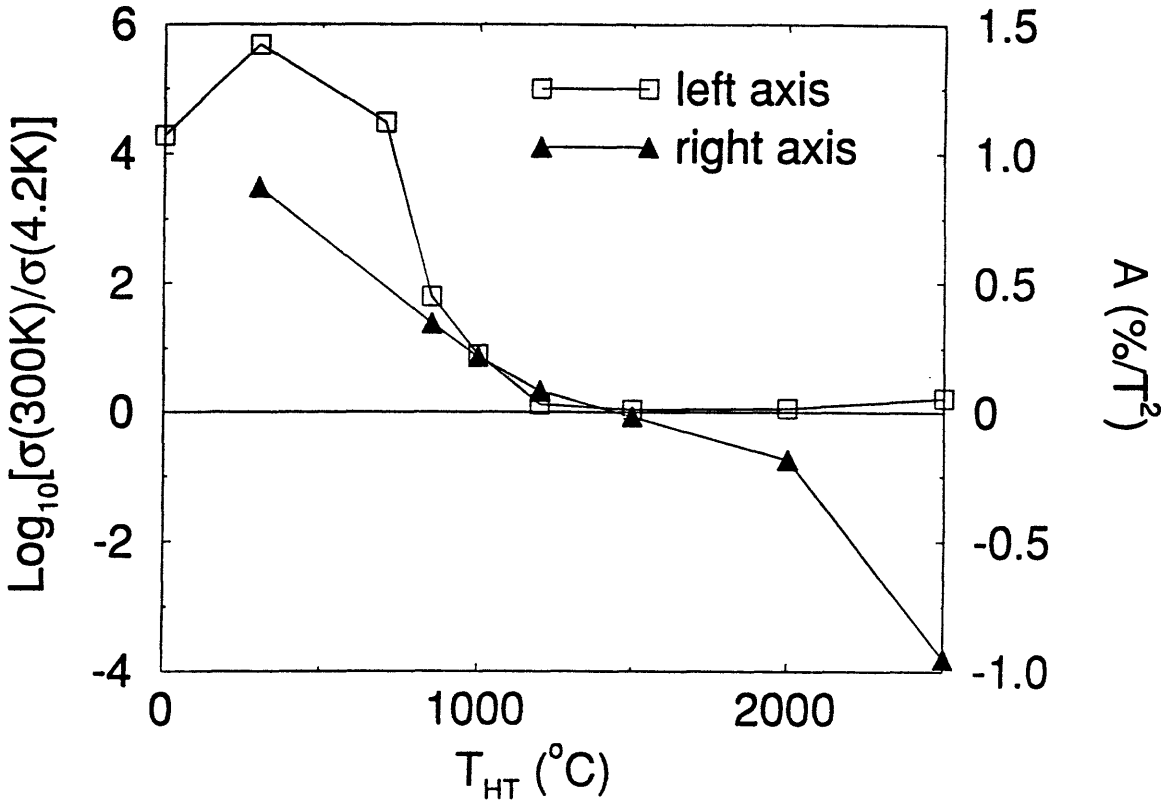

Figure 7-6: (a) Ratio of the conductivity at 300 K to that at 4.2 K and (b) quadratic coefficient A (see text) for the magnetoresistance at 4.2 K for ACFs heat-treated in the range 300°C < T_{HT} < 2500°C. These data suggest that the metal-insulator transition occurs between 1000°C and 1400°C.

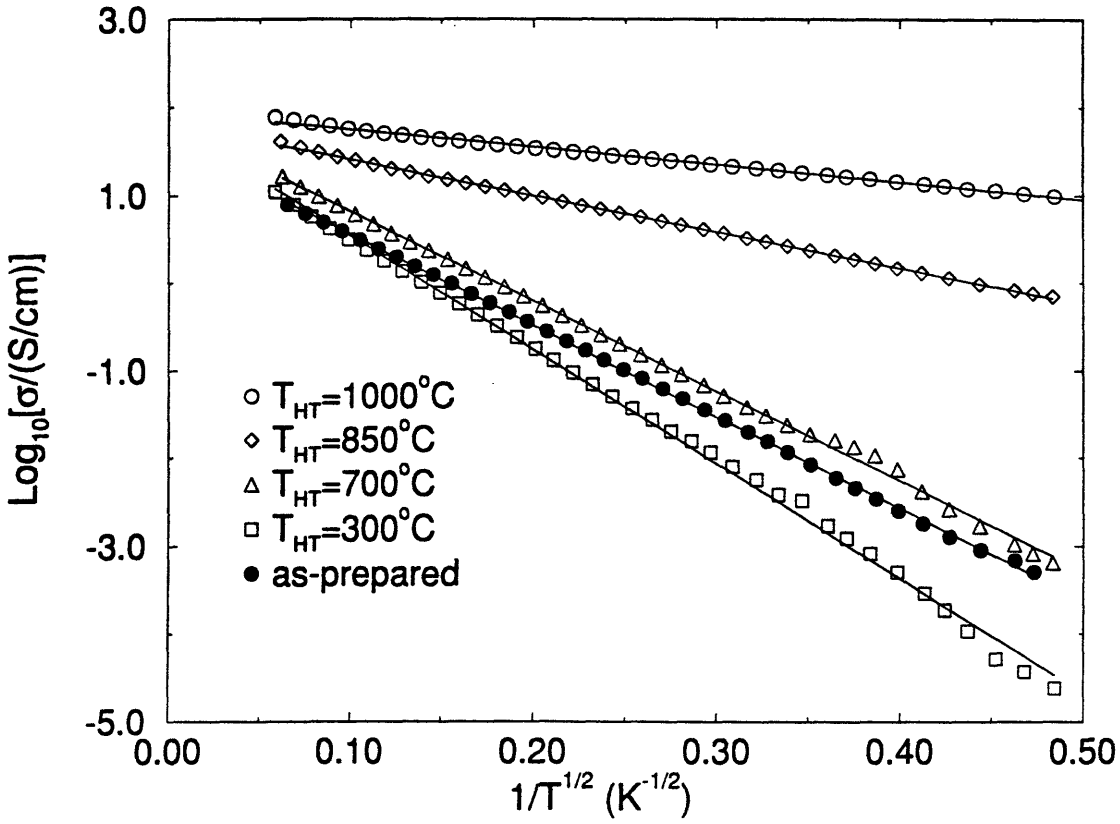

Figure 7-7: Logarithm of conductivity versus square root of the reciprocal temperature for ACFs heat-treated below 1000°C. The linearity of these data in the temperature range $T < 100$ K is characteristic of a granular metallic system. The solid lines are the linear fits to the data.

Chapter 8

Weak Localization and Anomalous Diffusion in Heat-Treated ACFs

Following the studies in the previous chapters on the transport properties of heat-treated ACFs approaching and crossing the metal-insulator (MI) transition from the insulator side, we now proceed to investigate the transport behavior in ACFs heat-treated at such high temperatures ($> 2000°C$) that they are on the metallic side of the MI transition.

ACFs are a nanoporous material and correspondingly a strongly localized system before heat treatment. Through heat treatment at progressively higher temperatures, extended planar structures begin to develop in ACFs, eventually allowing percolative transport to occur. Since the Raman scattering results presented in Chapter 6 indicate that the growth of the in-plane microcrystallite size L_a is only possible for T_{HT} above 2000°C [8.1], these ACFs are therefore heat-treated to 2000°C and above to further study the behavior of localization transport in the now percolating and weakly disordered system. Unlike carbon aerogels, the microstructural change in ACFs with respect to heat treatment is well understood and not complicated, as has been demonstrated in Chapter 6, thus permitting a more quantitative study to be made of weak localization in annealed porous carbon systems.

It was found, quite surprisingly, that for ACFs heat-treated to 2000°C and above, a negative magnetoresistance (MR) could be observed at measurement temperatures even as high as near room temperature, and that the MR curves for all measurement temperatures and all samples fit with excellent precision the conventional two-dimensional weak localization theory. Weak localization is a quantum-mechanical phenomemon that is usually not

observable in a homogeneous system at high temperatures where the phase coherence of the carriers is destroyed by inelastic scattering events. Being near the metal-insulator transition, our ACF system obeys the condition $k_F l \sim 1$, where l is the mean free path of the conduction carriers, making it possible for the dephasing distance L_ϕ to remain longer than l even at high temperatures. As discussed below, the weakened temperature dependence of L_ϕ due to the anomalous diffusion process in a percolating system is also believed to sustain the condition $L_\phi > l$ over a higher temperature range than for a homogeneous system.

The proximity to the percolation transition point is characterized by a correlation distance ξ_p. Above the percolation threshold, ξ_p is defined as the length scale beyond which the percolation network looks uniform (the *homogeneous* limit), and below which the system exhibits self-similarity (the *inhomogeneous limit*). We propose, following Aronov *et al.* [8.2], that the transport behavior could also be significantly different in these two regimes. In the inhomogeneous limit, where $L_\phi \ll \xi_p$, anomalous diffusion should set in, effectively causing L_ϕ to have a weaker temperature dependence than in the homogeneous limit ($L_\phi \gg \xi_p$), and consequently preserving part of the quantum coherence of the carriers which would otherwise be destroyed by inelastic events at high temperatures.

In the following, we first review the concept of anomalous diffusion and the existing theories on combining anomalous diffusion with weak localization. The theoretical work of Aronov *et al.* [8.2] is subsequently extended to the 2D case with some slight modifications and approximations. We then present our experimental results for the temperature dependence of the conductivity and for the dependence of the magnetoresistance on temperature and magnetic field for ACFs with $T_{\mathrm{HT}} = 2000°\mathrm{C}$ and $2500°\mathrm{C}$, emphasizing the anomalous behavior that is observed. It is shown that the inclusion of the concept of anomalous diffusion in weak localization theories does not affect the functional forms of the conductivity or the MR due to weak localization, but it is essential to the interpretation of the anomalous temperature dependence of the inelastic scattering time in ACFs as well as other inhomogeneous systems near the percolation threshold.

8.1 Experimental Details

The ACFs studied in this work are made from phenol (FRL) precursors. The manufacturing procedure for the synthesis of the as-prepared phenol-based ACFs (supplied by

Kuraray Chemical Co. in Japan) is described in Chapter 2. The SSA as determined by BET measurements is $1000\,\mathrm{m}^2/\mathrm{g}$ prior to heat treatment. Subsequent heat treatments were carried out in an Ar atmosphere at specified temperatures of 2000°C and higher for 1 hour. Each ACF is labelled by HTxx00 with the numerals xx00 indicating the heat-treatment temperature.

As before, all transport measurements were made on a single ACF using the 4-point method with silver paint contacts. The temperature scans from 4.2 K to 300 K were allowed to take place by natural warming. The transverse magnetoresistance was measured in a field up to 15 T at several measurement temperatures up to almost room temperature at the Francis Bitter National Magnet Laboratory at MIT. The diameter of the ACFs ($\sim 10\,\mu$m on the average) was measured by Scanning Electron Microscopy (SEM) and the length by an optical microscope.

8.2 Theory

In heat-treated ACFs, two-dimensional structures are evidenced by TEM and Raman scattering results. We therefore only concentrate on the 2D version of the theories in this section. All theoretical expressions for the conductivity σ are given in their 2D versions while the experimental σ values are presented in the next section in their bulk values [i.e., σ = length/(resistance)(cross-sectional area of fiber)]. The conversion from $\sigma_{expt.}$ to $\sigma_{theo.}$ is thus likely to incur an error due to the uncertainties in determining either the thickness of the 2D film on which transport takes place or the real cross-sectional area of the percolation path.

The weak localization (WL) theory in a homogeneous system is well established. The temperature-dependent conductivity correction $\Delta\sigma(T)$ due to two-dimensional WL is given by [8.3, 8.4]:

$$\Delta\sigma(T) = -\frac{e^2}{\pi^2\hbar}\ln\left(\frac{L_\phi}{l}\right) \tag{8.1}$$

$$= -\frac{e^2}{2\pi^2\hbar}\ln\left(\frac{\tau_\phi}{\tau}\right) \tag{8.2}$$

$$= p\frac{e^2}{2\pi^2\hbar}\ln\left(\frac{T}{T_0}\right) \tag{8.3}$$

where l is the mean free path, τ the elastic scattering time, $\tau_\phi = L_\phi^2/D$ the dephasing time

and D the diffusion constant of the carrier. The $\ln(T)$ temperature dependence of $\Delta\sigma$ can be seen by noting that τ_ϕ could be the inelastic scattering time τ_i, which is proportional to T^{-p} for some power of p depending on the inelastic scattering mechanism. However, τ_ϕ is not in general equivalent to the inelastic scattering time τ_i, as discussed later.

The magnetoresistance in 2D in a homogeneous system is given by [8.3, 8.4]:

$$\frac{\Delta\rho}{\rho} \equiv \frac{\rho(H)-\rho(0)}{\rho(0)} = -\lambda\frac{\rho(0)}{L_c}\frac{e^2}{2\pi^2\hbar}\left[\Psi\left(\frac{1}{2}+\frac{H_\phi}{H\cos(\Theta)}\right)-\ln\left(\frac{H_\phi}{H\cos(\Theta)}\right)\right] \tag{8.4}$$

where ρ is the measured resistivity of the sample, Ψ the digamma function, and L_c is the thickess of the 2D system, assumed to be one graphitic layer thick. The inhomogeneity factor $0 < \lambda \leq 1$ accounts for: (i) the use of an over-estimate of the cross-sectional area in the calculation of ρ; and (ii) a possible underestimate of the number of graphitic layers constituting the 2D system. Since even the few radicals that exhibit paramagnetic properties should already have been removed from the ACFs upon heat treatment, and since carbon has a low atomic mass, magnetic scattering and spin-orbit scattering are insigificant in ACFs. Hence, only inelastic scattering is considered in Eq. (8.4), resulting in only one characteristic field, $H_\phi = \hbar c/4eD\tau_\phi$. The effect of the angle Θ that the magnetic field makes with the c-axis of the 2D plane is considered later.

In an inhomogeneous system near the percolation threshold p_c, where the length scale is larger than the correlation distance (ξ_p) (i.e., the homogeneous limit), the correlation distance ξ_p, the conductivity σ, and the strength of the infinite cluster P (the probability of a site being connected to the infinite cluster) scale as:

$$\begin{aligned}
\xi_p &\sim |p-p_c|^{-\nu} \\
\sigma_0 &\sim (p-p_c)^t \sim \xi_p^{-\tilde{t}} \qquad (\tilde{t} \equiv t/\nu) \\
P_0 &\sim (p-p_c)^\beta \sim \xi_p^{-\tilde{\beta}} \qquad (\tilde{\beta} \equiv \beta/\nu)
\end{aligned} \tag{8.5}$$

where the ξ_p dependences in the second and the third lines hold only in the homogeneous limit, as indicated by the subscripts on both σ_0 and P_0. It is understood that even in the "homogeneous" limit, so named only because of the morphological uniformity in the system, the transport properties (such as σ_0 and the diffusion constant) in an inhomogeneous system could still be different from those in a homogeneous system, according to Eq. (8.5).

In the inhomogeneous limit, where the transport length scale is shorter than the correla-

tion distance (ξ_p), the squared diffusion distance $\langle R(t)^2 \rangle$ of a random walk no longer scales as t, implying that the diffusion constant D becomes spatially dispersive [8.5]. The spatial dependence of D can still be found by using the Einstein relation $D = \sigma/e^2N$ and noting that the effective density of states (DOS) N is now a fraction P of the DOS in a homogeneous metal because only those electrons belonging to the infinite cluster are involved in conduction. On a length scale $\mathcal{L} \ll \xi_p$, P is only $(\mathcal{L}/\xi_p)^{-\tilde{\beta}}$ of its value in the homogeneous limit ($\mathcal{L} \gg \xi_p$), so that

$$N(\mathcal{L}) \sim N_0 \begin{cases} 1 & \mathcal{L} \gg \xi_p \\ \left(\frac{\xi_p}{\mathcal{L}}\right)^{\tilde{\beta}} & \mathcal{L} \ll \xi_p \end{cases} \tag{8.6}$$

where N_0 is the effective DOS in the homogeneous limit. The scaling relation for $\sigma(\mathcal{L})$ can be similarly written with the critical exponent $\tilde{t}$, and then used with Eq. (8.6) to deduce the following relation for the diffusion constant:

$$D(\mathcal{L}) \sim D_0 \begin{cases} 1 & \mathcal{L} \gg \xi_p \\ \left(\frac{\xi_p}{\mathcal{L}}\right)^{\tilde{t}-\tilde{\beta}} & \mathcal{L} \ll \xi_p \end{cases} \tag{8.7}$$

where D_0 is the diffusion constant in the homogeneous limit. Solving $D(\mathcal{L}_\phi)\,\tau_i = \mathcal{L}_\phi^2$ to obtain the τ_i dependence of $\mathcal{L}_\phi$ in Eq. (8.7) for $\mathcal{L} \ll \xi_p$ results in:

$$\mathcal{L}_\phi = [D_0 \tau_i \xi_p^{\tilde{t}-\tilde{\beta}}]^{1/(2+\tilde{t}-\tilde{\beta})} \tag{8.8}$$

$$\sim T^{-p/(2+\tilde{t}-\tilde{\beta})} \sim T^{-0.35p} \qquad \text{(in 2D)} \tag{8.9}$$

where the values $\tilde{t} \simeq 1$ and $\tilde{\beta} \simeq 0.13$ for a 2D system are well documented [8.6], and τ_i is understood to have a T^{-p} temperature dependence, with p dependent on the nature as well as the dimensionality of the inelastic scattering event. The label for the dephasing length has been changed from L_ϕ to $\mathcal{L}_\phi$ to reflect its value in the inhomogeneous limit. As a result of the anomalous diffusion process, the temperature dependence of $\mathcal{L}_\phi$ is reduced from $T^{-0.5p}$ to $T^{-0.35p}$, thereby making it possible to observe a negative MR to much higher temperatures (even to near room temperature for ACFs) because the phase coherence of the carriers is now preserved to higher temperatures.

WL theories that include the effect of the spatial dispersion of D have been developed by Khmelnitskii [8.7] and Aronov *et al.* [8.2]. The approaches in these two papers are essentially the same, in that when the Cooper poles are summed in q-space, the diffusion

constant assumes a q-dependence in the integral, according to Eq. (8.7). Aronov *et al.* calculated the conductivity correction as follows:

$$\frac{\Delta\sigma}{\sigma} = -\frac{2}{\pi\hbar}\int_0^{1/\mathcal{L}_\phi} \frac{d\vec{q}}{N(q)[D(q)q^2 + 1/\tau_i]} \tag{8.10}$$

where $D(q) = D_0(\xi_p\, q)^{\tilde{t}-\tilde{\beta}}$ is the diffusion constant in the percolation limit, and $N(q) = N_0(\xi_p\, q)^{\tilde{\beta}}$ is the effective DOS now limited by the strength of the infinite cluster. They found, for $\Delta\sigma/\sigma$ in 3D, an expression which is different from the conclusion of Khmelnitskii because of the latter's neglect of the critical exponent in the DOS, namely β. The following development in this chapter will therefore reflect the more detailed treatment by Aronov *et al.* [8.2]

Since $\sigma(\mathcal{L}) = e^2 D(\mathcal{L}N(\mathcal{L})$ has a spatial dispersion itself on a length scale $\mathcal{L} \ll \xi_p$, Eq. (8.10) is incorrect. Strictly speaking, the Kubo formalism calculates $\Delta\sigma$ and not $\Delta\sigma/\sigma$ [8.4]. We therefore calculate $\Delta\sigma(\mathcal{L}_\phi)$ using:

$$\Delta\sigma(\mathcal{L}_\phi) = -\frac{2e^2}{\pi\hbar}\int_0^{1/\mathcal{L}_\phi} \frac{D(q)d\vec{q}}{D(q)q^2 + 1/\tau_i} \tag{8.11}$$

and obtain for the conductivity correction due to both 2D WL and anomalous diffusion the same expression as Eq. (8.1), except that now L_ϕ is replaced by $\mathcal{L}_\phi$ given in Eq. (8.8). It will be seen later why $\Delta\sigma$ is not scaled back to the supposedly bulk value using the scaling factor $(\mathcal{L}_\phi/\xi_p)^{\tilde{t}}$.

The calculation of the magnetoresistance (MR) for 2D WL in the inhomogeneous limit involves approximations that are motivated by the MR calculation in the homogeneous limit. In the homogeneous limit, the Cooper pole, with $D(q) = D_0$ and $-i\omega$ restored in the denominator of the integral in Eq. (8.11), describes a particle-particle diffusion equation which coincides in form with the Schrödinger equation with imaginary time for a particle with charge $2e$ and mass $\hbar/2D_0$. Therefore, in a magnetic field, the q-space is quantized into the Landau orbits, and the corresponding cyclotron frequency is given by $\omega = 4D_0eH/\hbar c$. The q-space quantization thus dictates that the integral in Eq. (8.11) be converted into a summation over the discrete values of $q_n^2 = (4eH/\hbar c)(n + 1/2)$.

In the inhomogeneous limit, however, the q-dependence of D changes the expression for the Cooper pole. The new differential equation for the modified Cooperon no longer resembles a Schrödinger equation and is in fact not well defined in real space, invalidating

the substitution of $q_n^2 = (4eH/\hbar c)(n+1/2)$ described above. It is noted that the integral in Eq. (8.11) is dominated by those terms with $q \sim 1/\mathcal{L}_\phi$, $\mathcal{L}_\phi$ having been defined in Eq. (8.8). We therefore propose to simplify the problem by approximating $D(q)$ in Eq. (8.11) by an effective diffusion constant $D(\mathcal{L}_\phi)$. In so doing, the form of the Schrödinger equation is preserved in the Cooperon equation, once again resulting in the Landau-orbit quantization of q-space. Such an approximation amounts to taking the cyclotron frequency as $\omega(\mathcal{L}) \simeq 4D(\mathcal{L}_\phi)eH/\hbar c$. It is easy to see that the MR in 2D is given by Eq. (8.4), the same MR expression calculated for the homogeneous limit, except for the replacement of $D_0\tau_i$ by $\mathcal{L}_\phi^2$ in the new expression for H_i, namely $H_\phi = \hbar c/4e\mathcal{L}_\phi^2$.

It is noted that in the literature [8.2,8.8], the microscopic value for $\Delta\sigma(T,H)$ on a length scale $\mathcal{L}_\phi^*(T,H) \sim \min(\mathcal{L}_\phi \equiv \mathcal{L}_\phi(T),\ L_H \equiv \sqrt{\hbar c/2eH})$ is usually scaled back to the bulk value $\Delta\sigma(L=\infty)$ according to:

$$\Delta\sigma(L=\infty) \simeq \Delta\sigma(\xi_p) \simeq \Delta\sigma(\mathcal{L}^*)\left(\frac{\mathcal{L}^*}{\xi_p}\right)^{\tilde{t}} . \tag{8.12}$$

The rescaling corrects the overestimation of the conductivity by taking into account the reduction of the extension of the "backbone" in the infinite cluster as the distance between the probing electrodes increases. We found from our experiments that there is no need for this rescaling, probably because the carriers hop before they could classically diffuse within ξ_p.

Because of the absence of the scaling factor, the temperature dependence of $\Delta\sigma$ and the field dependence of MR remain unaffected by the anomalous diffusion process, the only important effect of which is to yield a new temperature dependence for the dephasing length. Our data analysis below emphasizes these observations.

8.3 Results and Discussion

Shown in Fig. 8-1 are the conductivity $\sigma(T)$ for two phenol-based ACFs heat-treated to 2000°C and 2500°C, separately labelled as HT2000 and HT2500 for later discussion in this chapter. Consistent with the finding from the Raman scattering experiment that L_a grows with $T_{\rm HT}$, Fig. 8-1 shows that the HT2500 fiber indeed has a higher σ value and hence a more ordered in-plane structure than the HT2000 fiber. Both $\sigma(T)$ curves show a finite zero-

temperature $\sigma(0)$ value and a weak temperature dependence, signifying that the system is already out of the strong localization regime but near the metal-insulator transition. Despite the slight downturn of σ above ~250 K, corresponding to metallic transport behavior, the negative temperature coefficient of resistivity indicates that these heat-treated ACFs are only poor metals and implies that granularity still plays an important role in transport, consistent with the Raman scattering finding [8.1] that $L_a < 100$ Å. The conduction path could conceivably be limited to only the percolation cluster, and not uniformly distributed across the entire solid in the transverse direction, as would be the case near the percolation transition.

The existence of a percolation cluster is assumed also for consistency with the weak localization (WL) effect, which is observed in both our conductivity and magnetoresistance data, but supposedly only takes place in systems having metallic conductivity values. The room temperature σ values in Fig. 8-1, however, are all lower than the minimum metallic conductivity values typically observed near the metal-insulator transition. A rescaling of σ is therefore required and could be attributed to the much smaller cross-sectional area of the percolation path in comparison with that of the whole sample. This rescaling factor, though not known, could actually account for the unusually large magnitude of the effects observed in our experiments and discussed below.

In accordance with the observation of WL in the magnetoresistance data discussed below, σ is also plotted versus $\log_{10} T$ in the inset to Fig. 8-1 [see Eq. (8.1)]. No logarithmic temperature dependence is observed for either the HT2000 or the HT2500 ACFs, as is also clear from the approximately linear temperature dependence below 150 K shown in Fig. 8-1 for both samples. The linear temperature dependence is further discussed after the subtraction of the WL conductivity term from $\sigma(T)$.

In Figs. 8-2(a) and (b), the temperature-dependent transverse magnetoresistance (MR) is shown for both the HT2000 and the HT2500 fibers. The solid lines show the excellent fits up to 289 K by the 2D WL theory in the *homogeneous* limit, given by Eq. (8.4) above. The effect of the angle Θ that the magnetic field makes with the c-axis of the 2D plane is considered below, but $\Theta = 0$ is used for the 2D fit shown in Fig. 8-2. The field dependence was also fit to the 3D WL theory, but the 2D theory provides a much better fit to the MR data at each measurement temperature than does the 3D theory for both the HT2500 and the HT2000 ACFs.

To study the 2D aspect of the system more carefully, we measured the longitudinal MR for the HT2500 ACF at 4.2 K. The results are plotted in Fig. 8-3, together with the transverse MR measured during the same run. Although a slight anisotropy is detected, the localization effect is approximately isotropic, suggesting that while the electrical conduction is along glassy-carbon-like ribbons that are locally two-dimensional, these ribbons are randomly oriented globally throughout the system. Such a picture is consistent with the typical microstructures found in graphite fibers made from either phenol or isotropic pitch precursors. The small anisotropy does indicate that a larger percentage of the microcrystallites are aligned with their c-axes along the radial direction of the fiber, and that their a-axes are preferentially along the fiber axis. Such a microstructural configuration seems to be a residual effect of the fiber formation process.

The good fit in Fig. 8-2 to a strictly 2-dimensional WL theory thus seems suspect for a globally isotropic system. At first sight, the microcrystallites should be considered to form a network of interconnected resistors, the analysis of which would then require numerical simulation. However, if conduction is indeed via a percolation cluster, for various probable reasons explained above, the microcrystallites involved in the percolation cluster should then be more or less connected in series. When these microcrystallites are assumed to be identical in size and also to have the same ρ value as that observed experimentally for the bulk, the analysis can further be simplified to a fit to the 2D WL theory but with angular averaging which takes account of the assumed uniform distribution of Θ among the microcrystallites. This fit (not shown) is found to yield values for the fitting parameters close to those obtained without the angular averaging. This is not surprising since it can be shown numerically that the angle-averaged 2D WL theoretical curve can be transformed as a good approximation into the ordinary 2D WL curve with only minor change in H_i and λ. We therefore take $\Theta = 0$ in our fitting procedure.

From the fit to Eq. (8.4), the dephasing distance L_ϕ is obtained from H_i and plotted in Fig. 8-4. A detailed analysis of the Raman scattering data for the heat-treated phenol-based ACFs is not available, but Raman scattering results [8.1] for the heat-treated pitch-based ACFs with similar transport characteristics showed that the in-plane microcrystallite sizes L_a, being ~ 40 and 100 Å for $T_{\rm HT} = 2000$ and 2500°C, respectively, are of the same order of magnitude as that of the $\mathcal{L}_\phi$ values quoted above for the same $T_{\rm HT}$ values. It is observed in Fig. 8-4 that above 100 K, L_ϕ decreases very slowly with temperature and, as long as

$L_\phi \geq l$, where $l \leq L_a$, WL remains possible, thus allowing the negative MR to be observed even at room temperature.

The temperature (T) dependence of the dephasing distance is further examined on a log-log plot in Fig. 8-5 for both the HT2000 and the HT2500 ACFs, and the dependence of $\log L_\phi$ is found to be $T^{-0.43}$ and $T^{-0.31}$, respectively, which are different from the $T^{-0.5}$ dependence expected for a homogeneous system with $p = 1$. The concept of anomalous diffusion could, however, explain this anomalous T-dependence of the dephasing distance, which should then be relabelled $\mathcal{L}_\phi$ in accordance with the percolation limit. According to Eq. (8.8), we have $\mathcal{L}_\phi \sim T^{-0.35p}$, in agreement with the observed T-dependence for the HT2500 fiber if $p = 1$. For the HT2000 fiber, the observed T-dependence of $\mathcal{L}_\phi$ indicates that the system is probably between the percolation limit and the homogeneous limit, consistent with the fact that ξ_p is physically expected to be smaller for the ACF with a lower T_{HT} value and could now be comparable to $\mathcal{L}_\phi$ in magnitude.

The dephasing mechanism in the heat-treated ACFs studied here is attributed to the electron-phonon scattering involving both the in-plane and the out-of-plane long-wavelength acoustic phonon modes, which are known to be responsible for carrier scattering processes in graphite fibers [8.9]. The resultant T-dependence of the electron-phonon scattering time is found by approximating the Bose-Einstein distribution to be T^{-1}, consistent with the value of $p = 1$ observed above for the heat-treated ACFs studied here.

The 2D WL theory also predicts a logarithmic temperature dependence according to Eq. (8.1), which is not supported by the inset to Fig. 8-1. In fact, the WL conductivity correction is obscured by a more dominant temperature-dependent conduction process at work, in parallel with WL. Because negative MR is equivalent to the destruction of the WL term, continuous temperature scans of the conductivity were taken in a field of 11 T and then subtracted from the zero-field temperature scans. The difference yields the WL term, while the $\sigma(T)$ curve obtained at 11 T corresponds to the remaining component.

In Figs. 8-6(a) and (b), $\sigma(0) - \sigma(B)$ is plotted as a function of temperature at different field values for both the HT2000 and the HT2500 ACFs. The solid lines are the results obtained from the continuous temperature scans, multiplied by a factor close to unity to match the discrete data points for two other HT2000 and HT2500 samples, which are extracted from Fig. 8-2. Not only have we shown our results to be reproduceable, but we also observe the $\ln(T)$ dependence in both samples at all fields at high temperature,

verifying the functional dependence of the conductivity correction predicted by the 2D WL theory in the *homogeneous* limit. At low temperatures ($T < 20$ K), the electron-electron interaction effects might begin to set in, offseting the negative magnetoresistance due to WL and causing the upturn of the $\sigma(0) - \sigma(B)$ curves observed in both Fig. 8-6(a) and Fig. 8-6(b).

The remaining component of $\sigma(T)$ after the subtraction of $\Delta\sigma$ due to WL is plotted in Fig. 8-7 for both the HT2000 and the HT2500 ACFs. The observed linear T-dependence of the remaining σ component in a field of 11 T is ascribed to the hopping conduction between large microcrystallites. Assuming the carrier hopping is phonon-assisted, we can write $D = L_i^2/\tau_i$, where the electron-phonon scattering time τ_i is found from Fig. 8-5 to have a T^{-1} dependence, thereby yielding $\sigma \propto T$ from the Einstein relation.

In Chapter 6, it was claimed that the effect of heat treatment dominates over that of the precursor in determining the transport properties of ACFs. This has been confirmed again for higher T_{HT} values in another transport study [8.10], which shows that a pitch-based ACF heat-treated to 2860°C also has a negative MR, similar in magnitude and in field dependence to that observed in the phenol-based ACFs studied here. It is believed that the effects described in this chapter are probably general in ACF systems.

References

[8.1] A. M. Rao, A. W. P. Fung, M. S. Dresselhaus, G. Dresselhaus, and M. Endo, J. Mat. Res., **7**, 1788 (1992).

[8.2] A. G. Aronov, M. E. Gershenzon, and Yu. E. Zhuravlev, Sov. Phys. JETP **60**, 554 (1984).

[8.3] B. l. Altshuler and A. G. Aronov, in *Electron-Electron Interactions in Disordered Systems*, ed. by A. F. Efros and M. Pollak, ch. 1, p. 1 (Elsevier Science Publishing, New York, 1985).

[8.4] G. Bergmann, Phys. Rep., **107**, 1 (1984).

[8.5] D. Stauffer and A. Aharony, *Introduction to Percolation Theory* (Taylor & Francis, London, 1992).

[8.6] B. I. Shklovskii and A. l. Efros, *Electronic Properties of Doped Semiconductors* (Springer, Berlin, Heidelberg, 1984).

[8.7] D. E. Khmelnitskii, JETP Lett. **32**, 229 (1980).

[8.8] Y. Gefen, D. J. Thouless, and Y. Imry, Phys. Rev. **B28**, 6677 (1983).

[8.9] M. S. Dresselhaus, G. Dresselhaus, K. Sugihara, I. l. Spain, and H. A. Goldberg, *Graphite Fibers and Filaments* (Springer, Berlin, Heidelberg, 1988).

[8.10] A. W. P. Fung, Z. H.Wang, M. S. Dresselhaus, G. Dresselhaus, and M. Endo, in *Electrical, Optical, and Magnetic Properties of Organic Solid State Materials*, edited by A. F. Garito, A. K.-Y. Jen, L. R. Dalton and C. Lee, MRS Symposia Proceedings, No. 328 (Materials Reseach Society, Pittsburgh, 1994), p. 793.

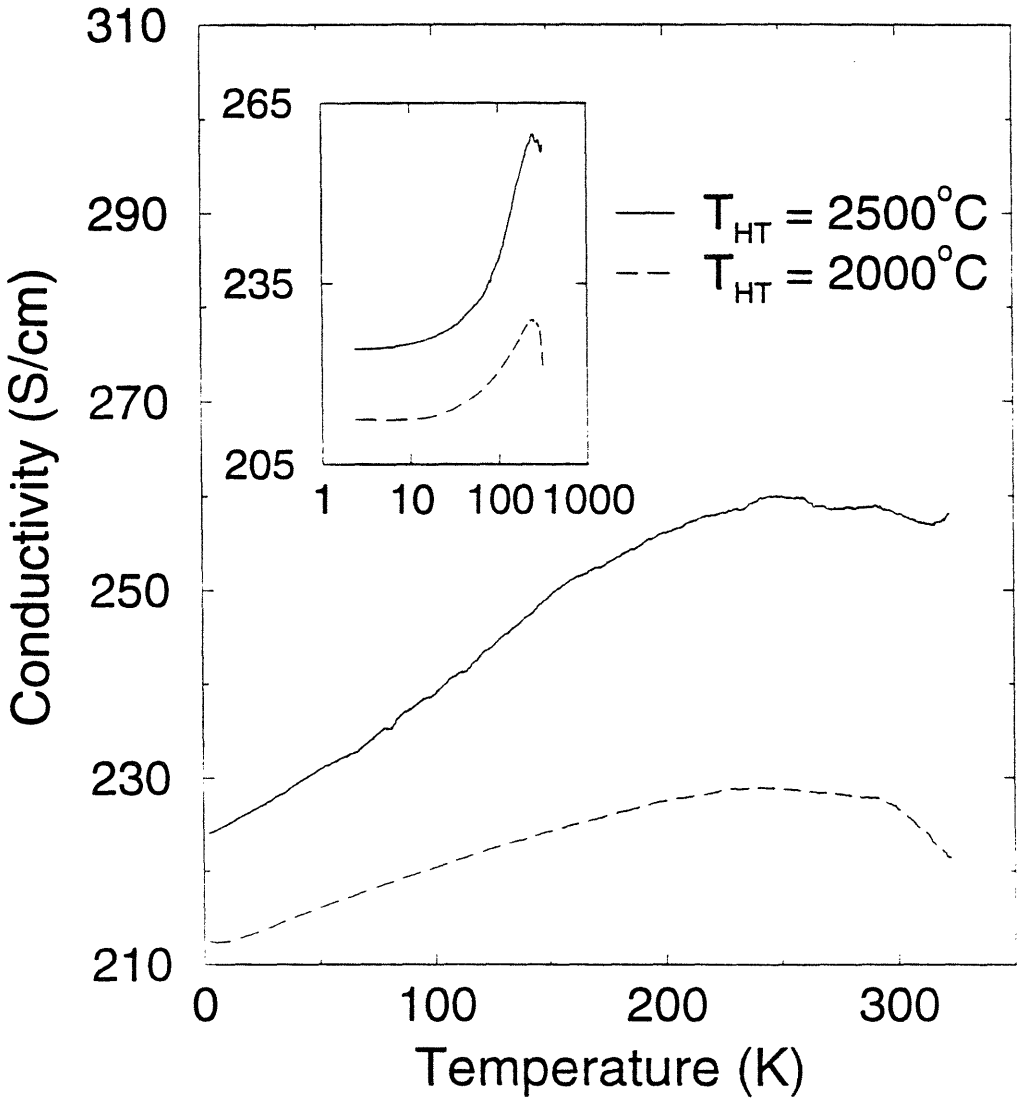

Figure 8-1: Temperature dependence of the dc electrical conductivity for the phenol-based ACFs with heat treatment temperatures (T_{HT}) of 2000°C and 2500°C. The inset shows the same plots on a logarithmic temperature scale.

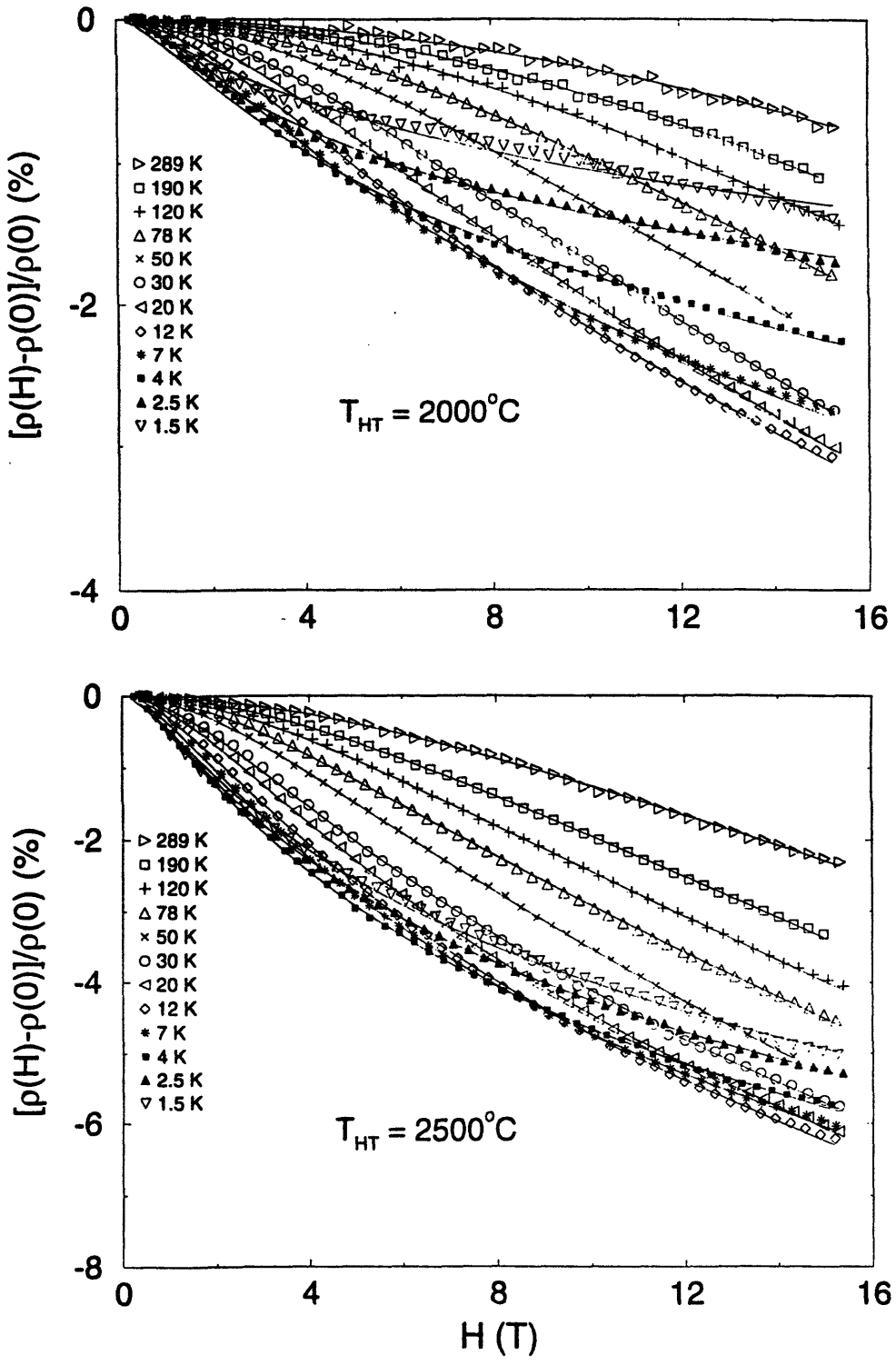

Figure 8-2: Magnetic field dependence of the magnetoresistance at a number of measurement temperatures for the phenol-based ACF heat-treated to (a) 2000°C and (b) 2500°C. The solid lines are the fits to 2D weak localization theory.

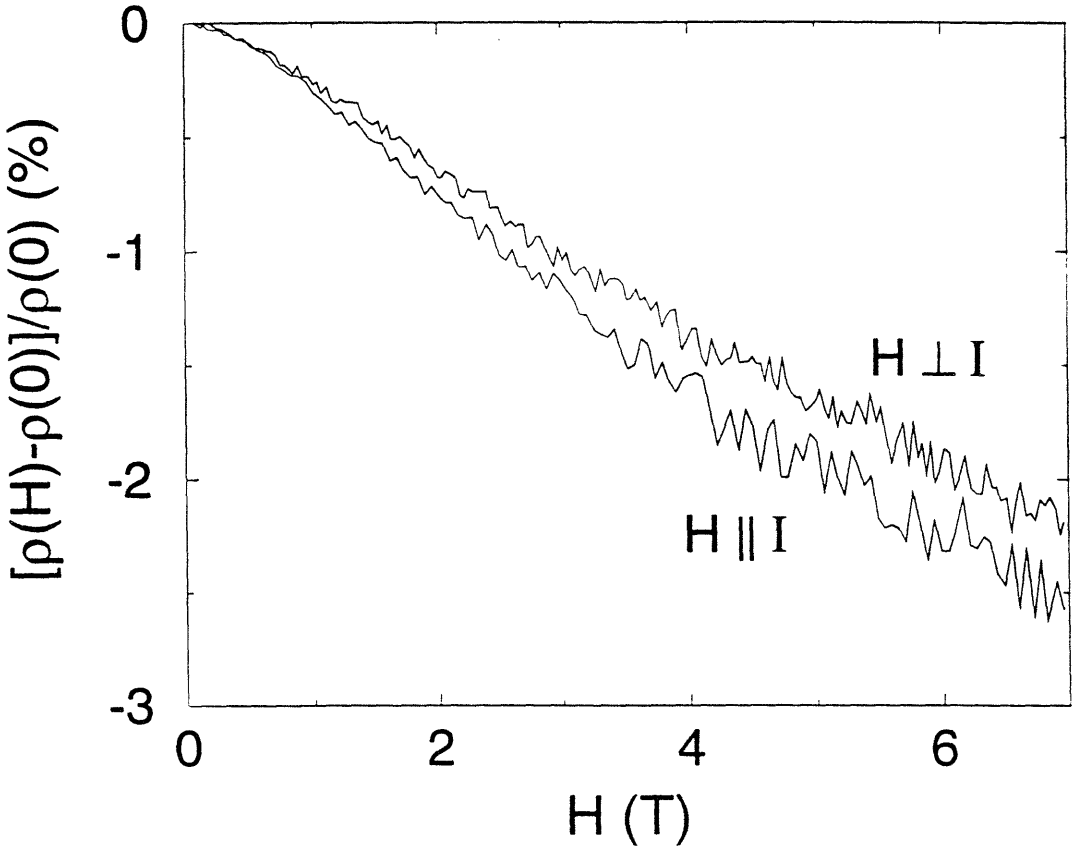

Figure 8-3: Longitudinal (H $\parallel$ I) and transverse (H $\perp$ I) magnetoresistance vs H for a phenol-based ACF heat-treated at 2500°C.

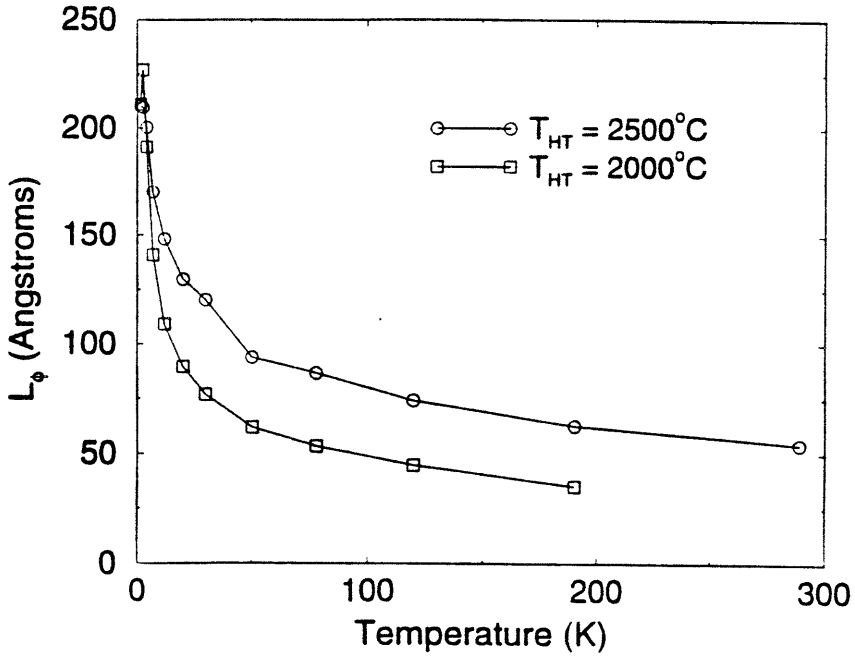

Figure 8-4: Temperature dependence of the dephasing distance L_ϕ for the phenol-based ACFs with heat treatment temperatures T_{HT} = 2000 and 2500°C, respectively.

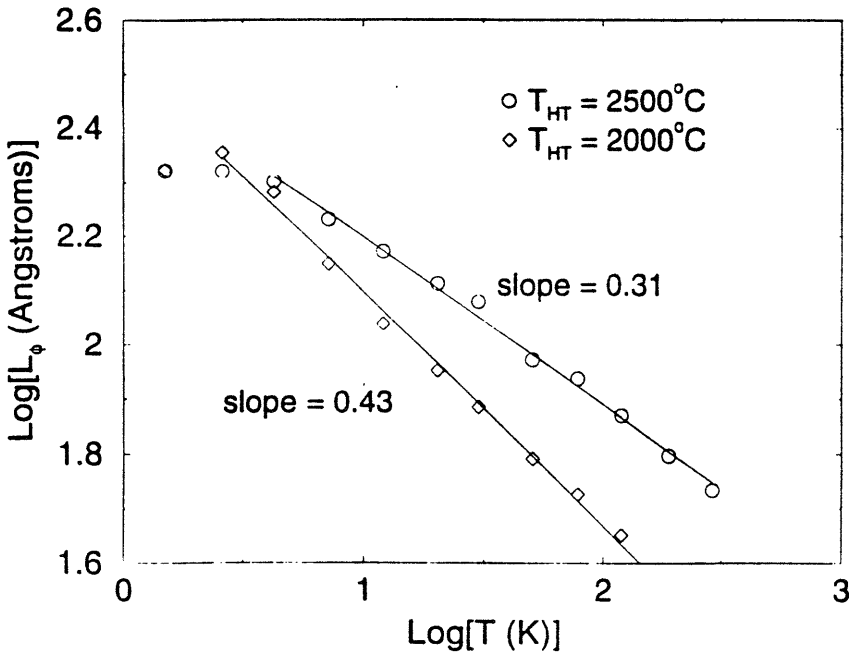

Figure 8-5: Temperature dependence of the dephasing distance L_ϕ plotted on a log-log scale for phenol-based ACFs heat-treated at 2000°C and 2500°C

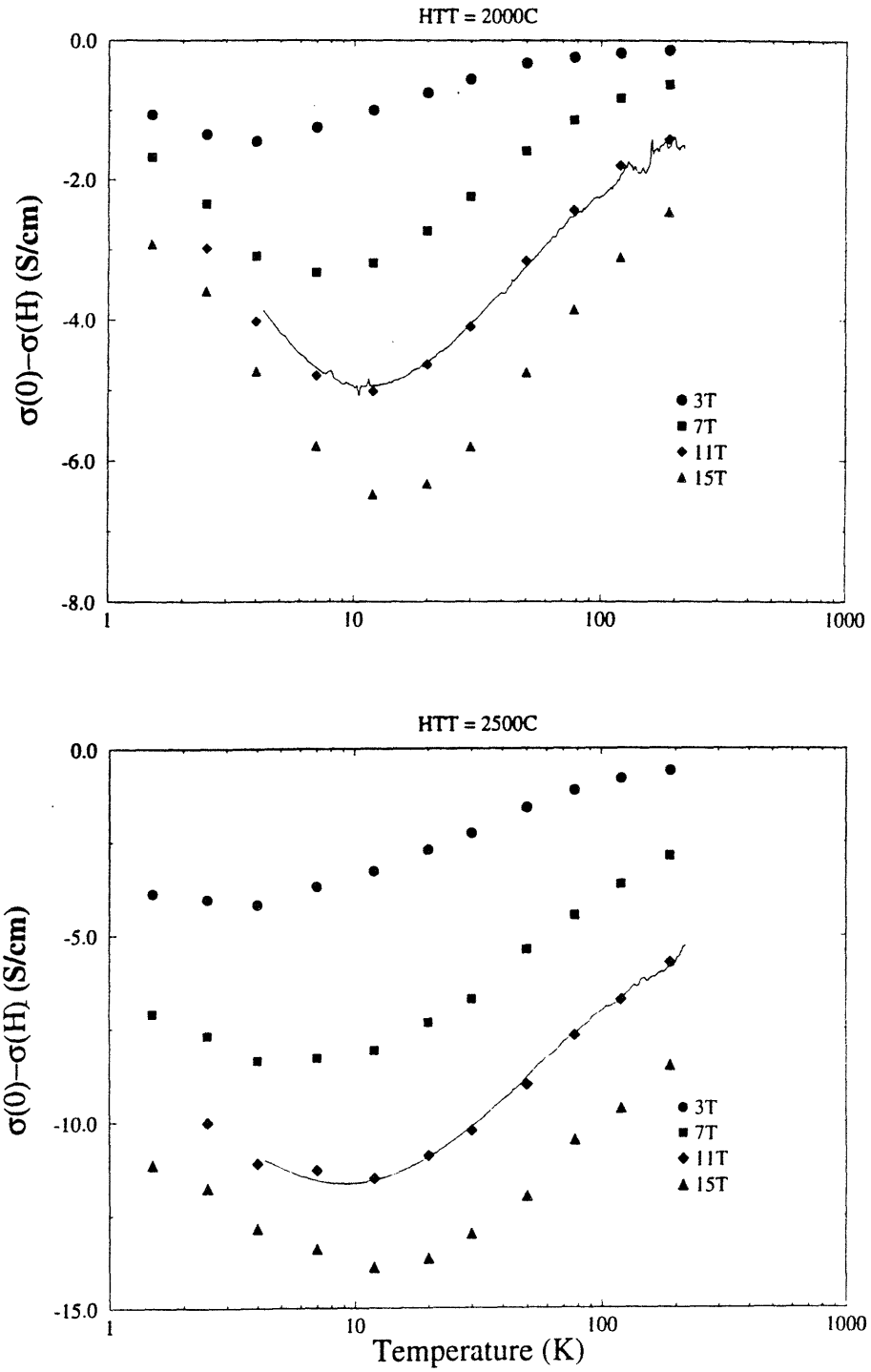

Figure 8-6: Temperature scans of the conductivity in different magnetic fields for phenol-based ACFs heat-treated at (a) 2000°C and (b) 2500°C. The solid lines in (a) and (b) are the difference between the continuous temperature scan in zero fields and that in 11 T, multiplied by a factor close to unity to match the discrete data points obtained from the magnetoresistance measurements at the indicated fields and temperatures.

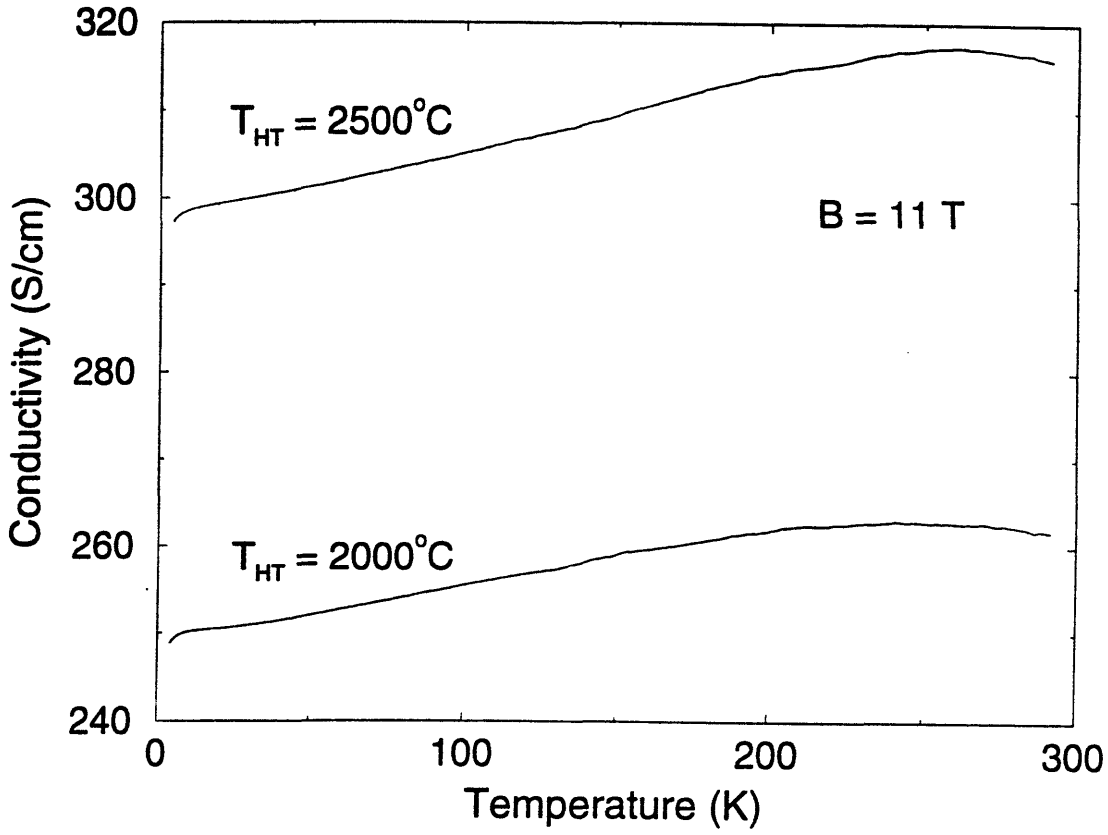

Figure 8-7: Temperature dependence of the conductivity in a magnetic field (B) of 11 T for phenol-based ACFs heat-treated at 2000°C and 2500°C.